



VARIABILITY IN THE CIRCULATION, TEMPERATURE, AND SALINITY FIELDS
OF THE EASTERN BERING SEA SHELF
IN RESPONSE TO ATMOSPHERIC FORCING

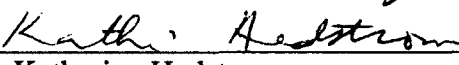
By

Seth Lombard Danielson


RECOMMENDED:

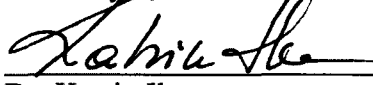

Dr. Knut Aagaard


Dr. Kenneth Coyle



Dr. Katherine Hedstrom

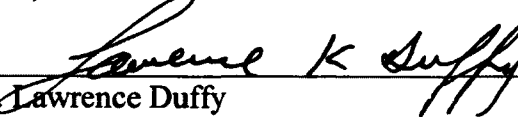

Dr. Zygmunt Kowalik


Dr. Thomas Weingartner
Advisory Committee Chair


Dr. Katrin Iken
Head, Program in Marine Science and Limnology

APPROVED:


Dr. Michael Castellini
Dean, School of Fisheries and Ocean Sciences


Dr. Lawrence Duffy
Dean of the Graduate School


Date

VARIABILITY IN THE CIRCULATION, TEMPERATURE, AND SALINITY FIELDS
OF THE EASTERN BERING SEA SHELF
IN RESPONSE TO ATMOSPHERIC FORCING

A
THESIS

Presented to the Faculty
of the University of Alaska Fairbanks
in Partial Fulfillment of the Requirements
for the Degree of
DOCTOR OF PHILOSOPHY

By

Seth Lombard Danielson, B.S., M.S.

Fairbanks, Alaska

May 2012

UMI Number: 3528857

All rights reserved

INFORMATION TO ALL USERS

The quality of this reproduction is dependent upon the quality of the copy submitted.

In the unlikely event that the author did not send a complete manuscript and there are missing pages, these will be noted. Also, if material had to be removed, a note will indicate the deletion.

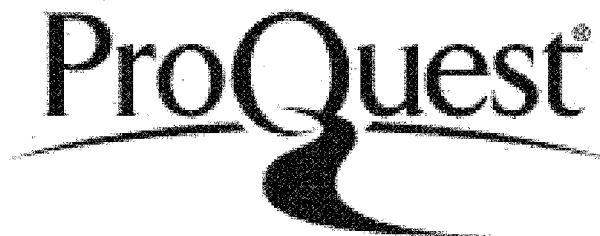


UMI 3528857

Published by ProQuest LLC 2012. Copyright in the Dissertation held by the Author.

Microform Edition © ProQuest LLC.

All rights reserved. This work is protected against unauthorized copying under Title 17, United States Code.



ProQuest LLC
789 East Eisenhower Parkway
P.O. Box 1346
Ann Arbor, MI 48106-1346

Abstract

Although the Bering Sea shelf plays a critical role in mediating the global climate and supports one of the world's largest fisheries, fundamental questions remain about the role of advection on its salt, fresh water, heat and nutrient budgets.

I quantify seasonal and inter-annual variability in the temperature, salinity and circulation fields. Shipboard survey temperature and salinity data from summer's end reveal that advection affects the inter-annual variability of fresh water and heat content: heat content anomalies are set by along-shelf summer Ekman transport anomalies whereas fresh water content anomalies are determined by wind direction anomalies averaged over the previous fall, winter and early spring. The latter is consistent with an inverse relationship between coastal and mid-shelf salinity anomalies and late summer – winter cross-shelf motion of satellite-tracked drifters. These advection anomalies result from the position and strength of the Aleutian Low pressure system.

Mooring data applied to the vertically integrated equations of motion show that the momentum balance is primarily geostrophic within at least one external deformation radius of the coast. Local accelerations, wind stress and bottom friction account for < 20% (up to 40%) of the along- (cross-) isobath momentum balance, depending on location and season. Wind-forced surface Ekman divergence is primarily responsible for flow variations. The shelf changes abruptly from strong coastal convergence conditions to strong coastal divergence conditions for winds directed to the south and for winds directed to the west, respectively, and substantial portions of the shelf's currents reorganize between these two modes of wind forcing.

Based on the above observations and supporting numerical model integrations, I propose a simple framework for considering the shelf-wide circulation response to variations in wind forcing. Under southeasterly winds, northward transport increases and onshore cross-isobath transport is relatively large. Under northwesterly winds, onshore transport decreases or reverses and nutrient-rich waters flow toward the central shelf from the north and northwest, replacing dilute coastal waters that are carried south and west. These results have implications for the advection of heat, salt, fresh water, nutrients, plankton, eggs and larvae across the entire shelf.

Table of Contents

	Page
Signature Page	i
Title Page	ii
Abstract	iii
Table of Contents.....	iv
List of Figures	viii
List of Tables	xii
Acknowledgements.....	xiii
Chapter 1: Introduction.....	1
1.1 Background	1
1.2 Approach.....	3
1.3 References.....	5
1.4 Figures.....	8
Chapter 2: Thermal and haline variability over the central Bering Sea shelf: Seasonal and inter-annual perspectives	9
2.1 Abstract	9
2.2 Introduction.....	10
2.3 Datasets and Methods	13
2.3.1 CTD data	13
2.3.2 Mooring data	14
2.3.3 Nutrient data	15
2.3.4 Ice cover data	15
2.3.5 Streamflow data.....	15
2.3.6 Drifter data	15
2.3.7 St. Paul meteorological data.....	16
2.3.8 Sea surface temperature data.....	16
2.3.9 Atmospheric model fields	17

2.3.10 HC and FWC computations	18
2.4 Temperature and salinity in late summer/early fall.....	18
2.4.1 Late summer/early fall mean T & S fields	18
2.4.2 Inter-annual variability of the late summer/early fall T & S fields.....	21
2.5 Fresh water and heat content variability and fluxes.....	22
2.5.1 Seasonal variability	22
2.5.2 FWC inter-annual variability	27
2.5.3 HC inter-annual variability.....	28
2.6 Discussion and concluding remarks.....	30
2.7 Acknowledgements.....	33
2.8 References.....	34
2.9 Tables.....	41
2.10 Figures.....	44
Chapter 3: On ocean and sea ice modes of variability in the Bering Sea	60
3.1 Abstract	60
3.2 Introduction	61
3.3 Numerical model description	65
3.4 Methods and data	67
3.4.1 Model output and evaluation metrics	67
3.4.2 Time series data for model evaluation	68
3.4.3 CTD and bottle data	69
3.4.4 Sea ice data.....	70
3.4.5 Ecosystem indicator time series	70
3.5 Model-data comparisons	70
3.5.1 Tides and currents	70
3.5.2 Temperature and salinity.....	75
3.5.3 Sea ice	77
3.6 Discussion	79
3.6.1 Model strengths and weaknesses.....	79

3.6.2 Trends in the annual duration of ice-free waters.....	80
3.6.3 Temperature and salinity variability	81
3.6.4 Biological covariates	85
3.7 Concluding remarks	87
3.8 Acknowledgements	87
3.9 References.....	88
3.10 Tables	100
3.11 Figures.....	107
Chapter 4: Circulation on the central Bering Sea shelf.....	122
4.1 Abstract	122
4.2 Introduction	123
4.3 Data and methods.....	126
4.3.1 Mooring configurations.....	126
4.3.2 Moored velocity data.....	127
4.3.3 Moored pressure, temperature and salinity data.....	128
4.3.4 Shipboard temperature and salinity data	129
4.3.5 Gridded sea surface temperatures and ice concentrations.....	130
4.3.6 Reanalysis winds	130
4.3.7 Model-generated sea surface heights	131
4.4 Results	131
4.4.1 Shelf conditions, July 2008 to July 2010	131
4.4.2 Temperature and salinity	132
4.4.3 Currents and winds.....	133
4.4.4 The momentum balance	135
4.4.5 Co-variability of the current, wind and SSH fields.....	140
4.5 Discussion	143
4.6 Conclusions	149
4.7 Acknowledgments.....	150
4.8 References:.....	150

4.9 Tables	159
4.10 Figures.....	163
Chapter 5: Wind-induced changes to the eastern Bering Sea shelf circulation field.....	180
5.1 Abstract	180
5.2 Introduction	180
5.3 Bering shelf circulation:.....	181
5.4 Transport over an idealized Bering Sea shelf	182
5.5 Transport over a more realistic Bering Sea shelf.....	184
5.6 Discussion and conclusions	187
5.7 Acknowledgements	188
5.8 References	189
5.9 Figures.....	192
Chapter 6: Conclusions	196
6.1 Summary of results	196
6.2 Future recommendations.....	199
6.3 References	202
6.4 Figures.....	204

List of Figures

	Page
Figure 1.1: Map of the Bering Sea region with place names.....	8
Figure 2.1: Map of the Bering Sea with place and feature names.....	44
Figure 2.2: Relation of total nitrate to salinity for 779 water samples collected across the Bering Shelf between 2002 and 2006.	45
Figure 2.3: BASIS program CTD station coverage over the eastern Bering Sea shelf, 2002-2007.	46
Figure 2.4: Mean late summer-early fall 2002-2007 distributions of temperature (left) and salinity (right) above (top) and below (bottom) the mixed layer depth.....	47
Figure 2.5: 2002-2007 mean maximum water column Brunt-Vaisala frequency.	48
Figure 2.6: Temperature and salinity anomalies above (\uparrow) and below (\downarrow) the mixed layer depth (MLD = depth where $\sigma_t = \sigma_t @ 5 \text{ m} + 0.1 \text{ kg m}^{-3}$).....	49
Figure 2.7: Late summer-early fall temperature (A) and salinity (B) vertical correlation maps, showing the temporal correlation between values above the MLD with values below the MLD at zero lag.	50
Figure 2.8: Late summer-early fall temperature and salinity horizontal correlation maps.	51
Figure 2.9: Climatology of the 0-100 m mean temperature (top row) and salinity (bottom row) in the eastern Bering Sea during the time periods indicated.	52
Figure 2.10: April to September estimated fresh water (FW) and heat fluxes and changes in standing stocks for the central Bering Sea shelf.	53
Figure 2.11: CTD transect occupied on 15-16 July 2009 between 61.70 °N, 166.31 °W and 61.97 °N, 171.98 °W.	54
Figure 2.12: Mean seasonal flow patterns derived from near-surface oceanographic drifters for June-August (left) and September-January (right).	55
Figure 2.13: Annual mean cycle of mean daily surface heat fluxes for the central shelf region over the years 2002-2007.....	56

Figure 2.14 Mean October to May 2002-2007 maps of sea level pressure	57
Figure 2.15: Mean April to August 2002-2007 maps of sea level pressure	58
Figure 2.16: Mean monthly Ekman Transport computed from the NCEPR 6-hourly wind fields between 2002 and 2007.....	59
Figure 3.1 Schematic of the eastern Bering Sea and adjacent regions with major (idealized) summertime current and water mass features, typical spring and fall ice extent bounds, and place names.....	107
Figure 3.2: NEP5 model domain extent and bathymetric depths plotted on a Mercator projection map.	108
Figure 3.3: Locations of data employed in model evaluations.	109
Figure 3.4: NEP5 model-derived M_2 co-tidal chart for the Bering Sea and Gulf of Alaska.	110
Figure 3.5: Comparison of model-derived M_2 tidal elevation and current analyses at the locations of the moored and coastal tide stations plotted in Figure 3.3.....	111
Figure 3.6: Vertical structure of the M_2 (left) and K_1 (right) tidal ellipse parameters....	112
Figure 3.7: Power spectra density (PSD) at 10 m (upper four panels) and 50 m (lower four panels) depths at mooring site M2 from observations (shading) and model (lines).	113
Figure 3.8: Mooring site M2 1995-2005 annual cycle of temperature and salinity monthly means and anomalies from 10 m (upper row) and 60 m (lower row) depths.	114
Figure 3.9: Temperature and salinity Taylor diagrams for the 10 m and 70 m depth levels.	115
Figure 3.10: Near-bottom contours of T' and S' from CTD data (upper panels) and model hind-casts (lower panels).	116
Figure 3.11: Bering Sea integrated ice extent and anomalies from the model and passive microwave satellite observations.	117
Figure 3.12: Comparison of modeled and observed ice concentrations.	118
Figure 3.13: Time series of the annual number of ice-free days.	119

Figure 3.14: Correlation maps of 1970-2005 NEP5 hindcast monthly average 0-20 m temperature (left) and salinity (right) time series.	120
Figure 3.15: EOFs of the NEP5 hindcast near surface (0-20 m) and subsurface (40-100 m) temperature (upper two rows) and salinity (lower two rows) fields.	121
Figure 4.1: The eastern Bering Sea with place names and mooring sites (squares).....	163
Figure 4.2: Contoured time series of temperature at moorings N55 (top), C55 (center), and S55 (bottom) from July 2008 to July 2010.	164
Figure 4.3: Daily mean salinity (S_p) time series.	165
Figure 4.4: Time series of 35 hr low-pass filtered, water column average along-principal axis component of currents at each mooring site.....	166
Figure 4.5: Time series of 35 hr low-pass filtered, water column average cross-principal axis component of the flow field at each mooring site.	167
Figure 4.6: Mean monthly decomposition of the flow field into ellipses denoting the along- and cross-principal axis of variation for currents at 20 m depth.	168
Figure 4.7: North-south ($0^\circ T$) and east-west ($90^\circ T$) wind components at the NARR grid point closest to mooring C55.	169
Figure 4.8 Coherence-squared of the NARR wind field with respect to NARR winds at a reference site located at $60^\circ N$, $170^\circ W$ for short (< 32 hr, left) and long (> 32 hr, right) periods from July 2008 to July 2010.....	170
Figure 4.9: Seasonal averages of water column average currents (upper panels) and winds (lower panels) in the study region.....	171
Figure 4.10: Time series of each term of the harmonically de-tided, vertically integrated equations of motion (eq. 1) at site C25.....	172
Figure 4.11: Pie charts depicting the relative contribution of the momentum balance terms to each site's total based on 35-hr low-pass filtered RMS magnitudes.	173
Figure 4.12: Geopotential height anomaly (color shading) and geostrophic current vectors computed over 0-30 db for 2006-2010 late winter and early spring (left) and late summer and early fall (right).	174

Figure 4.13: Coherence-squared (γ^2) between NARR winds at each mooring site with currents measured at 5 m depth.	175
Figure 4.14: Rotary coherence-squared (γ^2) of vertically averaged currents from all mooring pair combinations.	176
Figure 4.15: Rotary coherence-squared (γ^2) between currents at 5 m and those at 10 m, 20 m, 30 m and 40 m depths for the 55 m (left), 40 m (center) and 25 m (right) moorings for the mid-frequency band (32-102 hr) as a function of calendar month.	177
Figure 4.16: SSH time series.	178
Figure 4.17: Composite oceanic response to various wind directions.	179
Figure 5.1: The Bering shelf.	192
Figure 5.2: Barotropic model results for a) no wind, b) southeasterly wind and c) northwesterly wind.	193
Figure 5.3: Vertically averaged current vectors from the three-dimensional model for a) the 1987-2007 mean, b) December 2000 (southeasterly winds) and c) December 1999 (northwesterly winds).	194
Figure 5.4: On-shelf transport at the grid points shown in Figure 1 for a) October-April and b) May-September.	195
Figure 6.1: Theoretical particle displacements at 5 m depth based on the assumption of spatially uniform flow field.	204

List of Tables

	Page
Table 2.1: Summary of BASIS CTD surveys and spring environmental conditions.	41
Table 2.2: Fresh water content estimates.	42
Table 2.3: Heat content estimates.	43
Table 3.1: Sources of historical tidal parameters, moored time series data, and net speed and direction statistics used in model evaluations.	100
Table 3.2: Number of CTD and bottle stations for each region shown in Figure 3.3D..	101
Table 3.3: Time series employed for correlation analyses and their sources.	102
Table 3.4: Statistics of current meter vectors compared to co-located (in space and time) model-derived vectors.	103
Table 3.5: Results of cross-correlations between the principal components and various environmental time series.	104
Table 3.6: Temporal correlations between ecosystem indicator time series and the principal components (PC).	105
Table 4.1: Mooring deployment details.	159
Table 4.2: Seasonal current meter statistics at all mooring sites for the water column vertical average (VA) and depths 5, 10, 20, 30 and 40 m below the surface.	160
Table 4.3: Relative contribution of individual momentum balance terms to the 35-hour filtered vertically integrated equations of motion, averaged across all mooring sites and separated by season.	161
Table 4.4: Comparison of the cross-correlation (r) between observed SSH fluctuations and the BESTMAS model SSH hindcasts for two time intervals.	162

Acknowledgements

This dissertation is the product of many interconnected collaborations. I thank my boss, advisor, and friend Tom Weingartner for his unusually flawless guidance and for the caring demeanor with which he oversees his team of students and staff members. It was with Tom that I learned to appreciate the ability to look at a dataset from as many perspectives as possible in order to find and tease out the underlying story. Most physical observations can be readily described; insight comes from identifying data that do not line up with preconceived notions or finding disparate observations that initially appear contradictory. It is hard to express the pleasure attained from achieving new knowledge and understanding through the application of a novel analysis. In pursuing the story of the St. Lawrence Island polynya with Tom and Knut Aagaard, I re-discovered the fun in chasing an elusive story hidden within the data and discovered for the first time that I did in fact enjoy the process of writing. These years as a student have allowed me to refine my analytical and writing skills. As an engineer, numerical data analysis and manipulations were always fun but writing never came easily and the process of learning to write was not easy. For all of these reasons, I thank both Tom and Knut for instilling within me the drive to undertake this PhD program, for providing me with the opportunity to help design and analyze the data from our Bering shelf mooring array, and for helping me develop a more compact, readable, and accurate writing style.

Kate Hedstrom and Enrique Curchitser (at Rutgers University) allowed me full access to their Northeast Pacific (NEP) numerical model results and I am thankful for their willingness to put up with my non-modelers perspective, critiques, questions, and idiosyncrasies. Kate went far beyond the call of duty in assisting my requests for special model runs to look at tides and implementing the idealized Bering Shelf integrations. Luckily, some of our hunches turned out to be good ones and these diversions proved to be remarkably illuminating. Wednesday dinners with Kate and Rob Cermak are one of the highlights of my week and give us a great chance to catch up and discuss work, life,

play and various issues we are grappling with, from home power systems to numerical modeling approaches.

No one compares with Zygmunt Kowalik. Zygmunt ensures that I keep grounded, always returns the conversation to the practical realities and reminds me that most new discoveries are simply re-discoveries of forgotten knowledge. Zygmunt's guidance in evaluating the model tides was invaluable. Likewise, Ken Coyle is more than a token biologist on my committee: Ken's wealth of knowledge about the marine ecosystem is a constant source of insight.

This work would not have achieved the same broad scope had it not been for the assistance and support of many researchers and research programs. In particular, the Bering-Aleutian Salmon International Survey (BASIS) program, a component of the NOAA Alaska Fisheries Science Center in Juneau, AK, kindly provided me with six years of conductivity-temperature-depth (CTD) survey data for analysis. I thank BASIS scientists Lisa Eisner and Ed Farley for their assistance and support. Phyllis Stabeno, of the NOAA Pacific Marine Environmental Laboratory (PMEL), provided moored velocity, temperature, and salinity data from Bering Sea mooring M2. Jackie Grebmeier and Lee Cooper have always unselfishly shared their data and I appreciate the opportunity to use their CTD survey data within my seasonally averaged compilations. Likewise, Rolf Gradinger, Katrin Iken and Bodil Bluhm provided rare in situ ice thickness and salinity data, these data provided an observational basis for the fresh water content of ice estimates. The Bering Sea Program, jointly funded by the National Science Foundation and North Pacific Research Board, supported the lion's share of the numerical modeling and observational data used in my research. I thank Bill Wiseman for his support and confidence in our team's approach.

Many other past and present students, staff and faculty and non-UAF colleagues also deserve thanks of gratitude. It is impossible to comprehensively list all of the other people who have provided to me their support, assistance, and encouragement over the years, and I apologize in advance to any who I inadvertently leave out. However, I am bound to try, so here goes: thank you to Rachel Potter, Hank Statscewich, David Leech,

Stephen Hartz, Jeremy Kasper, Bill Williams, Markus Janout, Bob Pickart, Eddy Carmack, Fred Castruccio, Peter Winsor, Mark Johnson, Harper Simmons, Dave Musgrave, Tom Royer, Dean Stockwell, Sarah Thornton, Dan Oliver, Russ Hopcroft, Cheryl Hopcroft, Jonathan Whitefield, Chase Stoudt, Jim Kelley, Kim Martini, Liz Dobbins, Georgina Gibson, Al Hermann, Nick Bond, Nici Murawski, Linda Lasota, Jennifer Elhard, Mark Vallarino, Gary Newman, John Haverlack, Chirk Chu, Army Blanchard, Igor Polyakov, Jim Johnson, Lewis Sharman, Brendan Moynahan, Bill Johnson, and all of the past crew on the *R/V Alpha Helix*.

I cannot adequately express my gratitude to my family for putting up with my long hours at work and many work-related trips away from home. I thank Mum, Dad, Pips, Danny and Mari for always being there. I thank Donna, Joe, Jody and Shana for sharing your wonderful Jen with me. I thank Iris and Helen for providing more pleasure to my life than I could have possibly imagined. I thank Jen for being my sounding board, my voice of reason, and my best friend. I love you all.

Chapter 1: Introduction

1.1 Background

The Bering Sea shelf (Figure 1.1) exerts strong influence on the earth's climate system due to its regulation of fresh water transport between the North Pacific and the Arctic Ocean [Aagaard and Carmack, 1989; Shaffer and Bendtsen, 1994; De Boer and Nof, 2004]. It also supports one of the most productive fisheries in the world [Van Voorhees and Lowther, 2011]. Fundamental questions remain, however, about controls on the along- and cross-isobath exchanges of heat, salt, fresh water, and nutrients [Aagaard et al., 2006] and how variations in these properties impact the climate and the regional ecosystem.

The Bering Sea shelf's geological characteristics and spatially and temporally varying physical processes define its marine environment. Along-shelf (1200 km) and cross-shelf (500 km) dimensions are vast and can exceed synoptic atmospheric length scales. With low relief and small mean cross-shelf bottom slopes ($\sim 4 \times 10^{-4}$), the shelf is bounded by land on all sides except along the southwest-facing continental slope and Bering Strait, the shelf's connection to the Chukchi Sea. Four large submarine canyons cut into the continental slope [Normak and Carlson, 2003]. As a strongly seasonal sub-arctic transition zone between the North Pacific and the arctic, the shelf's annual cycle of heating, cooling and sea ice extent follow the surface heat fluxes, determined primarily by the solar angle. Winter and spring pack ice extent is controlled by winds and storm tracks [Pease, 1980; Overland and Pease, 1982]. Rivers supply a strongly seasonal input of fresh water ($\sim 320 \text{ km}^3 \text{ yr}^{-1}$) to the coastal zone [Aagaard et al., 2006]. Strong wind events are common through fall, winter and spring months due to storms associated with the Aleutian Low pressure system [Overland et al., 1999; Rodionov et al., 2007]. Tidal currents over most of the shelf are strong and help maintain a well-mixed region close to shore and a weakly stratified near-bottom layer farther offshore [Pearson et al., 1981; Coachman, 1986; Kowalik, 1999]. A large shelf outflow ($\sim 0.8 \text{ Sv}$; $1 \text{ Sv} = 10^6 \text{ m}^3 \text{ s}^{-1}$) through Bering Strait links the North Pacific to the Arctic [Coachman and Aagaard,

1966; *Aagaard et al.*, 1985; *Roach et al.*, 1995; *Woodgate et al.*, 2005] due to a steric height difference of ~ 0.5 m [*Stigebrandt*, 1984] caused by global-scale processes.

The narrow (80 km), shallow (50 m) Bering Strait flow impacts both regional and global scale processes [*Paquette and Bourke*, 1981; *Aagaard and Carmack*, 1989; *Broecker and Denton*, 1990; *Goosse et al.*, 1997; *De Boer and Nof*, 2004; *Grebmeier et al.*, 2006; *Spall*, 2007; *Woodgate et al.*, 2010]. Bering shelf waters cross the Chukchi Sea and ultimately feed the arctic halocline, which acts as an insulating layer between the surface pack ice and the relatively warm Atlantic-origin water below [*Aagaard et al.*, 1981]. Heat advected north through Bering Strait impacts the regional ice dynamics [*Paquette and Bourke*, 1981; *Spall*, 2007; *Woodgate et al.*, 2010] and may play a role in the Arctic ice extent and the albedo-ocean heat feedback loop. Fresh water advected north through Bering Strait represents a first order contribution to the Arctic's fresh water budget [*Aagaard and Carmack*, 1989], which in turn likely helps regulate the global thermohaline circulation by modifying rates of deepwater formation in the North Atlantic [*Shaffer and Bendtsen*, 1994; *Wadley and Bigg*, 2006].

The Bering Sea's productive ecosystem supplies approximately one-half of our nation's ocean-caught seafood and supports commercial fisheries that include pollock, herring, halibut, snow crab, king crab, and salmon [*Van Voorhees and Lowther*, 2011]. The biological production also supports large seabird and marine mammal populations. Subsistence fisheries and marine mammal harvests supply dozens of coastal indigenous communities with traditional foods. Challenges to the fisheries management include identification of sustainable harvest levels within this dynamic ecosystem, where inter-species competition, fishing effects, climate, and other factors play a role [*North Pacific Fishery Management Council (NPFMC)*, 2011].

The Bering Sea is also the site of significant and increasing industrial activities. Dutch Harbor is an important port in the great circle route for transits between Pacific Rim nations. Tankers carrying natural gas southward from the Arctic are recent additions to the seascape and will continue to grow in number [*Orr*, 2011]. With projections of decreased summer ice extent in the Arctic [e.g., *Zhang and Walsh*, 2006], it is likely that

other trans-Arctic cargo vessel traffic will also increase. Local industrial activities, aside from fishing, include subsea mining, cruise ship tourism, and barge traffic to western Alaska villages, towns and terrestrial mines. In the last decade, the federal government has opened and then subsequently closed a large portion of the southeastern Bering Sea to oil and gas exploration. Future exploration nevertheless remains an option. The frequency of stormy weather conditions together with the number of vessels associated with all of these activities and the locations of critical habitat for several endangered species (e.g., the spectacled eider, northern sea otter, North Pacific right whale) places the Bering Sea at particular risk for at-sea accidents, such as the 2004 *M/V Selendang Ayu* oil and soybean spill [Brewer, 2006].

Better management of the fisheries and ecosystem, planning for and assisting incident response operations (e.g., search and rescue; oil spill cleanup), assessing the potential impacts of future development, and understanding of global climate systems that are linked to regional Bering Sea processes requires a more complete mechanistic understanding of the Bering Sea shelf.

1.2 Approach

This thesis provides a description of spatial and temporal variability of the eastern Bering Sea shelf circulation, temperature and salinity fields and identifies processes that control their variations. I seek new insight into the nature and structure of these variations and their subsequent impacts upon the shelf environment.

I employ *in situ* and remotely sensed observational data as well as results from atmospheric and oceanographic numerical models. The data include shipboard profile and bottle data, moored time series, satellite data, land-based weather station data, satellite-tracked oceanographic drifter data, and measurements of river discharge and ice thickness. Numerical model output includes atmospheric reanalysis hind-casts, three-dimensional ocean-ice circulation hind-casts and an idealized barotropic process model.

In Chapter 2, I examine recently collected and historical CTD data in order to quantify the magnitude of seasonal and inter-annual variations in integrated fresh water content (FWC) and heat content (HC) budgets. The analysis reveals that alteration of the

shelf advective field results in inter-annual variability of thermal and haline fields, and that these are controlled by the location and strength of the Aleutian Low.

Chapter 3 undertakes a comparison of Northeast Pacific (NEP) model hindcasts over 1970-2005 to spatially and temporally co-located observational data. I compiled a new, publically available, high-resolution (~ 1 km) bathymetric digital elevation model (DEM) for the greater Alaska region to support these modeling efforts. I analyze the model results, identifying major modes of temperature, salinity and sea ice variations. Correlation analysis reveals these modes are significantly correlated to common indices of North Pacific climate variability. These results provide a better appreciation of the shelf response to climate variability in the study region where oceanic observations are limited. I show that the primary modes of variability co-vary with numerous ecosystem indicator time series.

Chapter 4 focuses on current meter mooring observations from the central shelf with supporting results from the Bering Ecosystem Study Ice-Ocean Modeling and Assimilation System (BESTMAS) numerical circulation model. The analysis identifies two distinct modes of shelf circulation that stem from the influence of Ekman transport during upwelling and downwelling wind conditions. I present these results in the context of the momentum balance, solving the vertically integrated and linearized equations of motion, and with respect to seasonal variations in the wind, ice, and stratification fields.

In Chapter 5, I develop a new but simple and encompassing framework for considering the Bering shelf circulation field as an integrated whole, using current meter moorings, hindcast winds, NEP model results and idealized barotropic model results. This framework conforms to well-known and newly described (in Chapters 2-4) characteristics of the Bering shelf temperature, salinity, and circulation fields. Ultimately this framework may prove useful for considering many functional links within the Bering Sea ecosystem, including aspects of shelf nutrient renewal and advection of passively drifting plankton, eggs and larvae. Chapter 5 ties together many findings of Chapters 2-4 and opens doors to many potentially fertile lines of future research.

Chapter 6 summarizes the dissertation, examines some broader implications of this work, and outlines an approach for applying the results to advancing our understanding of the Bering Sea. Throughout all chapters, insights into the physical mechanisms that control variations in the Bering Sea's physical environment inform discussion about possible implications for nutrient, phytoplankton, zooplankton and upper trophic level dynamics.

1.3 References

- Aagaard, K., L. K. Coachman, and E. C. Carmack, 1981. On the halocline of the Arctic Ocean, *Deep-Sea Res.*, 28, 529-545.
- Aagaard, K., A. T. Roach, and J. D. Schumacher, 1985. On the wind-driven variability of the flow through Bering Strait, *J. Geophys. Res.*, 90, 7213-7221.
- Aagaard, K., and E. Carmack, 1989. The role of sea-ice and other fresh water in the Arctic Circulation, *J. of Geophys. Res.*, 94, 14,485-14,498, doi:10.1029/89JC01375.
- Aagaard, K., T. J. Weingartner, S. L. Danielson, R. A. Woodgate, G. C. Johnson, and T. E. Whitledge, 2006. Some controls on flow and salinity in Bering Strait, *Geophys. Res. Lett.* 33, L19602, doi:10.1029/2006GL026612.
- Brewer, R., 2006. The *Selendang Ayu* oil spill: lessons learned, conference proceedings, August 16-19, 2005, Unalaska, Alaska, edited by R. Brewer, Alaska Sea Grant College Program publication *AK-SG-06-02*, Univ. of Alaska Fairbanks, Fairbanks, AK.
- Broecker, W. S., and G. H. Denton, 1990. The role of ocean-atmosphere reorganizations in glacial cycles, *Quat. Sci. Rev.* 9, 305-341.
- Coachman, L. K., and K. Aagaard, 1966. On the water exchange through Bering Strait, *Limnol. Oceanogr.*, 11(1), 44-59.
- Coachman, L. K., 1986. Circulation, water masses, and fluxes on the southeastern Bering Sea shelf, *Cont. Shelf Res.*, 5, 23-108.
- De Boer, A. M., and D. Nof, 2004. The exhaust valve of the North Atlantic, *J. Climate*, 17, 417-422.
- Grebmeier, J. M., J. E. Overland, S. E. Moore, E. V. Farley, E. C. Carmack, L. W. Cooper, K. E. Frey, J. H. Helle, F. A. McLaughlin, and S. L. McNutt, 2006. A major ecosystem shift in the northern Bering Sea, *Science*, 311, 1461-1464.

- Goosse, H., J. M. Campin, T. Fichefet, and E. Deleersnijder, 1997. Sensitivity of a global ice–ocean model to the Bering Strait throughflow, *Clim. Dyn.*, 13(5), 349-358.
- Kowalik, Z., 1999. Bering Sea Tides, in *Dynamics of The Bering Sea: A Summary of Physical, Chemical and Biological Characteristics, and a Synopsis of Research on the Bering Sea*, edited by T. R. Loughlin and K. Ohtani, pp. 93-127, Univ. of Alaska Sea Grant, Fairbanks, AK.
- Normark, W. R., and P. R. Carlson, 2003. Giant submarine canyons: Is size any clue to their importance in the rock record? *Geo. Soc. of Am.*, 370, 175-190.
- NPFMC, 2011. Fishery management plan for groundfish of the Bering Sea and Aleutian Islands Management Area, North Pacific Fishery Management Council, Anchorage, AK.
- Orr, V., 2011. As ice melts, new opportunities, challenges arise for Alaska's northern communities, *Alaska Bus. Mon.*, 27(3), March 2011, Anchorage, AK.
- Overland, J. E., and C. H. Pease, 1982. Cyclone climatology of the Bering Sea and its relation to sea ice extent, *Mon. Wea. Rev.*, 110, 5-13.
- Overland, J. E., J. M. Adams, and N. A. Bond, 1999. Decadal variability of the Aleutian Low and its relation to high-latitude circulation, *J. Climate*, 12, 1542-1548, doi: [http://dx.doi.org/10.1175/1520-0442\(1999\)012<1542:DVOTAL>2.0.CO;2](http://dx.doi.org/10.1175/1520-0442(1999)012<1542:DVOTAL>2.0.CO;2).
- Paquette, R. G., and R. H. Bourke, 1981. Ocean circulation and fronts as related to ice melt-back in the Chukchi Sea, *J. Geophys. Res.*, 86(C5), 4215-4230, doi:10.1029/JC086iC05p04215.
- Pearson, C. A., H. O. Mofjeld, and R. B. Tripp, 1981. Tides of the Eastern Bering Sea shelf, in *The Eastern Bering Sea Shelf, Oceanography and Resources*, vol. 1., edited by D. W. Hood, and J. A. Calder, J.A., pp. 111-130, Univ. of Wash. Press, Seattle, WA.
- Pease, C. H., 1980. Eastern Bering Sea ice processes, *Mon. Wea. Rev.*, 108, 2015-2023.
- Roach, A. T., K. Aagaard, C. H. Pease, S. A. Salo, T. Weingartner, V. Pavlov, and M. Kulakov, 1995. Direct measurements of transport and water properties through Bering Strait, *J. Geophys. Res.*, 100, 18,443-18,457.
- Rodionov, S.N., N. A. Bond, and J. E. Overland, 2007. The Aleutian Low, storm tracks, and winter climate variability in the Bering Sea, *Deep-Sea Res. II*, 54(23–26), 2560-2577.

- Shaffer, G., and J. Bendtsen, 1994. Role of the Bering Strait in controlling North Atlantic ocean circulation and climate, *Nature*, 367, 354-357, doi:10.1038/367354a0.
- Spall, M. A., 2007. Circulation and water mass transformation in a model of the Chukchi Sea, *J. Geophys. Res.*, 112, C05025, doi:10.1029/2005JC003364.
- Stigebrandt, A., 1984. The North Pacific: A global-scale estuary, *J. Phys. Ocean.*, 14, 464-470.
- Van Voorhees, D., and A. Lowther, 2011. Fisheries of the United States, 2010, National Marine Fisheries Service, Office of Science and Technology, Silver Spring, MD.
- Wadley, M. R., and G. R. Bigg, 2006. Are “great salinity anomalies” advective? *J. Climate*, 19, 1080-1088, doi: <http://dx.doi.org/10.1175/JCLI3647.1>.
- Woodgate, R. A., K. Aagaard, and T. J. Weingartner, 2005. Monthly temperature, salinity, and transport variability of the Bering Strait through flow, *Geophys. Res. Lett.*, 32, L04601.
- Woodgate, R. A., T. Weingartner, and R. Lindsay, 2010. The 2007 Bering Strait oceanic heat flux and anomalous Arctic sea-ice retreat, *Geophys. Res. Lett.*, 37, L01602, doi:10.1029/2009GL041621.
- Zhang, X. D., and J. E. Walsh, 2006. Toward a seasonally ice-covered Arctic ocean: Scenarios from the IPCC AR4 model simulations, *J. Climate*, 19, 1730-1747.

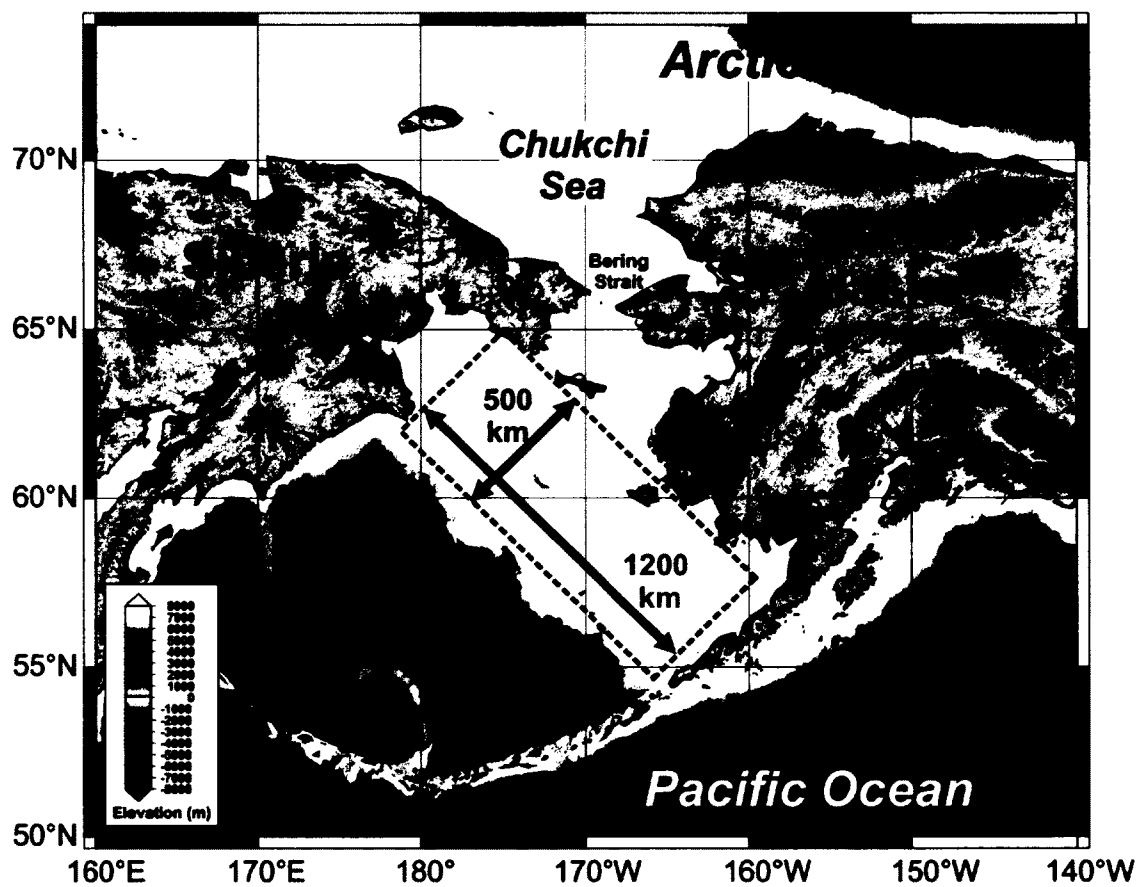
1.4 Figures

Figure 1.1: Map of the Bering Sea region with place names. Typical along-shelf (1200 km) and cross-shelf (500 km) scale dimensions are noted. Bathymetric depths are shaded; the new bathymetric DEM shown here was developed in support of the NEP modeling efforts.

Chapter 2: Thermal and haline variability over the central Bering Sea shelf: Seasonal and inter-annual perspectives¹

2.1 Abstract

We examine multi-year conductivity-temperature-depth (CTD) data to better understand temperature and salinity variability over the central Bering Sea shelf. Particular consideration is given to observations made annually from 2002 to 2007 between August and October, although other seasons and years are also considered. Vertical and horizontal correlation maps show that near-surface and near-bottom salinity anomalies tend to fluctuate in phase across the central shelf, but that temperature anomalies are vertically coherent only in the weakly or unstratified inner shelf waters. We formulate heat content (HC) and fresh water content (FWC) budgets based on the CTD observations, direct estimates of external fluxes (surface heat fluxes, ice melt, precipitation (P), evaporation (E) and river discharge), and indirect estimates of advective contributions. Ice melt, P-E, river discharge, and along-isobath advection are sufficient to account for the mean spring-to-fall increase in FWC, while summer surface heat fluxes are primarily responsible for the mean seasonal increase in HC, although inter-annual variability in the HC at the end of summer appears related to variability in the along-isobath advection during the summer months. On the other hand, FWC anomalies at the end of summer are significantly correlated with the mean wind direction and cross-isobath Ekman transport averaged over the previous winter. Consistent with the latter finding, salinities exhibit a weak but significant inverse correlation between the coastal and mid-shelf waters. The cross-shelf transport likely has significant effect on nutrient fluxes and other processes important to the functioning of the shelf ecosystem. Both the summer and winter advection fields appear to result from the seasonal mean position and

¹Danielson, S., L. Eisner, T. Weingartner and K. Aagaard, 2011. Thermal and haline variability over the central Bering Sea shelf: Seasonal and inter-annual perspectives, *Cont. Shelf Res.*, doi:10.1016/j.csr.2010.12.010.

strength of the Aleutian Low. We find that inter-annual thermal and haline variability over the central Bering Sea shelf are largely uncoupled.

2.2 Introduction

The enormous biological production of the Bering Sea shelf (Figure 2.1) is evident in its primary productivity [*Sambrotto et al.*, 1986; *Walsh et al.*, 1989; *Springer et al.*, 1996], commercial fisheries [*Failor-Rounds*, 2005; *Bowers et al.*, 2008], and large marine mammal populations [*Lowry et al.*, 1982]. While there are apparent connections between variations in climate and biological production [*Grebmeier et al.*, 2006; *Zheng and Kruse*, 2006; *Aydin and Mueter*, 2007], the physical mechanisms underlying these linkages are poorly understood.

We examine the seasonal (April to September) and the inter-annual (for late summer/early fall) variability of the temperature (T) and salinity (S) fields, employing both recently collected and historical data. The data allow a spatially broad and integrative analysis that permits us to quantify sources and sinks for fresh water content (FWC) and heat content (HC) and to identify advective effects that impact coastal and mid-shelf water mass exchanges. We will show that the processes resulting in thermal and haline inter-annual variability are largely uncoupled from one another both seasonally and mechanistically. Although we emphasize physical processes, the results likely bear on shelf nutrient distributions and biological productivity. For example, exchanges that introduce low-salinity (< 31) and nitrate-poor (Figure 2.2) inshore waters onto the central shelf may inhibit primary production.

The Bering Sea shelf is vast: its cross-shelf extent is 800 km between the mouth of Norton Sound and the continental slope, and the shelfbreak extends 1200 km northwestward from Unimak Pass to Cape Navarin. The slope is incised by several canyons (Navarin, Pervenets, Pribilof, Bering and Zhemchug), all likely play an important role in shelf/basin exchange [*Schumacher and Reed*, 1992; *Stabeno and Van Meurs*, 1999; *Mizobata and Saitoh*, 2004]. Our focus here is on the shallower waters on the mid- and inner shelf.

Previous studies [*Kinder and Schumacher, 1981a; Coachman, 1986*] discuss the outer (100-200 m), middle (50 m-100 m) and coastal (0-50 m) biophysical domains of the southeastern Bering Sea shelf. The northern limit of these domains is not well described, but *Coachman [1986]* notes that the inner front, which marks the boundary between the coastal and middle domains, separates from the 50 m isobath north of Nunivak Island. Due to the distribution of available conductivity-temperature-depth (CTD) data (Figure 2.3), we focus on the region that overlaps both the middle and coastal domains, and which extends from western Bristol Bay to south of St. Lawrence Island. In particular, we consider the part of the central Bering Sea shelf lying 1) west of 162 °W; 2) east of 174 °W; 3) north of 57 °N; 4) south of 62.5 °N; and 5) between the 20 m and 70 m isobaths (delineated in Figure 2.3). This region forms our integration domain and represents the maximum area common to CTD surveys conducted annually from 2002 to 2007 by the Bering-Aleutian Sustainable Salmon International Survey (BASIS) program. It encompasses $\sim 2.07 \times 10^5 \text{ km}^2$ with a mean water depth of 45 m and a volume of $\sim 9.3 \times 10^3 \text{ km}^3$. For comparison, the entire shelf has an area of $1.8 \times 10^6 \text{ km}^2$, a mean depth of 43 m, and a volume of $7.7 \times 10^4 \text{ km}^3$ between the 100 m isobath and the coast.

In assessing causes of anomalies in HC and FWC we examine integrated surface heat fluxes, ice extent and melting, river discharge, precipitation (P) and evaporation (E), sea level pressure, winds, and ocean currents. Although mean currents are typically small ($1\text{-}5 \text{ cm s}^{-1}$ [*Schumacher and Kinder, 1983; Danielson et al., 2006*]), we show that wind-forced advection of both heat and fresh water are nevertheless important and are associated with variations in the seasonal position and strength of the Aleutian Low. The Aleutian Low influences the cloud cover [*Reed, 1978*], wind mixing [*Overland et al., 2002*], and heat fluxes, as well as the wind stresses that advect water [*Bond et al., 1994*] and ice [*Overland and Pease, 1982*].

On this shelf, both temperature and salinity affect the location and strength of fronts and of the pycnocline [*Kinder and Schumacher, 1981b*], across which nutrient fluxes influence summer primary production [*Bond and Overland, 2005; Sambrotto et al., 2008*]. The annual evolution of the temperature and salinity fields is as follows. North

of ~ 60 °N, the water column is reset to the freezing point (~ -1.8 °C) by the end of each winter (annual HC minimum), coincident with the annual shelf salinity maximum (annual FWC minimum) [Schumacher *et al.*, 1983]. Winter ice extent is variable, since it depends upon both local ice formation and southward advection by winds [Muench and Ahlins, 1976; McNutt, 1981], but ice occasionally extends as far as the Alaska Peninsula [Niebauer and Schell, 1993]. Throughout winter, ice melts continually along its southernmost boundary [Pease, 1981]. Rapid ablation from the seasonal increase in solar radiation occurs in May, while the southerly winds [Niebauer *et al.*, 1999] advect thinning ice northward [Overland and Pease, 1982]. Melting and warming then initiate the water column stability required for the spring phytoplankton bloom [Alexander and Niebauer, 1981; Stabeno *et al.*, 2001]. Solar heating through spring and summer further strengthens the thermal stratification [Reed and Stabeno, 2002]. Hence, mid-shelf waters evolve toward a strongly stratified two-layer system, maintained primarily by wind mixing and solar heating in the surface layer and tidal mixing of cold winter water in the lower layer [Coachman, 1986; Overland *et al.*, 1999].

Here we present CTD data from 2002-2007, collected over the shelf between mid-August and early October of each year as part of the U.S. BASIS program (Figure 2.3 and Table 2.1). Observations include physical and chemical data, as well as phytoplankton, zooplankton and fisheries sampling. The primary goal of BASIS is to understand the effects of climate change and climate variability on the pelagic ecosystem of the eastern Bering Sea. The fisheries and oceanographic data are employed to reduce uncertainty in forecasting groundfish and western Alaska salmon populations. The survey grid achieves unprecedented CTD coverage. Although the sampling is not synoptic (40-60 days per year are required), we will show that the surveys span the period when both the FWC and HC of the shelf waters are at their annual maxima, and that inter-annual variability in FWC and HC is not obscured by seasonal or synoptic variability. We also employ both recently collected (2007-2009) CTD data from the Bering Sea Ecosystem Study (BEST) and historical CTD data (1929-2009) from the National Ocean Data Center

(NODC) World Ocean Database 2009 (WOD-09) [Boyer *et al.*, 2009] to evaluate seasonal changes in FWC and HC.

Section 2.3 contains detailed descriptions of the data and their processing. In Section 2.4 we present the mean and variability of the late summer/early fall T and S fields and investigate spatial correlations in T and S anomalies. Upon integrating across the central shelf region, we relate the seasonal and inter-annual anomalies in FWC and HC to direct flux estimates and to indirect measures of oceanic advection (Section 2.5). Section 2.6 summarizes the key results and discusses implications of the analyses.

2.3 Datasets and Methods

2.3.1 CTD data

The BASIS CTD data were collected with a variety of Sea-Bird Electronics (SBE) CTDs over the years: SBE-19 and SBE-19+ (2002), SBE-25 (2003, 2004 & 2005), SBE-917 (2005-2007) and SBE-911 (2005-2007). Instruments were calibrated prior to each season, and 2004-2006 salinity measurements were compared to discrete bottle samples. The CTD profiles were processed using the SBE data processing subroutines [SBE, 2009], and final data were binned to 1-m depths and inspected for spikes and/or spurious density inversions. Temperature and salinity measurement spikes exceeding ~ 0.01 were removed by linearly interpolating through adjacent depths levels. Based on post-calibrations, comparison with secondary probes, and discrete salinity samples, we consider the accuracy of the temperatures to be better than 0.01 °C and salinities better than 0.02 . Because there are year-to-year differences in station spacing and sampling grids, we linearly interpolated the temperature and salinity data to regular 2- and 3-dimensional grids to ensure consistency in subsequent calculations. The CTD data from the BEST cruises of 2007, 2008, and 2009 (HLY0701, HLY0802, HLY0803, HLY0901, KN19510, and PS0909) were collected with SBE-911 instruments and processed and evaluated following procedures similar to those applied to the BASIS CTD data.

Historical CTD and bottle data from the NODC WOD-09 [Boyer *et al.*, 2009] were screened for position errors (samples appearing on land and deep samples from a

site known to be shallow) and anomalous temperatures and salinities. Questionable values and outliers, defined in part by the binning method described below, were discarded. A relatively small number of profiles in the WOD-09 were collected from 1930-1960; most were collected from 1960-present.

Combining the various data, we formed 0-100 m monthly and seasonal vertical profiles across a regular geographic grid with spacing of one degree of latitude and two degrees of longitude. The BASIS sampling occurred between August and October (late summer to early fall); it coincided with the annual FWC and HC maxima. February-April (late winter to mid-spring) represents the annual FWC and HC minima and May-July (late spring to mid-summer) encompasses the transition from late spring to late summer. Linear interpolation between depths at stations with discrete bottle samples created full water column profiles. In order to avoid biasing the gridded results toward years with more CTD casts, data were first reduced into a single representative profile for each grid cell, year and month. The monthly profiles were then averaged into a single mean monthly profile representing each grid cell.

Twenty of the grid cells are more than 50% contained within our integration domain (Figure 2.3), and for these 20 cells data were collected in 16-48 discrete years in May-July and 18-33 years in August-October. We place a moderate to high level of confidence in results derived from these data. During February-April one cell was sampled in only two years, while the remaining 19 cells were sampled in 4-23 years. We ascribe low to moderate confidence in these results because of the few number of samples in some cells. For November-January the data distribution was too sparse to be useful, so we neglect this period.

2.3.2 Mooring data

Temperature and salinity data from NOAA mooring M2 (56.9 °N, 164.1 °W) [Stabeno, unpubl. data] and collected between 1995 and 2006 near 10 m and 60 m are used to assess seasonal HC and FWC changes, and to estimate the probable end-of-winter water column HC. Data were inspected for spikes and consistency with other nearby

measurements on the mooring line. Suspect data were discarded, and the resultant dataset was averaged into monthly mean values.

2.3.3 Nutrient data

Nitrate plus nitrite concentrations were determined from discrete water samples collected using Niskin bottles attached to the CTD. Whole water samples were stored frozen at -20 °C and analyzed within eight months at the University of Washington Marine Chemistry Laboratory using colorimetric protocols [UNESCO, 1994].

2.3.4 Ice cover data

Ice cover data are obtained from the National Snow and Ice Data Center (NSIDC) passive microwave satellite Level 3 archives [Cosimo, 2008], available on a 25 km grid. Data from 1988 to the present are daily, while data from 1979 to 1987 were collected every other day. We estimate the number of ice-free days by employing a concentration-extent time series computed over the region south of 66 °N (Bering Strait) and east of 170 °E (Cape Navarin). Ice decay and growth occur relatively rapidly and extensively, and so we employ a fixed ice concentration-extent threshold ($5 \times 10^4 \text{ km}^2$) to determine the onset of the open water and ice-covered seasons. For comparison, the area of Norton Sound encompasses approximately $5 \times 10^4 \text{ km}^2$. Experiments indicate that our results are relatively insensitive to the threshold value.

2.3.5 Streamflow data

Daily discharge data were obtained from the U.S. Geological Survey streamflow database (<http://waterdata.usgs.gov/nwis>) for the Yukon and Kuskokwim rivers at Pilot Station and near Crooked Creek, respectively. Data gaps were filled with the mean daily climatological value.

2.3.6 Drifter data

Satellite-tracked oceanographic drifter data are employed to examine nearshore and mid-shelf surface advection in the summer and fall. Fifteen drifters were deployed in 2002 and 32 were deployed in each of 2008 and 2009. Seventy of these were CODE

surface drifters drogued at 1 m depth [Davis, 1985] and the remaining nine drifters (2002 deployment only) had holey sock drogues centered at 10 m depth. The drifters acquire GPS position fixes (measured on a beached drifter to be accurate to ~ 20 m) every 30 or 60 minutes. After inspection for faulty position or time fixes, the data are converted into velocities and gridded onto 1/2 degree latitude by 1 degree longitude cells. To avoid tidal aliasing, only cells that contain at least 5 drifter-days (120 hours) are used.

2.3.7 *St. Paul meteorological data*

Daily precipitation data collected at St. Paul Island and obtained from the National Climate Data Center are scaled by the central shelf area to estimate precipitation fluxes within our integration domain. Long-term precipitation records from coastal meteorological stations at Nunivak Island, Cape Newenham, St. Lawrence Island, and Nome show that their mean monthly values are within +60% and -120% for the April to September integration period and $\pm 70\%$ for October to May with respect to that measured at St. Paul Island. The average differences between St. Paul and the other stations for these two time periods, given as a percentage of the St. Paul measurements, are 2% and 23%, respectively.

2.3.8 *Sea surface temperature data*

The *Smith et al.* [2008] extended reconstructed sea surface temperature (ERSST) dataset, version ERSST.v3, is employed to assess the late winter distribution of surface temperatures. The ERSST data, gridded monthly onto a 2 degree global grid, are constructed from a temporal-spatial interpolation scheme applied to the International Comprehensive Ocean-Atmosphere Data Set (ICOADS) sea surface temperature data. To gain a relative measure of the accuracy of this product in our region, we compare the ERSST data to the near-surface (~ 10 m depth) temperature record from the NOAA M2 mooring. We find the ERSST has an offset of $+0.54$ °C, which may be explained by the difference in depth levels. Monthly anomaly standard deviations are 0.76 °C and 1.2 °C for the ERSST and M2 data, respectively. The ERSST monthly anomalies account for

35% of the variability observed at M2: $r = 0.59$ and $p=0$ (Pearson's r correlation coefficient).

2.3.9 Atmospheric model fields

Winds, surface pressures, and surface heat fluxes are taken from the NCEP/NCAR Reanalysis Project 1 (NCEPR [Kalnay *et al.*, 1996]). We use this product rather than Reanalysis 2 output fields because the model performance summaries described below were developed for the NCEPR results, and the model run extends further back in time. The NCEPR consists of six-hourly hind casts of major atmospheric variables on a $\sim 2.5^\circ$ global grid from 1948 to the present. Monthly output fields are employed for retrospective analyses and six-hourly fields for comparison to the BASIS records.

The net surface heat flux is the sum of the net shortwave, net longwave, latent and sensible heat fluxes. The NCEPR model surface heat flux performance varies around the globe [e.g., Weller *et al.*, 1998; Rouault *et al.*, 2003], but typical evaluations indicate net shortwave root-mean-square (RMS) errors of 30-70 $W m^{-2}$ and biases of up to 40 $W m^{-2}$ [Scott and Alexander, 1999; Taylor, 2000]. Sensible and latent heat fluxes have RMS errors and mean biases of 6 and 20 $W m^{-2}$, respectively, when compared to ship-based measurements [Smith *et al.*, 2001]. While a constant bias will not affect the results of our anomaly analysis, it will impact our estimates of the seasonal heat flux. For the southeast Bering Sea, Ladd and Bond [2002] find that the NCEPR overestimates the shortwave radiation flux by 50-70 $W m^{-2}$ in summer, and they ascribe the discrepancy to the model's inability to simulate low clouds and fog. Reed and Stabeno [2002] computed the surface heat fluxes at the NOAA mooring site M2 for three months in the summer of 1996. In comparing their results to the NCEPR monthly mean heat fluxes, we find that for May, June and July 1996 the NCEPR had mean biases of +36, -33, +3 and +5 $W m^{-2}$ for the shortwave, longwave, latent and sensible heat fluxes, respectively. The biases in the shortwave and longwave terms nearly balance, resulting in a total bias of +11 $W m^{-2}$, or $\sim 4\%$ of the net surface heat flux in summer. We take this value to be representative of the

net surface heat flux error for the NCEPR over the Bering Sea in summer, and we therefore reduce the NCEPR net surface heat flux computations by this same amount.

Although *Smith et al.* [2001] find a NCEPR underestimate of near-surface wind speeds of $\sim 2\text{-}3 \text{ m s}^{-1}$, *Ladd and Bond* [2002] find good agreement between the winds recorded at the NOAA surface mooring M2 and the NCEPR wind vectors, and so no speed correction was applied to the model winds.

2.3.10 HC and FWC computations

The oceanic HC and FWC computations are described by equations (1) and (2):

$$HC = \iiint C_p(x, y, z) \rho(x, y, z) T(x, y, z) dx dy dz \quad (1)$$

$$FWC = \iiint \frac{\bar{S} - S(x, y, z)}{\bar{S}} dx dy dz, \quad (2)$$

where C_p is the heat capacity, ρ is the density, and $\bar{S} = 31.5$ is the mean salinity for the BASIS data within our integration domain. Anomalies in seasonal and inter-annual HC and FWC are presented as differences between the observed values and the annual or multi-year means respectively. By employing differences (which rely on integration over a standardized volume), the reference values for both T and S become arbitrary: the HC (FWC) anomalies reflect the actual amount of heat (FW) required to transform the volume considered from the mean state to that observed.

2.4 Temperature and salinity in late summer/early fall

This section provides a detailed examination of the late summer/early fall (August-October) shelf conditions as depicted by the BASIS data. We first examine the mean conditions (Section 2.4.1) and then variability about the mean (Section 2.4.2).

2.4.1 Late summer/early fall mean T & S fields

We compute the mean T and S distributions for 2002-2007 above and below the mixed layer depth (MLD), with the MLD defined as the depth where σ_t is 0.10 kg m^{-3} greater than the value at 5 m depth.

The panels in Figure 2.4 show T and S fields that differ substantially with respect to the along-isobath direction. Below the MLD, horizontal temperature gradients are generally cross-isobath, and the “cold pool” tongue (winter-formed waters with temperatures $< 2\text{ }^{\circ}\text{C}$ [Takenouti and Ohtani, 1974]) extends southeastward, centered on the 70 m isobath. Above the MLD, temperature gradients south of $60\text{ }^{\circ}\text{N}$ are primarily along-isobath, whereas north of $60\text{ }^{\circ}\text{N}$ these gradients are chiefly cross-isobath. For waters $< 30\text{ m}$ deep, the warm tongue that extends northwestward toward Nunivak Island suggests the presence of a front and associated jet, for which we present additional evidence below.

In contrast to the temperature field, salinity gradients are generally oriented in the cross-isobath direction both above and below the MLD. Therefore, in the along-isobath direction, advection will play a different role in setting the heat and fresh water budgets at the end of summer. For example, for waters south of $60\text{ }^{\circ}\text{N}$ and above the MLD, where the along-shelf temperature gradient is $\sim 1\text{ }^{\circ}\text{C}$ per 100 km, along-isobath advection will not affect the salt budget, but will impact the heat budget.

As previously observed by Takenouti and Ohtani [1974] and Coachman [1986], we find that isohalines cross the isobaths west and north of Nunivak Island, first directed NW offshore of the 30 m isobath and then turning NE toward Norton Sound. The latter turning reflects the influence of the eastward flow south of St. Lawrence Island that carries relatively dense water from the Gulf of Anadyr [Schumacher *et al.*, 1983; Danielson *et al.*, 2006]. This saline water, along with the fresher coastal waters adjacent to the Alaskan mainland, flows northward through Shpanberg Strait, where the largest horizontal density gradients are found. The westward bulge of low salinity water centered along $61\text{ }^{\circ}\text{N}$ may consist in part of water from the Yukon and Kuskokwim, but also of other low-salinity coastal waters advected from farther south.

The relative position of the 31 isohaline above and below the MLD reflects the combined effects of stratification, advection, and mixing as mid-shelf and coastal waters flow northward. Offshore of Cape Newenham, the near-bottom 31 isohaline is directed approximately WNW. Above the MLD, it is directed NW, and the distance between the

surface and bottom 31 isohalines exceeds 100 km. Near 60 °N, the locations of this isohaline at the surface and at the bottom converge, indicating that the water column is nearly homogeneous in salinity (also see Figure 2.5). North of 60 °N, the isohalines diverge again as the fresh surface waters presumably spread offshore.

Strong thermal stratification ($N_T^2 > 1 \times 10^{-3}$) develops in summer in waters seaward of the inner front, and the stratification is a maximum along the 70 m isobath, coincident with the “cold pool” tongue extending from the NW (Figure 2.5). Inshore of the inner front, the water column is only weakly stratified thermally. In contrast, strong salt stratification occurs near the Yukon River plume, south of St. Lawrence Island, and in western Bristol Bay. Within the extensive region between about 58 °N and 61 °N, however, the salinity contribution to stratification is minimal ($N_S^2 < 0.5 \times 10^{-3}$), suggesting that low-salinity coastal waters do not penetrate far offshore at the end of summer.

Evaluating volumetric T-S contributions over the 0-20 m depth range (46% of the central shelf volume), we find that temperatures range between 5-14 °C and salinities between 28-32.5. Major volumetric T-S modes are centered at (~ 6 °C, 31) and (~ 8 °C, 31), and a smaller third peak is at (12 °C, 31.5). These modal peaks primarily represent low-nitrate waters, since concentrations of $[\text{NO}_3 + \text{NO}_2]$ are 0 – 1 μM for salinities < 31 (Figure 2.2). For the 0-20, 21-40 and 41-70 m depth levels, the mean observed $[\text{NO}_3 + \text{NO}_2]$ concentrations are 0.5, 3.8 and 7.0 μM respectively. The 41 - 70 m depth range (18% of the central shelf volume) consists of one dominant T-S volumetric mode (4 °C, 32) and one secondary mode (0 °C, 31.5). The deep salinities vary narrowly (31-33) and temperatures are mainly between -2 and 6 °C. Mid-depth waters (36% of the central shelf volume) occupy nearly the entire range of temperatures encompassed by the surface and bottom layers (-2 to 12 °C) but cover only a portion of the salinity range (30 to 32.5). At the end of summer, waters colder than 2 °C are geographically isolated from waters with salinity < ~ 30 since the former are offshore and deep while the latter are nearshore and shallow.

2.4.2 Inter-annual variability of the late summer/early fall T & S fields

The late summer/early fall 2002-2007 annual anomalies above and below the MLD, referenced to the 2002-2007 means (Figure 2.4), are mapped in Figure 2.6. Strong positive and negative temperature or salinity anomalies can occur in the same year, and they can encompass areas of $2 \times 10^4 \text{ km}^2$ or more. Hence, classifying a particular year as “warm” or “fresh” can be misleading, since one portion of the shelf may be anomalously warm while another is anomalously cold. The anomaly maps further show that: 1) salinity anomalies are sometimes out of phase between the inner and middle shelf; 2) inter-annual variability in the thermal and haline contributions to stratification is relatively large and spatially variable; 3) boundaries between positive and negative anomalies generally coincide with bio-physical domain boundaries such as the inner front, although this was not the case in 2005 (e.g., for temperatures below the MLD); 4) waters north of Nunivak Island were fresh in 2002; 5) 2004 was a warm year both above and below the MLD; 6) extensive regions of both cold and warm anomalies occurred in 2005; and 7) 2006 and 2007 were cold and fresh below the MLD except on the inner shelf and north of Nunivak Island in 2007.

Figures 2.7 and 2.8 are correlation maps of the anomalies. (For Pearson's correlation coefficient r with N independent samples, the appropriate number of degrees of freedom is $N-2$. With $N=6$ years of data, statistical significance at the 95% confidence level occurs for $|r| \geq 0.81$ [Mendenhall and Sincich, 1988]). Figure 2.7A shows the correlation at each grid point between the temperature anomalies above and below the MLD for 2002-2007. Significant vertical temperature correlations are restricted to well-mixed waters within and inshore of the inner front. Elsewhere the correlations are generally weak, implying little communication between the upper and lower waters after stratification sets up. In contrast, salinity is significantly correlated and in phase above and below the MLD over most of the region (Figure 2.7B), suggesting that whatever process sets the shelf salinity anomalies operates during the time of year when the water column is well mixed.

Figure 2.8 depicts horizontal structure in the temperature and salinity anomalies both above and below the MLD, mapping the correlation between the anomaly at each of four reference points (near Cape Newenham, near NOAA mooring M2, south of St. Lawrence Island, and offshore of the Yukon River) with the anomaly at all other grid points in the domain. The reference points are chosen to represent nearshore, offshore, southern and northern regions of the domain. The nearshore reference points are located close to the Yukon and Kuskokwim river discharge points. We observe that 1) the correlation scales are much broader than the station spacing, hence the BASIS sampling sufficiently resolves inter-annual anomalies; 2) the de-correlation length scale for temperature anomalies generally exceeds that of the salinity anomalies in the southern portion of the domain, suggesting that different processes control the spatial variability of temperature and salinity; 3) the temperature de-correlation length scale in the southern portion of the domain (200-500 km) is greater than in the north (100-200 km); 4) correlated temperature anomalies span coastal and mid-shelf regions in both the south and the north; and 5) salinity is generally anti-correlated between the nearshore and mid-shelf regions, although the statistically significant extent of the anti-correlations is limited.

2.5 Fresh water and heat content variability and fluxes

In this section we investigate seasonal (Section 2.5.1 and Figures 2.9 and 2.10) and inter-annual (Sections 2.5.2-2.5.3 and Tables 2.2 and 2.3) variability in FWC and HC parameters. Subsequent scaling arguments, dynamical considerations, and flux estimates will allow us to examine possible advective contributions to the heat and salt budgets.

2.5.1 Seasonal variability

We place the late summer/early fall period described above within a seasonal context by compiling quarterly depth-averaged means of the 0-100 m temperature and salinity fields across the eastern Bering Sea using the historical, the BEST and the BASIS CTD data (Figure 2.9).

Late winter/early spring (February-April) is characterized by near-freezing temperatures north of 60 °N and a high-salinity pool north of 62 °N. The salty waters surrounding St. Lawrence Island reflect winter ice formation and the eastward advection of Anadyr waters [*Schumacher et al.*, 1983; *Drucker et al.*, 2003; *Danielson et al.*, 2006]. While the saline water found between Nunivak and St. Lawrence islands might be an artifact of the small sample size, it more likely results from locally produced brine because *Danielson et al.* [2006] did not observe southerly fluxes of dense water from the St. Lawrence Island region and the sample size on the southern end of this feature is not small.

A pool of relatively fresh water extends northward between St. Matthew Island and Nunivak Island. This water may be coastal water remnant from the previous fall (see later discussion) and/or melt waters from the ice pack edge. Low salinity observations ($S < 31$) in Norton Sound at the end of winter are difficult to evaluate: they are comprised of only one year sampled in each of two grid cells. While these measurements may not be representative, we note that previous drifter deployments suggest that the residence time of near-surface waters within Norton Sound may be many months (T. Weingartner, unpubl. data; see also <http://www.ims.uaf.edu/drifters/>), and so these observations may in fact reflect over-wintered Yukon discharge.

By late spring and mid-summer (May-July), waters begin warming in shallow coastal waters along the Alaskan Peninsula and in Norton Sound. Relatively fresh (< 31) coastal water envelops the entire coast north of eastern Bristol Bay as river discharge increases. Though not resolved in the 3-month mean, in July a salty tongue protrudes onto the shelf near Zhemchug Canyon, likely a mid-summer source of high-nitrate waters to the outer and middle shelf. The appearance of this intrusion coincides with the seasonal relaxation of the Aleutian low and the associated cyclonic wind stress across the Bering Sea basin [*Brower et al.*, 1988], and the intrusion may reflect the interaction of the canyon with the adjustment of the shelfbreak front to changing winds [*Gawarkiewicz and Chapman*, 1992; *Chapman and Lentz*, 1994; *Chapman and Lentz*, 1997].

By late summer/early fall (August-October) the central shelf's annual HC and FWC are both maximum (although we do not have data from November to January).

We next use the 0-100 m gridded CTD data to compute quarterly and monthly FWC and HC anomalies on the central shelf, and we show in Figure 2.10 the magnitude of their seasonal changes between April and September, along with the dominant flux terms. A measure of sensitivity to the choice of base climatology is gained by comparing changes in HC and FWC from using the 2005 version of the WOD [*Boyer et al.*, 2006], instead of WOD-09 and excluding the BEST data. We find that the integrated HC estimates change by less than 15%, but the integrated FWC estimates change by up to 50%, showing that we likely still do not have a robust estimate of FWC for the late winter and early spring time period.

Employing monthly and seasonal averaging periods, the net spring-to-fall ranges in FWC and HC anomalies are 140-190 km³ and 2.3-2.6 x 10²⁰ J, respectively. Lacking sufficient CTD data to make spatially explicit annual estimates of the Bering shelf seasonal FWC and HC variability, we turn to the long-term moored dataset at NOAA site M2 (57 °N, 167 °W) for comparison (P. Stabeno, unpublished data). The 1995-2006 April to September mean freshening and heating measured at 10 and 60 m depths is typically -0.12 and 5.3 °C, respectively (with ranges of -0.03 to -0.2 and 2.3 to 8.3 °C). A -0.1 salinity change represents freshening by ~ 30 km³ fresh water when integrated across the central shelf volume, and a warming of 5.3 °C represents a HC increase of 2.0 x 10²⁰ J. Given the large temperature anomaly de-correlation scale, the M2 temperature record likely represents the seasonal HC increase on the shelf reasonably well. The salinity anomaly de-correlation scales are smaller, and so the M2 salinity record may not reflect the seasonal salinity decrease over the broader region.

We now compare the various flux terms to the observed seasonal FWC changes (Figure 2.10). Following *Aagaard et al.* [2006], we use precipitation data collected at St. Paul Island and apply it uniformly to the entire region. We estimate evaporation from the NCEPR latent heat flux. For 1 April to 1 September, P-E for the central shelf is 23 km³ on average.

Passive microwave satellite sea ice measurements provide surface area estimates of ice cover, but not of thickness. From 250 direct ice thickness measurements made between March and May in 2008 and 2009, the mean thickness was 0.4 m, and the mean ice salinity 6.4 (R. Gradinger, B. Bluhm and K. Iken, pers. comm.). Melting an ice pack with an area of $1.0 \times 10^5 \text{ km}^2$ (representing the northern half of our domain), thickness of 0.4 m, and ice density of 900 kg m^{-3} releases 36 km^3 of fresh water, which would reduce the salinity of the entire domain by 0.2 if distributed vertically over the entire water column, or by 0.85 if mixed over only the upper 10 m. Neglecting advection and applying the observed mean March/April ice extents (Table 2.1), the probable FW contribution from ice melt is 20-40 km^3 .

A mean along-shelf flow of 2 cm s^{-1} [Schumacher and Kinder, 1983] traverses 250 km in 145 days. Ice melt and shelf water over the southeast shelf therefore likely remains within the integration domain through summer, while that on the northern shelf is advected away by the end of summer [Danielson et al., 2006]. The mean spring-late winter salinity difference between the waters north and south of 60°N is 0.24 (Figure 2.9), so along-isobath (northward) advection would tend to replace the higher salinity northern waters with fresher waters from the south, accounting for a freshening of $\sim 20 \text{ km}^3$. This freshening tendency diminishes through summer as the northerly waters are flushed and eventually become fresher than the southerly waters due to offshore spreading of river discharge.

The Yukon ($202 \text{ km}^3 \text{ yr}^{-1}$) and Kuskokwim ($38 \text{ km}^3 \text{ yr}^{-1}$) rivers are the largest sources of fresh water to the inner shelf. Coastal discharge increases rapidly from winter minima (Yukon, $900\text{-}1500 \text{ m}^3 \text{ s}^{-1}$; Kuskokwim, $170\text{-}450 \text{ m}^3 \text{ s}^{-1}$) to maxima in May or June (Yukon, $13000\text{-}33000 \text{ m}^3 \text{ s}^{-1}$; Kuskokwim, $2000\text{-}11000 \text{ m}^3 \text{ s}^{-1}$). The cumulative 1 April to 1 September discharge for both rivers averages 152 km^3 . Most of this fresh water probably departs the shelf through Bering Strait [Coachman et al., 1975; Aagaard et al., 2006]. Due to the paucity of data inshore of the 20 m isobath, the circulation and hydrography of the broad inner shelf have not been described, however. Visible and infrared satellite imagery of sediment plumes and thermal structure suggest that frontal

systems develop inshore of the 30 m isobath in summer. These fronts probably impede cross-shelf spreading of low-salinity coastal waters. This hypothesis is supported both by recent CTD data and drifter trajectories. For example, a July 2009 CTD transect along 62°N between the 55 m and 7 m isobaths shows a strong temperature and salinity front inshore of the 20 m isobath (Figure 2.11). Furthermore, in the summers of 2008 and 2009, drifters deployed in northern Kuskokwim Bay (Figure 2.12) typically remained inshore of the 20 m isobath, slowly progressing northward past Nunivak Island. Below, we will also show that winds in summer are weak and not conducive to spreading fresh water offshore. In fall, however, drifters moved westward across the shelf. The 2008 and 2009 deployment results are consistent with the drifter trajectories shown by *Danielson et al.* [2006], which were deployed in September 2002, just north of Nunivak Island. Hence, while river discharge represents a substantial summer fresh water influx to the inner shelf, most of it is probably retained nearshore and outside of our integration domain. Nevertheless, with on average 23 km³ fresh water available from P-E, 29 km³ from ice melt and 20 km³ from along-shelf flow, less than one-half of the mean river discharge (152 km³) needs to enter the integration domain to account for the observed April-September FWC increase of ~ 140 km³ (Figure 2.10).

The onset of the heating season (Figure 2.13) occurs near the spring equinox, when the daily mean net surface heat flux switches from negative (oceanic heat loss) to positive (oceanic heat gain). We therefore compute the cumulative heat gain between 1 April (year day 91) and 1 September (year day 244) using the NCEPR heat fluxes interpolated over our domain and, for comparison, repeat the calculation beginning on 1 May (year day 121). The seasonally integrated surface heat flux is 350 (300) EJ using the 1 April (1 May) start, so that regardless of the start date, the surface heat flux is sufficient to account for the observed heat gain of ~ 300 EJ (Figure 2.10).

Similar to flushing the northern domain of saline water during summer, along-isobath advection would also flush the cold winter water, but could account for a mean seasonal HC increase of only ~ 35 EJ. We conclude that in the mean, seasonal advective heat fluxes are relatively small (~ 10% of the total flux) and of the same order as the heat

budget uncertainty. This is consistent with the results of *Reed and Stabeno* [2002] who concluded that advective and diffusive processes amount to $\sim 5\%$ of the summer heat increase near mooring M2. More precise balancing of the seasonal mean heat budget will require substantially better knowledge of both the surface heat fluxes and of advection.

2.5.2 FWC inter-annual variability

For 2002-2007, the late summer range in FWC is $\sim 130 \text{ km}^3$ (Table 2.2), which is similar to the mean FWC seasonal change noted in Section 2.5.1. There are no significant correlations among anomalies of end-of-summer FWC and sea ice melt, P-E, or discharge, neither individually nor when the fluxes are summed.

Because the end-of-summer FWC standard deviation (48.3 km^3) is not balanced by the variability of the runoff (18.4 km^3), P-E (2.5 km^3), and ice melt (7.7 km^3) terms, other processes must also contribute. We compared a number of environmental time series at various time lags, including winds integrated over various time periods and regions, ice extent and retreat, river discharge, and salinities measured in the Gulf of Alaska at oceanographic station GAK1 (59.85°N , 149.47°W). Station GAK 1 is representative of the properties of the Gulf of Alaska coastal current that enters the Bering Sea shelf through Unimak Pass [*Stabeno et al.* 1995, *Weingartner et al.* 2005; *Aagaard et al.*, 2006]). Among these, only the cross-shelf Ekman transport (Table 2.2), derived from the preceding year's October-May along-shore wind stress, is significantly correlated ($r = -0.93$; $p = 0.0072$) with FWC anomalies. Using NCEPR winds, the Ekman transports were estimated across the two line segments connecting the points (62.5°N , 167.5°W), (60°N , 167.5°W), and (58.5°N , 162°W), following the convention that offshore (onshore) transport is negative (positive). The cross-shelf Ekman transports would be particularly effective in changing the FWC, since they are directed along the shelf salinity gradient. Moreover the offshore flux begins in fall, when the salinity gradient is at its annual maximum. Presumably the fall winds also erode the frontal structure as river discharge diminishes, thus weakening the inner front and enhancing the cross-shelf transport. This mechanism, which varies year-to-year, is also consistent with the drifter trajectories shown in Figure 2.12.

An average cross-shore salinity difference of 1 is sufficient to supply the central shelf with $\sim 60 \text{ km}^3$ of fresh water by offshore Ekman transport when integrated over the 2006 winter, although we do not know the actual cross-shelf salinity gradient through the winter months. In contrast, the on-shore component of Ekman transport in 2005 would have removed 70 km^3 of fresh water from the integration domain. Both of these fluxes are therefore of the proper magnitude and sign to nearly balance the FWC anomaly observed the following end-of-summer. Considering the shelf from a simplified two-dimensional perspective, upwelling of more saline subsurface waters would presumably replace the near surface low-salinity waters. In this case, the cross-shelf salt gradient would need to be only one-half of the value employed above in order to account for the observed FWC anomaly. It is not clear, however, what the role of upwelling onto the central shelf would be in a more realistic three-dimensional representation.

The Ekman transport computations, made across a two-segment transect, are sensitive to the changing orientation of the isobaths north and south of 60°N , so that merely using the winter mean north-south wind component does not yield a high correlation with the FWC anomaly. Inspection of Figure 2.14 (second row) reveals that inter-annual differences in wind direction are just as pronounced as changes in magnitude. Indeed, there is a strong correlation ($r = -0.87$) between the FWC anomaly and the wind direction anomaly at 60°N , 170°W . The seasonal mean wind field in turn results from the large-scale atmospheric pressure distribution. Thus, years with the greatest positive FWC anomalies (and the largest westward Ekman transport over the shelf) coincide with low pressure over the northern Gulf of Alaska (Figure 2.14). Note that other studies have also highlighted the importance of the zonal position of the Aleutian Low to a variety of problem sets, including those of *Pease et al.*, [1982], *Rodionov et al.* [2005], *Rodionov et al.* [2007], *Janout et al.* [2010], *Pickart et al.* [2009] and *Wang et al.* [2009].

2.5.3 HC inter-annual variability

Integrating from 1 April to 1 September, we find a significant correlation between the net surface heat flux anomaly and the oceanic HC anomaly (Table 2.3). The summer

surface heat flux anomaly standard deviation (11 EJ), however, represents only about 30% of the end-of-summer HC anomaly standard deviation (36.5 EJ). The end-of-winter HC standard deviation (16 EJ) accounts for ~ 40%, but it is not significantly correlated. Expressed in terms of percent variance accounted for, the summer heat flux anomaly and winter's end HC anomaly represent only 9% and 20% of the summer's end HC variance. The end-of-winter HC is estimated as follows. Convection and winter wind mixing produce a nearly homogeneous end-of-winter water column [Stabeno *et al.*, 2001; Stabeno *et al.*, 2002]. Over the mean March and April shelf area occupied by sea ice with concentrations >30%, we assume a near-freezing mean water column temperature of -1.5 °C and over the region with sea ice concentrations < 30%, we assume a mean water column temperature of +2 °C. The former value is likely good to within -0.3/+1.5 °C, the latter to +/- 2 °C, based on ERSST data, NOAA mooring M2 records (*P. Stabeno*, unpubl. data), and CTD profiles [Reed, 1995]. The end-of-winter HC computed using these extremes does not vary by more than 25%.

Can advective heat fluxes account for the unexplained portion of the heat balance? We address this by using the heat balance equation

$$\underbrace{H_{se}}_{\text{end-of-summer heat content}} = \underbrace{H_{we}}_{\text{end-of-winter heat content}} - \underbrace{H_i}_{\text{heat required to melt ice}} + \underbrace{\iiint Q_s dt dx dy}_{\text{Apr. 1 to Sept. 1 surface heat flux}} + \underbrace{\int v \frac{\partial H}{\partial y} dt}_{\text{alongshelf heat flux}} \quad (3)$$

We can estimate all terms except the along-shelf velocity (v). For example, we estimate H_{we} as described above. Cross-shelf transport is neglected, which is consistent with the summer drifter data (Figure 2.12). We then find that the along-shelf velocity fluctuations required to balance the heat budget anomalies are +/-2 cm s⁻¹.

We can also estimate the surface Ekman transport. For 1 April to 1 September, the along-isobath Ekman transport anomalies computed across latitude 60 °N are significantly correlated with the end-of-summer HC anomalies (Table 2.3), although the cross-isobath Ekman transport is not. While compensating return flows in the bottom

Ekman layer could support differential heat advection in subsurface waters, the along-isobath thermal gradients below the MLD are much smaller than those above the MLD (Figure 2.4) and are thus ignored. Assuming an Ekman depth equal to a typical mid-shelf summer mixed layer depth (~ 20 m), the mean along-shelf Ekman velocity is 0.1 cm s^{-1} , and the 2002-2007 range is between -1 and $+1 \text{ cm s}^{-1}$, about half that estimated from the heat budget and of the right magnitude to satisfy equation (3).

The atmospheric conditions responsible for the correlation between the along-shelf velocity and HC anomaly are evident in the sea level pressure maps and associated Ekman transport vectors presented in Figure 2.15. In 2004, the warmest year encountered during the BASIS surveys, a deep Aleutian Low developed over the western Bering Sea while high pressure characterized the Alaskan mainland, resulting in strong northward Ekman transport over the shelf. The coldest two years, 2006 and 2007, had mean westward/southwestward transport over the shelf, resulting from a split Aleutian Low pattern manifested by closed sea level pressure contours in both the northern Gulf of Alaska and the western Bering Sea.

In summary, both the heat budget and Ekman transport estimates of the along-isobath summer heat flux show similar magnitudes and year-to-year trends (not shown), strongly suggesting that variability in the along-shelf flow accounts for much of the inter-annual variability observed in the end-of-summer integrated HC.

2.6 Discussion and concluding remarks

Central shelf waters respond with nearly equal magnitude to the mean seasonal cycle of thermohaline forcing and to inter-annual differences in the regional wind forcing. Our estimates of the HC and FWC budgets indicate that while we can reasonably account for the April to September increases in HC and FWC, improved data sets with an emphasis on advective estimates are required to tighten these budgets. Nevertheless, the observations in hand are sufficient to show that inter-annual HC and FWC anomalies generally do not co-vary because HC anomalies result in large part from variability in along-isobath advection during spring and summer months, whereas FWC anomalies

depend substantially on cross-isobath advection during fall and winter. In both cases, the Ekman transport is determined by the seasonal mean zonal position of the Aleutian Low.

Results from the correlation maps, Ekman transport computations, and drifter releases are all consistent with the hypothesis that winter cross-isobath exchange is an important control of salinity variability on this shelf. Inspection of estimated monthly mean surface Ekman transports (Figure 2.16) shows that particularly in October and November, shelf surface flows are driven westward across the isobaths. The wind-driven cross-shelf flux occurs to a greater or lesser degree each winter (Figure 2.14 and Table 2.2), resulting in a near-shore/mid-shelf inverse correlation (Figure 2.8) of salinities. In years that the Aleutian Low is displaced eastward, Ekman transport helps flush the nearshore region to the middle shelf. In years that the Aleutian Low is displaced westward, the fresh coastal waters tend to be trapped to the coast and/or are advected northward.

Cross-isobath exchange has implications for macronutrient [*Whitledge and Luchin, 1999*] and micronutrient [*Aguilar-Islas et al., 2007*] transport and biological utilization, as well as for the transport of passively drifting eggs and larvae [*Wespestad et al., 2000; Lanksbury et al., 2007*]. In addition to carrying coastal waters to the mid-shelf region, iron-rich shelf water [*Aguilar-Islas et al., 2007*] may be carried still farther seaward to the productive continental slope [*Springer et al., 1996*] and deep basin, while compensating flows transport mid- and outer shelf waters landward, helping resupply nitrate to these shallower waters. Whether westward advection to the basin acts as a significant sink for Yukon and Kuskokwim discharge is at this point unclear, but highly relevant to determining the formation and modification of water masses on the Bering shelf and their subsequent northward advection [*Coachman et al., 1975*]. The issue is particularly important because the Bering Strait throughflow accounts for a large percentage of the Arctic Ocean fresh water input [*Aagaard and Carmack, 1989; Dickson et al., 2007*] and so ultimately impacts both Arctic Ocean stratification and conditions in the North Atlantic [*Aagaard et al., 1981; Goosse et al., 1997; Peterson et al., 2002; Woodgate and Aagaard, 2005*].

The time series of Figures 2.14 and 2.15 place the 2002-2007 mean October-May and April-August wind anomalies within a 60 yr historical context. The October-May normalized wind direction anomaly at 60 °N, 170 °W (correlation to FWC anomaly: $r = -0.87$, $p = 0.023$, Pearson's r correlation coefficient) is a surrogate for the winter cross-isobath Ekman transport. The mean October to May wind direction is toward 225 °T. This parameter is normally distributed with a standard deviation of 20 °, and so a two-standard deviation anomaly is equivalent to a rotation of 40 ° away from the mean winter wind direction; the NCEPR directional range is 133 °. The 2002-2007 time period includes no outstanding positive anomalies, but 2006 and 2007 stand out as the lowest (-2.5) and third lowest (-1.5) anomalies since 1948. Strikingly, 2006-2008 is the first three-year period since the mid-1970s regime shift [*Hare and Mantua*, 2000] to exhibit three negative anomalies in a row. The April-August net zonal wind run (mean wind speed multiplied by time) anomaly at 60 °N, 170 °W (correlation to HC anomaly: $r = -0.87$, $p = 0.024$, Pearson's r correlation coefficient) is a measure of the along-isobath summer Ekman transport; negative values reflect easterly winds that promote northward Ekman transport. Figure 2.15 shows that 2004 and 2006 are notably anomalous, ranking as the second lowest (-1.9) and third highest (+2.1) anomaly years over the record, respectively. Taken together, Figures 2.14 and 2.15 show that the Bering shelf system has many possible states. Indeed, the two 60-year time series are uncoupled from each other ($r = 0.21$, $p = 0.10$, Pearson's r correlation coefficient).

In this effort we have identified mechanisms that likely modulate or control the thermal and haline properties of the central Bering Sea shelf. For example, wind-driven transport changes appear to determine the inter-annual variability of both FWC and HC. While these ideas are promising, our analysis is based on a limited data set. Future studies will need to assess whether or not our hypotheses and conclusions are robust, as well as to rigorously quantify the various fluxes that we can only crudely estimate (e.g., *Whitney and Garvine*, [2005]; *Fewings et al.*, [2008]). Although we have suggested chemical and biological components that may be sensitive to the proposed processes and circulation schemes, a proper assessment of the impacts on nutrients, primary

productivity, and larval transport, for example, will likely prove to be significantly challenging undertakings, as will certainly be the extent to which these physical processes influence the broader ecosystem.

2.7 Acknowledgements

This manuscript would not have been possible without the cross-institutional and cross-disciplinary collaboration that has been fostered through the BASIS and BEST programs. We particularly thank Ed Farley and the rest of the BASIS scientists at NOAA/AFSC for their support. Many thanks to Kristin Cieciel for survey logistics, oceanographic data collection, CTD data processing and database maintenance; John Pohl and Alex Andrews for oceanographic data collection; Jennifer Lanksbury for database design and maintenance; Rolf Gradinger, Katrin Iken and Bodil Bluhm for sharing their ice station data; and Phyllis Stabeno for sharing M2 mooring data and BEST CTD data, both collected with the support of the NOAA/PMEL Eco-FOCI program. We thank the dedicated crews of the F/V Sea Storm, F/V NW Explorer, R/V Oscar Dyson, R/V Knorr, R/V Point Sur and the USCGC Healy for the many successful BASIS and BEST cruises. We thank the BEST program scientists and field crews for the CTD data collections and processing. Data from NSF sponsored BEST cruises HLY-07-01, HLY-08-03 and KN195-10 were taken under the direction of chief scientist R. Sambrotto, Lamont-Doherty Earth Observatory, Palisades, NY; data from cruise HLY-08-02 were taken under the direction of chief scientist Carin Ashjian, Woods Hole Oceanographic Institute, Woods Hole, MA; and data from cruise HLY-09-01 were taken under the direction of chief scientist Lee Cooper, University of Maryland Center for Environmental Science, Solomons, MD. The manuscript was improved with valuable comments from two anonymous reviewers. The Arctic-Yukon-Kuskokwim Sustainable Salmon Initiative, the Bering Sea Fisherman's Association, NOAA Fisheries and the Environment (FATE) program, and the National Marine Fisheries Service funded BASIS oceanographic data collection and analysis. Drifter data were collected under funding from the North Pacific Research Board, grant NPMRI T2130, and the Arctic Yukon Kuskokwim Sustainable Salmon Initiative, grant ADN #1195952. This manuscript is listed as BEST/BSIERP

Publication #6. K. Aagaard was supported by NSF grant ARC-0732428. S. Danielson and T. Weingartner received financial support from the Bering Sea Fisherman's Association grant AC-299 and NSF grant ARC-0732771.

2.8 References

- Aagaard, K., L. K. Coachman, and E. C. Carmack, 1981. On the halocline of the Arctic Ocean, *Deep-Sea Res.*, 28, 529-545.
- Aagaard, K., and E. Carmack, 1989. The role of sea-ice and other fresh water in the Arctic Circulation, *J. of Geophys. Res.*, 94, 14485-14498, doi:10.1029/89JC01375.
- Aagaard, K., T. J. Weingartner, S. L. Danielson, R. A. Woodgate, G. C. Johnson, and T. E. Whitledge, 2006. Some controls on flow and salinity in Bering Strait, *Geophys. Res. Lett.*, 33, L19602, doi:10.1029/2006GL026612.
- Aguilar-Islas, A. M., M. Hurst, K. Buck, B. Sohst, G. J. Smith, M. C. Lohan, and K. W. Bruland, 2007. Micro- and macronutrients in the southeastern Bering Sea: Insight into iron-replete and iron-depleted regimes, *Prog. Oceanogr.*, 73(2), 99-126, doi:10.1016/j.pocean.2006.12.002.
- Alexander, V. and H. J. Niebauer, 1981. Oceanography of the eastern Bering Sea ice-edge zone in spring, *Limnol. Oceanogr.*, 26(6), 1111-1125.
- Aydin, K., and F. Mueter, 2007. The Bering Sea-A dynamic food web perspective, *Deep Sea Res. II*, 54(23-26), 2501-2525, doi:10.1016/j.dsr2.2007.08.022.
- Bond, N. A., J. E. Overland, and P. Turet, 1994. Spatial and temporal characteristics of the wind forcing of the Bering Sea, *J. Climate*, 7(7), 1119-1130.
- Bond, N.A. and J. E. Overland, 2005. The importance of episodic weather events to the ecosystem of the Bering Sea shelf, *Fish. Oc.*, 14(2), 97-111.
- Bowers, F. R., M. Schwenzfeier, K. Milani, M. Salmon, K. Herring, J. Shaishnikoff, E. Russ, R. Burt, and H. Barnhart, 2008. Annual Management Report for the Commercial and Subsistence Shellfish Fisheries of the Aleutian Islands, Bering Sea and the Westward Region's Shellfish Observer Program, 2007/08, *Fishery Management Report 08-73*, Alaska Dep. of Fish and Game, Anchorage, AK.
- Boyer, T. P., J. I. Antonov, H. E. Garcia, D. R. Johnson, R. A. Locarnini, A. V. Mishonov, M. T. Pitcher, O. K. Baranova, and I. V. Smolyar, 2006. World Ocean Database 2005, edited by S. Levitus, *NOAA Atlas NESDIS 60*, U.S. Gov. Printing Office, Wash., D.C.

- Boyer, T. P., J. I. Antonov, O. K. Baranova, H. E. Garcia, D. R. Johnson, R. A. Locarnini, A. V. Mishonov, T. D. O'Brien, D. Seidov, I. V. Smolyar, and M. M. Zweng, 2009. World Ocean Database, 2009, edited by S. Levitus, *NOAA Atlas NESDIS 66*, U.S. Gov. Printing Office, Wash., D.C.
- Brower, W. A., Jr., R. G. Baldwin, C. N. Williams Jr., J. L. Wise, and L. D. Leslie, (Eds.), 1988. *Climate Atlas of the Outer Continental Shelf Waters and Coastal Regions of Alaska*, vol. 2, Bering Sea, Natl. Clim. Data Cent., Asheville, NC.
- Chapman, D. C., and S. J. Lentz, 1994. Trapping of a coastal density front by the bottom boundary layer, *J. Phys. Oceanogr.*, 24, 1464-1479.
- Chapman, D. C., and S. J. Lentz, 1997. Adjustment of stratified flow over a sloping bottom, *J. Phys. Oceanogr.*, 27, 340-356.
- Coachman, L. K., K. Aagaard, and R. B. Tripp, 1975. *Bering Strait: The Regional Physical Oceanography*, Univ. of Wash. Press, Seattle, WA.
- Coachman, L. K., 1986. Circulation, water masses and fluxes on the southeastern Bering Sea shelf, *Cont. Shelf Res.*, 5, 23-108.
- Comiso, J., 1999, updated 2008. Bootstrap Sea Ice Concentrations from NIMBUS-7 SMMR and DMSP SSM/I, [1979-2007], Boulder, CO, USA, National Snow and Ice Data Center. Digital media.
- Danielson, S., K. Aagaard, T. Weingartner, S. Martin, P. Winsor, G. Gawarkiewicz, and D. Quadfasel, 2006. The St. Lawrence polynya and the Bering shelf circulation: New observations that test the models, *J. Geophys. Res.*, J111, C09023, doi:10.1029/2005JC003268.
- Davis, R.E., 1985. Drifter observations of coastal surface currents during CODE: the method and descriptive view, *J. Geophys. Res.*, 90, 4741-4755.
- Dickson, R., B. Rudels, S. Dye, M. Karcher, J. Meincke, and I. Yashayaev, 2007. Current estimates of fresh water flux through Arctic and subarctic seas, *Prog. Oceanogr.*, 73 (3-4), 210-230, doi:10.1016/j.pocean.2006.12.003.
- Drucker, R., S. Martin, and R. Moritz, 2003. Observations of ice thickness and frazil ice in the St. Lawrence Island polynya from satellite imagery, upward looking sonar, and salinity/temperature moorings, *J. Geophys. Res.*, 108(C5), 3149, doi:10.1029/2001JC001213.
- Failor-Rounds, B., 2005. Bering Sea-Aleutian Islands area state-waters groundfish fisheries and groundfish harvest from parallel seasons in 2004, Alaska Dep. of Fish and Game, *Fishery Management Report No. 05-71*, Anchorage, AK.

- Fewings, M., S. J. Lentz, and J. Fredericks, 2008. Observations of cross-shelf flow driven by cross-shelf winds on the inner continental shelf, *J. Phys. Oceanogr.*, 38, 2358-2378.
- Gawarkiewicz, G., and D. C. Chapman, 1992. The role of stratification in the formation and maintenance of shelfbreak fronts, *J. Phys. Oceanogr.*, 22, 753-772.
- Goosse, H., J. M. Campin, T. Fichelet, and E. Deleersnijder, 1997. Sensitivity of a global ice-ocean model to the Bering Strait throughflow, *Clim. Dyn.*, 13, 349-358.
- Grebmeier, J. M., J. E. Overland, S. E. Moore, E. V. Farley, E. C. Carmack, L. W. Cooper, K. E. Frey, J. H. Helle, F. A. McLaughlin, and S. L. McNutt, 2006. A major ecosystem shift in the northern Bering Sea, *Science*, 311, 1461-1464.
- Hare, S. R., and N. J. Mantua, 2000. Empirical evidence for northeast Pacific regime shifts in 1977 and 1989, *Prog. Oceanogr.*, 47, 103-145.
- Janout, M. A., T. J. Weingartner, T. C. Royer, and S. L. Danielson, 2010. On the nature of winter cooling and the recent temperature shift on the northern Gulf of Alaska shelf, *J. Geophys. Res.*, 115, doi:10.1029/2009JC005774.
- Kalnay E., M. Kanamitsu, R. Kistler, W. Collins, D. Deaven, L. Gandin, M. Iredell, S. Saha, G. White, J. Woollen, Y. Zhu, M. Chelliah, W. Ebsuzaki, W. Higgins, J. Janowiak, K. Mo, C. Ropelewski, J. Wang, A. Leetma, R. Reynolds, R. Jenne, and D. Joseph, 1996. The NCEP/NCAR 40-year reanalysis project, *Bull. Am. Meteor. Soc.*, 77, 437-470.
- Kinder, T.H., and J. D. Schumacher, 1981a. Circulation over the continental shelf of the Southeastern Bering Sea, in *The Eastern Bering Sea Shelf, Oceanography and Resources*, vol. 1., edited by D. W. Hood and J. A. Calder, pp. 53-75, Univ. of Wash. Press, Seattle, WA.
- Kinder, T. H. and J. D. Schumacher, 1981b. Hydrographic structure over the continental shelf of the southeastern Bering Sea, in *The Eastern Bering Sea Shelf, Oceanography and Resources*, vol. 1., edited by D. W. Hood and J. A. Calder, pp. 31-52, Univ. of Wash. Press, Seattle, WA.
- Ladd, C., and N. Bond, 2002. Evaluation of the NCEP/NCAR reanalysis in the NE Pacific and the Bering Sea, *J. Geophys. Res.*, 107(C10), 10.1029/2001JC001157.
- Lanksbury, J. A., J. T. Duffy-Anderson, K. L. Mier, M. S. Busby, and P. J. Stabeno, 2007. Distribution and transport patterns of northern rock sole, *Lepidopsetta polyxystra*, larvae in the southeastern Bering Sea, *Prog. Oceanogr.*, 72(1), 39-62, doi: 10.1016/j.pocean.2006.09.001.

- Lowry, L. F., K. J. Frost, D. G. Calkins, G. L. Swartzman, and S. Hills, 1982. Feeding habits, food requirements and status of Bering Sea marine mammals, *Counc. Doc. Nos. 19 and 19A* (annotated bibliography), North Pacific Fisheries Management Council, Anchorage AK..
- McNutt, L. 1981. Remote sensing analysis of ice growth and distribution in the eastern Bering Sea, March 1979, in *The Eastern Bering Sea Shelf, Oceanography and Resources*, vol. 1., edited by D. W. Hood, and J. A. Calder, J.A., pp. 141-166, Univ. of Wash. Press, Seattle, WA.
- Mendenhall, W. and T. Sincich, 1988. *Statistics for the engineering and computer sciences*, 2nd ed., ISBN 0-02-380460-2, Dellen Publishing Co., San Fransisco, CA.
- Mizobata, K., and S. Saitoh, 2004. Variability of Bering Sea eddies and primary productivity along the shelf edge during 1998-2000 using satellite multi-sensor remote sensing, *J. Mar. Sys.*, 50, 101-111.
- Muench, R., and K. Ahlnas, 1976. Ice movement and distribution in the Bering Sea from March to June 1974, *J. Geophys. Res.*, 81(24), 4467-4476.
- Niebauer, H. J., and D. M. Schell, 1993. Physical environment of the Bering Sea population, in *The bowhead whale*, edited by J. J. Burns et al., pp. 23-44, Allen Press, Lawrence, KS.
- Niebauer, H. J., N. A. Bond, L. P. Yakunin, and V. V. Plotnikov, 1999. An update on the climatology and sea ice of the Bering Sea, in *Dynamics of The Bering Sea: A Summary of Physical, Chemical and Biological Characteristics, and a Synopsis of Research on the Bering Sea*, edited by T. R. Loughlin and K. Ohtani, pp. 29-59, Univ. of Alaska Sea Grant, Fairbanks, AK.
- Overland, J. E., and C. H. Pease, 1982. Cyclone climatology of the Bering Sea and its relation to sea ice extent, *Mon. Wea. Rev.*, 110, 5-13.
- Overland, J. E., S. A. Salo, L. H. Kantha, and C. A. Clayson, 1999. Thermal stratification and mixing on the Bering Sea shelf, in *Dynamics of The Bering Sea: A Summary of Physical, Chemical and Biological Characteristics, and a Synopsis of Research on the Bering Sea*, edited by T. R. Loughlin and K. Ohtani, pp. 129-146, Univ. of Alaska Sea Grant, Fairbanks, AK.
- Overland, J. E., N. A. Bond, and J. M. Adams, 2002. The relation of surface forcing of the Bering Sea to large-scale climate patterns, *Deep-Sea Res. II*, 49(26), 5855-5868.
- Pease, C. H., 1981. Eastern Bering Sea ice dynamics and thermodynamics, in *The Eastern Bering Sea Shelf, Oceanography and Resources*, vol. 1., edited by D. W. Hood, and J. A. Calder, J.A., pp. 213-222, Univ. of Wash. Press, Seattle, WA.

- Pease, C. H., S. A. Schoenberg, and J. E. Overland, 1982. A climatology of the Bering Sea and its relation to sea ice extent, *NOAA Tech. Report ERL 419-PMEL 36*, NTIS: PB82-246950, Seattle, WA.
- Peterson B. J, R. M Holmes, J. W. McClelland, C. J. Vörösmarty, R. B. Lammers, A. I. Shiklomanov, I. A. Shiklomanov, and S. Rahmstrof, 2002. Increasing river discharge to the Arctic Ocean, *Science*, 298, 2171–2173, doi:10.1126/science.1077445.
- Pickart, R. S., G. W. K. Moore, A. M. Macdonald, I. A. Renfrew, J. E. Walsh, and W. S. Kessler, 2009. Seasonal evolution of Aleutian low-pressure systems: Implications for North Pacific sub-polar circulation, *J. Phys. Oceanogr.*, 39, 1317-1339.
- Reed, R. K., 1978. The heat budget of a region in the eastern Bering Sea, summer 1976, *J. Geophys. Res.*, 83, 3635-3645.
- Reed, R. K., 1995. Water properties over the Bering Sea shelf: climatology and variations, *NOAA Tech. Report, ERL 452-PMEL 42*, Seattle, WA.
- Reed, R. K., and P. J. Stabeno, 2002. Surface heat fluxes and subsurface heat content at a site over the southeastern Bering Sea shelf, May–June 1996, *Deep-Sea Res. II*, 49, 5911-5917.
- Rodionov, S. N., J. E. Overland, and N. A. Bond, 2005. The Aleutian low and winter climatic conditions of the Bering Sea, Part I: Classification, *J. Climate*, 18(1), 160-177.
- Rodionov, S. N., N. A. Bond, and J. E. Overland, 2007. The Aleutian low, storm tracks, and winter climate variability in the Bering Sea, *Deep-Sea Res. II*, 54(23-26), 2560-2577.
- Rouault, M., C. J. C. Reason, J. R. E. Lutjeharms, and A. C. M. Beljaars, 2003. Underestimation of latent and sensible heat fluxes above the Agulhas Current in NCEP and ECMWF Analyses, *J. Climate*, 16, 776-782.
- Sea-Bird Instruments, Inc (SBE), 2009. *SEASOFT V2: SBE Data Processing Users Manual*, Sea-Bird Electronics, Inc., Bellevue, WA.
- Sambrotto, R. N., H. J. Niebauer, J. J. Georing, and R. L. Iverson, 1986. Relationships among vertical mixing, nitrate uptake and phytoplankton growth during the spring bloom in the southeast Bering Sea middle shelf, *Cont. Shelf Res.*, 5, 161-198.
- Sambrotto, R. N., C. Mordy, S. I. Zeeman, P. J. Stabeno, and S. A. Macklin, 2008. Physical forcing and nutrient conditions associated with patterns of Chl-a and phytoplankton productivity in the southeastern Bering Sea during summer, *Deep-Sea Res. II*, 55(16–17), 1745-1760.

- Schumacher, J., K. Aagaard, C. Pease, and R. Tripp, 1983. Effects of a shelf polynya on flow and water properties in the Northern Bering Sea, *J. Geophys. Res.*, 88(C5), 2723-2732.
- Schumacher, J. D., and T. H. Kinder, 1983. Low-frequency current regimes over the Bering Sea Shelf, *J. Phys. Oceanogr.*, 13, 607-623.
- Schumacher, J. D., and R. K. Reed, 1992. Characteristics of currents over the continental slope of the eastern Bering Sea, *J. Geophys. Res.*, 97(C6), 9423-9433.
- Scott, J. D., and M. A. Alexander, 1999. Net shortwave fluxes over the ocean, *J. Phys. Oceanogr.*, 29, 3167-3174.
- Smith, S. R., D. M. Legler, and K. V. Verzone, 2001. Quantifying uncertainties in NCEP Reanalyses using high-quality research vessel observations, *J. Climate*, 14, 4062-4072.
- Smith, T. M., R. W. Reynolds, T. C. Peterson, and J. Lawrimore, 2008. Improvements to NOAA's historical merged land-ocean surface temperature analysis (1880-2006), *J. Climate*, 21, 2283-2296.
- Springer, A., C. P. McRoy, and M. Flint, 1996. The Bering Sea Green Belt: shelf-edge processes and ecosystem production, *Fish. Oceanogr.*, 5, 205-223.
- Stabeno, P. J., R. K. Reed, and J. D. Schumacher, 1995. The Alaska Coastal Current: continuity of transport and forcing, *J. Geophys. Res.* 100, 2477-2485.
- Stabeno, P. J., and P. Van Meurs, 1999. Evidence of episodic on-shelf flow in the southeastern Bering Sea, *J. Geophys. Res.*, 104(C12), 29, 715-29,720.
- Stabeno, P. J., N. A. Bond, N. B. Kachel, S. A. Salo, and J. D. Schumacher, 2001. On the temporal variability of the physical environment over the south-eastern Bering Sea, *Fish. Oceanogr.*, 10(1), 81-98.
- Stabeno, P. J., and J. E. Overland, 2001. The Bering Sea shifts toward an earlier spring transition, *Eos Trans. AGU*, 82(29), 317-321.
- Stabeno, P. J., N. B. Kachel, M. Sullivan, and T. E. Whitledge, 2002. Variability of physical and chemical characteristics along the 70-m isobath of the southeast Bering Sea, *Deep-Sea Res. II*, 49(26), 5931-5943.
- Takenouti, A.Y. and K. Ohtani, 1974. Currents and water masses in the Bering Sea: a review of Japanese work, , in *Oceanography of the Bering Sea*, edited by D.W. Hood and E. J. Kelley, pp. 39-58, Occ. Public. No. 2, Inst. Mar. Sci., Univ. of Alaska, Fairbanks, Fairbanks, AK.

- Taylor, P. K., 2000. Intercomparison and validation of ocean-atmosphere energy flux fields: Final report of the Joint World Climate Research program and Scientific Committee on Ocean Research working group on air-sea fluxes, edited by P. K. Taylor, *World Climate Research Program Report WCRP-112:303*.
- UNESCO, 1994. Protocols for the Joint Global Ocean Flux Study (JGOFS) Core Measurements, *IOC Manual and Guides 29*, Paris, France.
- Wang, J., H. Hu, K. Mizobata, and S. Saitoh, 2009. Seasonal variations of sea ice and ocean circulation in the Bering Sea: A model-data fusion study, *J. Geophys. Res.*, 114(C02011), doi:10.1029/2008JC004727.
- Wash, J. J., C. P. McRoy, L. K. Coachman, J. J. Goering, J. J. Nihoul, T. E. Whitledge, T. H. Blackburn, P. L. Parker, C. D. Wirick, P. G. Shuert, J. M. Grebmeier, A. M. Springer, R. D. Tripp, D. A. Hansell, S. Djenidi. E. Deleersnijder, K. Henriksen, B. A. Lund, P. Andersen, F. E. Muller-Karger, and K. Dean, 1989. Carbon and nitrogen cycling within the Bering Chukchi seas: source regions for organic matter effecting AOU demands of the Arctic Ocean, *Prog. Oceanogr.*, 22(4), 277-358.
- Weingartner, T. J., S. L. Danielson, and T. C. Royer, 2005. Fresh water variability and predictability in the Alaska Coastal Current, *Deep-Sea Res. II*, 52, 169-192.
- Weller, R. A., M. F. Baumgartner, S. A. Josey, A. S. Fisher, and J. C. Kindle, 1998. Atmospheric forcing in the Arabian Sea during 1994–1995: Observations and comparison with climatological models, *Deep-Sea Res. II*, 45, 1961-1999.
- Wespestad, V. G., L. W. Fritz, W. J. Ingraham, and B. A. Megrey, 2000. On relationships between cannibalism, climate variability, physical transport, and recruitment success of Bering Sea walleye pollock (*Theragra chalcogramma*), *J. Mar. Sci.*, 57, 268-274.
- Whitledge, T. E., and V. A. Luchin, 1999. Summary of chemical distributions and dynamics in the Bering Sea, in *Dynamics of The Bering Sea: A Summary of Physical, Chemical and Biological Characteristics, and a Synopsis of Research on the Bering Sea*, edited by T. R. Loughlin and K. Ohtani, pp. 217-249, Univ. of Alaska Sea Grant, Fairbanks, AK.
- Whitney, M. M., and R. W. Garvine, 2005. Wind influence on a coastal buoyant outflow, *J. Geophys. Res.*, 110, C03014, doi:10.1029/2003JC002261.
- Woodgate, R. A., and K. Aagaard, 2005. Revising the Bering Strait fresh water flux into the Arctic Ocean, *Geophys. Res. Lett.*, 32, L02602, doi:10.1029/2004GL021747.
- Zheng, J., and G. H. Kruse, 2006. Recruitment variation of eastern Bering Sea crabs: climate forcing or top-down effects? *Prog. Oceanogr.*, 68, 184-204.

2.9 Tables

Table 2.1: Summary of BASIS CTD surveys and spring environmental conditions. The number of CTDs reported reflects only those taken over the eastern Bering Sea shelf. The date of maximum ice extent and mean retreat date are computed for the greater eastern Bering Sea shelf area, while the ice extent column is given for the central region only. A 5-day moving average window was applied to the net surface heat flux time series to estimate the heating season onset date.

Year	# of CTD Stations	CTD Survey Start Date	CTD Survey End Date	Date of Maximum Ice Extent	Date of Ice Retreat	March-April Mean Ice Extent (km ²)	Heating Season Onset (170 °W, 60 °N)
2002	154	20 Aug	7 Oct	20 Feb	18 May	52000	4 Apr
2003	129	21 Aug	8 Oct	26 Mar	6 May	51000	9 Apr
2004	143	14 Aug	30 Sep	2 Apr	11 May	65000	6 Apr
2005	128	14 Aug	6 Oct	9 Apr	21 May	62000	21 Apr
2006	137	17 Aug	20 Sep	4 Feb	31 May	88000	29 Apr
2007	166	15 Aug	8 Oct	24 Mar	24 May	101000	20 Apr

Table 2.2: Fresh water content estimates. Annual anomalies of the 2002-2007 summer's end FWC, mean FWC of sea ice (March-April mean), FWC of the May-August P-E, FWC of the March-August Yukon and Kuskokwim discharge, and the preceding October-May cross-isobath Ekman transport. The bottom three rows show standard deviation (σ), correlation coefficients (r) and p-values (p) for the anomalies. The correlation and p-values summarize cross-correlation computations between column 2 and columns 3-5. Correlations significant at the 95% level are highlighted in boldface type.

Year	Summer's End FWC	Ice FWC	P-E	River Discharge	Cross-shore Ekman Transport
	km ³	km ³	km ³	km ³	x10 ³ m ³ s ⁻¹
2002	-51	-7.4	-1.6	-11	36
2003	-13	-7.1	2.9	-9	2
2004	2	-1.5	-2.2	-4	5
2005	-45	-2.5	-1.8	38	103
2006	77	6.7	-1.1	6	-99
2007	31	11.8	3.7	-5	-46
σ	48.3	7.7	2.5	18	
r		.78	0.24	0.16	-0.93
p		0.065	0.650	0.760	0.007

Table 2.3: Heat content estimates. Annual anomalies of the 2002-2007 summer's end oceanic HC, winter's end oceanic HC, April-August net surface heat flux and April-August along-isobath Ekman Transport. The bottom three rows show standard deviation (σ), correlation coefficients (r) and p-values (p) for the anomalies. The correlation and p-values summarize cross-correlation computations between column 2 and columns 3-5. Correlations significant at the 95% level are highlighted in boldface type. $1 \text{ EJ} = 10^{18} \text{ J}$.

Year	Summer's End HC	Winter's End HC	April-August Surface Heat Flux	April-August Along-isobath Ekman Transport
	EJ	EJ	EJ	$\times 10^3 \text{ m}^3 \text{ s}^{-1}$
2002	12.0	23	9	6
2003	28.0	14	6	7
2004	45.0	1	13	35
2005	3.0	-9	-7	-9
2006	-42.0	-22	-15	-32
2007	-47.0	-7	-6	-8
σ	36.5	16.4	11.0	
r		0.64	0.86	0.85
p		0.175	0.027	0.031

2.10 Figures

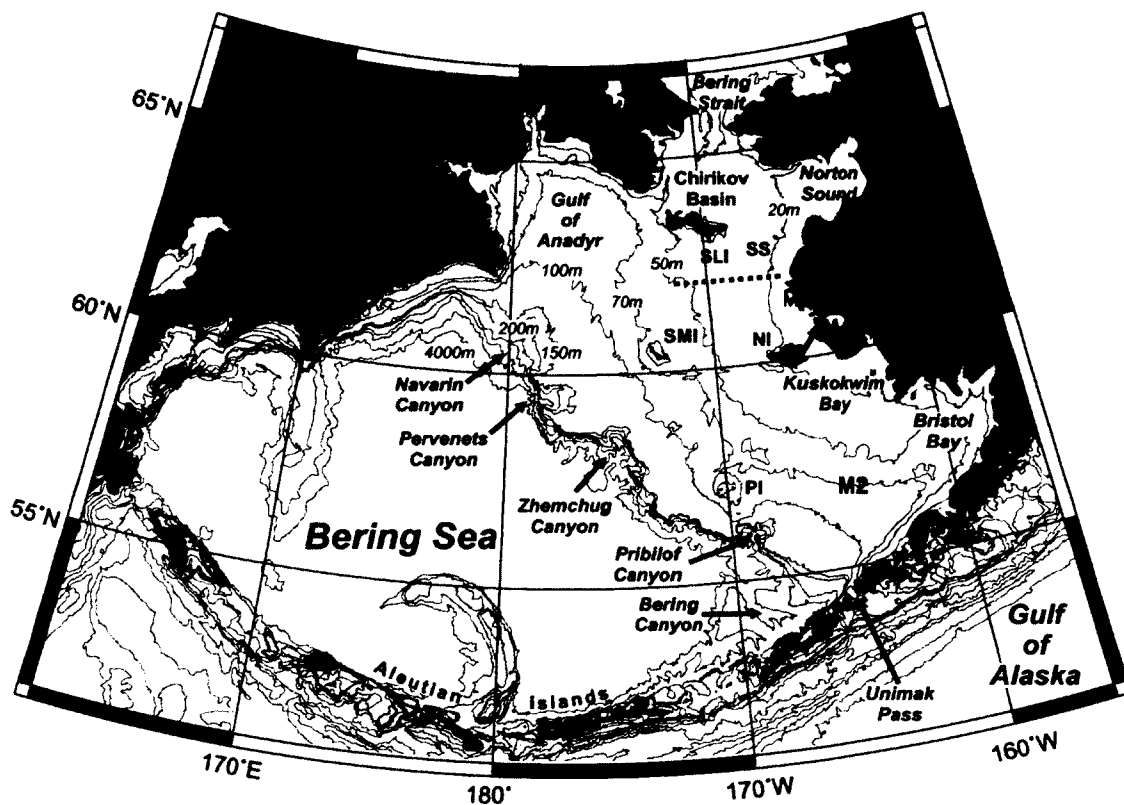


Figure 2.1: Map of the Bering Sea with place and feature names. Abbreviations denote: YR = Yukon River; KR = Kuskokwim River; SS = Shpanberg Strait; SLI = St. Lawrence Island; SMI = St. Matthew Island; PI = Pribilof Islands; NI = Nunivak Island. M2 denotes the site of NOAA Mooring 2 on the 70 m isobath. The CTD transect of July 2009 is denoted by a dotted line along 62 °N. The Arctic Ocean lies to the north of Bering Strait and the greater Pacific Ocean lies south of the Aleutian Islands. Depth contours are plotted at the following depth levels: 20 m, 50 m, 70 m, 100 m, 150 m, 200 m, 500 m, 1000 m, 2000 m, 3000 m, 4000 m, 5000 m and 6000 m.

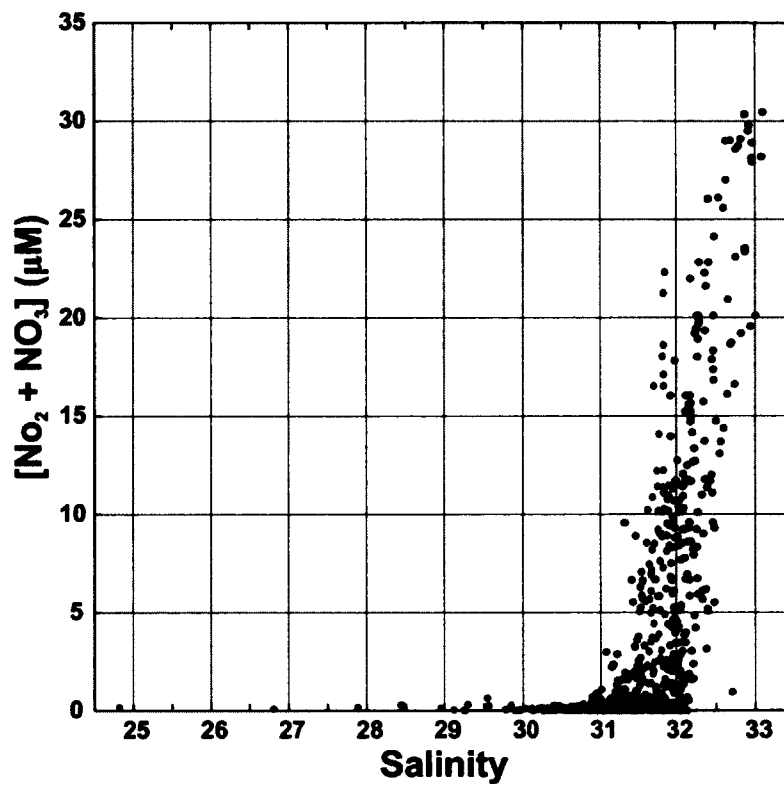


Figure 2.2: Relation of total nitrate to salinity for 779 water samples collected across the Bering Shelf between 2002 and 2006. Red (blue) points denote stations where the total water depth is less than or equal to (greater than) 30 m. Data collected by the U.S. Bering Aleutian Sustainable Salmon International Survey (BASIS) program.

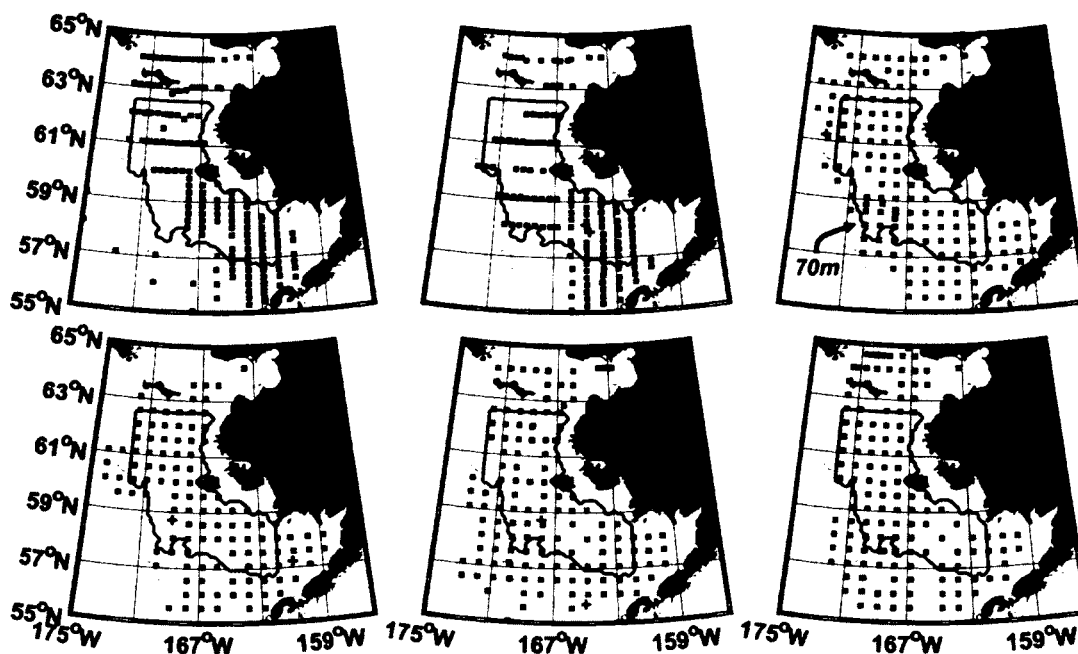


Figure 2.3: BASIS program CTD station coverage over the eastern Bering Sea shelf, 2002-2007. The region that bounds heat and fresh water integrations is denoted in each panel by a contour line. Dots show locations of good temperature and salinity data; plus signs show locations of good temperature data only. Nominal station spacing of $\frac{1}{2}^\circ$ latitude (56 km) is achieved in 2004-2007 across most of the focus domain; west of Nunivak Island in 2002 and 2003 the station spacing is 1° of latitude, or about 111 km. All samples are taken between August and mid-October.

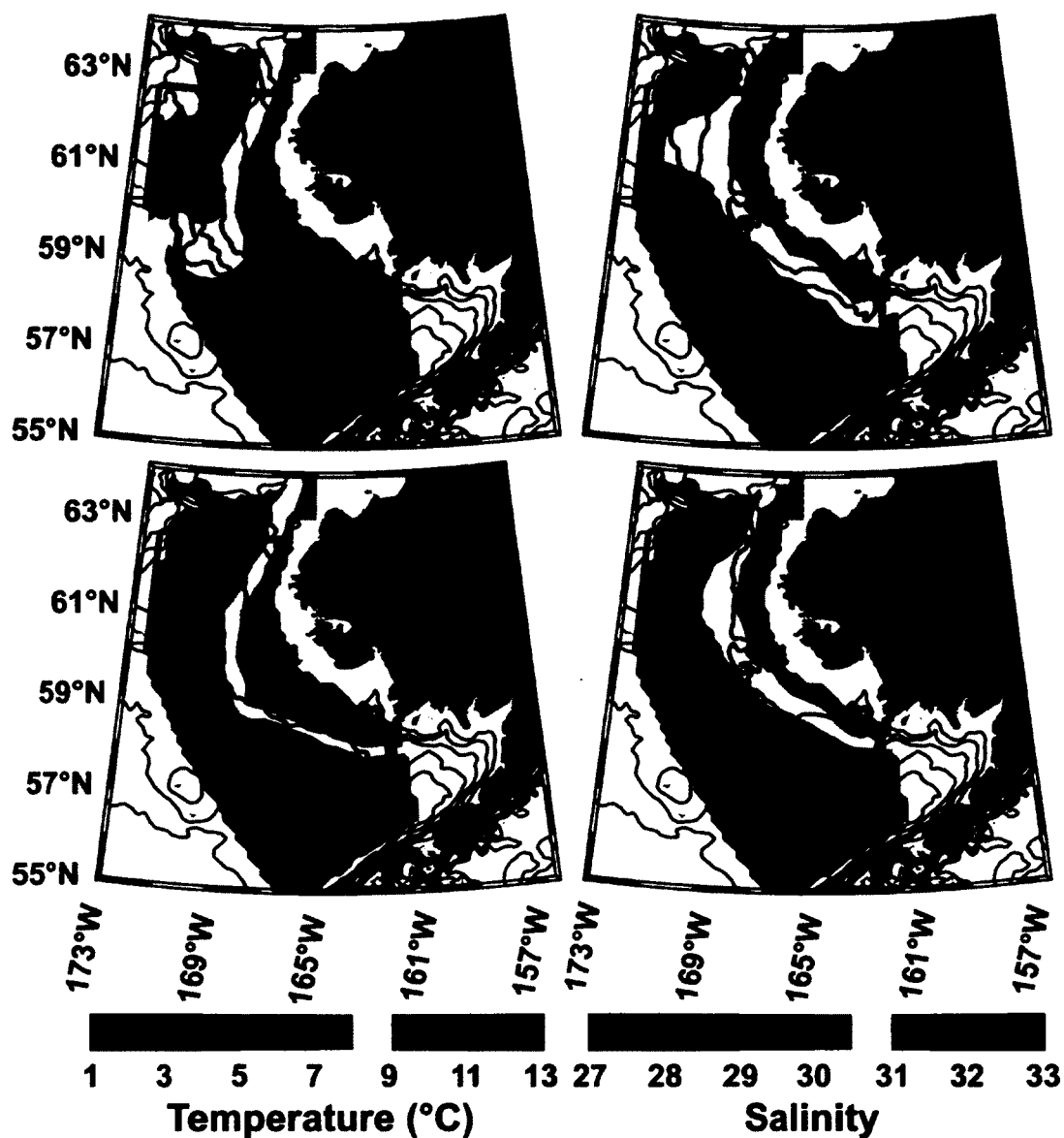


Figure 2.4: Mean late summer-early fall 2002-2007 distributions of temperature (left) and salinity (right) above (top) and below (bottom) the mixed layer depth. The region that bounds heat and fresh water integrations is denoted in each panel by a thick contour line. Depth contours are plotted at the following levels: 20 m, 30 m, 40 m, 50 m, 60 m, 70 m, 100 m and 200 m.

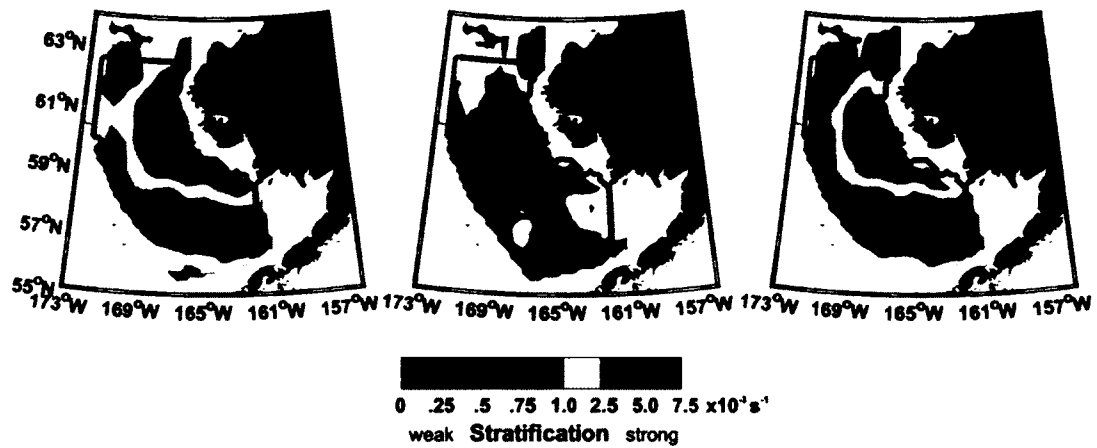


Figure 2.5: 2002-2007 mean maximum water column Brunt-Vaisala frequency. The Brunt-Vaisala frequency is computed by holding the salinity constant at the water column mean (left); by holding the temperature constant (center); and by allowing both temperature and salinity to vary (right). Note the nonlinear color scale.

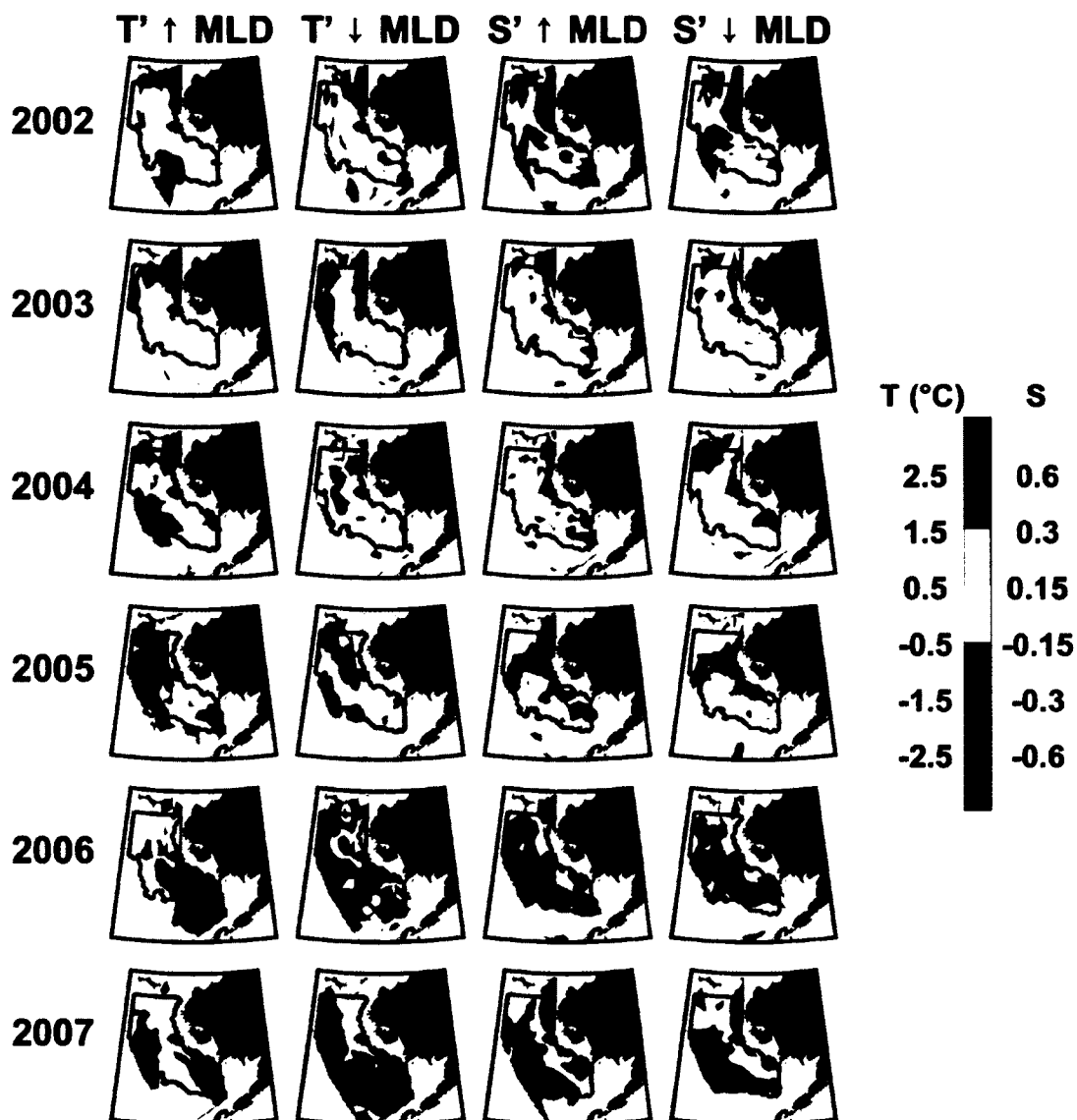


Figure 2.6: Temperature and salinity anomalies above (\uparrow) and below (\downarrow) the mixed layer depth (MLD = depth where $\sigma_t = \sigma_t @ 5 \text{ m} + 0.1 \text{ kg m}^{-3}$). Anomalies are computed in temperature and salinity units with respect to the multi-year means shown in Figure 2.4. Blue (red) colors indicate that the temperature/salinity anomalies are warmer/saltier (cooler/fresher) than the mean fields. The region that bounds heat and fresh water integrations is denoted in each panel by a thick contour line.

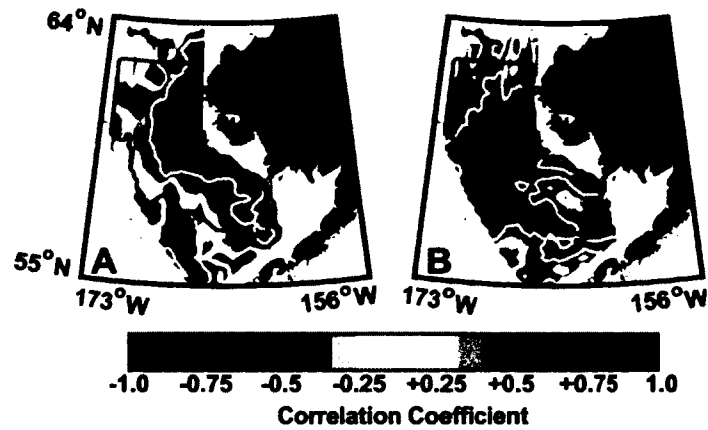


Figure 2.7: Late summer-early fall temperature (A) and salinity (B) vertical correlation maps, showing the temporal correlation between values above the MLD with values below the MLD at zero lag. Red indicates positive correlation; blue indicates negative. Yellow contours denote significance at the 95% confidence level ($r = \pm 0.81$). The region that bounds heat and fresh water integrations is denoted in each panel by a black contour line.

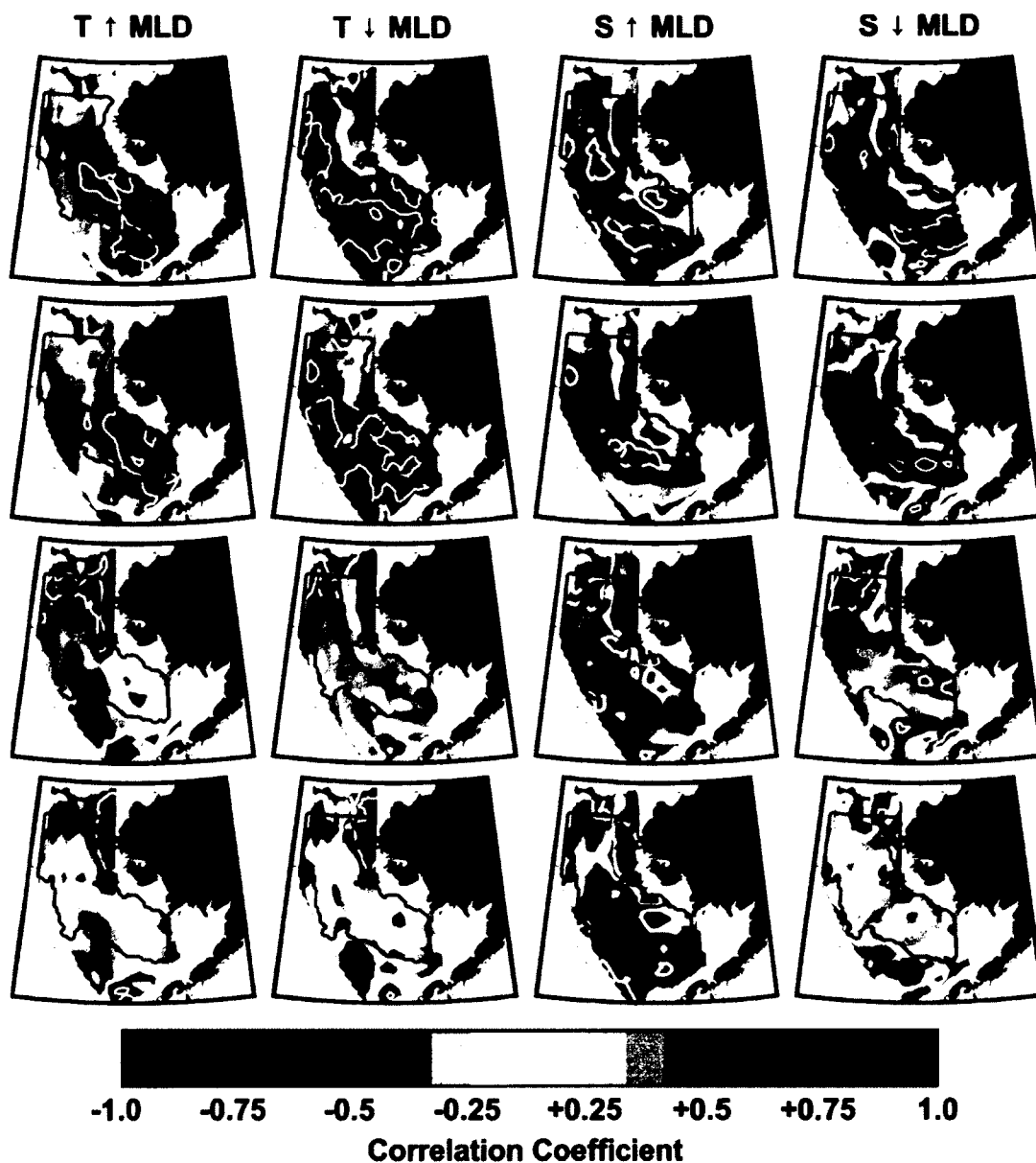


Figure 2.8: Late summer-early fall temperature and salinity horizontal correlation maps. Color scheme and map bounds are as given in Figure 2.7. Correlations are computed at between the point marked by an “X” on each panel and all other grid points for each column from left to right as marked: Temperatures above the MLD; Temperatures below the MLD; Salinity above the MLD; and Salinity below the MLD. Yellow contours denote significance at the 95% confidence level ($r = \pm 0.81$).

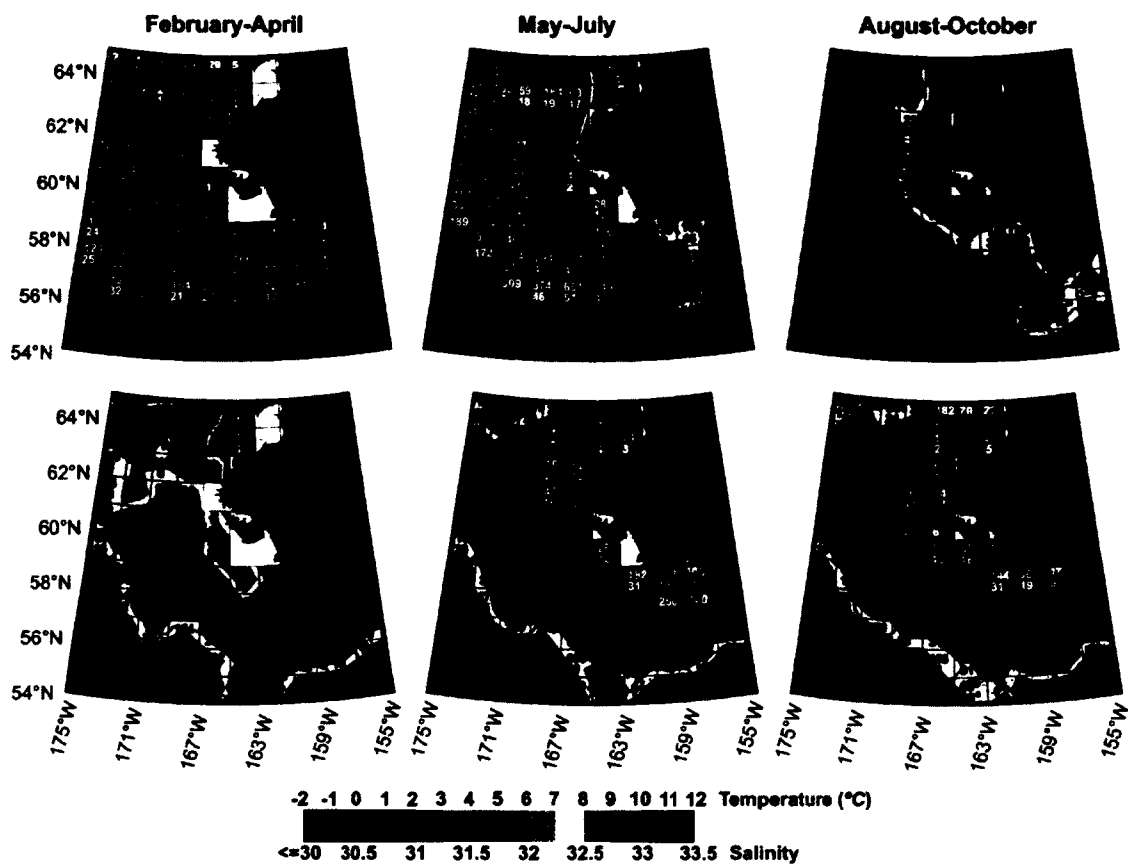


Figure 2.9: Climatology of the 0-100 m mean temperature (top row) and salinity (bottom row) in the eastern Bering Sea during the time periods indicated. The upper number in each grid cell indicates the total number of casts for the cell; the lower number denotes the number of years represented by these casts. Note the existence of some cells with no or few data points.

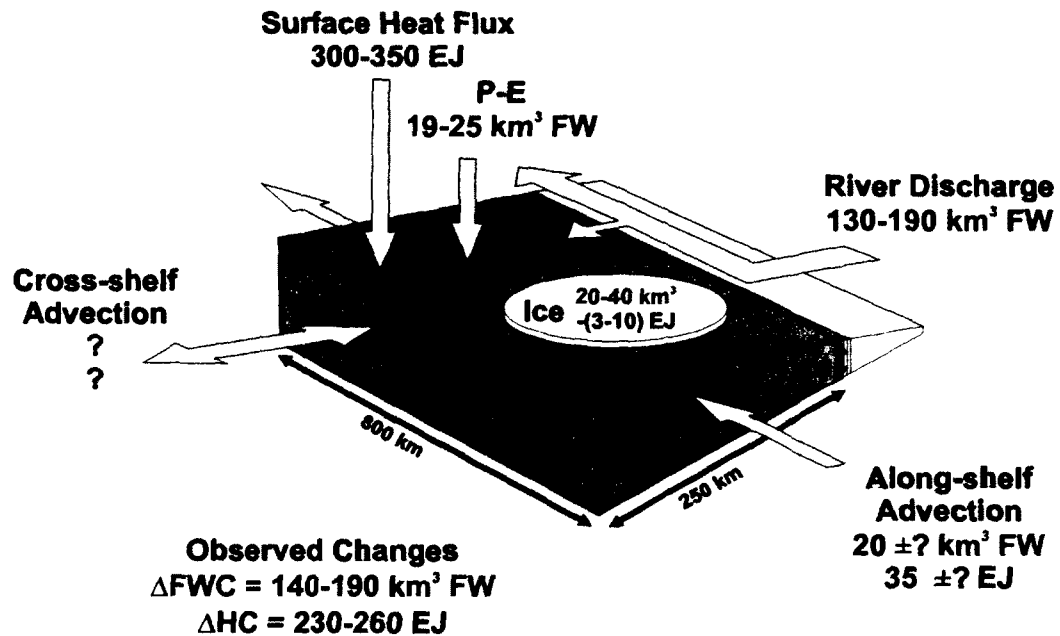


Figure 2.10: April to September estimated fresh water (FW) and heat fluxes and changes in standing stocks for the central Bering Sea shelf. Question marks denote unknown fluxes. 1 EJ = 10^{18} J.

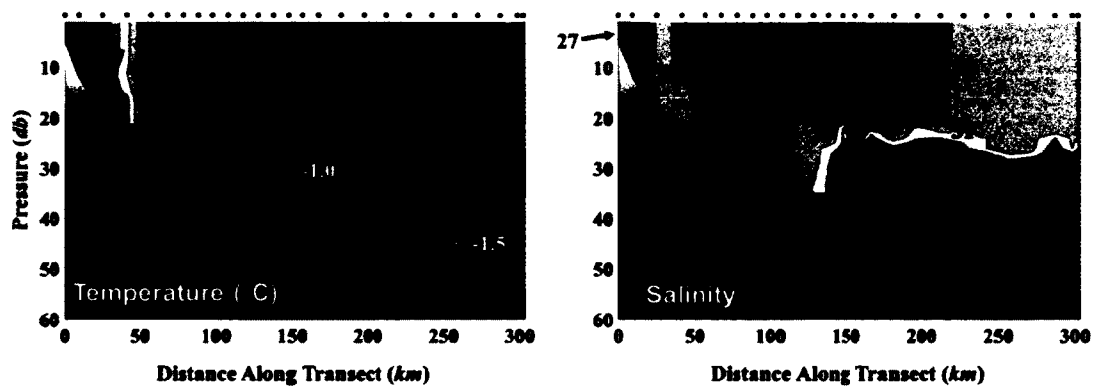


Figure 2.11: CTD transect occupied on 15-16 July 2009 between 61.70 °N, 166.31 °W and 61.97 °N, 171.98 °W. Dots along top of graphs denote location of CTD stations.

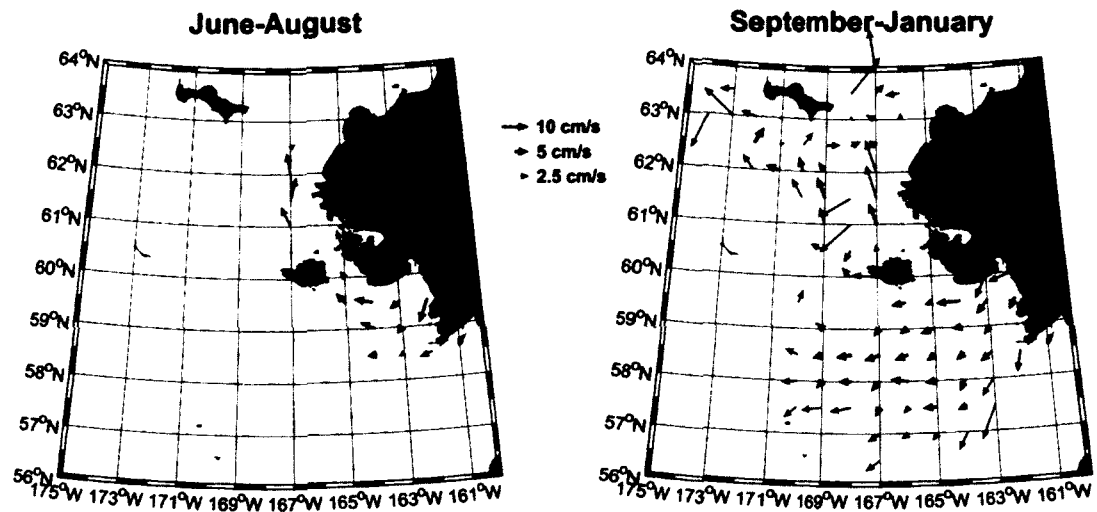


Figure 2.12: Mean seasonal flow patterns derived from near-surface oceanographic drifters for June-August (left) and September-January (right). Black vectors denote grid cells with at least 30 drifter-days worth of data; gray vectors represent at least five drifter-days of data.

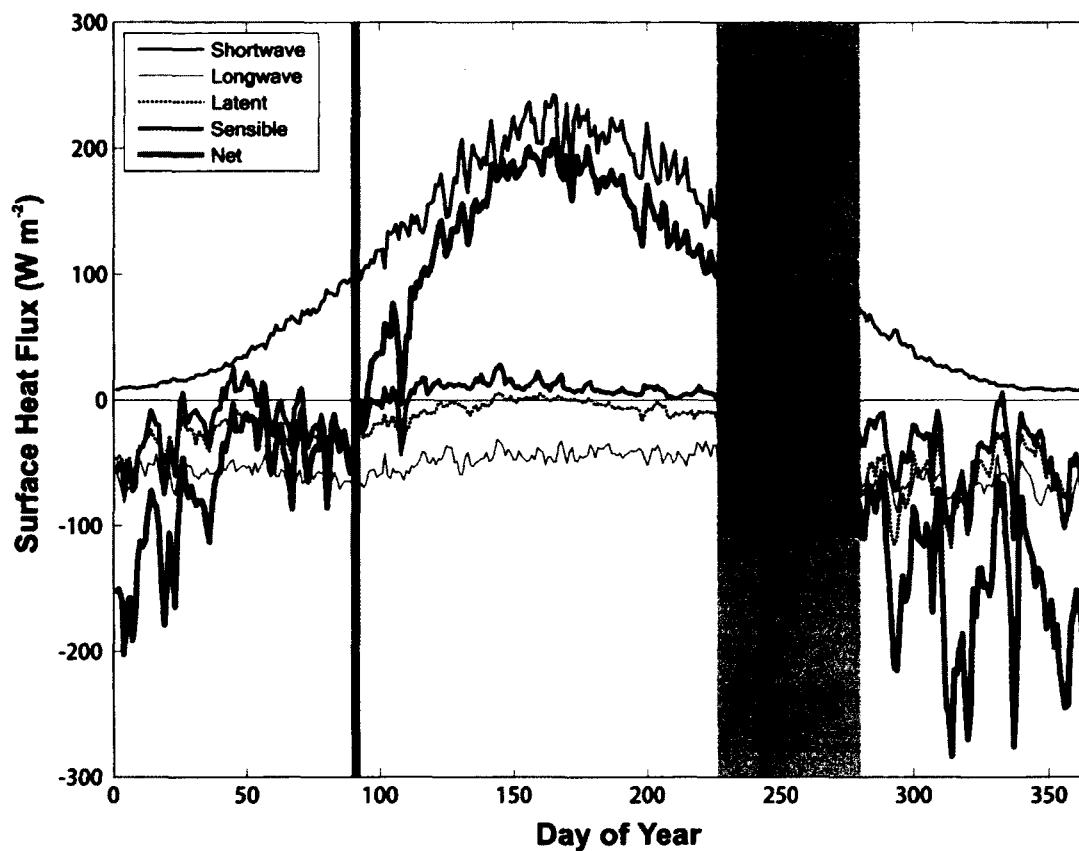


Figure 2.13: Annual mean cycle of mean daily surface heat fluxes for the central shelf region over the years 2002-2007. Vertical grey lines denote 1 April and 1 September. The heating season begins on the date near April 1 when the net surface heat flux crosses from oceanic heat loss to oceanic heat gain. The BASIS cruises span days 226 to 281, depicted by the gray shading.

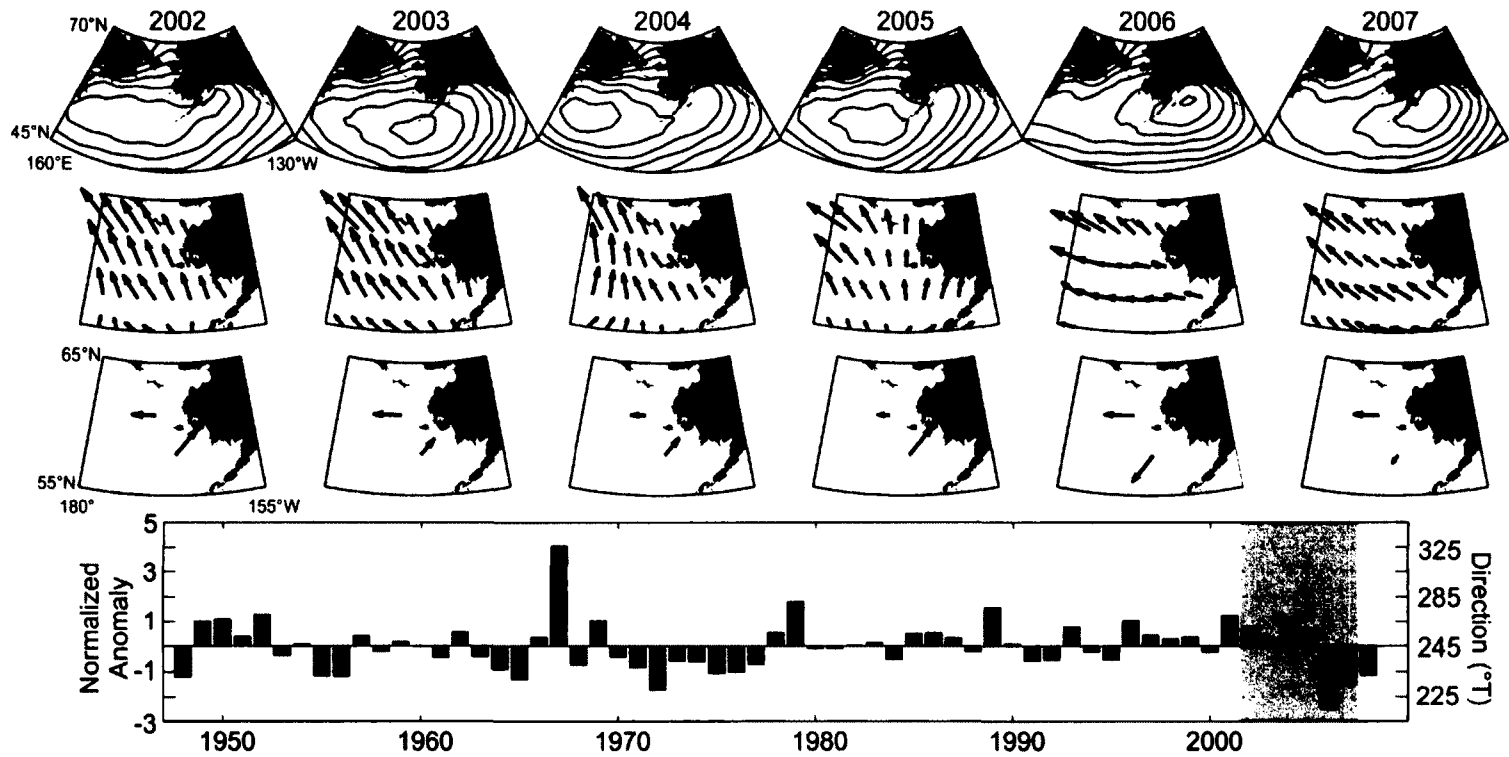


Figure 2.14 Mean October to May 2002-2007 maps of sea level pressure (first row), maps of Ekman transport vectors (second row), maps of the cross-shore component of the Ekman transport for sub-domains north and south of 60°N (third row) and time series of the mean October to May 1948-2008 wind direction anomaly computed at 60°N, 170°W (bottom row). Sea level pressure is contoured at even integer millibar levels. High pressure exists in the lower right corner of all panels; closed contours bound low pressure minima. Scale vectors on land denote $5.3 \times 10^2 \text{ kg s}^{-1} \text{ m}^{-1}$ and $5.0 \times 10^4 \text{ m}^3 \text{ s}^{-1}$ for the second and third rows respectively.

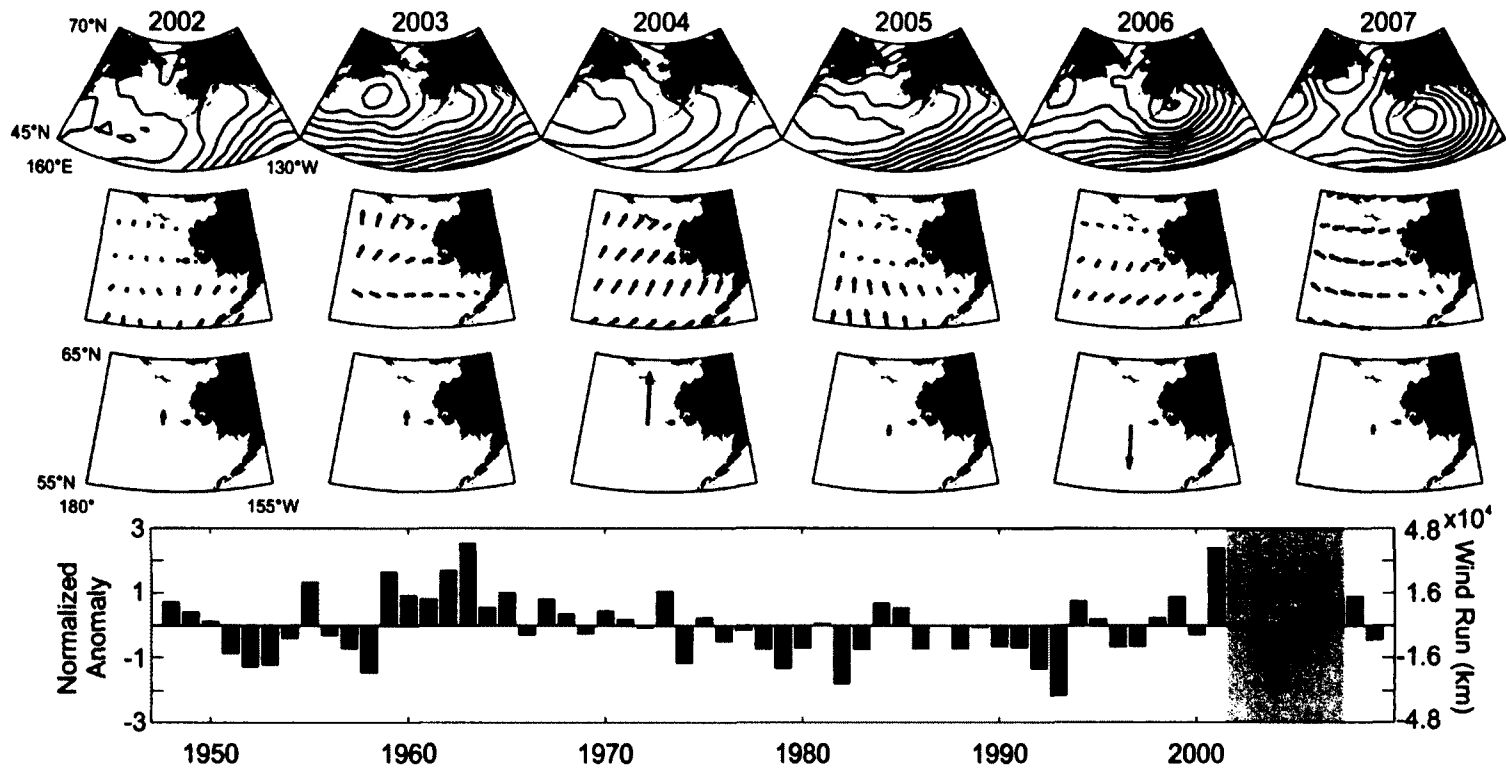


Figure 2.15: Mean April to August 2002-2007 maps of sea level pressure (first row), maps of Ekman transport vectors (second row), maps of the Ekman Transport N-S component across 60°N (third row) and time series of the mean April to August 1948-2009 E-W wind run anomaly computed at 60°N, 170°W (bottom row). Sea level pressure is contoured at all integer millibar levels. High pressure exists in the lower right corner of all panels; closed contours bound low pressure minima. Scale vectors on land denote $5.3 \times 10^2 \text{ kg m}^{-1} \text{ s}^{-1}$ and $2.0 \times 10^4 \text{ m}^3 \text{ s}^{-1}$ for the second and third rows respectively.

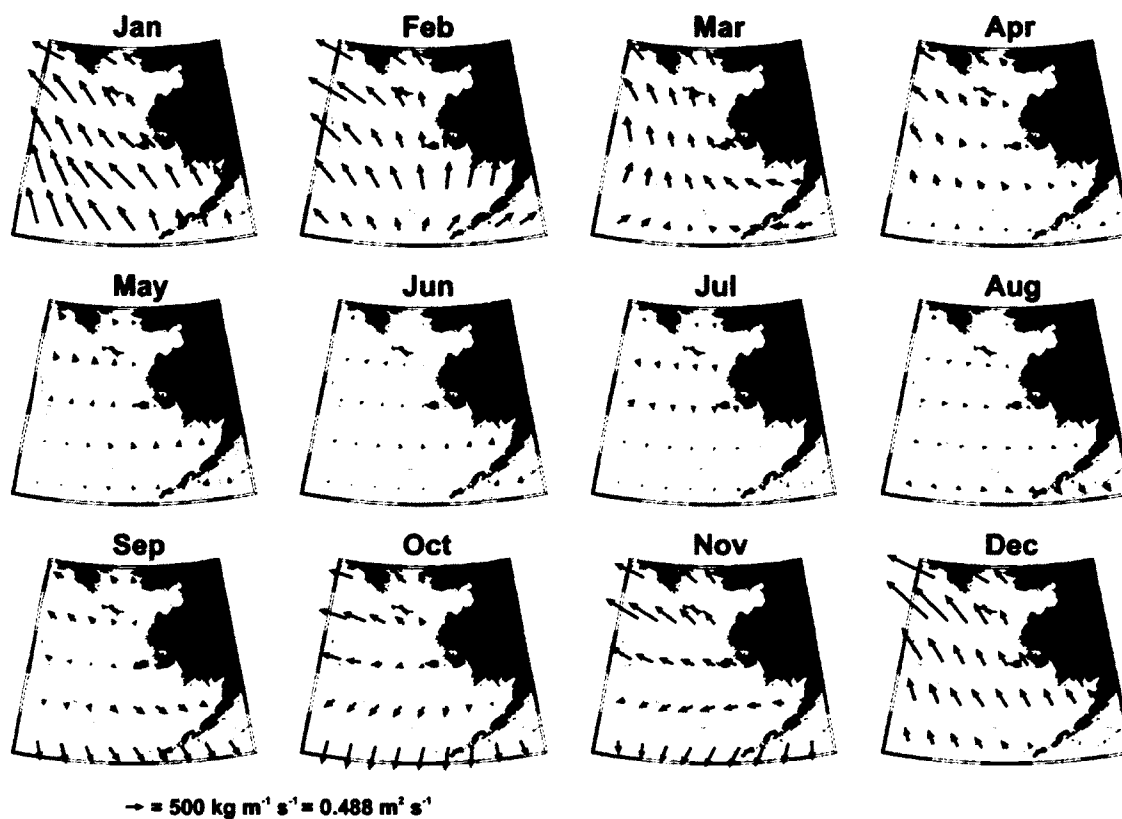


Figure 2.16: Mean monthly Ekman Transport computed from the NCEPR 6-hourly wind fields between 2002 and 2007. Scale vector for all panels is shown at the bottom.

Chapter 3: On ocean and sea ice modes of variability in the Bering Sea¹

3.1 Abstract

Results from a 35-year hindcast of Northeast Pacific Ocean conditions are confronted with observational data collected over the Bering Sea shelf within the integration time period. Rotary power spectra of the hindcast currents near NOAA mooring site M2 site fall within the 95% confidence bounds for the observational spectra except for a high-bias in the counter-clockwise rotating component at 10 m depth in the high frequencies (periods < 24 hr). The model exhibits the most skill in reproducing anomalies of the integrated annual sea ice concentration and monthly subsurface (60 m depth) temperature fields, accounting for 85% and 50% of their observed variability, respectively. Analysis of the integrated ice concentration time series reveals evolution in the mean duration of ice-free waters (40 year trend of +6.8 days/decade) and changes in this parameter's variance with time. Correlation and EOF analyses reveal the primary temporal-spatial patterns of variability in the temperature and salinity fields over the Bering Sea and northern Gulf of Alaska for near-surface (0-20 m) and subsurface (40-100 m) depth layers. Correlation analysis between the EOF principal components and various climate index and observed time series show that the Pacific Decadal Oscillation (PDO), the North Pacific Gyre Oscillation (NPGO) and the Bering Sea annually integrated ice area (IIA) anomalies are important indices of thermohaline variability; the spatial structure of these modes gives insight to their potential impacts upon the ecosystem. We identify a number of ecologically and economically important species whose temporal variability is significantly correlated with the identified spatial patterns.

¹Danielson, S., E. Curchitser, K. Hedstrom, T. Weingartner, and P. Stabeno (2011), On ocean and sea ice modes of variability in the Bering Sea, *J. Geophys. Res.*, 116, C12034, doi:10.1029/2011JC007389.

3.2 Introduction

The physical oceanography of the eastern Bering Sea is influenced by tides, winds, buoyancy, topography, shelf-slope exchanges through canyons, flows through narrow passes and the yearly formation, drift, and melting of sea ice [Schumacher *et al.*, 2003]. The shelf supports a productive ecosystem, which delivers substantial benefit for both subsistence and commercial harvests, resulting in about half of the total U.S. fisheries landings [NPFMC, 2005]. There are also increasing levels of commercial vessel activity [Orr, 2011]. To better manage these interests, a fuller understanding of the Bering Sea's physical environment is required [ACIA, 2005]. Our study provides a step toward this goal by the implementation, evaluation, and analysis of a 35-year numerical hindcast of the thermohaline, circulation and ice fields with sufficient resolution to address some pertinent questions in the Bering Sea.

The Bering Sea spans 20 degrees in longitude and 15 degrees in latitude (Figure 3.1). As a subarctic sea, seasonal variations in forcing are large and reflected in the circulation field, mixing and stratification, and sea ice distribution. Ecosystem structures are intrinsically tied to the physical features in the Bering Sea. For example, hydrographic features segregate predators from their prey (e.g. adult pollock from young of the year [Wepstead *et al.*, 2000]); the strength of stratification impacts the success of euphausiids [Coyle *et al.*, 2008] and consequently, the over-wintering success of juvenile pollock [Heintz and Vollenweider, 2010; Andrews *et al.*, 2011]; convergent fronts aggregate prey for feeding seabirds [Harrison *et al.*, 1990]. The location, timing, and thickness of sea ice cover impacts the trophic system: Pacific walrus use the ice for resting and pupping [Fay, 1982], spectacled eiders use the St. Lawrence polynya as a winter feeding ground [Peterson *et al.*, 1999; Lovvorn *et al.*, 2003], late summer foraging by thick-billed murre near the Pribilof Islands is observed to be related to the previous winter's ice extent [Kokubun *et al.*, 2010]. Hunt *et al.*, [2002] propose that the timing of ice melt exerts a strong control on the timing of phytoplankton blooms and the fate (benthic/pelagic) of ice-edge production and zooplankton recruitment.

Large inter-annual variability and multi-decadal trends or regime shifts have been observed in many atmospheric and oceanographic parameters over the Bering Sea shelf [Overland *et al.*, 1999; Stephens *et al.*, 2001; Stabeno *et al.*, 2002a; Bograd *et al.*, 2005; Woodgate *et al.*, 2005; Rodionov *et al.*, 2007; Danielson *et al.*, 2011]. Many of these changes coincide with changes in the biota [Benson and Trites, 2002; Hunt *et al.*, 2002; Mueter and Litzow, 2008], including population changes in both managed and unmanaged species. Examples of such fluctuations include the onset of previously unobserved coccolithophorid blooms in the Bering Sea [Stockwell *et al.*, 2001], increases and subsequent decreases in the biomass of medusae [Brodeur *et al.*, 2002; 2008], variability in zooplankton biomass [Sugimoto and Tagdokoro, 1997; Napp *et al.*, 2002], northward shifts of many groundfish species [Mueter and Litzow, 2008] and declines in bird and marine mammal populations [Byrd *et al.*, 1997, Trites *et al.*, 1999]. Many of the underlying causes of these population fluctuations are not known.

The principal currents in the eastern Bering Sea basin are the Aleutian North Slope Current (ANSC [Stabeno and Reed, 1994; Stabeno *et al.*, 1999], which flows eastward along the north side of the Aleutian Islands and the Bering Slope Current (BSC [Schumacher and Reed, 1992]), which is fed by the ANSC and flows northward along the continental slope. Exchange between shelf and slope waters provides nutrients to maintain high production on the shelf [Coachman, 1986]. The controlling mechanisms are not well known although they are likely mediated by flow-topography interactions, slope current instabilities, and tides [Schumacher and Reed, 1992; Stabeno and Van Meurs, 1999; Mizobata *et al.*, 2006]. Net flows over the eastern Bering Sea shelf are northward due to a mean 0.8 Sv transport through Bering Strait [Roach *et al.*, 1995]. Wind-driven flows over the central shelf appear to laterally redistribute fresh water and heat on a seasonal basis [Danielson *et al.*, 2011]. On the inner Bering Sea shelf, the Alaska Coastal Current enters the Bering Sea through Unimak Pass from the Gulf of Alaska (GOA). Shelf tides account for 50-95% of the total kinetic energy south of St. Lawrence Island [Coachman, 1986; Danielson and Kowalik, 2005]. The tides diffuse the

ACC frontal system, which is fed in part by terrestrial runoff that occurs between Bristol Bay and Norton Sound [*Coachman et al.*, 1975; *Kachel et al.*, 2002].

Vertical mixing due to tides, winds, and freezing compete with the stratifying tendencies of solar heating, river discharge, and ice melt. The resulting balance forms three distinct biophysical domains on the southeastern shelf [*Coachman*, 1982; *Coachman*, 1986; *Schumacher and Stabeno*, 1998], which are nominally delineated by bathymetric strata. The coastal domain (0-50 m bottom depth) is well mixed or weakly stratified whereas the middle domain (50-100 m) consists of a strongly stratified two-layer system from spring through early fall. The outer domain (100 m to the shelfbreak) is more oceanic in character and includes surface and bottom mixed layers separated by a stratified layer.

By the beginning of winter, ice forms over the northern shelf [*Pease*, 1980; *Schumacher et al.*, 1982] and is advected as far south as the Alaska Peninsula in extreme years. The leading edge normally encounters melting throughout winter and ice retreat begins in the southeast Bering as early as February. However, ice can remain over the northern shelf well into June. These processes result in the annual formation of a “cold pool” (water < 2 °C) that forms over the northern shelf every year and over the southern shelf in years of extensive ice cover [*Takenouti and Ohtani*, 1974]. Fresh water from melting ice plays an important role in the spring setup of the stratified summer conditions on the northern shelf and much less so on the southern shelf [*Stabeno et al.*, 2010]. The cold pool breaks down in the fall for a short period of time as wind mixing and surface heat losses drive water column homogenization.

Our main objective is identifying dominant modes of inter-annual variability in the thermohaline and ice fields over the Bering Sea shelf based on the results of a 35-year (1970-2005) integration of a 3-dimensional coupled ocean-ice model. Before doing so, we quantitatively assess the skill of the model in order to show its value as a tool to study some aspects of this shelf and to identify some of the model’s limitations and capabilities. We compare model results to moored current/temperature/salinity records, satellite-derived sea ice concentrations, shipboard conductivity-temperature-depth (CTD)

observations, and tidal current/elevation harmonics. Temperature, salinity, and ice climatologies are removed in order to assess the model's ability to hindcast observed anomalies with respect to the mean daily, monthly, or annual conditions.

Previous numerical simulations of Bering Sea physical processes examine transport in straits and passes [*Overland and Roach*, 1987; *Spaulding et al.*, 1987; *Overland et al.*, 1994; *Hu and Wang*, 2010]), sea ice dynamics [*Kantha and Mellor*, 1989; *Pease and Overland* 1989; *Pritchard et al.*, 1990; *Zhang and Hibler*, 1991; *Clement et al.*, 2004], tides [*Kowalik*, 1999; *Kowalik and Stabeno*, 1999; *Danielson and Kowalik*, 2005; *Foreman et al.*, 2006], storm surges [*Johnson and Kowalik*, 1986], and shelf circulation [*Brasseur*, 1991; *Nihoul et al.*, 1993; *Hermann et al.*, 2002]. Three-dimensional coupled ice-ocean models have been applied to the entire Bering Sea with the primary focus being on mass transports and sea ice dynamics [*Clement et al.*, 2005; *Clement Kinney et al.*, 2009; *Wang et al.*, 2009; *Hu and Wang*, 2010; *Zhang et al.*, 2010].

Our model falls into this latter category and we refer to it as the Northeast Pacific model-5 (called NEP5 hereafter because the current implementation represents the fifth major code and grid iteration). It was initially developed as a component of the Northeast Pacific Global Ocean Ecosystem Dynamics (GLOBEC) program [*Curchitser et al.*, 2005] and its results (from previous versions) were used directly or as boundary conditions for a variety of Bering Sea and Gulf of Alaska studies [*Lanksbury et al.*, 2007; *Dobbins et al.*, 2009; *Fiechter et al.*, 2009; *Hermann et al.*, 2009a; *Hermann et al.*, 2009b; *Hinckley et al.*, 2009]. *Curchitser et al.*, [2010] ran the NEP5 model in a study supporting evaluation of potential impacts associated with possible offshore hydrocarbon development on the southeast Bering shelf. NEP5 results provide boundary conditions for multi-component ecosystem models that are part of the North Pacific Research Board's (NPRB) Bering Sea Integrated Ecosystem Research Program (BSIERP) [*BEST-BSIERP Program Summary*, 2010].

The manuscript is organized as follows. The model formulation is described in Section 3.3 and the observational datasets are described in Section 3.4. Model-data comparisons are presented in Section 3.5. The comparisons show that, in aggregate, the

model integrations provide useful proxy time series that extend *in situ* ice, salinity, temperature and velocity observations over the integration period and domain. In section 3.6, we use trend, correlation and empirical orthogonal function (EOF) analyses to identify patterns of variability and their relation to fluctuations in ecosystem and climate records.

3.3 Numerical model description

We implemented a coupled ocean/sea ice model based on the Regional Ocean Modeling System (ROMS), building upon *Curchitser et al.* [2005]. ROMS is a free-surface, hydrostatic primitive equation ocean circulation model (subversion accessed via Git at <https://www.myroms.org/> on March 10, 2010). It is a finite volume (Arakawa C-grid) model with several advanced features including sustained performance on multi-processor computing platforms using Message Passing Interface (MPI) communication protocol; high-order, weakly dissipative algorithms for tracer advection; a unified treatment of surface and bottom boundary layers (e.g., K-Profile Parameterization [*Large et al.*, 1994]), and atmosphere-ocean flux computations based on the ocean model prognostic variables using bulk-formulae [*Large and Yeager*, 2008]. The vertical discretization is based on a terrain-following coordinate system with the ability to increase the resolution near the surface and bottom boundary layers.

The foundation of the sea ice module is described by *Røed and Debernard* [2004] and was implemented in ROMS by *Budgell* [2005]. The algorithms consist of the elastic-viscous-plastic (EVP) rheology [*Hunke and Dukowicz*, 1997; *Hunke* 2001] and thermodynamics by *Mellor and Kantha* [1989]. It is fully explicit, implemented on the ROMS Arakawa C-grid, and therefore fully parallel using MPI. The model also includes frazil ice growth in the ocean being passed to the ice [*Steele et al.*, 1989]. It currently follows a single ice category, which exhibits accurate results in a marginal ice zone such as the Bering Sea.

One-way nesting was implemented using a hybrid of nudging and radiation approaches [*Marchesiello et al.*, 2001]. The global-to-regional downscaling via open boundary conditions has several desirable features for the implementation of regional

models: for multi-decadal integrations, climate signals project onto the high-resolution inner domains through boundary forcing; tidal forcing is naturally implemented on the domain's open boundaries but for extensive integrations a tidal potential correction is applied to ensure proper tidal phasing. The approach allows affordably generating ensembles of high-resolution, multi-decadal simulations with realistic boundary forcing and provides the ability to test the robustness of solutions and understand model errors.

The NEP5 model domain (Figure 3.2) extends from approximately 20 °N to 71 °N and extends 2250 km offshore from the North American coast at a nominal horizontal resolution of 10 km and with 60 vertical levels stretched towards the surface boundary. The grid (a rectangle in a Lambert Conical projection) is rotated relative to lines of constant longitude so as to minimize computations over land.

We generated our own bathymetric grid by compiling an extensive collection of bottom soundings from sources that include the National Ocean Service hydrographic trackline database, soundings from NOAA's Electronic Navigational Charts (ENCs), other U.S. trackline/multibeam data archives and scientific research cruises. We also incorporated ENC soundings from the Canadian Hydrographic Service. In Russian waters, point soundings from nearly 150 historical Russian military nautical charts were digitized and geo-referenced. The resulting compilation of sounding data was gridded to a regular 30 arc-second (~ 1 km) mesh with the Generic Mapping Tools [*Wessel and Smith, 1991*] suite of algorithms and the final gridded DEM is publicly available for download (www.ims.uaf.edu/~seth/bathy/). The Alaska region grid spans 130 °E to 120 °W and 45 °N to 75 °N. The final grid was smoothed, subsampled, and merged with the General Bathymetric Chart of the Oceans [*GEBCO, 2003*] grid at 45 °N in order to complete the coverage across the southern portion of the domain. Maximum grid stiffness ratios $rx_0 = 0.42$ [*Haidvogel and Beckmann, 1999*] and $rx_1 = 24$ [*Haney, 1991*] imply that while the model likely has some difficulty in regions of steep topography such as near the Aleutian Islands, our focus area of the greater shelf should not be adversely impacted by baroclinic pressure gradient errors.

We integrated the model from January 1969 to November 2005. Spin-up adjustments are evident in the 1969 thermohaline fields and so our analyses are based only on the 1970-2005 results. The surface forcing for the NEP model is derived from the Common Ocean-ice Reference Experiments (CORE [Large and Yeager, 2008]), which consists of 6-hourly winds, air temperatures, sea level pressure and specific humidity, daily short-wave and downwelling long-wave radiation, and monthly precipitation. The air-sea fluxes are computed using bulk formulae [Large and Yeager, 2008]. The oceanic surface boundary layer is computed using the k-profile parameterization [Large *et al.*, 1994]. To ensure stability in regions with near-resonant tides (e.g., Bristol Bay and Cook Inlet), bottom stress is parameterized with a spatially variable linear coefficient of friction based on total water column depth, varying from $3 \times 10^{-4} \text{ m s}^{-1}$ for depths deeper than 1000 m to $6 \times 10^{-3} \text{ m s}^{-1}$ at 10 m depth. Surface salinities are restored to the monthly Polar Science Center Hydrographic Climatology (PHC), version 3.0, of Steele *et al.* [2001]. River discharge is implemented as a spatially dependent, time invariant surface fresh water flux, which is designed to preserve regional fresh water budgets. Boundary and initial conditions for this domain were derived from the Simple Ocean Data Assimilation (SODA) ocean reanalysis [Carton and Giese, 2008]. The geographical northern boundary has a sink term that enforces a constant 0.8 Sv northward transport through the Bering Strait.

3.4 Methods and data

3.4.1 Model output and evaluation metrics

Model output files containing results from the entire computational grid are stored as daily and monthly averages; nearly 200 individual grid points (most located near historical mooring deployment sites) are also stored at hourly intervals at all depth levels. Numerous shorter integrations were performed in order to spot-check and tune model performance before the full 35-year integration was executed. All results presented in this manuscript are from NEP5 integration #42 except for the cotidal chart (Figure 3.3),

which was generated by integration #45 and which output hourly records for the entire grid over a time period of six months.

With the exception of the tidal harmonic parameters, which do not require coincident analysis, model results extracted for comparison conform to the same time window and latitude, longitude and depth of the observations. We avoid temporally discrete and singular model/data comparisons where possible, focusing instead on the bulk statistics of measurement ensembles. The exception to this is that in comparisons with CTD data, the model's daily mean T/S profile for the specific day sampled is employed at the grid point closest to the sampling location.

We quantitatively compare the model with the observations following *Willmott et al.* [1985] and *Taylor* [2001] using the mean, standard deviation, cross-correlation, and root-mean-square difference (RMSD) as comparative metrics. Taylor diagrams [*Taylor*, 2001] facilitate incorporating all of these parameters into one graphic, which we use for the comparisons between the model and discrete CTD observations. Following *Taylor* [2001], the approach uses the pattern root mean square difference

$RMSD' = \sqrt{\sigma_M^2 + \sigma_O^2 - \sigma_M \sigma_O r}$, where σ is the standard deviation, r the cross correlation and subscripts M and O refer to the model and observations, respectively. The prime indicates that values are normalized so that the observational data represent unity variance, unity autocorrelation and zero RMSD', allowing multiple comparisons to be shown on a single graphic. Rotary power spectra and least squares harmonic fits for tidal parameters are used in other comparisons.

3.4.2 Time series data for model evaluation

We employ tidal amplitude and current harmonic parameters and net speed and direction statistics from various sources (Table 3.1) and locations (Figures 3.3A, 3.3B and 3.3C). Tidal parameters for measurements made by the National Data Buoy Center North Pacific Deep-ocean Assessment and Reporting of Tsunamis DART moorings (www.ndbc.noaa.gov) were computed using the MATLAB based T_TIDE algorithms of *Pawlowicz et al.* [2002]. For the net speed and direction statistics (based on 177

observational records), the shortest averaging period is 1.6 months, the longest is 24 months, the mean length is 7.6 months, and the median record length is 5.1 months. *Schumacher and Kinder* [1983] provide the greatest number of net speed and direction records, but the deployment intervals are not explicitly tabulated, so we estimated each record's start and stop date from their graphical Table 3.1. We believe that the accuracy in selecting the record endpoints is good to within one-half month. This uncertainty is associated with larger differences between the model and observed fields and degrades the accuracy of comparisons for the shorter records. Thus, we neglect *Schumacher and Kinder* [1983] records that are less than six months.

Temperature, salinity and current velocity time series records from the NOAA EcoFOCI program's mooring M2 (56.88 °N, 164.06 °W, 72 m water depth) between 1995-2005 are re-analyzed to compare the observed thermohaline annual cycle, monthly anomalies and current spectra with corresponding analyses from the model results.

3.4.3 CTD and bottle data

CTD and discrete bottle data are from the National Ocean Data Center (NODC) World Ocean Database 2009 (WOD-09, [*Boyer et al.*, 2009]), the US Bering-Aleutian Salmon International Survey (BASIS) program, the Bering Ecosystem Study (BEST) and miscellaneous cruises from the UAF Institute of Marine Science's (IMS) database, which includes cruise data from the 1970s to the present. We limit analysis to one near-surface depth level (10 m depth) and one depth level below the summer pycnocline (70 m depth). Multiple observations recorded within the same model grid cell and sampled on the same year-month-day were averaged, resulting in 5,939 unique observations at 70 m depth and 11,500 at 10 m depth. Data were grouped into regions that coarsely represent six major biophysical domains over the eastern shelf (Figure 3.3D and Table 3.2). Regions 1, 3 and 5 represent the inner, middle and outer shelf domains south of 60 °N; Regions 2, 4 and 6 cover the inner, middle and outer domains north of 60 °N.

3.4.4 Sea ice data

Sea ice concentration measurements (from the Nimbus-7 Scanning Multichannel Microwave Radiometer (SMMR) and Defense Meteorological Satellite Program (DMSP) Special Sensor Microwave/Imager (SSM/I) satellites) are from the National Snow and Ice Data Center [Cavalieri *et al.*, 1996, updated 2008]. These data are projected onto a 25-km grid and are available on a bi-daily (1979-1987) and daily (1987-2010) basis. Bi-daily data are linearly interpolated to create a daily time series for the period of observation. For spatial comparisons of the data with model results, ice concentrations from the model output were linearly re-gridded to match the dataset resolution.

3.4.5 Ecosystem indicator time series

The first three temporal components of each EOF are correlated with various climate and biological time series to assess how resolved modes co-vary with potential driving mechanisms and to examine possible ecosystem responses (Table 3.3). Cross-correlation significance (at the 95% level) is determined following *Pyper and Peterman* [1998]. Their method helps account for autocorrelation within each time series and results in a better determination of the effective degrees of freedom and an adjusted critical value for the cross-correlation. By doing so it reduces the frequency of Type I error. Records that exhibit significant linear trends are de-trended prior to computing the cross-correlation.

3.5 Model-data comparisons

3.5.1 Tides and currents

The NEP5 model-derived M_2 co-tidal map is shown in Figure 3.4. Amphidrome locations correspond closely with those of *Kowalik* [1999], *Foreman et al.* [2000], and *Foreman et al.* [2006]. Phase lines depict a westward travelling M_2 wave across the GOA and a northeastward propagating wave over the Bering Sea shelf. Amplitudes over the deep GOA waters are similar to those of *Kowalik* [1999] and the observations; however, in the western north Pacific and Bering Sea the NEP5 amplitudes are about 10 cm higher. As shown below, this difference extends onto the Bering Sea shelf, where

both the tide wave and the error magnitude are amplified. Tidal elevations are largest in the semi-enclosed basins of Cook Inlet and Bristol Bay, each of which are $\sim 200 - 300$ km long and 30 - 50 m deep. Here, the wavelength of a freely propagating tide wave

closely matches the resonance scale $L_R = \frac{T\sqrt{gH}}{4} = 200\text{-}250$ km, where g is gravitational acceleration, H is the average water column depth and T is the tidal period [Gill, 1982; Oey *et al.* 2007]. In the northeast GOA, amplification may be due to matching of the shelf width, L_S , to the tidal, ω , and inertial, f , frequencies, and the shelf bottom slope, α

(e.g., $L_S = \frac{g\alpha}{(\omega^2 - f^2)}$, [Clarke and Battisti, 1981]). In the northern GOA, L_S is $\sim 100\text{-}200$ km, and while the bathymetry is irregular, α is primarily between 10^{-3} and 10^{-4} and the lower portion of this range satisfies the resonance criterion.

Figures 3.5A and 3.5C compare the M_2 tidal elevations and phases from harmonic analyses of the model results and observations at the sites shown in Figure 3.3B. The median amplitude error expressed as a fraction of the observed amplitude is 30% when all locations are considered; this error is 80% when only the Bering shelf stations are included. Comparisons to Kowalik [1999] suggest that this overestimate is likely due to insufficient damping of the M_2 wave as it crosses the Aleutian Island chain. Errors in model bathymetry (smoothness; cross-sectional area of passes) and/or parameterization of bottom friction are likely causes for the excess flux of energy to the Bering Sea basin. The points clustered nearly on the 1:1 phase line at $\sim 300^\circ$ consist primarily of the deep-ocean stations south of the Aleutian Islands, indicating that the model accurately reproduces the phase of the tide wave in the northern North Pacific. However, north of the Aleutians and over the Bering shelf, the model tidal wave phase is retarded relative to the observations. For the Bering shelf, the modeled M_2 tide lags the observations on average by about 60° (two hours).

Figures 3.5B and 3.5C compare harmonic analyses of current observations and the model's depth-averaged currents located at the closest grid cell to the observations. The semi-major axes of the current ellipses are evenly distributed about the 1:1 line

although the relative scatter is greater than for the elevations. As with the tidal elevations, the Bering shelf shows larger errors than the GOA shelf. Because the tidal current timing is strongly dependent upon the elevation phase, the modeled tidal current phase also lags the observations, but on average by ~ 30 degrees. This difference may be partially explained by the proximity of historical current meters to the bottom, which were often deployed within the M_2 bottom boundary layer (BBL). Hence the observations may both underestimate the water column average M_2 semi-major axis magnitude (Figure 3.6A) and slightly advance the phase (Figure 3.6D).

To examine the vertical structure of the tidal currents, Figure 3.6 compares modeled and observed ellipse parameters from mooring site F8, located just south of St. Lawrence Island. The observations are from a moored ADCP, which misses the water column's uppermost 5 m and bottommost 7 m. In addition, the water column depth at site F8 is 50 m, whereas the depth at the closest model grid point is 46 m, so we expect a 4 m offset between the two profiles. To focus attention on the vertical structure rather than differences in magnitude, phase or bottom depth, the ellipse parameters in Figure 3.6 are scaled as follows. Water column depths (Z_r) are scaled between 0 (sea surface) and 1 (seafloor). At $Z_r = 0.10$, amplitudes are scaled to unity and the phase and inclination parameters are offset to 0° . The M_2 BBL is thicker than the K_1 BBL, because the M_2 (K_1) frequencies are on opposite sides of the inertial frequency resulting in different dynamics between the sub-inertial and super-inertial waves [Defant, 1960; Prandle, 1982]. Both the observed and modeled M_2 ellipses rotate clockwise (CW) in the upper portion of the water column and counter-clockwise (CCW) near the seafloor. For the K_1 tide, the CW component dominates everywhere. The observed M_2 profile has a slight mid-depth maximum due to tidal enhancement near the pycnocline during the summer when the water column is strongly stratified [Danielson and Kowalik, 2005]. The NEP5 model does not reproduce this feature, suggesting that the model may not contain sufficient late-summer stratification near this site. The model and observed 95% confidence ranges overlap throughout the observed depth range for all of the K_1 ellipse parameters. The confidence limits also overlap for the M_2 parameters except at mid-depth

for the currents and in the lower third of the water column for the orientation and phase angles.

Rotary spectra [Mooers, 1973] derived from the 10 m and 50 m depth levels at mooring site M2 are shown in Figure 3.7. The spectra were calculated from non-overlapping windows and then smoothed with a five point moving average to highlight the tidal frequencies.

In the short-period (10 - 30 hr) portion of the spectrum, the 95% confidence limits of the model and observed spectra overlap for both depths except for the counterclockwise (CCW) component at 10 m depth. The moored spectrum flow is strongly polarized in the CW component for these periods, implying that motions are nearly circular. In contrast, the magnitudes of the model CW and CCW components are similar to one another, indicating that the model's high frequency motions are overly elliptical and that in this band the model contains too much kinetic energy. The model's high-frequency bias is not present at 50 m depth. In both the observed and model spectra the inertial peak is well defined at 10 m depth but is barely discernible at 50 m depth.

The long period (> 30 hr) observed and model spectral envelopes have similar variations and the confidence limits overlap across this frequency range. While the 10 m observed and model spectra are nearly indistinguishable from one another, the modeled 50-m spectrum is consistently larger than the observed; it is larger by about one-half the observed confidence limit range. Both the observed and modeled spectra have many corresponding peaks and troughs and, importantly, similar background noise levels. We conclude that the spectral character of the subtidal model currents at this particular location is in general agreement with the observed spectra.

Our final comparison between model-derived and observed currents is based on mean current vector magnitude and direction records from the sources in Table 3.1. Corresponding model results were generated from de-tided and then daily averaged currents at the model grid cell closest to the deployment location. The model currents were aligned in time and depth with the observations. Table 3.4 shows the relation between the hindcast and observed mean velocity records, grouped into zonal clusters.

The mean flow over the Bering shelf is generally weak ($< 10 \text{ cm s}^{-1}$) and oriented along isobaths toward the north. Flow reversals are common [*Schumacher and Kinder, 1983*] so that many of the mean observed (and modeled) low frequency vector components are not statistically different than zero. Such large variability renders statistical comparisons of mean velocity estimates difficult and results in the large ratios of mean speed to a) the error magnitude and b) the model/observed speed difference (Table 3.4). Strong ($\sim 25 \text{ cm s}^{-1}$) northward currents in Bering Strait are the exception: here the mean RMSD is only 14% of the mean speed and typical errors are within 30%. For observations reported with 95% confidence limits on the current speed, the model mean speed falls within these limits for approximately 40% of the records. Away from the Aleutian Islands and Bering Strait (rows 2 and 3 of Table 3.4), mean speeds are small ($2.5\text{-}5.2 \text{ cm s}^{-1}$) and the average model speeds are typically within 3 cm s^{-1} of those observed. With a few exceptions, mean differences in speed (represented as a percentage of the observed speed) are similar to the error estimates of the mean observed speed. Differences in current direction range between 10° and 79° . The largest discrepancy is in the southernmost latitude band, along the Aleutian Islands, where narrow passes, complex bathymetry, and strong tidal currents occur. The two northern most comparison ensembles show closest agreement in both the magnitude and direction.

In summary, we find that the model somewhat overestimates the tidal elevation amplitude and current magnitude over the Bering shelf although geographic distribution of these parameters and the vertical structure of the currents are reasonably reproduced. The spectral character of the model currents generally follows that of the observations, although the modeled tidal and subtidal currents generally have greater kinetic energy. Given the large synoptic variability with respect to the mean, it is difficult to make meaningful comparisons to the available suite of published mean velocity vector statistics. Bulk comparisons indicate that the model performance varies in space and we have at least bounded the range of probable errors in the modeled mean flow. Fronts and stratification also affect the shelf response to external forcing, so modeled currents also depend upon the model's ability to reproduce the shelf thermohaline structure.

3.5.2 Temperature and salinity

We next compare the temperature and salinity fields, considering first the long-term mooring records from mooring site M2 (Figure 3.1) and then shipboard hydrography.

Figure 3.8 shows the observed annual cycle of temperature and salinity at M2 depicted by the monthly means and their monthly anomalies computed between 1995 and 2005. Observed and modeled temperatures at 10 m and 60 m depth vary in-phase and have identical annual amplitudes. The only significant (at the 95% confidence limits) differences between temperatures at 10 m depth occur in April, October and November. The higher temperatures in the two fall months are due to a delayed onset of fall cooling and, as shown below, this leads to a corresponding delay in model sea ice growth. The 60 m model temperatures are $\sim 1-2$ °C warmer than observed from April through November. Observed 60 m temperatures do not increase from October to November; however, in the model fall temperatures continue to rise through November. Both near-surface (10 m) and deep (60 m) model salinities are consistently ~ 0.5 less than observed (with non-overlapping error bars), but observed and modeled 10-m salinities vary in-phase and have the same annual amplitudes (January to September decrease of $\sim 0.3-0.4$). In contrast, the deep model salinities show a February to June increase of ~ 0.1 while over the same period the observed salinities decrease by the same amount. The error bars show that neither of these seasonal trends is statistically significant.

Monthly anomaly comparisons in Figure 3.8 address the model's ability to reproduce seasonal and inter-annual variability in the thermohaline fields. At the 10 m (60 m) depth level, the model reproduces 37% (49%) of the observed temperature variability. Salinity anomalies are less accurately hindcast: the model captures 13% (17%) of the observed variability at the 10 m (60 m) depths. These results are consistent with our expectations: thermodynamic balances are more straightforward to accurately compute; fresh water variability on the shelf is tied to complex freezing and thawing processes, surface fluxes, coastal river discharges and cross-shelf exchanges. River

discharge in particular is not accurately implemented in NEP5 because the prescribed fluxes do not include seasonal or inter-annual variability.

To examine temperature and salinity variability more broadly across the shelf, we assembled historical CTD and discrete bottle measurements for six Bering shelf sub-regions (Table 3.2 and Figure 3.3D). We selected the 10 m (near surface) and 70 m (subsurface) depth levels for comparison and computed statistics based on each calendar month separately in order to investigate inter-annual rather than seasonal variability (Figure 3.9).

As with the moored records, the temperature comparisons are more favorable than those for salinity. More than one-half of the 10 m temperature comparisons in Figure 3.9 lie within $0.7 < r > 0.95$, $\text{RMSD}' < 1$ and $0.5 < \sigma < 1.5$. Temperature comparisons at 70 m depth mostly fall within $0.5 < r < 0.9$, $\text{RMSD}' < 1$, and $0.6 < \sigma < 1$. For both depths, many of the salinity comparisons lie within $\text{RMSD}' < 1$ and $0.3 < r < 0.7$. The model exhibits some differences in performance amongst regions: at 10 m depth, for example, Region 5 (outer shelf, south of 60 °N) temperatures agree best with the observations in most months, while in Region 1 (inner shelf, south of 60 °N) temperatures have the largest RMSD' . Salinities in all other regions occupy a similar range of correlations as those in Region 3 (mid-shelf, south of 60 °N); however, the standard deviations in Region 3 are closest to unity. These analyses are consistent with the comparisons made with the moored temperature and salinity records: the model has some ability to hindcast both temperature and salinity fields at surface and subsurface depths and has more skill with the thermal field than with salinity. The model exhibits slightly better performance in some regions than in others.

Our analyses of hydrographic data focused on the model's ability to reproduce inter-annual variability; however, spatial variability within each region impacts our results. We can estimate the magnitude of this by comparing results from Region 3 to results from mooring site M2 (containing temporal variability only). Within Region 3 we find temperature correlations (Pearson's r correlation coefficient) mostly between ~ 0.7 and 0.9 at 10 m depth (Figure 3.9) versus $r = 0.61$ computed from the moored mooring

data (Figure 3.8). These comparisons suggest that spatial autocorrelations improve the 10 m temporal correlation by about 0.1 - 0.3; at the 70 m depth level the correlation improves by about 0.1. Region 3 salinity correlations are only slightly smaller ($\Delta r < 0.1$) than those at M2 suggesting that any spatial autocorrelations have minor influence on the salinity results in Figure 3.9. The correlations will also reflect the extent that spatial variability across each region represents an appreciable fraction of inter-annual variability. This is most apt to be the case in the near-shore regions during late summer and early fall when horizontal gradients are largest.

Using the 2004 BASIS program CTD survey, we compare the *in situ* near-bottom temperature and salinity fields with those hindcast by the model (Figure 3.10) after linearly interpolating and truncating the model output to match the BASIS grid, and subtracting the mean value from each field. This latter transformation highlights spatial gradients rather than the offsets found with the moored record comparisons above. We find that the spatial structure of the hindcast temperature field matches the observed pattern with the exception of the cold tongue immediately south of St. Lawrence Island. This tongue extends to the eastern reaches of the island in the observations but not in the model, suggesting that eastward flow observed on the south side of St. Lawrence Island [Schumacher *et al.*, 1982; Danielson *et al.*, 2006] is not fully reproduced in the model. While the model shows higher salinity waters in the mid-shelf region, it does not capture the pronounced near-shore freshening that extends from Kuskokwim Bay to Norton Sound. This discrepancy may be a consequence of the time-invariant coastal discharge used in the model. Bering Sea river discharges exhibit strong seasonal variability because of the annual freeze-thaw cycle. Incorporating this variability in future models should lead to more realistic shelf salinity fields. The shelf salinity is also modulated by ice melting and formation processes, which we consider next.

3.5.3 Sea ice

In this section, we compare model ice concentrations to measurements made by passive microwave satellites. We form daily averages of ice extent weighted by percent concentration for the period January 1979 to November 2005 by integrating over the

region east of 170 °E and south of 66 °N, which represents most of the Bering Sea area subject to seasonal ice cover.

The mean annual cycle of ice cover (Figure 3.11A) indicates that the model closely reproduces the observed annual amplitude. Although the modeled spring ice retreat onset coincides with the observed, the model retreat rate is considerably slower. This discrepancy may be because the model currently lacks the ability to alter the ice albedo (and melt rates) due to wet ice conditions, melt ponds, and ice algae or debris within the ice [Curry *et al.*, 1995]. In addition, passive satellite measurements have difficulty in distinguishing between open water and wet or subsurface ice [Comiso *et al.*, 1997], so the satellite observations likely underestimate the spring ice extent. Consistent with the delayed onset of fall water column cooling noted in Section 3.5.2, fall ice development in the model lags the observations by ~ 3 weeks, although growth rates thereafter are comparable to observed. Comparison of the daily ice extent anomalies (Figures 3.11B and 3.11C) suggests that the model captures much of the integrated synoptic variability, accounting for 75% of the observed daily variance ($r = 0.87$, $p < 0.001$, Pearson's r correlation coefficient). The model reproduces 85% of the observed inter-annual variance ($r = 0.92$, $p < 0.001$) and there is no discernible trend in either the observed or modeled annual ice extent anomaly time series (Figure 3.11E).

Spatial distributions of mean monthly sea ice concentration over the eastern Bering Sea are plotted with blue contours in all panels of Figure 3.12. The first row of panels shows that model-observed differences in concentration are $< 10\%$ over most of the analyzed domain. Exceptions are in the Gulf of Anadyr and Chirikov Basin for December and March where the model underestimates ice concentrations by up to 30%. The delayed onset in freeze-up noted above is primarily due to the underestimated concentrations here, suggesting that the model may generate too much polynya and/or lead area in early and late winter. Overestimates of ice extent in May and June are mostly confined to the central northern shelf. Standard deviations of ice concentration (second row of Figure 3.12) are generally within 10% of each other with the exception of higher model variance south of Nunivak Island in May and across the northern shelf in

June; both a consequence of delayed melt. Absolute (RMSD) error between the model and observations (third row of Figure 3.12) is typically in the range of 10-20% through the winter; however, in May and June extensive regions with concentration errors of 20-40% persist. The correlation maps (fourth row of Figure 3.12) show that for most months, the region of significantly correlated (at the 95% level) variability greatly exceeds the area bounded by the 10% concentration contour. This verifies that when the ice edge is located far south (or north) of its mean position, the model captures this signal. Correlations weaken in the Gulf of Anadyr and Chirikov Basin, perhaps because of this region's proximity to the northern model boundary, where advection influences are strong and the northern boundary condition artificially specifies a constant northward transport.

3.6 Discussion

3.6.1 Model strengths and weaknesses

Our comparisons focused on the NEP5 model's skill at hindcasting observed variability of the thermohaline, sea ice and circulation fields of the eastern Bering Sea shelf. On monthly to annual time scales, we find that the model's primary strengths include its ability to reproduce 85% of the inter-annual variability in the integrated sea ice extent (Figure 3.11) and to account for up to nearly 50% of the variance in monthly temperature anomalies (Figure 3.8). On tidal and synoptic time scales, the model reproduces with significant skill the horizontal (not shown) and vertical structure of tidal currents (Figure 3.6) and the frequency distribution of current kinetic energy (Figure 3.7), although the model has somewhat greater kinetic energy overall (Figures 3.5 and 3.7).

The model less accurately hindcasts the sea ice extent during the melt season and the monthly salinity anomalies (Figures 3.11 and 3.8). However, errors in the salinity field are not particularly surprising given the prescribed coastal discharges and the large fresh water sources for the Bering shelf including the Yukon River and the integrated GOA discharge [Royer, 1982], a significant portion of which enters the Bering shelf [Stabeno, *et al.*, 2002a; Weingartner *et al.*, 2005; Aagaard *et al.*, 2006]. The GOA

discharge is particularly difficult to capture with a 10-km resolution given the complex land orography and coastline of this shelf. Improvements to the model are presently underway with respect to a more realistic coastal discharge and for the northern boundary condition. These changes, along with the wave-mixing parameterization of *Hu and Wang* [2010] may improve the modeled stratification for the shelf.

Notwithstanding these shortcomings, in its present form the model does allow us to examine aspects of the inter-annual variability in sea ice, temperature and salinity over the Bering Sea shelf.

3.6.2 Trends in the annual duration of ice-free waters

Danielson et al. [2011] quantified an increasing trend in the duration of the 1979-2009 open water season, defined as the last spring day (first fall day) that the eastern Bering Sea concentration-weighted integrated ice area falls below (rises above) 50,000 km² (the IIA index in Table 3.3). The model results allow us to extend this analyses to 1970 (Figure 3.13), nearly a decade longer than the modern satellite record. The model hindcast results suggest that there was a step change in open water duration that coincided with the mid-seventies “regime shift” [*Minobe*, 1999; *Mantua et al.*, 1997; *Stephens et al.*, 2001]. This result is consistent with reports that the early- to mid-1970s were a period of heavy Bering Sea and western Arctic ice cover [*Gibson and Schullinger*, 1998; *Niebauer*, 1998]. Over the 1979-2004 period of overlap between the model and observations we find a marginally significant increasing trend in the length of the open water season in the observed (7.4 days/decade, $r = 0.40$, $p = 0.041$, Pearson’s r correlation coefficient) but not the hindcast (7.1 days/decade, $r = 0.33$, $p = 0.095$, Pearson’s r correlation coefficient) time series. The model’s mean open water season is 8.5 days shorter than that observed, a result of the model’s apparent inability to melt ice fast enough in the late spring and early summer (Figure 3.11).

We also observe a change in the variance of open-water season duration between the first half (1979-1991) and the second half (1992-2004) of the record. The observations indicate increase in variance from 32 days² to 306 days² between the two periods and the model variance increases from 151 days² to 418 days². Given the large

inter-annual variability in the duration of the ice-free waters since 1992, it appears that Bering shelf is presently within a state characterized by higher year-to-year variability. This increased variance may imply increased ecosystem variability by altering spring production dynamics that propagate through seasons and across trophic levels [e.g., *Hunt et al.*, 2002].

The hindcast open water season duration for 1970-1978 (corrected for the 8.5 day offset) combined with the 1979-2009 observational record results in a time series with a highly significant 1970-2009 increasing trend of 6.8 days/decade ($r = 0.52$, $p < 0.001$, Pearson's r correlation coefficient). This trend will not persist because the ice growth season can be truncated only so far given winter ocean-atmosphere heat loss at this latitude. The model also indicates thinning ice by winter's end from 1970 to 2005; the trend is not significant.

3.6.3 Temperature and salinity variability

Near-surface shipboard CTD data collected by the BASIS program depict an apparent anti-correlation in the cross-shelf salinity field, while the cross-shelf temperature field exhibits an in-phase relation [*Danielson et al.*, 2011]. Selecting the grid point closest to M2 as our reference, we perform a similar analysis using monthly fields and find distinct patterns in each of the model-generated parameters (Figure 3.14). The in-phase temperature relation reflects the long (>1000 km) length scales associated with atmospheric forcing (e.g., the Aleutian Low). *Danielson et al.* [2011] attribute the cross-shelf salinity pattern to the redistribution of fresh coastal waters by the winter (October to May) wind field; the signal was significantly correlated with the previous winter's cross-shelf Ekman transport and the winter wind direction anomaly (WDA index in Table 3.3) computed at 60 °N, 170 °W. The salinity correlation pattern depicted in Figure 3.14 is similar to that found by *Danielson et al.* [2011]; however, the boundary between the two opposing phases is farther offshore in the model results. Thus, the model pattern less clearly signifies a coastal and middle shelf water mass exchange phenomena but may instead reflect ice dynamics: in years of extensive ice more brine is released in the north and more melt occurs in the south.

Based on the monthly average model fields, we compute EOFs for annually averaged temperature (T) and salinity (S) anomaly fields using every 4th model grid point over the Bering Sea and northern GOA. We consider the first three EOF modes from upper (U; 0 – 20 m) and lower (L; 40 – 100 m) depth layers. To remove the annual cycle and to minimize spatial biases, the records at each grid point were normalized into a standard monthly anomaly time series having unity variance and zero mean. Seasonal EOFs were similarly calculated and yielded results nearly identical to those described below. Following *North et al.* [1982], all modes discussed are fully resolved. Principal components are correlated to the time series listed in Table 3.3.

Within the upper layer EOFs (Figure 3.15), the first temperature mode (mode T1U) accounts for 47% of the total variance, and modes T2U and T3U account for 14% and 6%, respectively. The T1U mode is in phase over the region considered and is significantly and positively correlated ($r = 0.59$, Pearson's r correlation coefficient) with the PDO (Table 3.5), suggesting the influence of large-scale atmosphere-ocean heat fluxes and the associated sea level pressure fields. This notion is consistent with the negative correlation ($r = -0.67$, Pearson's r correlation coefficient) between T1U and the IIA index, which depends on the regional winds [*Overland and Pease*, 1982]. T1U is also correlated (but less strongly) to the North Pacific (NP) ($r = -0.36$, Pearson's r correlation coefficient) and the (WDA) ($r = 0.44$, Pearson's r correlation coefficient) indices, which are influenced by the position and strength of the Aleutian Low [*Trenberth and Hurrell*, 1994; *Danielson et al.*, 2011].

EOF T2U depicts an out-of-phase relationship between the northern GOA/southeastern Bering Sea and the western Bering basin/southwestern GOA. The pattern is positively correlated with the near-bottom (200-250 m) temperature at GAK1, the NPGO, the PNA and the GOA discharge record. The NPGO, the second mode of sea surface height variability in the North Pacific Ocean, is related to the sea surface elevation gradient between the North Pacific subarctic and subtropical gyres [*Di Lorenzo et al.*, 2008]. Positive anomalies in the NPGO imply enhanced transport within the North Pacific Current and the GOA gyre [*Di Lorenzo et al.*, 2008]. This gyre advects relatively

warm waters into the GOA and so the NPGO index is positively correlated with temperature anomalies at station GAK1. The southeastern Bering Sea shelf is in phase with the GOA shelf and basin for mode T2U, presumably reflecting the advective or atmospheric connections between these two regions.

EOF T3U exhibits positive phase over the northern Bering basin and GOA shelf and negative phase over the northern Bering shelf/southern Bering basin. Although it is unclear what establishes the spatial structure of this mode, it is correlated with two winter processes that are functions of the location and strength of the Aleutian Low: the winter (October-May) wind direction anomaly (WDA) and the ice extent index. The WDA index is also correlated with the summer's end central shelf salinity anomaly and may reflect inter-annual variability in the winter surface circulation [Danielson *et al.*, 2011]. EOF T3U suggests that the southern Bering shelf and GOA shelf may be linked by advective processes that are confined to the outer Bering shelf and shelfbreak, unlike the signal of T2U for which the positive phase extends across all of Bristol Bay.

Modes T1L and T2L (the 40-100 m layer) resemble the spatial and temporal structure of their corresponding upper layer modes and are correlated with the PDO (T1L, $r = 0.69$, Pearson's r correlation coefficient) and NPGO (T2L, $r = -0.63$, Pearson's r correlation coefficient), respectively. While T1L and T2L are more strongly correlated with these indices than T1U and T2U, they have a weaker correlation with ice extent ($r = -0.56$).

Although the model has shortcomings in capturing the observed salinities, model salinity fields are internally consistent since these conform to the model dynamics. Hence, the modeled salinity variations, such as those presented in Figure 3.14 and discussed below, reflect physical processes that may bear on ecologically important processes.

The first three upper layer salinity EOFs (Figure 3.15) represent a much smaller fraction of the total salinity variance than the corresponding temperature modes. For the 0-20 m layer, EOF S1U (13%) shows that the northeastern Bering shelf salinities are strongly out-of-phase with southwestern shelf salinities. This mode is correlated with the

IIA ($r = -0.79$, Pearson's r correlation coefficient) and the WDA ($r = 0.52$, Pearson's r correlation coefficient) indices. The correlations suggest that the mode structure reflects salinization due to ice formation processes in the northeast combined with ice melt in the southwest [Pease, 1980] and/or the winter cross-shelf transport of fresh coastal waters per Danielson *et al.* [2011]. Mode S2U (10%) is a weak out-of-phase relation between the middle shelf of the Bering Sea and the GOA shelf and in fact the pattern, when restricted to both shelves alone resembles the correlation structure in Figure 3.14. S2U is correlated to near-bottom temperatures at GAK1 ($r = 0.70$, Pearson's r correlation coefficient), GOA runoff ($r = 0.59$, Pearson's r correlation coefficient) and the PNA ($r=0.37$, Pearson's r correlation coefficient). Higher GOA runoff is related to an eastward shift of the Aleutian Low (increase in the along-shore sea level pressure gradient) because it increases the precipitation rates over southeast Alaska [Weingartner *et al.*, 2005] and likely leads to less cooling of deep GOA coastal temperatures due to enhanced stratification [Janout *et al.*, 2010]. This same atmospheric pattern forces enhanced ice growth (and salinization) over the northern Bering Sea shelf [Overland and Pease, 1982], so the model results appear to conform to our notion of regional thermohaline dynamics. EOF S3U is in phase along the GOA shelf and shelfbreak and along the Aleutian Islands and over the outer Bering shelf; the out of phase centers are in Bristol Bay and the western GOA basin. It is negatively correlated with the PDO ($r = -0.65$, Pearson's r correlation coefficient) and positively correlated with the NP index ($r = 0.57$, Pearson's r correlation coefficient). The continuity of the EOF patterns S2U and S3U from the GOA shelf across the Aleutians hints at an advective connection between the two regions, a connection that can be driven by the dependence of Unimak pass transport upon wind-forced sea level fluctuations [Schumacher *et al.*, 1982] and the distance of the Alaskan Stream axis from the passes [Favorite, 1974; Stabeno *et al.*, 2005].

In the deeper layer, EOF S1L (25%) accounts for the largest percentage of salinity variability in any mode and is negatively correlated with the PDO ($r = -0.55$, Pearson's r correlation coefficient). The GOA shelf and Bering basin are in phase with each other for S1L and out of phase with the outer Bering shelf and GOA basin. Hence, salinities tend

to increase (decrease) over the central GOA and outer Bering shelf, and decrease (increase) over the Bering Sea basin. This is consistent with the wind anomalies associated with the PDO [Mantua *et al.*, 1997]. In the positive phase of the PDO, cyclonic wind stress curl strengthens over the central GOA basin (carrying excess precipitation to the south-central coastal GOA) and weakens over the Bering basin. In addition, southerly wind anomalies develop over the eastern Bering shelf and slope, possibly resulting in stronger upwelling along the shelfbreak. Mode S2L is primarily a GOA shelf/basin mode with the GOA shelf signal perhaps extending for a few degrees of latitude along the Bering Sea shelf break. EOF S3L is correlated with the NPGO ($r = -0.57$, Pearson's r correlation coefficient) and is out of phase between the central GOA and the western Bering basin. The pattern implies that when the NPGO is in its positive phase, salinity anomalies increase within the GOA gyre, presumably due to enhanced upwelling in the gyre center. The S3L pattern is similar to the structure of EOFs T2U and T2L, which are also both correlated to the NPGO.

Note that the various EOFs do not necessarily correspond to recognized Large Marine Ecosystem boundaries [Sherman, 1991; Francis and Hare, 1994] or the Bering Sea shelf's biophysical domains [Coachman, 1986]. For example, T2U closely links the eastern Bering Sea with the GOA shelf, S2L depicts an apparent connection between the GOA shelf and the eastern Bering continental slope, and S3L shows that the central GOA basin and the outer Bering shelf fluctuate in concert.

3.6.4 Biological covariates

With these patterns of physical variability in hand we now ask if there are simple statistically significant relationships (Table 3.6) between these modes and indices that measure variability within the Bering Sea ecosystem (Table 3.3). Although pinpointing mechanistic links between EOF and biological covariates is outside the focus of this paper, we briefly describe a few relations.

Significant correlations (at the 95% level) are found with species that span many trophic levels. Spring bloom, chlorophyll, primary productivity and condition indices for pollock, yellowfin sole and pacific cod are short timeseries ($N = 7$ or 8 years) but all are

significantly correlated to one or more principal components. Longer ($N = 23 - 35$ years) fish and shellfish time series that correlate to the principal components include walleye pollock (T1U), pacific herring (T3U), rock sole (T3U, S1U, S2U, S2L), capelin (S1U), yellowfin sole (S3U, S1L), snow crab (T2U, T1L) and a number of multi-species composite indices (T2U, S3U, T2L, T3L, S2L). For those time series with at least 15 effective degrees of freedom, the EOFs account for up to 36% of the observed variability.

Snow crabs are a commercially important epibenthic species whose distribution has fluctuated with temperature changes [Zheng *et al.*, 2001], although repopulation of southern Bering Sea regions following warm periods can be difficult [Orensanz *et al.*, 2004]. Mode T1L (strongest correlation to the PDO) captures 35% of the variance ($N = 25$) within the snow crab spawner-recruitment index. Fluctuation of mode T3U (apparently related to the winter position of the Aleutian Low and the sea ice extent) is positively correlated with the Togiak pacific herring stocks ($r = 0.62$, $N = 27$, Pearson's r correlation coefficient) and negatively correlated with rock sole ($r = -0.52$, $N = 30$, Pearson's r correlation coefficient). The strongly negative pattern of T3U over the Bering Shelf resembles the mean winter's end ice extent and so these correlations may reflect population dynamics tied to the annual preconditioning set by the winter ice extent or the wind and current regime that helps define the ice system. Should a changing climate tend to favor one phase of mode T3U over the other, the relation indicates that either the Togiak herring or the rock sole stock would benefit and the other would suffer.

The above relations show that the NEP5 model output can be a useful tool for targeted retrospective studies of biological responses to environmental change. The NEP5 model is also being integrated forward in time based on International Panel on Climate Change (IPCC) future climate scenarios. Examining stability of the modes and possible trends in their principal components within the forecast simulations together with the hindcast biological correlations may provide researchers the ability to diagnose potential ecosystem impacts of climate change, to the extent that the correlated relationships reflect stationary processes. Identifying mechanistic links between the biophysical covariates should remain a topic of high priority in future Bering Sea research.

3.7 Concluding remarks

Our analyses show that a number of lower and upper tropic level population indices are related to the physical variability predicted by the NEP5 results. The model results allow us to complement the limited set of physical observations and examine spatial and temporal patterns of variability. In aggregate, this approach has provided additional insights on ecosystem variations, or at least suggested future directions for examining this variability.

The application of a 35-year ocean-ice hindcast to the Bering Sea shelf region provides some insights to the variability of the sea ice and thermohaline conditions on the Bering Sea shelf. Model strengths include the ability to reproduce 85% of the annually integrated ice variability and up to 50% of the monthly temperature variability; weaknesses include the low skill in reproducing monthly salinity anomalies and somewhat overly energetic circulation fields. Although the model provides some useful proxy time series in regions that lack observational data, it does not capture all of the *in situ* variability and improving the hindcast skill remains a high priority for the future.

Model improvements that are currently being implemented will provide additional utility and should strengthen several of the comparisons made above. These modifications include: the incorporation of a coastal discharge field that contains both monthly and inter-annual variability [Dai *et al.*, 2009], the relaxation of the northern boundary condition so that the Bering Strait fluxes can more realistically respond to the instantaneous wind field and a spatially varying light attenuation coefficient. Our initial investigations suggest that accounting for water opacity improves the bottom temperature high bias seen in NEP5. Presumably these improvements will lead to a better mechanistic understanding of this shelf ecosystem, its variability, and perhaps its future trajectory. In the meantime, this work provides a baseline set of model evaluations that will help guide future improvements, applications and analyses.

3.8 Acknowledgements

The authors thank the numerous researchers whose data have made the model/data evaluations presented herein possible. In particular, Lisa Eisner and the

BASIS program have kindly provided CTD survey data. Peggy Sullivan tracked down many historical mooring positions. Zygmunt Kowalik graciously provided his compilation of historical amplitude and current tidal harmonic parameters and helped implement and evaluate the tidal forcing. We thank Franz Mueter for the use of his ecosystem indicator time series, helpful discussions, and statistical guidance. We thank Paul Budgett and one anonymous reviewer for thoughtful, constructive reviews that strengthened the manuscript. Mooring M2 data are provided by and supported through the NOAA EcoFOCI program. The Arctic Region Supercomputing Center (ARSC) at UAF, the National Center for Atmospheric Research (NCAR), and the Texas Advanced Computing Center (TACC) provided computational resources. This is publication 3769 from Pacific Marine Environmental Laboratory, North Pacific Research Board publication 312, and BEST-BSIERP Bering Sea Project publication 28. This work was supported by the Department of Interior Bureau of Ocean Energy Management (BOEM), award M07PC13368, and the National Science Foundation, awards ARC-0732771, ARC-0732431 and ARC-0957985.

3.9 References

- Aagaard, K., T. J. Weingartner, S. L. Danielson, R. A. Woodgate, G. C. Johnson, and T. E. Whitledge, 2006. Some controls on flow and salinity in Bering Strait, *Geophys. Res. Lett.* 33, L19602, doi:10.1029/2006GL026612.
- ACIA, 2005. *Arctic Climate Impact Assessment*. Cambridge Univ. Press, Cambridge, United Kingdom.
- Andrews, A. G., R. A. Heintz, and E. V. Farley, 2011. Age-1 Walleye Pollock in the Eastern Bering Sea: Distribution, Abundance, Diet, and Energy Density, paper presented at Alaska Marine Science Symposium, January 2011, Anchorage, AK.
- Benson, A. J., and A. W. Trites, 2002. Ecological effects of regime shifts in the Bering Sea and eastern North Pacific Ocean, *Fish Fisher.*, 3, 95-113.
- BEST-BSIERP Program Summary, 2010, Bering Ecosystem Study and Bering Sea Integrated Ecosystem Research Project Program Summary, North Pacific Research Board, Anchorage, AK.

- Bograd, S. J., R. Mendelssohn, F. B. Schwing, and A. J. Miller, 2005. Spatial heterogeneity of sea surface temperature trends in the Gulf of Alaska, *Atmos. Ocean*, 43, 241–247.
- Boyer, T. P., J. I. Antonov, O. K. Baranova, H. E. Garcia, D. R. Johnson, R. A. Locarnini, A. V. Mishonov, T. D. O'Brien, D. Seidov, I. V. Smolyar, and M. M. Zweng, 2009. World Ocean Database, 2009, edited by S. Levitus, *NOAA Atlas NESDIS 66*, U.S. Gov. Printing Office, Wash., D.C.
- Brasseur, P. P., 1991. A variational inverse method for the reconstruction of general circulation fields in the Northern Bering Sea, *J. Geophys. Res.*, 96 (C3), 4891-4907.
- Brodeur, R. D., H. Sugisaki, and G. L. Hunt Jr., 2002. Increases in jellyfish biomass in the Bering Sea: implications for the ecosystem, *Mar. Ecol. Prog. Ser.*, 233, 89-103.
- Brodeur, R.D., M.B. Decker, L. Ciannelli, J.E. Purcell, N.A. Bond, P.J. Stabeno, E. Acuna, and G.L. Hunt, Jr., 2008. Rise and fall of jellyfish in the eastern Bering Sea in relation to climate regime shifts, *Prog. Oceanogr.*, 77, 103-111.
- Budgell, W.P., 2005. Numerical simulation of ice-ocean variability in the Barents Sea region: Towards dynamical downscaling, *Ocean Dyn.*, 55, 370-387.
- Byrd, G. V., J. C. Williams, Y. B. Artukhin, and P. S. Vyatkin, 1997. Trends in populations of Red-legged Kittiwake *Rissa brevirostris*, a Bering Sea endemic, *Bird Conserv. Internat.*, 7, 167-180, doi:10.1017/S0959270900001489.
- Carton, J. A., and B. S. Giese, 2008. A reanalysis of ocean climate using simple ocean data assimilation (SODA), *Mon. Wea. Rev.*, 136, 2999-3017.
- Cavalieri, D., C. Parkinson, P. Gloersen, and H. J. Zwally, 1996. Updated 2008. Sea Ice Concentrations from Nimbus-7 SMMR and DMSP SSM/I-SSMIS Passive Microwave Data, 1979-2009, National Snow and Ice Data Center, Boulder, CO, digital media.
- Clarke, A. J., and D. S. Battisti, 1981. The effect of continental shelves on tides, *Deep-Sea Res. A*, 28(7), 665–682.
- Clement, J.L., L. W. Cooper, and J. M. Grebmeier, 2004. Late winter water column and sea-ice conditions in the northern Bering Sea, *J. Geophys. Res.*, 109 (C3), C03022.
- Clement, J. L., W. Maslowski, L. W. Cooper, J. M. Grebmeier, and W. Walczowski, 2005. Ocean circulation and exchanges through the northern Bering Sea: 1979-2001, *Deep-Sea Res. II*, 52, 3509-3540, doi:10.1016/j.dsr2.2005.09.010.

- Clement Kinney, J., W. Maslowski, and S. Okkonen, 2009. On the processes controlling shelf-basin exchange and outer shelf dynamics in the Bering Sea, *Deep-Sea Res. II*, 56 (17), 1351-1362, doi:10.1016/j.dsr2.2008.10.023.
- Coachman, L. K., 1982, Flow convergence over a broad, flat continental shelf, *Cont. Shelf Res.*, 1, 1-14.
- Coachman, L. K., 1986. Circulation, water masses, and fluxes on the southeastern Bering Sea shelf, *Cont. Shelf Res.*, 5, 23-108.
- Coachman, L. K., K. Aagaard, and R. B. Tripp, 1975. *Bering Strait: The Regional Physical Oceanography*, Univ. of Wash. Press, Seattle, WA.
- Comiso J. C., D. J. Cavalieri, C. L. Parkinson, and P. Gloersen, 1997. Passive microwave algorithms for sea ice concentration: A comparison of two techniques, *Remote Sens. Env.*, 60(3), 357-384, doi:10.1016/S0034-4257(96)00220-9.
- Coyle, K. O., A. I. Pinchuk, L. B. Eisner, and J. M. Napp, 2008. Zooplankton species composition, abundance and biomass on the eastern Bering Sea shelf during summer: the potential role of water column stability and nutrients in structuring the zooplankton community, *Deep-Sea Res. II*, 55, 1755-1791.
- Curchitser, E. N., D. B. Haidvogel, A. J. Hermann, E. L. Dobbins, T. M. Powell, and A. Kaplan, 2005. Multi-scale modeling of the North Pacific Ocean: Assessment and analysis of simulated basin-scale variability (1996-2003), *J. Geophys. Res.*, 110, C11021, doi:10.1029/2005JC002902.
- Curchitser, E. N, K. Hedstrom, S. L. Danielson, and T. J. Weingartner, 2010. Modeling of Circulation in the North Aleutian Basin, Department of Interior, *OCS Study BOEMRE 2010-028*, Anchorage, AK.
- Curry, J. A., J. E. Schramm, and E. E. Ebert, 1995. On the ice albedo climate feedback mechanism, *J. Climate*, 8, 240-247.
- Dai, A., T. Qian, K. E. Trenberth, and J. D Milliman, 2009. Changes in continental fresh water discharge from 1948-2004, *J. Climate*, 22, 2773-2791.
- Danielson, S., and Z. Kowalik, 2005. Tidal currents in the St. Lawrence Island region, *J. Geophys. Res.*, 110, C10004, doi:10.1029/ 2004JC002463.
- Danielson, S., K. Aagaard, T. Weingartner, S. Martin, P. Winsor, G. Gawarkiewicz, and D. Quadfasel, 2006. The St. Lawrence polynya and the Bering shelf circulation: new observations that test the models, *J. Geophys. Res.*, J111, C09023, doi:10.1029/2005JC003268.

- Danielson, S., L. Eisner, T. Weingartner, and K. Aagaard, 2011. Thermal and haline variability over the central Bering Sea shelf: Seasonal and inter-annual perspectives, *Cont. Shelf Res.*, 31, 539-554, doi:10.1016/j.csr.2010.12.010.
- Defant, A., 1960. *Physical Oceanography*, vol. 2, 598 pp., Elsevier, New York, NY.
- Di Lorenzo E., N. Schneider, K. M. Cobb, K. M. K. Chhak, P. J. S. Franks, A. J. Miller, J. C. McWilliams, S. J. Bograd, H. Arango, E. Curchister, T. M. Powell, and P. Rivere, 2008. North Pacific Gyre Oscillation links ocean climate and ecosystem change, *Geophys. Res. Lett.*, 35, L08607, doi:10.1029/2007GL032838.
- Dobbins, E. L., A. J. Hermann, P. J. Stabeno, N. A. Bond, and R. C. Steed, 2009. Modeled transport of fresh water from a line-source in the coastal Gulf of Alaska, *Deep-Sea Res. II*, 56, 2409-2426, doi:10.1016/j.dsr2.2009.02.004.
- Favorite, F., 1974. Flow into the Bering Sea through Aleutian island passes, in *Oceanography of the Bering Sea*, edited by D.W. Hood and E. J. Kelley, Occ. Public. No. 2, Inst. Mar. Sci., Univ. of Alaska, Fairbanks, Fairbanks, AK.
- Fay, F.H., 1982. *Ecology and biology of the Pacific walrus (Odobenus rosmarus divergens)*, *N. Am. Fauna*, 74, U.S. Fish Wildl. Serv., Wash. D.C.
- Fiechter, J., A. M. Moore, C. A. Edwards, K. W. Bruland, E. Di Lorenzo, C. V. W Lewis, T. M. Powell, E. N. Curchitser, and K. Hedstrom, 2009. Modeling iron limitation of primary production in the coastal Gulf of Alaska, *Deep-Sea Res. II*, 56, 2503-2519, doi:10.1016/j.dsr2.2009.02.010.
- Foreman, M. G. G., W. R. Crawford, J. Y. Chemiawsky, R. F. Henry, and M. R. Tarbotton, 2000. A high-resolution assimilating tidal model for the northeast Pacific Ocean, *J. Geophys. Res.*, 105, 28,629-28,651.
- Foreman, M. G. G., P. F. Cummins, J. Y. Cherniawsky, and P. Stabeno, 2006. Tidal energy in the Bering Sea, *J. Mar. Res.*, 64, 797-818.
- Francis, R. C., and S. R. Hare, 1994. Decadal-scale regime shifts in the large marine ecosystems of the North-east Pacific: a case for historical science, *Fish. Oceanogr.*, 3, 279-291, doi:10.1111/j.1365-2419.1994.tb00105.x.
- GEBCO, 2003. Centenary Edition of the GEBCO Digital Atlas, published on CD-ROM on behalf of the Intergovernmental Oceanographic Commission and the International Hydrographic Organization as part of the General Bathymetric Chart of the Oceans, British Oceanographic Data Centre, Liverpool, U.K., Digital data.

- Gibson, M. A., and S. B. Schullinger, 1998. Answer from the ice edge. The consequences of climate change on life in the Bering and Chukchi seas, Report prepared for Arctic Network and Greenpeace, USA, Wash. DC.
- Gill, A. E., 1982. *Atmosphere–Ocean Dynamics*, Academic Press, San Diego, CA.
- Greisman, P., 1985, Western Gulf of Alaska tides and circulation, Report prepared for NOAA/DOA, Anchorage, AK.
- Haidvogel, D. B., and A. Beckmann, 1999. *Numerical Ocean Circulation Modeling. Series on Environmental Science and Management*, Vol. 2, Imperial College Press.
- Haney, R. L., 1991. On the pressure gradient force over steep topography in sigma coordinate ocean models, *J. Phys. Oceanogr.* 21, 610-619.
- Harrison, N. M., G. L. Hunt Jr., and R. T. Cooney, 1990. Front affecting the distribution of seabirds in the northern Bering Sea, *Polar Res.*, 8, 29-31.
- Heintz, R. A. and J. J. Vollenweider, 2010. Influence of size on the sources of energy consumed by overwintering walleye pollock (*Theragra chalcogramma*), *J. Exp. Mar. Biol. Ecol.* 393, 43-50.
- Hermann, A. J., P. J. Stabeno, D. B. Haidvogel, and D. L. Musgrave, 2002. A regional tidal/subtidal circulation model of the southeastern Bering Sea: development, sensitivity analyses and hindcasting, *Deep-Sea Res. II*, 49, 5945-5967.
- Hermann, A. J., E. N. Curchitser, D. B. Haidvogel, and E. L. Dobbins, 2009a. A comparison of remote versus local influence of El Nino on the coastal circulation of the Northeast Pacific, *Deep-Sea Res. II*, 56, 2427-2443, doi:10.1016/j.dsr2.2009.02.005.
- Hermann, A. J., S. Hinckley, E. L. Dobbins, D. B. Haidvogel, N. A. Bond, C. Mordy, N. Kachel, and P. J. Stabeno, 2009b. Quantifying cross-shelf and vertical nutrient flux in the Gulf of Alaska with a spatially nested, coupled biophysical model, *Deep-Sea Res. II*, 56, 2472-2486, doi:10.1016/j.dsr2.2009.02.008.
- Hinckley, S., K. O. Coyle, G. Gibson, A. J. Hermann, and E. L. Dobbins, 2009. A biophysical NPZ model with iron for the Gulf of Alaska: Reproducing the differences between an oceanic HNLC ecosystem and a classical northern temperate shelf ecosystem, *Deep-Sea Res. II*, 56, 2520-2536, doi:10.1016/j.dsr2.2009.03.003.
- Hu, H., and J. Wang, 2010. Modeling effects of tidal and wave mixing on circulation and thermohaline structures in the Bering Sea: Process studies, *J. Geophys. Res.*, 115 C01006, doi:10.1029/2008JC005175.

- Hunke, E. C., 2001. Viscous-plastic sea ice dynamics with the EVP model: linearization issues, *J. Comp. Phys.*, 170, 18-38.
- Hunke, E. C., and J. K. Dukowicz, 1997. An elastic-viscous-plastic model for sea ice dynamics, *J. Phys. Oceanogr.*, 27, 1849-1868.
- Hunt, G.L. Jr., P.J. Stabeno, G. Walters, E. Sinclair, R.D. Brodeur, J.M. Napp, and N.A. Bond, 2002. Climate change and control of the southeastern Bering Sea pelagic ecosystem, *Deep-Sea Res. II*, 49, 5821-5853.
- Isaji T., and M. L. Spaulding, 1987. A numerical model of the M2 and K1 tide in the northwestern Gulf of Alaska, *J. Phys. Oceanogr.*, 17, 698-704.
- Janout, M. A., T. J. Weingartner, T. C. Royer, and S. L. Danielson, 2010. On the nature of winter cooling and the recent temperature shift on the northern Gulf of Alaska shelf, *J. Geophys. Res.*, 115, C05023, doi:10.1029/2009JC005774.
- Johnson, W., and Z. Kowalik, 1986. Modeling of storm surges in the Bering Sea and Norton Sound, *J. Geophys. Res.*, 91(C4), 5119-5128.
- Kachel, N. B., G. L. Hunt Jr., S. A. Salo, J. D. Schumacher, P. J. Stabeno, and T. E. Whitledge, 2002. Characteristics and variability of the inner front of the southeastern Bering Sea, *Deep-Sea Res. II*, 49, 5889-5909.
- Kantha, L. H., and G. L. Mellor, 1989. A two-dimensional couple ice-ocean model of the Bering Sea marginal ice zone, *J. Geophys. Res.*, 94, 10,921-10,935.
- Kokubun N., A. Takahashi, M. Ito, K. Matsumoto, A.S. Kitaysky, and Y. Watanuki, 2010. Annual variation in the foraging behaviour of thick-billed murres in relation to upper-ocean thermal structure around St. George Island, Bering Sea, *Aquat. Biol.*, 8, 289-298.
- Kowalik, Z., 1999. Bering Sea Tides, in *Dynamics of The Bering Sea: A Summary of Physical, Chemical and Biological Characteristics, and a Synopsis of Research on the Bering Sea*, edited by T. R. Loughlin and K. Ohtani, pp. 93-127, Univ. of Alaska Sea Grant, Fairbanks, AK.
- Kowalik, Z., and P. Stabeno, 1999. Trapped motion around the Pribilof Islands in the Bering Sea, *J. Geophys. Res.*, 104, 25,667-25,684, doi:10.1029/1999JC900209.
- Lanksbury, J. A., J. T. Duffy-Anderson, K. L. Mier, M. S. Busby, and P. J. Stabeno, 2007. Distribution and transport patterns of northern rock sole, *Lepidopsetta polyxystra*, larvae in the southeastern Bering Sea, *Prog. Oceanogr.*, 72, 39-62, doi: 10.1016/j.pocean.2006.09.001.

- Large, W. G., J. C. McWilliams, and S. C. Doney, 1994. Oceanic vertical mixing: a review and a model with a nonlocal boundary layer parameterization, *Rev. Geophys.*, 32, 363-403.
- Large, W. G., and S. G. Yeager, 2008. The global climatology of an interannually varying air-sea flux data set, *Clim. Dyn.*, 33, 341-364.
- Lovvorn, J. R., S. E. Richman, J. M. Grebmeier, and L. W. Cooper, 2003. Diet and body condition of spectacled eiders wintering in pack ice of the Bering Sea, *Polar Biol.*, 26, 259-267, doi: 10.1007/s00300-003-0477-0.
- Mantua, N., S. Hare, Y. Zhang, J. Wallace, and R. Francis, 1997. A Pacific interdecadal climate oscillation with impacts on salmon production, *Bull. Am. Meteorol. Soc.*, 78, 1069-1079.
- Marchesiello, P., J. C. McWilliams, and A. Shchepetkin, 2001. Open boundary conditions for long-term integration of regional oceanic models, *Ocean Modelling*, 3, 1-20.
- Mellor, G. L., and L. Kantha, 1989. An ice-ocean coupled model, *J. Geophys. Res.*, 94, 10,937-10,954.
- Minobe, S., 1999. Resonance in bidecadal and pentadecadal climate oscillations over the north Pacific: Role in climate regime shifts, *Geophys. Res. Lett.*, 26, 855-858.
- Mizobata, K., J. Wang, and S. Saitoh, 2006. Eddy-induced cross-slope exchange maintaining summer high productivity of the Bering Sea shelf break, *J. Geophys. Res.*, 111, C10017, doi:10.1029/2005JC003335.
- Mofjeld, H. O., 1984. Recent observations of tides and tidal currents from the northeastern Bering Sea shelf, *NOAA Tech. Memo, ERL PMEL-57*, Seattle, WA.
- Mofjeld, H. O., 1986. Observed tides on the northeastern Bering Sea shelf, *J. Geophys. Res.*, 91(C2), 2593-2606.
- Mofjeld, H. O., J. D. Schumacher, and D. J. Pashinski, 1984. Theoretical and observed profiles of tidal currents at two sites on the southeastern Bering Sea shelf, *NOAA Tech. Memo, ERL, PMEL-62*, Seattle, WA.
- Mooers, C. N. K., 1973. A technique for the cross spectrum analysis of pairs of complex-valued time series, with emphasis on properties of polarized components and rotational invariants, *Deep-Sea Res.*, 20, 1129-1141.

- Muench, R. D., and J. D. Schumacher, 1980. Physical oceanographic and meteorological conditions in the northwest Gulf of Alaska, *NOAA Tech. Memo, ERL PMEL-22*, Seattle, WA.
- Muench, R. D., J. D. Schumacher, and S. A. Salo, 1988. Winter currents and hydrographic conditions on the northern central Bering Sea shelf, *J. Geophys. Res.*, 93(C1), 516-526, doi:10.1029/JC093iC01p00516.
- Mueter, F. J., and M. A. Litzow, 2008. Sea ice retreat alters the biogeography of the Bering Sea continental shelf, *Ecol. Appl.*, 18, 309-320.
- Napp, J. M., C. T. Baier, K. O. Coyle, R. D. Brodeur, N. Shiga, and K. Mier, 2002. Interannual and decadal variability in zooplankton communities of the southeastern Bering Sea, *Deep-Sea Res. II*, 49(26), 5991-6008, doi: 10.1016/S0967-0645(02)00330-2.
- Niebauer, H.J., 1998. Variability in the Bering Sea ice cover as affected by a regime shift in the North Pacific in the period 1947-1996, *J. Geophys. Res.*, 103, 27,717-27,737.
- Nihoul, J. C. J., P. Adam, P. Brasseur, E. Deleersnijder, S. Djenidi, and J. Haus, 1993. Three-dimensional general circulation model of the northern Bering Sea's summer ecohydrodynamics, *Cont. Shelf Res.*, 13, 509-542, doi:10.1016/0278-4343(93)90093-D.
- North, G. R., T. L. Bell, R. F. Cahalan, and F. J. Moeng, 1982. Sampling errors in the estimation of empirical orthogonal functions, *Mon. Wea. Rev.*, 110, 699-706.
- NPFMC, 2005. Fishery management plan for groundfish of the Bering Sea and Aleutian Islands Management Area, North Pacific Fishery Management Council, Anchorage, AK.
- Oey, L.-Y., T. Ezer, C. Hu, and F. Muller-Karger, 2007. Baroclinic tidal flows and inundation processes in Cook Inlet, Alaska: Numerical modeling and satellite observations, *Ocean Dyn.*, 57, 205-221.
- Orensanz, J., B. Ernst, D. Armstrong, P. Stabeno, and P. Livingston, 2004. Contraction of the geographic range of distribution of snow crab (*Chionoecetes opilio*) in the eastern Bering Sea: an environmental ratchet?, *CalCOFI Reports*, 45, 65-79.
- Orr, V., 2011. As ice melts, new opportunities, challenges arise for Alaska's northern communities, *Alaska Bus. Mon.*, March 2011, Anchorage, AK.
- Overland, J.E., and C. H. Pease, 1982. Cyclone climatology of the Bering Sea and its relation to sea ice extent, *Mon. Wea. Rev.* 110, 5-13.

- Overland, J.E., and A. T. Roach, 1987. Northward flow in the Bering and Chukchi seas, *J. Geophys. Res.*, 92, 7097-7105.
- Overland, J. E., M. C. Spillane, H. Y. Hurlburt, and A. J. Wallcraft, 1994. A numerical study of the circulation of the Bering Sea basin and exchange with the north Pacific Ocean, *J. Phys. Oceanogr.*, 24, 736-758, doi:10.1175/1520-0485.
- Overland, J. E., J. M. Adams, and N. A. Bond, 1999. Decadal variability of the Aleutian low and its relation to high latitude circulation, *J. Climate*, 12, 1542-1548.
- Pawlowicz, R., B. Beardsley, and S. Lentz, 2002. Classical tidal harmonic analysis including error estimates in MATLAB using T_TIDE, *Comput. Geosci.*, 28, 929-937.
- Pearson, C. A., H. O. Mofjeld, and R. B. Tripp, 1981. Tides of the Eastern Bering Sea shelf, in *The Eastern Bering Sea Shelf, Oceanography and Resources*, vol. 1., edited by D. W. Hood and J. A. Calder, pp. 111-130, Univ. of Wash. Press, Seattle, WA.
- Pease, C. H., 1980. Eastern Bering Sea ice processes, *Mon. Wea. Rev.*, 108, 2015-2023.
- Pease, C., and J. E. Overland, 1989: An atmospherically driven sea ice drift model for the Bering Sea, *Ann. Glaciol.*, 5, 111-114.
- Petersen, M. R., W. W. Larned, and D. C. Douglas, 1999. At-sea distribution of spectacled eiders: A 120-year-old mystery resolved, *The Auk*, 116 (4), 1009-1020.
- Prandle, D., 1982. The vertical structure of tidal current, *Geophys. Astrophys. Fluid Dyn.*, 22, 22-49.
- Pritchard, R. S., A. C. Mueller, D. J. Hanzlick, and Y. S. Yang, 1990. Forecasting Bering Sea ice edge behavior, *J. Geophys. Res.*, 95(C1), 775-788, doi:10.1029/JC095iC01p00775.
- Pyper, B. J., and R. M. Peterman, 1998. Comparison of methods to account for autocorrelation in correlation analysis of fish data, *Can. J. Fish. Aquatic Sci.*, 55, 2127-2140.
- Roach, A. T., K. Aagaard, C. H. Pease, S. A. Salo, T. Weingartner, V. Pavlov, and M. Kulakov, 1995. Direct measurements of transport and water properties through Bering Strait, *J. Geophys. Res.*, 100, 18,443-18,457.
- Rodionov, S. N., N. A. Bond, and J. E. Overland, 2007. The Aleutian Low, storm tracks, and winter climate variability in the Bering Sea, *Deep-Sea Res. II*, 54(23-26), 2560-2577.

- Røed, L. P., and J. Debernard, 2004. Description of an integrated flux and sea-ice model suitable for coupling to an ocean an atmosphere model, *Norwegian Met. Inst. Rep. 4*, Oslo, Norway.
- Royer, T. C., 1982. Coastal fresh water discharge in the northeast Pacific. *J. Geophys. Res.*, 87, 2017-2021.
- Schumacher, J. D., and T. H. Kinder, 1983. Low-frequency current regimes over the Bering Sea shelf, *J. Phys. Oceanogr.*, 13, 607-623.
- Schumacher, J. D., and R. K. Reed, 1992. Characteristics of currents over the continental slope of the eastern Bering Sea, *J. Geophys. Res.*, 97 (C6), 9423-9433.
- Schumacher, J. D., and P.J. Stabeno, 1998. Continental shelf of the Bering Sea coastal segment, in *The Sea, the Global Coastal Ocean*, vol. 11, edited by A. R. Robinson and K. H. Brink, pp. 789-822, Wiley, New York, NY.
- Schumacher, J., K. Aagaard, C. Pease, and R. Tripp, 1983. Effects of a shelf polynya on flow and water properties in the northern Bering Sea, *J. Geophys. Res.*, 88 (C5), 2723-2732.
- Schumacher, J. D., C. A. Pearson, and J. E. Overland, 1982. On exchange of water between the Gulf of Alaska and the Bering Sea through Unimak Pass, *J. Geophys. Res.*, 87, 5785-5795.
- Schumacher, J. D., N. A. Bond, R. D. Brodeur, P. A. Livingston, J. M. Napp, and P. J. Stabeno, 2003. Climate change in the southeastern Bering Sea and some consequences for biota, in *Large Marine Ecosystems of the World*, edited by G. Hempel and K. Sherman, pp. 17-40, Elsevier, Amsterdam, Netherlands.
- Sherman, K., 1991. The Large Marine Ecosystem concept: research and management strategy for living marine resources, *Ecolog. Applic.*, 1(4), 350-360.
- Spaulding, M., T. Isaji, D. Mendelsohn, and A. C. Turner, 1987. Numerical simulation of wind-driven flow through the Bering Strait, *J. Phys. Oceanogr.*, 17, 1799-1816.
- Stabeno, P. J., and R. K. Reed, 1994. Circulation in the Bering Sea basin by satellite tracked drifters, *J. Phys. Oceanogr.*, 24, 848-854.
- Stabeno, P. J., and P. Van Meurs, 1999. Evidence of episodic on-shelf flow in the southeastern Bering Sea, *J. Geophys. Res.*, 104(C12), 29,715-29,720.

- Stabeno, P. J., J. D. Schumacher, and K. Ohtani, 1999. The physical oceanography of the Bering Sea, in *Dynamics of The Bering Sea: A Summary of Physical, Chemical and Biological Characteristics, and a Synopsis of Research on the Bering Sea*, edited by T. R. Loughlin and K. Ohtani, pp. 1-28, Univ. of Alaska Sea Grant, Fairbanks, AK.
- Stabeno, P. J., R. K. Reed, and J. M. Napp, 2002a. Transport through Unimak Pass, Alaska, *Deep-Sea Res. II*, 49, 5919-5930.
- Stabeno, P. J., N. B. Kachel, M. Sullivan, and T. E. Whitledge, 2002b. Variability of physical and chemical characteristics along the 70-m isobath of the southeast Bering Sea, *Deep-Sea Res. II*, 49, 5931-5943.
- Stabeno, P. J., D. G. Kachel, N. B. Kachel, and M. E. Sullivan, 2005. Observations from moorings in the Aleutian Passes: temperature, salinity and transport, *Fish. Oceanogr.* 14, 39-54.
- Stabeno, P. J., J. Napp, C. Mordy, and T. Whitledge, 2010. Factors influencing physical structure and lower trophic levels of the eastern Bering Sea shelf in 2005: Sea ice, tides and winds, *Prog. Oceanogr.*, 85(3-4), 180-196, doi:10.1016/j.pocean.2010.02.010.
- Steele, M., G. L. Mellor, and M. G. McPhee, 1989. Role of the molecular sublayer in the melting or freezing of sea ice, *J. Phys. Oceanogr.*, 19, 139-147.
- Steele, M., R. Morley, and W. Ermold, 2001. PHC: A global ocean hydrography with a high-quality Arctic Ocean, *J. Climate*, 14, 2079-2087, doi:10.1175/1520-0442(2001)014<2079:PAGOHW>2.0.CO;2.
- Stephens, C., S. Levitus, J. Antonov, and T. P. Boyer, 2001. On the Pacific Ocean regime shift, *Geophys. Res. Lett.*, 28, 3721-3724.
- Stockwell, D. A., T. E. Whitledge, S. I. Zeeman, K. O. Coyle, J. M. Napp, R. D. Brodeur, A. I. Pinchuk, and G. L. Hunt, 2001. Anomalous conditions in the south-eastern Bering Sea, 1997: nutrients, phytoplankton and zooplankton, *Fish. Oceanogr.*, 10, 99-116. doi: 10.1046/j.1365-2419.2001.00158.x.
- Sugimoto, T., and K. Tadokoro, 1997. Interannual–interdecadal variations in zooplankton biomass, chlorophyll concentration and physical environment in the subarctic Pacific and Bering Sea, *Fish. Oceanogr.*, 6, 74-93, doi: 10.1046/j.1365 2419.1997.00031.x.
- Takenouti, A.Y., and K. Ohtani, 1974. Currents and water masses in the Bering Sea: a review of Japanese work, , in *Oceanography of the Bering Sea*, edited by D.W. Hood and E. J. Kelley, pp. 39-58, Occ. Public. No. 2, Inst. Mar. Sci., Univ. of Alaska, Fairbanks, Fairbanks, AK.

- Taylor, K. E., 2001. Summarizing multiple aspects of model performance in a single diagram, *J. Geophys. Res.*, 106, 7183-7192, doi:10.1029/2000JD900719.
- Trenberth, K. E., and J. W. Hurrell, 1994. Decadal atmosphere-ocean variations in the Pacific, *Climate Dyn.*, 9, 303-319.
- Trites, A. W., P. A. Livingston, M. C. Vasconcellos, S. Mackinson, A. M. Springer, and D. Pauly, 1999. Ecosystem change and the decline of marine mammals in the Eastern Bering Sea: testing the ecosystem shift and commercial whaling hypotheses. *Fish. Centre Res. Rep.*, 7(1), 106 pp.
- Wang, J., H. Hu, K. Mizobata, and S. Saitoh, 2009. Seasonal variations of sea ice and ocean circulation in the Bering Sea: A model-data fusion study, *J. Geophys. Res.*, 114, C02011, doi:10.1029/2008JC004727.
- Weingartner, T. J., S. L. Danielson, and T. C. Royer, 2005. Fresh water variability and predictability in the Alaska Coastal Current, *Deep-Sea Res. II*, 52, 169-191.
- Wepestad, V.G., L. W. Fritz, W. J. Ingraham, and B. A. Megrey, 2000. On relationships between cannibalism, climate variability, physical transport and recruitment success of Bering Sea walleye pollock (*Theragra chalcogramma*), *J. Mar. Sci.*, 57, 272-278.
- Wessel, P., and W. H. F. Smith, 1991. Free software helps map and display data, *EOS Trans. AGU*, 72, 441.
- Willmott, C. J., S. G. Ackleson, R. E. Davis, J. J. Feddema, K. M. Klink, D. R. Legates, J. O'Donnell, and C. M. Rowe, 1985. Statistics for the evaluation and comparison of models, *J. Geophys. Res.*, 90(C5), 8995-9005, doi:10.1029/JC090iC05p08995.
- Woodgate, R. A., K. Aagaard, and T. J. Weingartner, 2005. Monthly temperature, salinity, and transport variability of the Bering Strait through flow, *Geophys. Res. Lett.*, 32, L04601.
- Zhang, J., R. Woodgate, and R. Moritz, 2010. Sea ice response to atmospheric and oceanic forcing in the Bering Sea, *J. Phys. Oceanogr.*, 40, 1729-1747, doi:0.1175/2010JPO4323.1.
- Zhang, J., and W. D. Hibler III., 1991. On the role of ocean circulation in seasonal and interannual ice-edge variations in the Bering Sea, *Ann. Glaciol.*, 15, 37-44.
- Zheng, J., G. H. Kruse, and D. R. Ackley, 2001. Spatial distribution and recruitment patterns of snow crabs in the eastern Bering Sea, in *Spatial processes and management of marine populations*, edited by G. H. Kruse et al., pp. 233-255, Alaska Sea Grant College Program, AK-SG-01-02, Univ. of Alaska, Fairbanks, Fairbanks, AK.

3.10 Tables

Table 3.1: Sources of historical tidal parameters, moored time series data, and net speed and direction statistics used in model evaluations. Locations of these data are shown in Figure 3.3A, Figure 3.3B and Figure 3.3C.

Source	Parameters or Dataset
<i>Muench and Schumacher, 1980</i>	Tidal harmonics
<i>Pearson et al., 1981</i>	Tidal harmonics
<i>Schumacher et al., 1982</i>	Net speed/direction
<i>Schumacher and Kinder, 1983</i>	Net speed/direction
<i>Schumacher et al., 1983</i>	Net speed/direction
<i>Moffeld, 1984</i>	Tidal harmonics
<i>Moffeld et al., 1984</i>	Tidal harmonics
<i>Moffeld, 1986</i>	Tidal harmonics
<i>Greisman, 1985</i>	Tidal harmonics
<i>Isaji and Spaulding, 1987</i>	Tidal harmonics
<i>Muench et al., 1988</i>	Net speed/direction
<i>Schumacher and Reed, 1992</i>	Tidal harmonics and net speed/direction
<i>Roach et al., 1995</i>	Net speed/direction
<i>Kowalik and Stabeno, 1999</i>	Tidal harmonics
<i>Stabeno et al., 2002a</i>	Net speed/direction
<i>Danielson and Kowalik, 2005</i>	Tidal harmonics
<i>Stabeno et al., 2005</i>	Net speed/direction
<i>Danielson et al., 2006</i>	Net speed/direction
<i>Z. Kowalik (unpubl. Data, 2008)</i>	Tidal harmonics
www.tidesandcurrents.noaa.gov	Tidal harmonics
http://www.nbdc.noaa.gov/	Sea surface elevation time series
NOAA/PMEL EcoFOCI program http://www.ecofoci.noaa.gov/efoci_data.shtml	Moored temperature, salinity and current records at site M2
UAF Institute of Marine Science database www.ims.uaf.edu	Moored current records at site F8

Table 3.2: Number of CTD and bottle stations for each region shown in Figure 3.3D.
 The region numbers correspond to those shown in Figure 3.3D and Figure 3.9. Symbols Θ = latitude, Φ = longitude.

Region	Region Number	Number of observations at 10 m depth	Number of observations at 70 m depth
$\Theta < 60^\circ\text{N}$, depth < 50 m, $\Phi > 176^\circ\text{E}$	1	1742	-
$\Theta > 60^\circ\text{N}$, depth < 50 m, $\Phi > 176^\circ\text{E}$	2	3084	-
$\Theta < 60^\circ\text{N}$, 50 m < depth < 100 m, $\Phi > 176^\circ\text{E}$	3	4012	3480
$\Theta > 60^\circ\text{N}$, 50 m < depth < 100 m, $\Phi > 176^\circ\text{E}$	4	777	497
$\Theta < 60^\circ\text{N}$, 100 m < depth < 200 m, $\Phi > 176^\circ\text{E}$	5	1668	1699
$\Theta > 60^\circ\text{N}$, 100 m < depth < 200 m, $\Phi > 176^\circ\text{E}$	6	253	263

Table 3.3: Time series employed for correlation analyses and their sources.

Index	Acronym	Parameter(s)	Source
Pacific Decadal Oscillation	PDO	First mode of North Pacific sea surface temperature variability	http://jisao.washington.edu/pdo
North Pacific Gyre Oscillation	NPGO	Second mode of North Pacific sea surface elevation variability	http://www.o3d.org/npgo/data/NPGO.txt
Arctic Oscillation	AO	First mode of northern hemisphere 1000 mb pressure variations	http://www.cpc.ncep.noaa.gov/products/precip/CWlink/daily_ao_index/monthly.ao.index.b50.current.ascii
Pacific-North American	PNA	Second mode of northern hemisphere 500 mb height variations	http://www.cpc.ncep.noaa.gov/products/precip/CWlink/pna/norm.pna.monthly.b5001.current.ascii
North Pacific Index	NP	Sea level pressure integrated over 30 °N – 65 °N and 160 °E – 140 °W	http://www.cgd.ucar.edu/cas/jhurrell/indices.data.html
Integrated Ice Area	IIA	Eastern Bering Sea concentration-weighted integrated ice area	Compiled by Danielson et al. (2011), data from: http://nsidc.org/data/seaice/pm.html
Wind direction anomaly	WDA	October-May wind direction at 60 °N, 170 °W	Compiled by Danielson et al. (2011), data from: http://www.esrl.noaa.gov/psd/data/gridded/data.ncep.reanalysis.html
GAK1 CTD	GAK1T GAK1S	Observed temperature and salinity anomalies over 0-20 m and 200-250 m depth strata	http://www.ims.uaf.edu/gak1/
Fresh water discharge	FWD	GOA coastal runoff	http://www.ims.uaf.edu/gak1/
Bering Sea ecosystem indicator time series		Phytoplankton, fish, shellfish and seabird indices including measures of biomass, recruitment, survival, condition, location, productivity, abundance, and phenology	Compiled by F. Mueter; http://bsierp.nprb.org/

Table 3.4: Statistics of current meter vectors compared to co-located (in space and time) model-derived vectors. From left to right, columns denote: latitude band of observations, N = number of current meter records within the latitude band and, in parentheses, the number of records with 95% confidence limits on the mean speed; L = mean record length in months; $O_{\text{rmse}}:O$ = magnitude of error represented as a fraction of the observed mean speed, $|O-M|:O$ = magnitude of observed-model speed difference represented as a fraction of the observed mean speed, $|O|$ = mean observed speed, $|O-M|$ = magnitude of observed-model speed difference, $\Delta\theta$ = magnitude of mean vector direction difference. Values in columns 4 and 5 reflect quantities that are only available for the subset of stations with error estimates.

Region	N	L (months)	$O_{\text{rmse}}:O$ (%)		$ O-M :O$ (%)		$ O $ (cm s^{-1})	$ O-M $ (cm s^{-1})		$\Delta\theta$ ($^{\circ}$)	
			mean	median	mean	median	mean	mean	median	mean	median
64.5 < Latitude	18 (1)	5.7	14	14	29	30	24.6	7.4	5.7	10	10
61 < Latitude < 64.5N	47 (14)	5.0	55	39	54	52	5.2	2.8	1.7	55	30
55 < Latitude < 61N	10 (10)	7.4	50	45	76	30	2.5	1.1	0.9	77	46
Latitude < 55 N	29 (4)	18.8	80	76	79	81	16.1	10.8	8.7	75	79

Table 3.5: Results of cross-correlations between the principal components and various environmental time series. Relations that are significant at the 95% level are boldfaced. Column headings with three-character alphanumeric abbreviations distinguish temperature (T) and salinity (S) principal components 1-3 over upper (U, 0-20 m) and lower (L, 40-100 m) depth layers.

Index	T1U	T2U	T3U	S1U	S2U	S3U	T1L	T2L	T3L	S1L	S2L	S3L
PDO	0.59	0.21	0.10	0.22	0.30	-0.65	0.69	0.17	0.27	-0.55	0.27	0.40
NPGO	-0.36	0.47	-0.09	-0.18	0.51	0.39	-0.04	-0.63	-0.16	0.22	0.40	-0.57
AO	-0.31	-0.10	0.02	0.10	-0.13	0.27	-0.47	-0.19	0.04	0.07	-0.19	-0.28
PNA	0.15	0.54	0.05	0.02	0.37	-0.31	0.47	-0.14	0.21	-0.30	0.22	0.22
NP	-0.36	-0.25	-0.06	0.02	-0.24	0.57	-0.49	-0.05	-0.24	0.31	-0.23	-0.34
IHA	-0.67	-0.16	0.59	-0.79	-0.23	0.20	-0.56	-0.06	0.10	0.23	-0.20	-0.29
WDA	0.44	0.08	-0.38	0.52	0.13	0.06	0.44	0.11	-0.22	-0.03	0.20	0.09
GAK1 0-20 m T	0.25	0.23	-0.26	0.27	0.12	-0.33	0.36	0.01	0.16	-0.43	0.04	0.16
GAK1 0-20 m S	-0.22	-0.03	0.13	-0.16	0.12	0.27	-0.16	0.02	-0.04	0.23	0.02	-0.17
GAK1 200-250 m T	0.40	0.62	-0.07	0.24	0.70	-0.33	0.63	-0.36	0.28	-0.46	0.52	0.04
GAK1 200-250 m S	0.08	-0.12	-0.06	0.20	-0.03	0.23	-0.12	-0.29	-0.01	0.10	-0.19	-0.29
FWD	-0.07	0.56	0.22	-0.12	0.59	-0.12	0.24	-0.43	0.15	-0.07	0.43	-0.14

Table 3.6: Temporal correlations between ecosystem indicator time series and the principal components (PC). All relations are significant at the 95% level. Columns include: r = correlation coefficient, r_c = critical value, N = number of years; EDOF = effective degrees of freedom. Three-character alphanumeric principal component abbreviations distinguish temperature (T) and salinity (S) EOF modes 1-3 over upper (U, 0-20 m) and lower (L, 40-100 m) depth layers.

PC	Index	r	r_c	N	EDOF
T1U	Average annual condition index (summer) for walleye pollock	0.87	0.75	7	5
	Average annual condition index (summer) for Pacific cod	0.86	0.82	8	4
T2U	Total net primary production (May-November) over southeastern Bering Sea shelf	-0.85	0.75	7	5
	Residuals from a spawner-recruitment relationship for snow crab	0.44	0.42	25	20
	Temperature adjusted depth distribution of 39 species in bottom trawl survey	-0.47	0.46	23	17
T3U	Total mature biomass of Togiak stock of Pacific herring based on stock assessment	0.62	0.58	27	10
	Female spawning stock biomass of rock sole based on stock assessment results	-0.52	0.48	30	15
S1U	Index of capelin abundance from summer bottom trawl survey	-0.60	0.44	23	18
	Female spawning stock biomass of rock sole based on stock assessment	0.46	0.44	30	18
	Estimated abundance index for common murre s at St. Paul Island	-0.41	0.38	29	25
	Productivity index for red-legged kittiwakes at St. Paul Island	-0.43	0.40	25	23
	Productivity index for red-legged kittiwakes at St. George Island	-0.39	0.37	29	27
S2U	Phenology of red-legged kittiwakes at St. Paul Island	0.41	0.40	24	22
	Estimated onset of spring bloom over inner shelf	-0.87	0.75	7	5
	Recruitment of age-4 rock sole by year class	0.54	0.48	33	15
	Counts of common murre s at index sites on St. George Island	-0.63	0.58	12	10
	Phenology of red-legged kittiwakes at St. Paul Island	-0.48	0.41	24	21
S3U	Phenology of common murre s at St. George Island	-0.42	0.40	27	23
	Estimated onset of spring bloom near mooring M2	0.78	0.77	7	5
	Female spawning stock biomass of yellowfin sole based on stock assessment results	-0.35	0.35	35	30
	Average annual condition index (summer) for yellowfin sole	-0.83	0.77	8	5
T1L	Temperature adjusted depth distribution of 39 species in bottom trawl survey	-0.45	0.44	23	18
	Estimated spring stratification date on middle shelf near mooring M2	-0.39	0.37	35	27
	Estimated onset of spring bloom over inner shelf	-0.81	0.75	7	5
	Recruitment of juvenile snow crab by approximate year class (25-50 mm, ~ age 5)	0.56	0.47	29	16
	Residuals from a spawner-recruitment relationship for snow crab	0.59	0.53	25	12
	Average annual condition index (summer) for Pacific cod	0.72	0.71	8	6
	Walleye pollock size-at-age anomalies during summer for the first age adequately sampled	0.82	0.79	7	4
T2L	Phenology of black-legged kittiwakes at St. George Island	0.40	0.37	28	26
	Phenology of common murre s at St. George Island	-0.48	0.44	27	19
	Combined groundfish stock standardized index of recruitment across 11 stocks	-0.55	0.41	35	21
T3L	Temperature adjusted depth distribution of 39 species from bottom trawl survey	0.49	0.46	23	17
	Counts of common murre s at index sites on St. George Island	0.62	0.59	12	9
	Average downward shift in depth distribution of 39 species in bottom trawl survey	0.46	0.41	23	21
S1L	Productivity index for black-legged kittiwakes at St. Paul Island	-0.51	0.42	25	20
	Productivity index for common murre s at St. Paul Island	-0.61	0.59	18	9
	Total yellowfin sole biomass based on 2007 stock assessment (age 2+)	-0.64	0.62	35	9
	Female spawning stock biomass of yellowfin sole based on stock assessment results	-0.65	0.62	35	8
	Productivity index for black-legged kittiwakes at St. Paul Island	0.55	0.43	25	19
	Productivity index for common murre s at St. George Island	0.53	0.46	20	17
S1L	First principal component of seabird productivity time series	0.48	0.43	25	19
	CS St. Paul Island thick billed murre	-0.65	0.49	20	15
	Phenology of common murre s at St. Paul Island	0.57	0.49	28	15

Table 3.6, Continued

PC	Index	r	r _c	N	EDOF
	Estimated onset of spring bloom over inner shelf	-0.95	0.91	7	3
	Recruitment of age 1 walleye pollock by year class	-0.38	0.36	35	28
	Recruitment of age-4 rock sole by year class	0.45	0.39	33	24
	Gadid recruitment anomaly : average of normalized pollock & cod recruitment series	-0.43	0.40	27	23
	First principal component of fish recruitment series	-0.45	0.43	26	19
S2L	Residuals from a spawner-recruitment relationship for walleye pollock	-0.47	0.40	35	23
	Average annual condition index (summer) for yellowfin sole	0.87	0.79	8	4
	Average downward shift in depth distribution of 39 species in bottom trawl survey	-0.47	0.41	23	21
	Phenology of red-legged kittiwakes at St.Paul Island	-0.46	0.41	24	21
	Phenology of thick-billed murre s at St.Paul Island	-0.60	0.46	28	17
	Phenology of black-legged kittiwakes at St.George Island	0.50	0.40	28	23
S3L	Estimated onset of spring bloom over southeast Bering shelf based on SeaWifs	-0.95	0.92	7	2

3.11 Figures

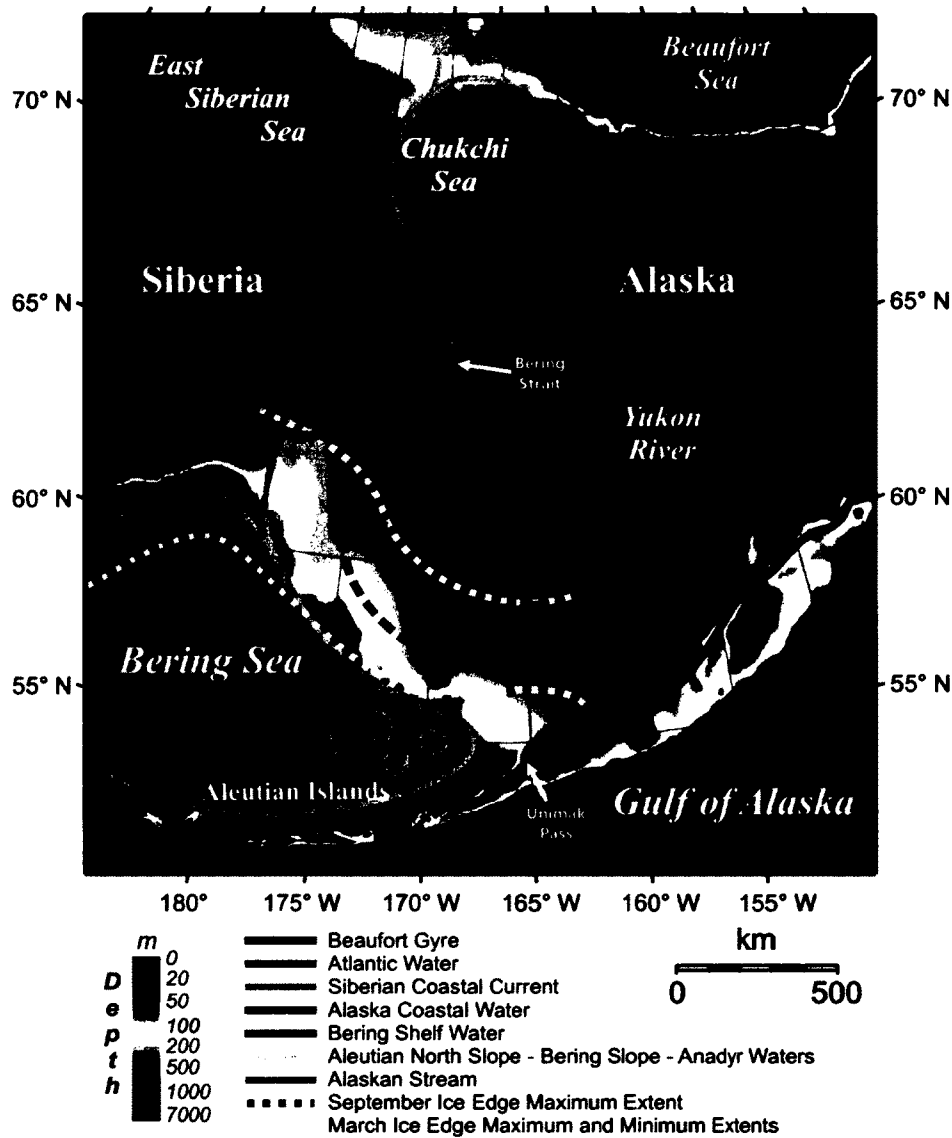


Figure 3.1 Schematic of the eastern Bering Sea and adjacent regions with major (idealized) summertime current and water mass features, typical spring and fall ice extent bounds, and place names. Mooring site and island abbreviations include: F8 = mooring F8; M2 = mooring M2; SLI = St. Lawrence Island; NI = Nunivak Island; PI = Pribilof Islands; SMI = St. Matthew Island.

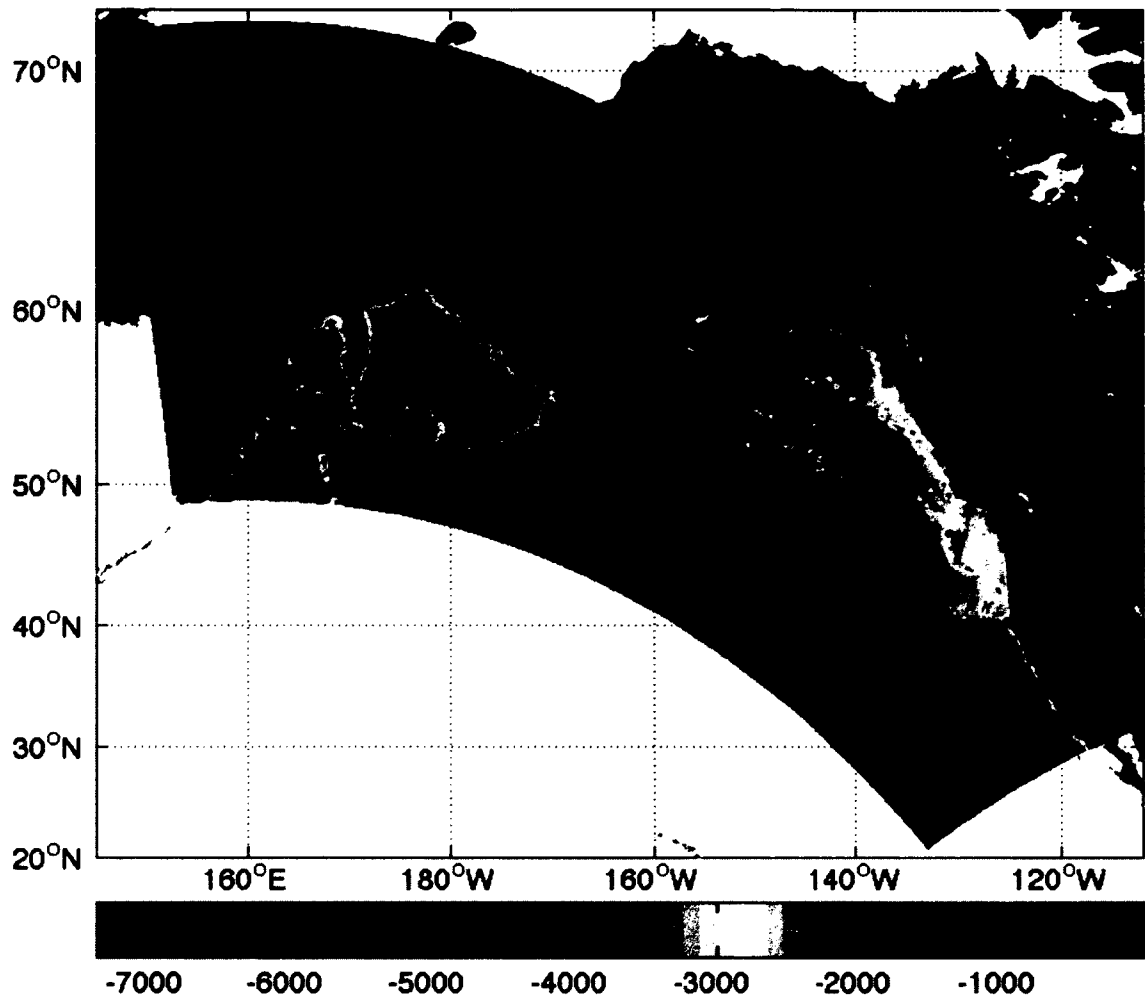


Figure 3.2: NEP5 model domain extent and bathymetric depths plotted on a Mercator projection map.

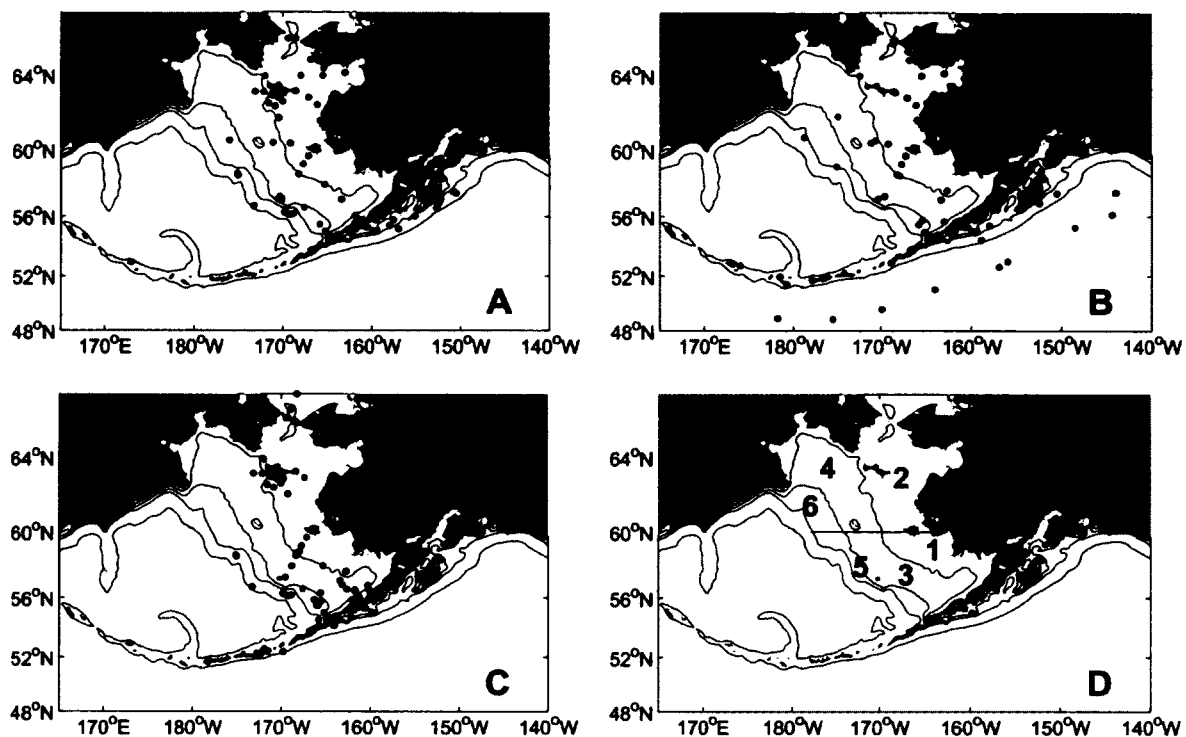


Figure 3.3: Locations of data employed in model evaluations. A) Moored current meter sites with tidal ellipse parameters; B) moored and coastal sea level elevation stations with tidal amplitude parameters; C) moored current meter sites with mean speed and direction statistics. D) Regions 1-6 bound CTD and discrete bottle samples listed in Table 3.2. Contours are drawn at 50 m, 100 m, 200 m and 2000 m depths.

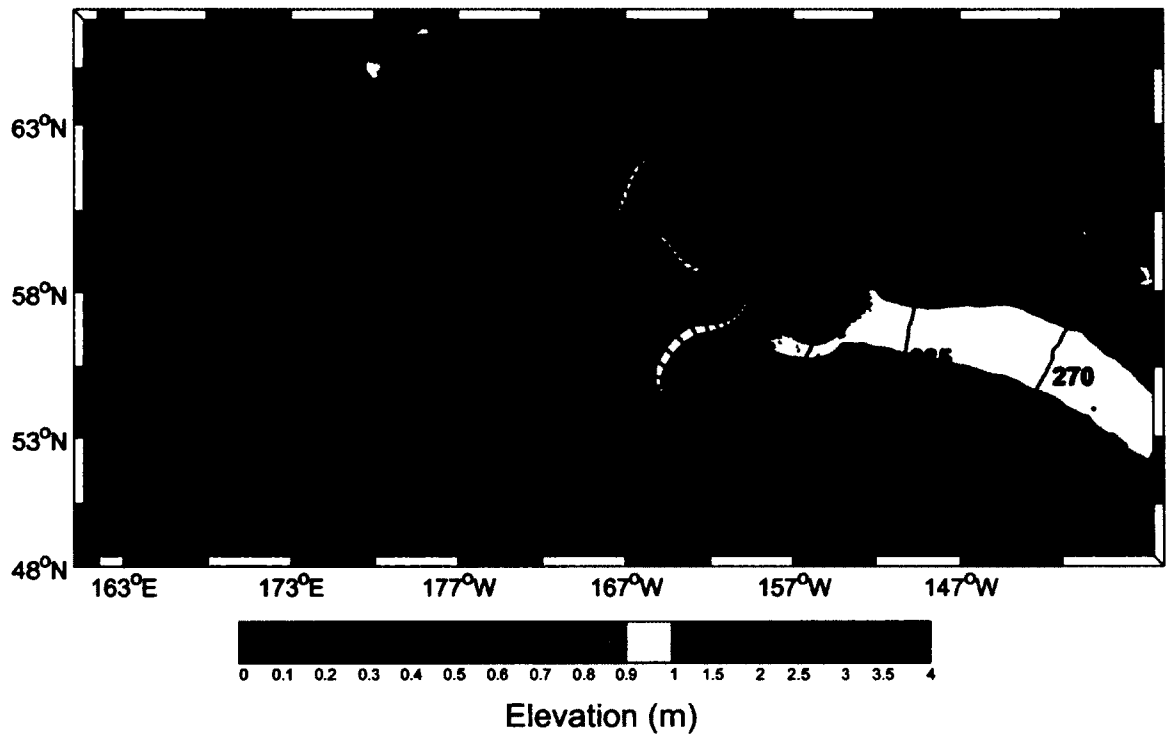


Figure 3.4: NEP5 model-derived M_2 co-tidal chart for the Bering Sea and Gulf of Alaska. Amplitudes are contoured with color shading; Greenwich phase contours are labeled in degrees.

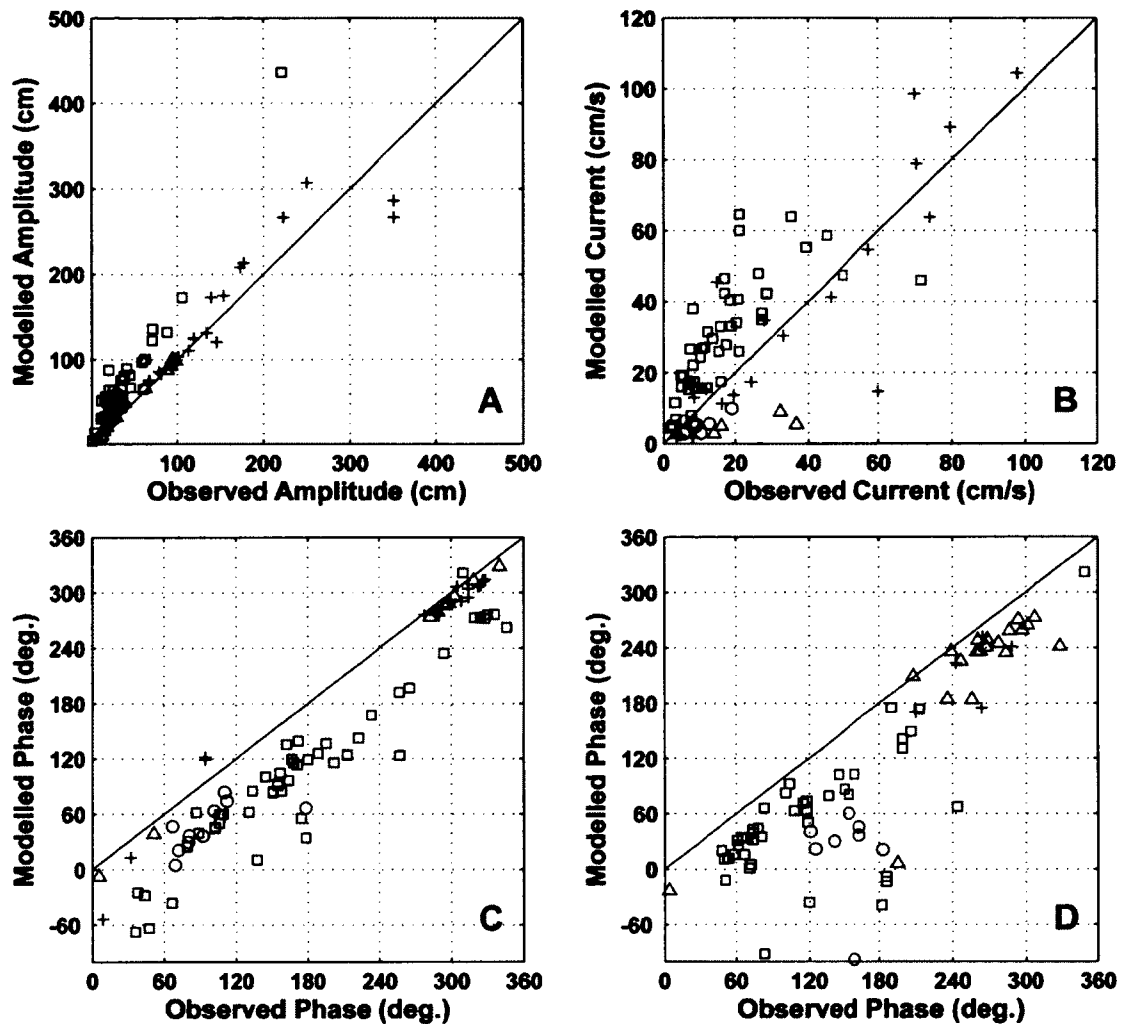


Figure 3.5: Comparison of model-derived M_2 tidal elevation and current analyses at the locations of the moored and coastal tide stations plotted in Figure 3.3. Panels show tidal elevation (A), elevation phase (C), tidal current ellipse semi-major axis magnitude (B) and current ellipse phase (D). Solid lines depict the 1:1 ratio. Symbols denote stations located in different regions: squares are from the Bering shelf, triangles from the deep North Pacific and Gulf of Alaska, pluses from the GOA shelf and circles from the deep Bering basin and Aleutian Islands.

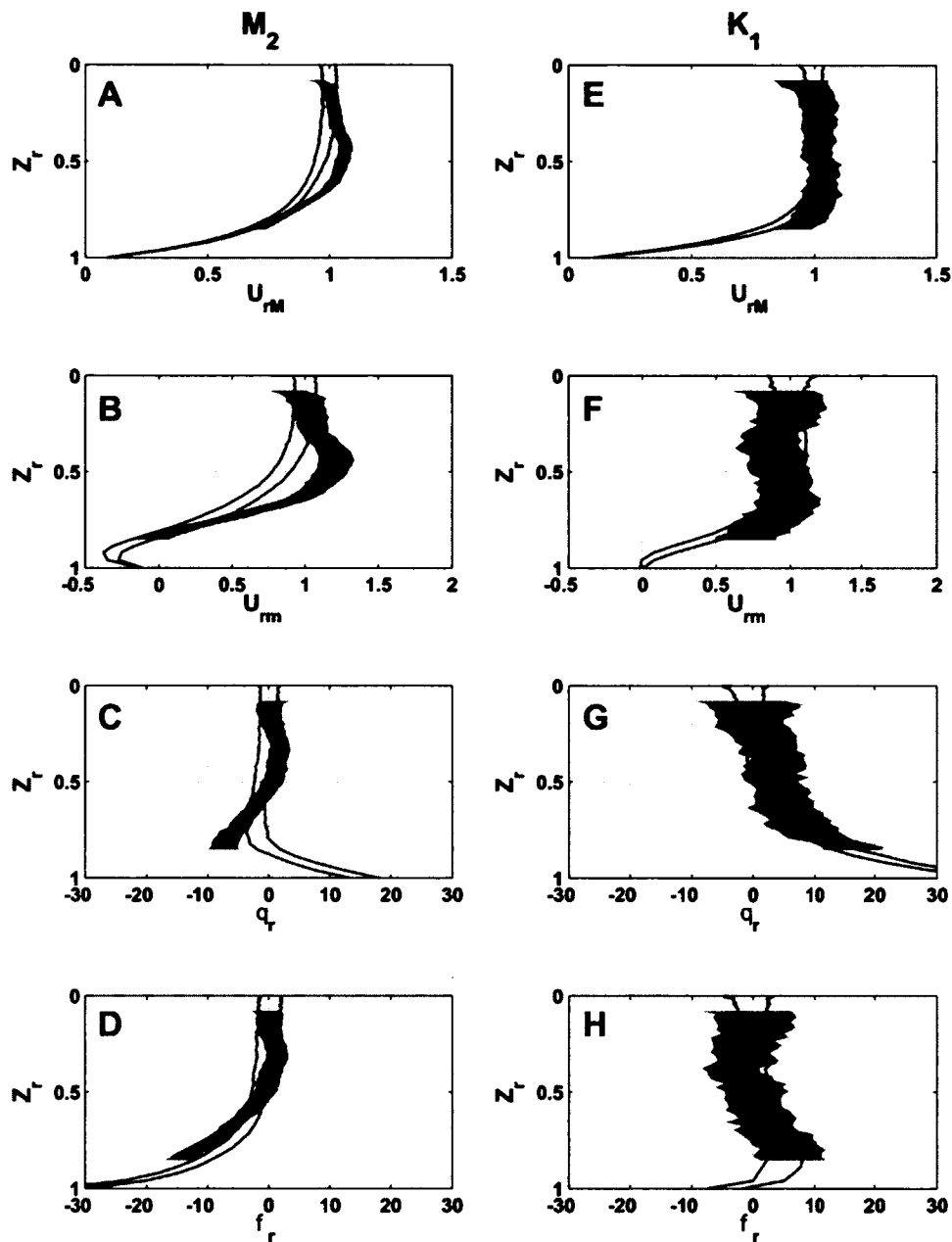


Figure 3.6: Vertical structure of the M_2 (left) and K_1 (right) tidal ellipse parameters. Depths (Z_r) and tidal parameters (U_{rM} = semi-major axis; U_{rm} = semi-minor axis; θ_r = inclination; ϕ_r = Greenwich phase) are scaled as described in the text. Shading and lines bound the 95% confidence limits on the observed and model ellipse parameters respectively.

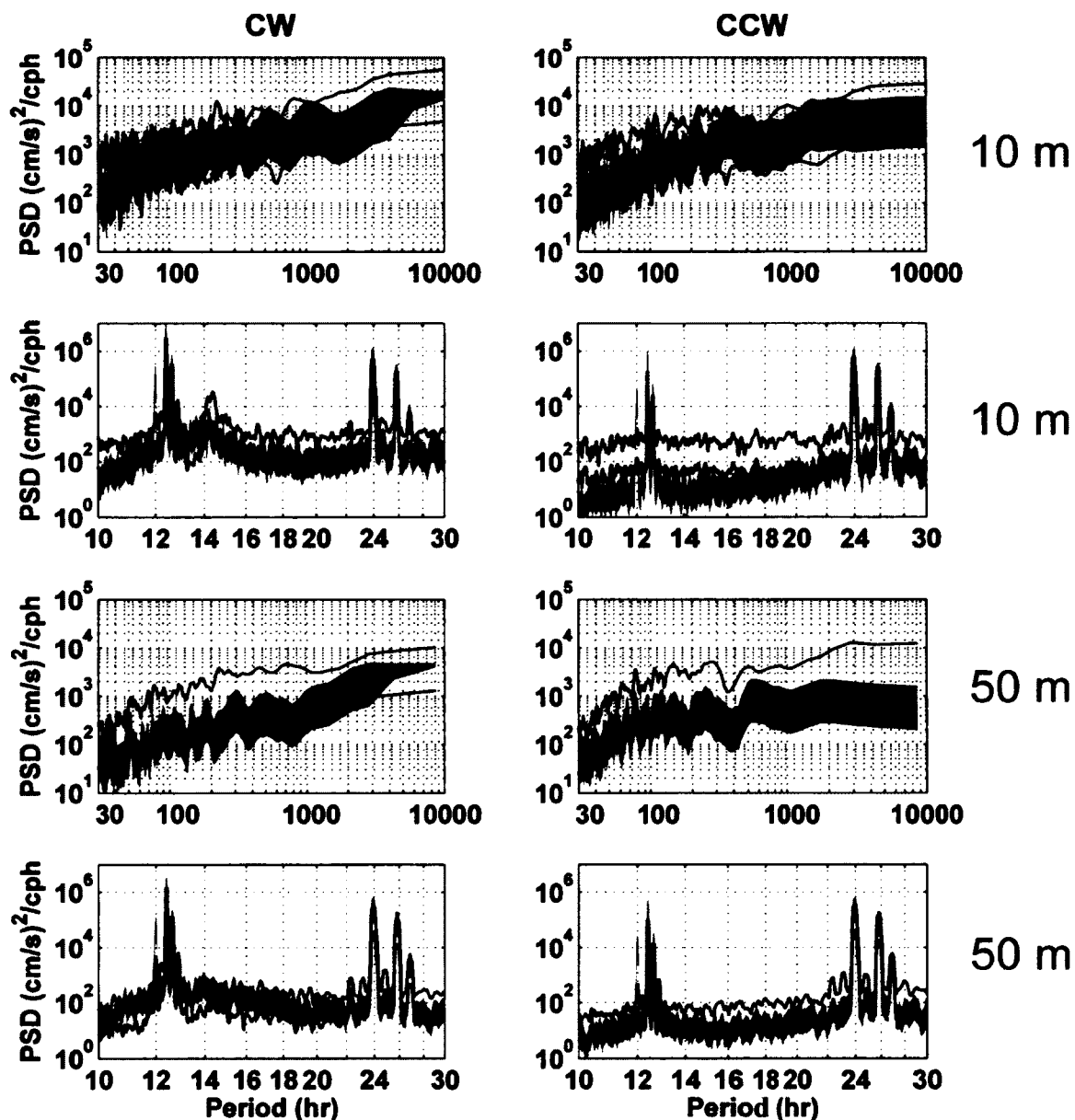


Figure 3.7: Power spectra density (PSD) at 10 m (upper four panels) and 50 m (lower four panels) depths at mooring site M2 from observations (shading) and model (lines). Shading and lines delimit the 95% confidence limits. Short (10-30 hr) and long (>30hr) period portions of each spectrum are shown separately. The clockwise (CW) and counterclockwise (CCW) rotating components are shown on the left and right, respectively.

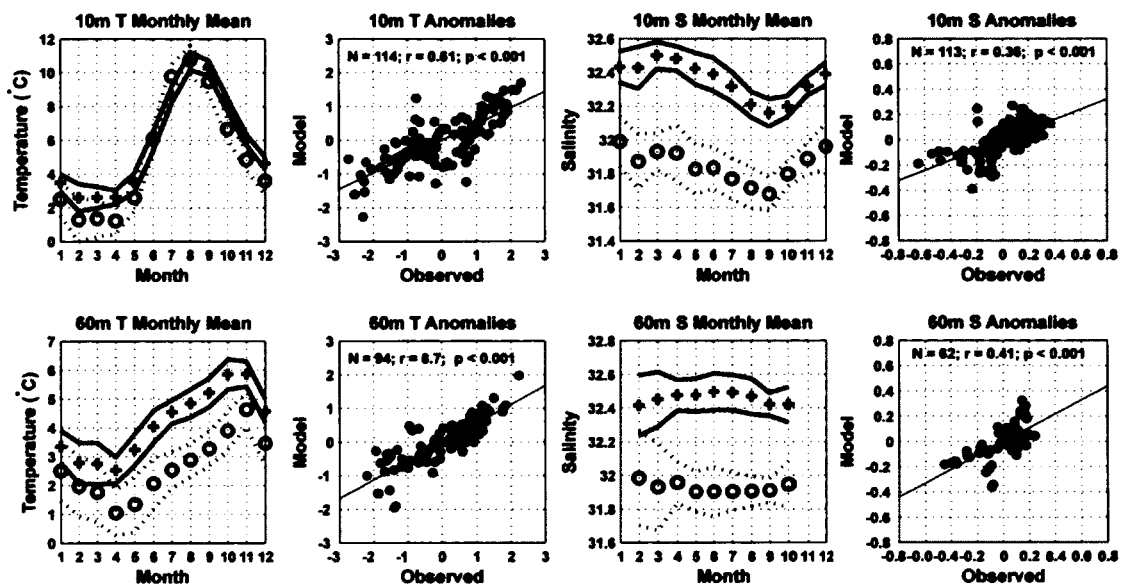


Figure 3.8: Mooring site M2 1995-2005 annual cycle of temperature and salinity monthly means and anomalies from 10 m (upper row) and 60 m (lower row) depths. Model (mooring) data are plotted with plus (circle) symbols and solid (dashed) lines indicate the 95% confidence interval upon each monthly mean. Notation indicates the number of months (N), correlation coefficients (r) and p-values for N-2 degrees of freedom. Straight lines depict the least squares best fit.

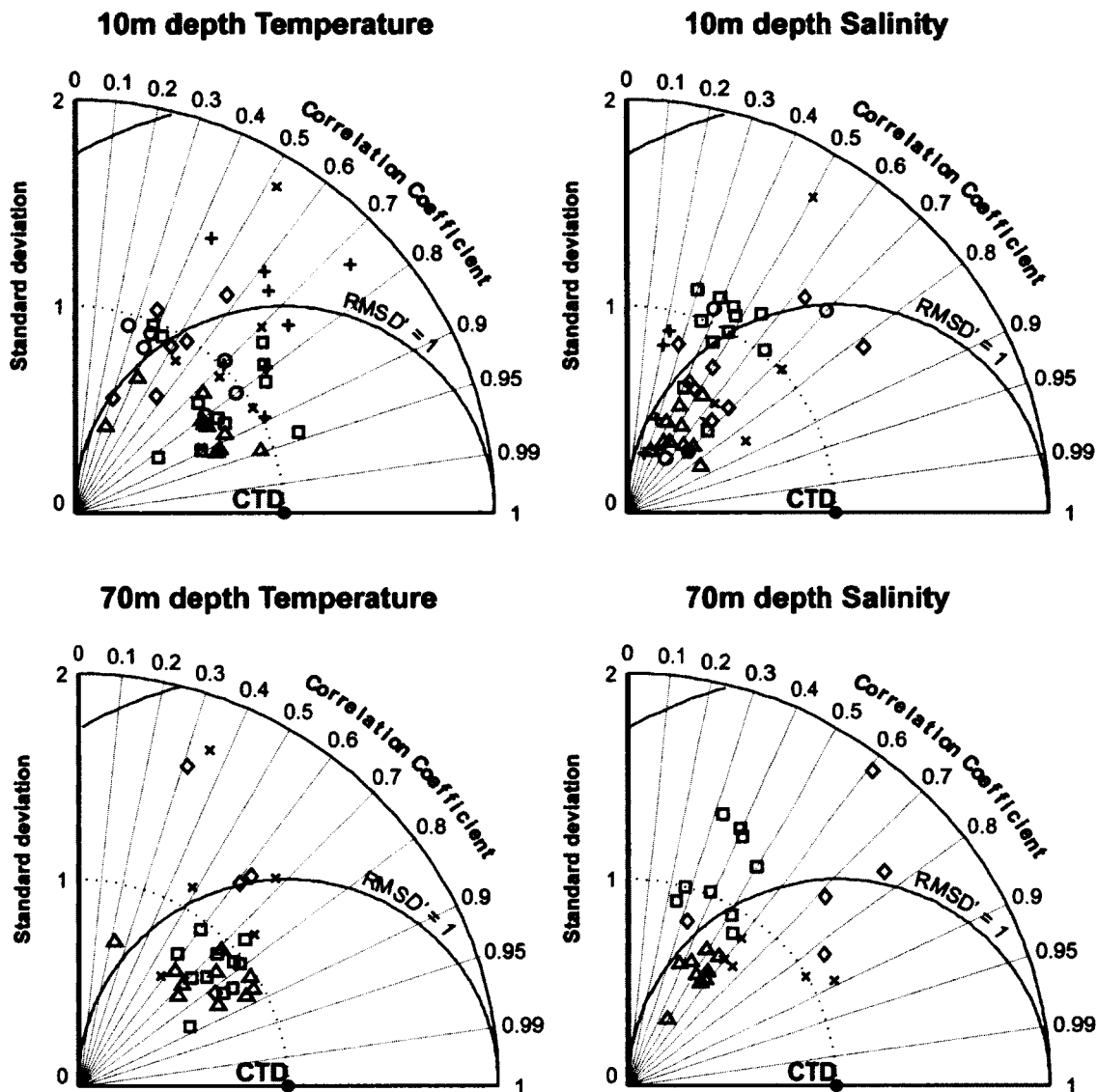


Figure 3.9: Temperature and salinity Taylor diagrams for the 10 m and 70 m depth levels. Symbols correspond to the regions listed Figure 3.3 and listed in Table 3.1. Regions 1-6 are associated with the plus, circle, square, diamond, triangle and cross symbols respectively. Each point represents month-specific summary statistics for the cases where $p < 0.05$ and the parameters fall within the ranges of the diagrams (a few points with large RMSD fall off the figures). The point marked CTD represents the observational reference with $RMSD' = 0$, $r = 1$, and $\sigma = 1$.

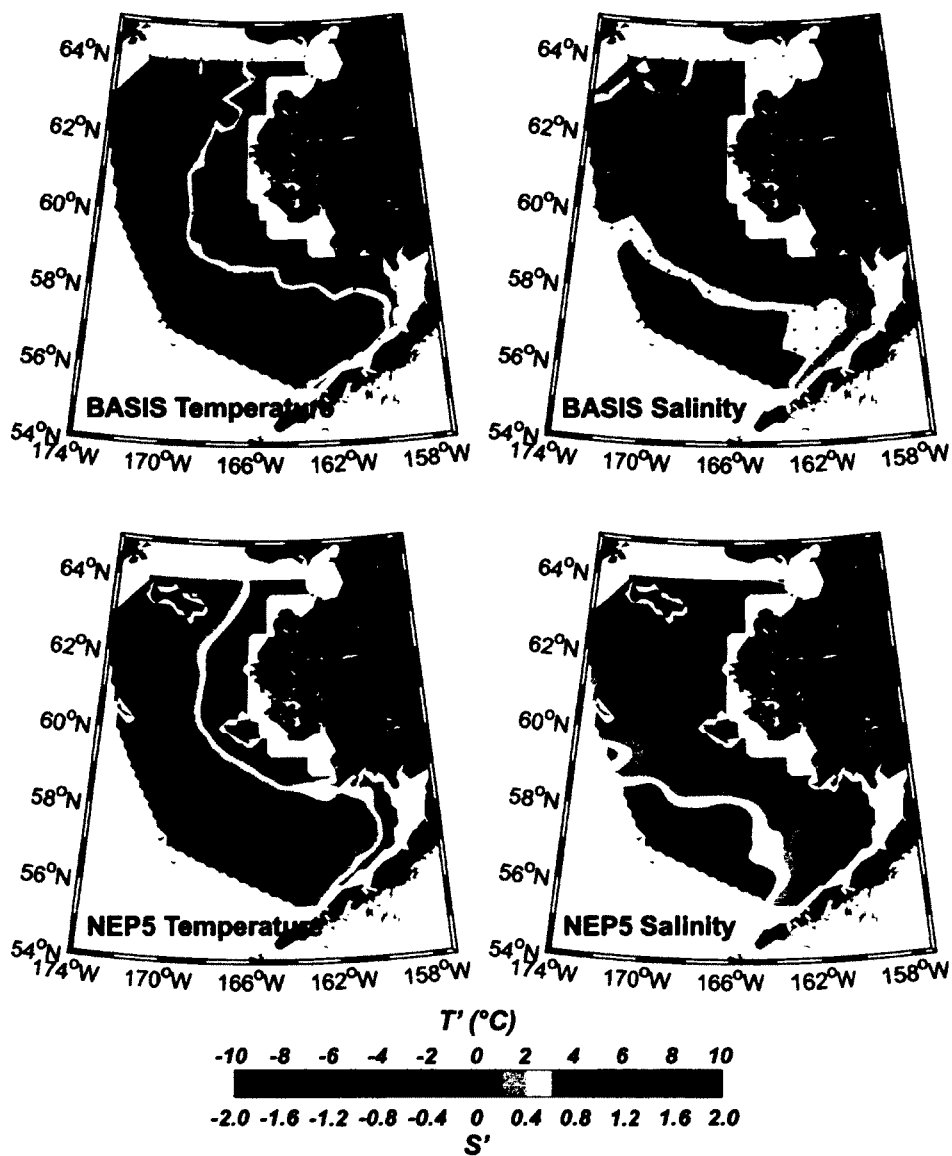


Figure 3.10: Near-bottom contours of T' and S' from CTD data (upper panels) and model hind-casts (lower panels). $T' = T - T_{\text{mean}}$ and $S' = S - S_{\text{mean}}$. BASIS CTD data were collected between 14 August and 30 September 2004; model results are the two-month average of the 2004 August and September fields. BASIS samples were collected at the locations marked with black dots.

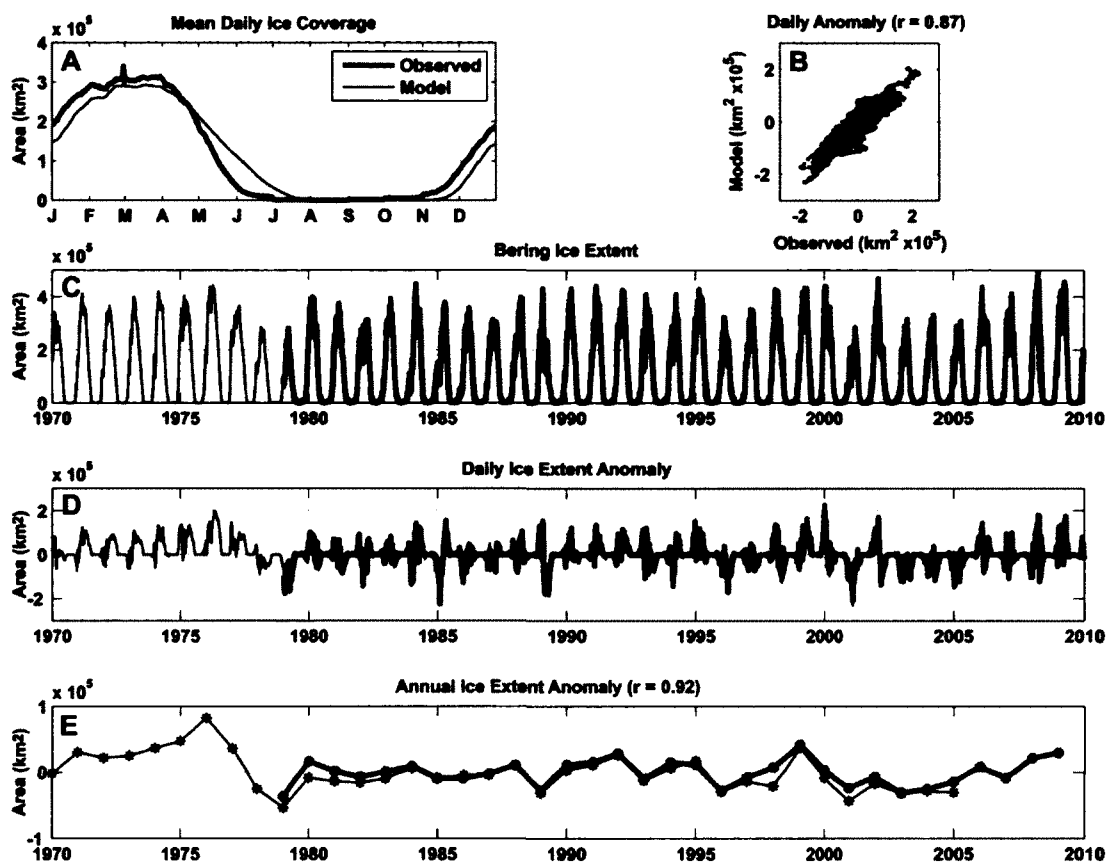


Figure 3.11: Bering Sea integrated ice extent and anomalies from the model and passive microwave satellite observations. Panels show the 1979-2009 daily mean annual cycle of ice extent (A), the daily anomalies (B), time series of total ice extent (C), daily anomalies (D) and annual anomalies (E). Observations are plotted in grey, model results with black.

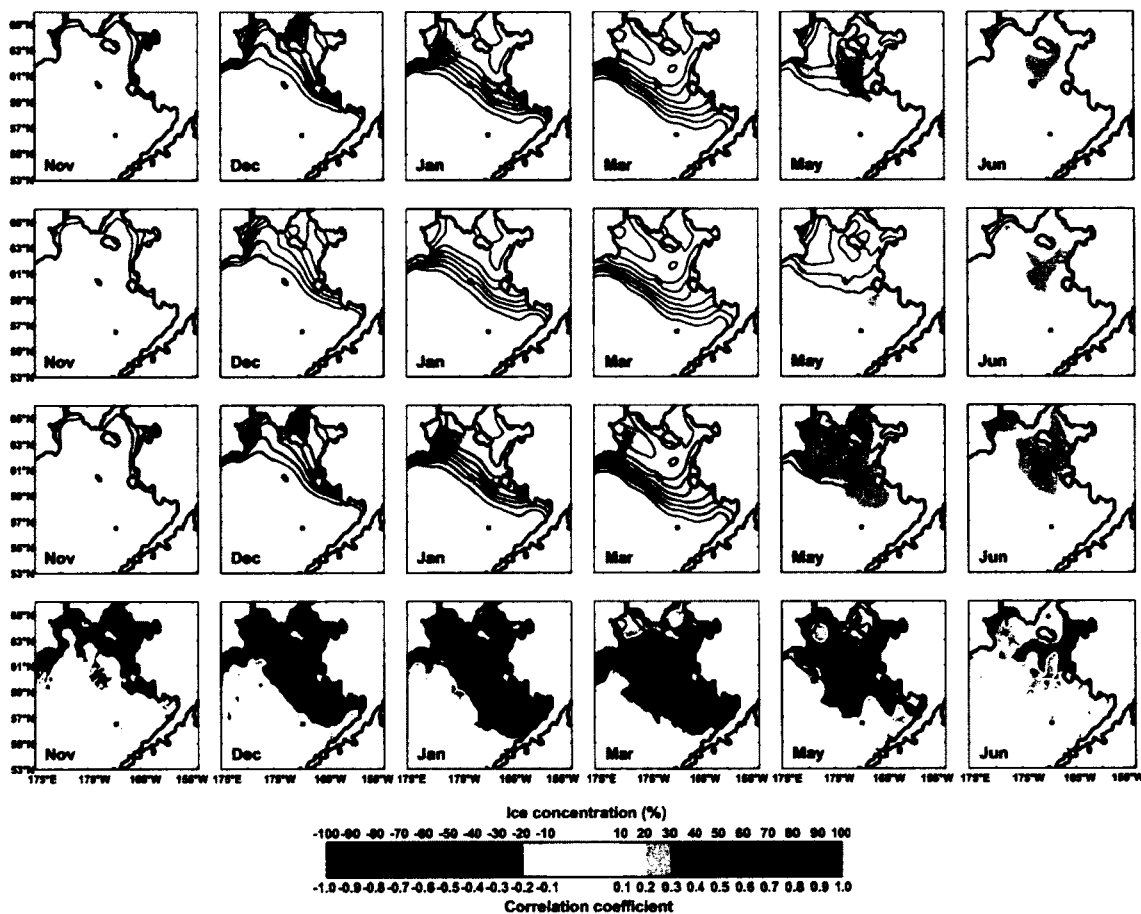


Figure 3.12: Comparison of modeled and observed ice concentrations. The observed mean monthly ice concentration is given with blue contours in all rows for the months indicated. Color shading depicts the mean model – observed ice concentration difference (top row); standard deviation of the model – observed difference (second row); model – observed RMSD (third row) and the model:observed cross-correlation (bottom row). Shading increments occur at integer multiples of 10% for the first three rows and at integer multiples of 0.1 for the cross-correlations. Yellow contours bound regions where the correlation is significant at the 95% level.

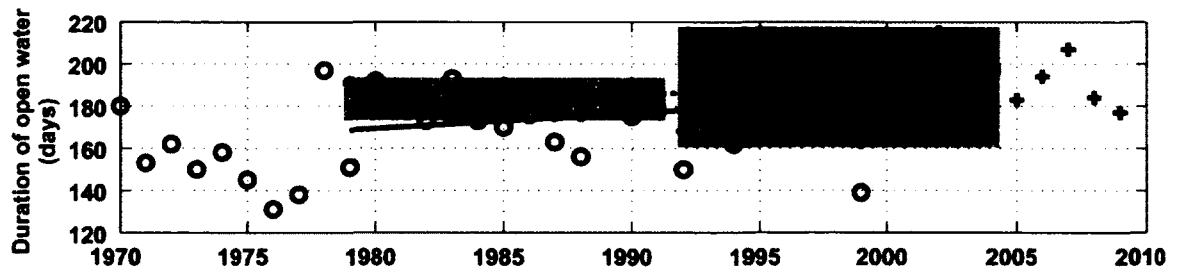


Figure 3.13: Time series of the annual number of ice-free days. Straight lines depict the least squares best fit linear trend to each series for the period of overlap (1979-2004). Observational results are represented with plus symbols and the dotted trend line. Model results are represented with circles and the solid trend line. The range of the observed open water season is shaded separately for the 1979-1991 and 1992-2004 time periods.

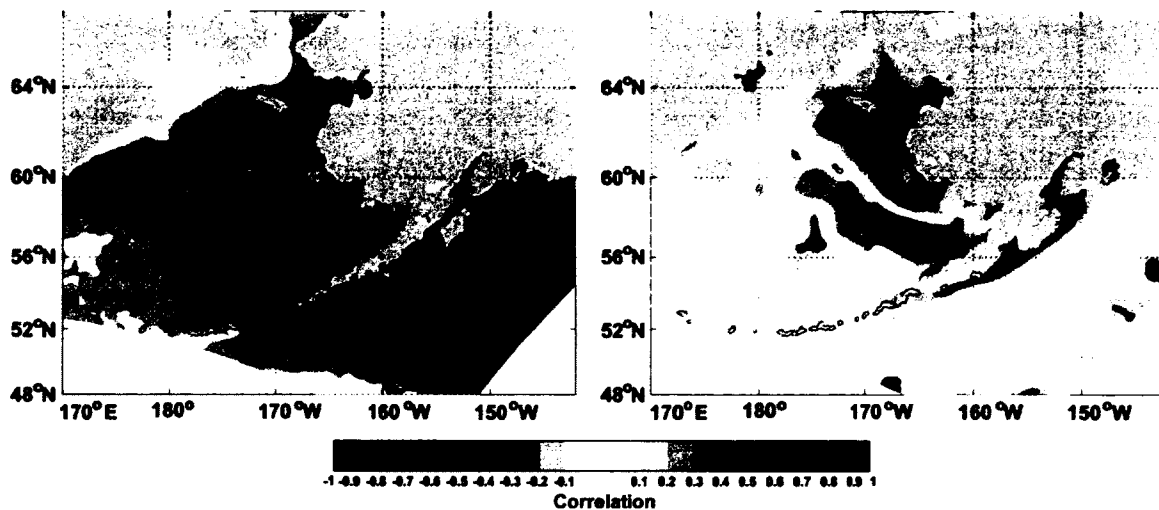


Figure 3.14: Correlation maps of 1970-2005 NEPS hindcast monthly average 0-20 m temperature (left) and salinity (right) time series. The reference point is located near mooring M2, denoted with a black dot.

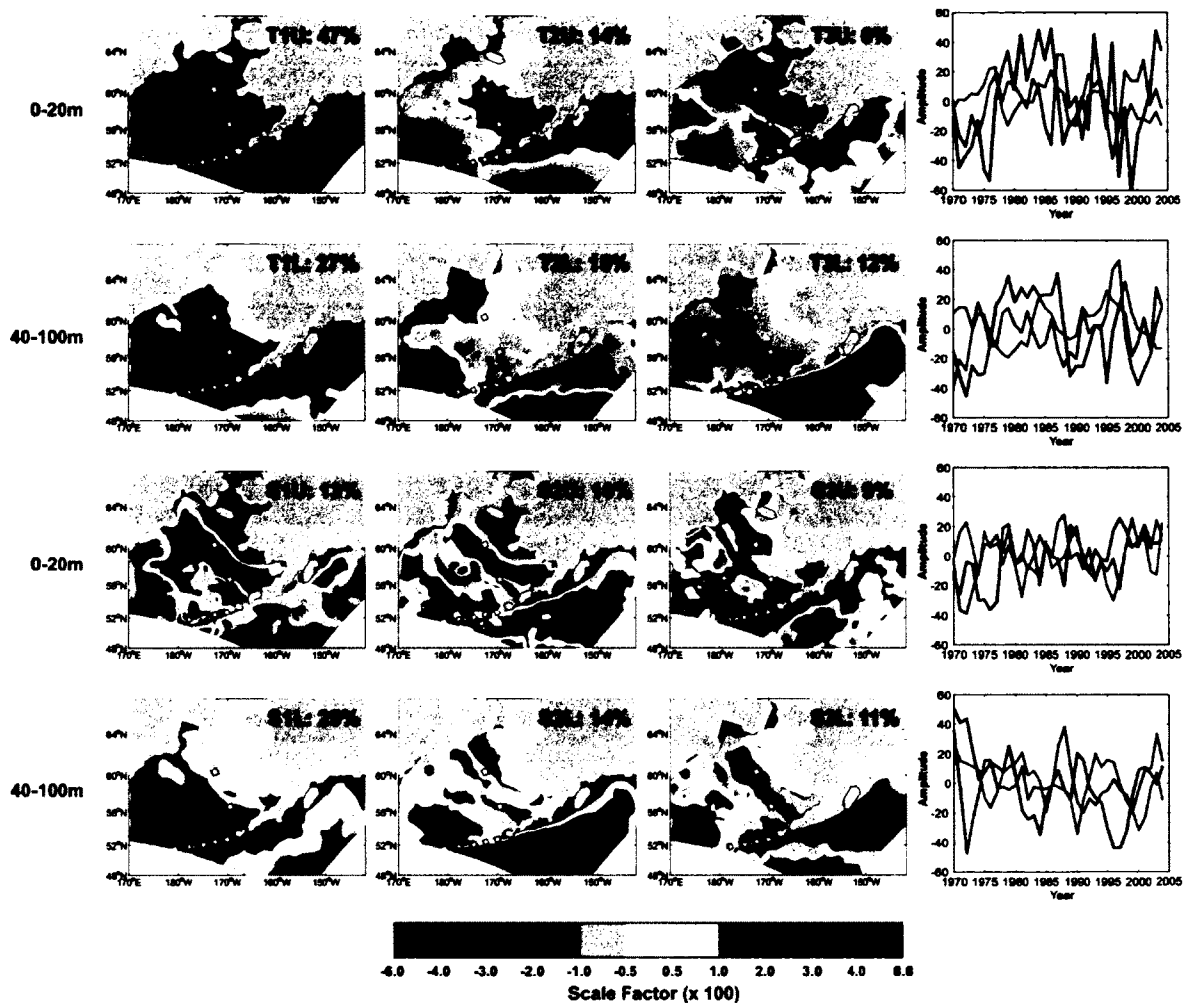


Figure 3.15: EOFs of the NEP5 hindcast near surface (0-20 m) and subsurface (40-100 m) temperature (upper two rows) and salinity (lower two rows) fields. Percentages describe the fraction of the total variance explained by each pattern. The right-most panels show the principal component amplitudes associated with the first (blue), second (green) and third (red) EOFs. EOF magnitudes are shown by the (nonlinear) colorbar and are scaled by a factor of 10^2 .

Chapter 4: Circulation on the central Bering Sea shelf¹

4.1 Abstract

We examine the July 2008 to July 2010 circulation over the central Bering Sea shelf, using measurements at eight instrumented moorings, hindcast winds and numerical model results. At sub-tidal time scales, the vertically integrated equations of motion show that the cross-shelf balance is primarily geostrophic. The along-shelf balance is also mainly geostrophic, but local accelerations, wind stress and bottom friction account for 10-40% of the momentum balance, depending on season and water depth. Water column average vector mean speeds are $< 5 \text{ cm s}^{-1}$ in all months. Mean/peak speeds in summer ($3\text{-}6 \text{ cm s}^{-1}/10\text{-}30 \text{ cm s}^{-1}$) are smaller than in winter and fall ($6\text{-}12 \text{ cm s}^{-1}/40\text{-}70 \text{ cm s}^{-1}$). Low frequency flows ($< 1/4 \text{ cpd}$) are horizontally coherent over distances $> 200 \text{ km}$. Vertical coherence varies seasonally and degrades with the onset of summer stratification. Wind-forced Ekman dynamics appear primarily responsible for flow variations. The system as a whole changes abruptly from strong northward flow (with coastal convergence) to strong southward flow (with coastal divergence) for northerly and easterly or southeasterly winds, respectively. Over these two years with extensive ice cover, northwesterly winds dominated (64% of the time), although southeasterly winds resulted in more energetic currents. These results suggest that a substantial portion of the entire shelf undergoes a major reorganization of currents and associated material fluxes as it changes between the two circulation modes. Under southeasterly winds, northward transport increases. Under northwesterly winds, nutrient-rich waters flow toward the central shelf from the north and northwest, replacing dilute coastal waters that are carried south and west.

¹Danielson, S., T. Weingartner, K. Aagaard, J. Zhang, and R. Woodgate, 2012. Circulation on the central Bering Sea shelf, Draft manuscript prepared for submission to *J. Geophys. Res.*

4.2 Introduction

The shallow and broad central Bering Sea shelf is the region south of St. Lawrence Island and north of Nunivak Island (Figure 4.1). It experiences cooling, ice production, and brine production in winter [Drucker *et al.*, 2003], solar heating in summer, strong winds in fall, winter and early spring [Brower, *et al.*, 1988; Bond *et al.*, 1994], large river discharges in summer [Brabets *et al.*, 2000], and strong tidal currents [Pearson *et al.*, 1981; Moffeld, 1984; Kowalik, 1999; Danielson and Kowalik, 2005]. Thermohaline characteristics exhibit large inter-annual variability [Takenouti and Ohtani, 1974; Coachman *et al.*, 1975; Danielson *et al.*, 2011], but the causes of these variations are not fully described.

North of St. Lawrence Island, the shelf flow is dominated by a net northward transport through Bering Strait of ~ 0.8 Sv ($1 \text{ Sv} = 10^6 \text{ m}^3 \text{ s}^{-1}$) [Roach *et al.*, 1995; Woodgate *et al.*, 2005a], ascribed to a sea surface height difference of ~ 0.5 m between the North Pacific and Arctic oceans [Stigebrandt, 1984; Overland and Roach, 1987; Aagaard *et al.*, 2006; Woodgate *et al.*, 2005b], and in opposition to the mean wind. Westward intensification associated with the topographic beta effect forces Bering Sea slope waters on-shelf through the Gulf of Anadyr [Kinder *et al.*, 1986]. Measurements [Muench *et al.*, 1988; Coachman, 1993] and models [Overland and Roach, 1987; Spaulding *et al.*, 1987; Clement *et al.*, 2005] suggest that 70-80% of the Bering Strait flow first passes through Anadyr Strait, with the rest flowing through Shpanberg Strait. Mooring- and satellite-based estimates of the instantaneous transport through Bering Strait range between about -3 Sv to +4 Sv [Coachman and Aagaard, 1988; Roach *et al.*, 1995; Cherniawsky *et al.*, 2005; Woodgate *et al.*, 2005a]. Numerical model results and observations [Overland and Roach, 1987; Muench *et al.*, 1988] indicate that flows in Shpanberg Strait can reverse to southward while the flow in Anadyr Strait is northward. Mean northerly winter winds (blowing toward the south) retard the northward flow in Bering Strait [Overland and Roach, 1987], and October-March northward transports are typically one-half to two-thirds those of April-August [Roach *et al.*, 1995; Woodgate *et al.*, 2005a].

Over the inner (0-50 m depths) and middle (50-100 m depths) southeastern Bering shelf, tidal currents are large (the two largest tidal constituents, M_2 and K_1 , sum to 25-55 cm s^{-1}) [Pearson *et al.*, 1981; Kowalik, 1999; Stabeno *et al.*, 2010], and mean subtidal flows are small (1-5 cm s^{-1}) [Schumacher and Kinder, 1983; Stabeno *et al.*, 2010]. The middle shelf contains cold waters below the summer pycnocline [Coachman, 1986]. The southern extent of this “cold pool” is primarily determined by the previous winter’s ice extent. Currents over the outer shelf (between the shelfbreak and 100 m isobath) are 1-10 cm s^{-1} , with the flow more or less steadily northwestward along the isobaths [Kinder and Schumacher, 1981; Schumacher and Kinder, 1983; Schumacher and Reed, 1992; Stabeno *et al.*, 2001; Stabeno *et al.*, 2002a]. Along the continental slope, the Bering Slope Current is a relatively swift (5-20 cm s^{-1}) and deep cyclonic boundary current with a transport of $\sim 6 \text{ Sv}$ [Favorite, 1974; Royer and Emery, 1984; Overland *et al.*, 1994; Roden, 1995; Johnson *et al.*, 2004; Stabeno *et al.*, 2009]. Inflow from the Gulf of Alaska through Unimak Pass [Schumacher *et al.*, 1982; Stabeno *et al.*, 2002b] delivers low-salinity waters from the Gulf of Alaska, representing a first-order contribution to the shelf fresh water budget [Weingartner *et al.*, 2005; Aagaard *et al.*, 2006].

Inter-annual temperature variations over the southeastern shelf in spring are related to the previous winter’s sea ice extent and timing of retreat [Stabeno *et al.*, 2001; Stabeno *et al.*, 2002b]. Ice extent, in turn, is related to the combination of southward advection of ice caused by winds from the north and low air temperatures [Overland and Pease, 1982; Niebauer *et al.*, 1999]. At the end of summer, water column heat content over the central and southeastern shelf reflects a combination of the heating season’s incoming solar radiation anomaly and along-shelf transport anomalies, whereas the salt content appears to be set by the previous winter’s cross-shelf transport anomaly [Danielson *et al.*, 2011].

The central shelf is understudied compared to the southeastern shelf and Bering Strait. The Yukon River (sixth-largest in North America), discharges adjacent to the central shelf, nearly 90% of its annual discharge ($\sim 200 \text{ km}^3$) occurring between May and October [Brabets *et al.*, 2000]. The mean eastward flow south of St. Lawrence Island

turns northward in Shpanberg Strait, where it encounters the Yukon plume. This eastward flow can reverse under strong northerly and easterly winds [*Schumacher et al.*, 1983; *Danielson et al.*, 2006]. There are relatively few measurements southward to St. Matthew and Nunivak islands, but the available data suggest small mean flows, high variance, and a net northward drift [*Kinder and Schumacher*, 1981; *Aagaard et al.*, 1985; *Muench et al.*, 1988; *Danielson et al.*, 2006]. Numerical models and the few available observations also suggest the possibility of prolonged westward and southward flows [*Overland and Roach*, 1987; *Muench et al.*, 1988].

Winter ice formation and southward drift depend on favorable winds [*Muench and Ahlmas*, 1976; *Pease*, 1980; *McNutt*, 1981] and lead to southward transport of comparatively fresh waters [*Zhang et al.*, 2010] produced by melting along the southern edge of the ice pack [*Pease*, 1981]. Brine generated by ice formation in polynyas results in density gradients capable of driving a baroclinic pressure gradient large enough to be important to the momentum balance [*Schumacher et al.*, 1983].

Density gradients along the Alaskan coast during summer imply a northward buoyancy-driven coastal jet [*Danielson et al.*, 2011]. The front, which presumably traps river discharge close to the coast through the summer months, likely breaks down in fall with the onset of strong wind forcing. *Danielson et al.* [2006] observed that near-surface (1 m and 10 m drogue depths) satellite-tracked drifters exhibited westward motion in the fall and suggested that this motion occurs annually.

Our primary goal here is to gain a better mechanistic understanding of the central shelf flow and its relation to the varying wind and thermohaline fields. Our results bear on numerous eco- and climate system issues, including aspects of salmon migratory behavior [*Mundy and Evenson*, 2011], advection of passively drifting larvae [*Wespestad et al.*, 2000; *Wilderbuer et al.*, 2002; *Orensanz et al.*, 2004], nutrient replenishment and net production over the Bering shelf [*Sambrotto et al.*, 1986; *Whitledge et al.*, 1986; *Mathis et al.*, 2010], and heat, nutrient, and fresh water fluxes northward into the Arctic Ocean [*Aagaard and Carmack*, 1989; *Woodgate et al.*, 2010].

We begin with a descriptive overview of the oceanic and atmospheric conditions during the course of our field program, and a kinematic summary of the flow field. We then investigate the circulation dynamics by examining the vertically integrated equations of motion, along with geostrophic velocity computations. Finally, we use model-based sea surface height (SSH) hindcasts and analyses of the vertical and horizontal structure of the flow field to investigate the effects of variable wind forcing, with particular emphasis on the wind direction.

The results described here are part of the National Science Foundation's Bering Ecosystem Study (NSF-BEST) program, the North Pacific Research Board's Bering Sea Integrated Ecosystem Research Program (NPRB-BSIERP) [*BEST-BSIERP Program Summary*, 2010] and the National Oceanic and Atmospheric Administration's Bering-Aleutian Salmon International Survey (NOAA-BASIS) program. Collectively, these programs supported an intensive set of collaborative field surveys, modeling efforts and analyses between 2007-2011. Our primary data set here is from eight moorings on the central Bering shelf, deployed during July 2008-July 2010 as part of the NSF-BEST program.

Data sets, data calibration and quality control, and numerical model fields are described in Section 4.3. Section 4.4 presents results in three major subsections: an overview of the current meter, temperature, salinity and wind records (4.4.1-4.4.3); the vertically integrated momentum balance and an evaluation of baroclinic contributions (4.4.4); and an analysis of co-variability of the current, wind and sea surface height (SSH) fields (4.4.5). A discussion of the results and a summary are given in Sections 4.5 and 4.6, respectively.

4.3 Data and methods

4.3.1 Mooring configurations

From July 2008 to July 2010, eight subsurface moorings were deployed on the 55 m, 40 m and 25 m isobaths (Figure 4.1 and Table 4.1) for one year at a time. Moorings located on the 40 m and 55 m isobaths were each equipped with an upward-looking

Teledyne RDI acoustic Doppler current profiler (ADCP) mounted just above the acoustic release. A Seabird (SBE) temperature/conductivity (T/C) data logger was co-located with the acoustic release; a second SBE T/C data logger was located near 20 m depth. Some of the T/C loggers also recorded pressure (P). Moorings on the 55 m isobath each had a T/C/P data logger at 10 m, connected to the rest of the mooring via a weak link, and an inductive modem transmitted the data to a remote data logger mounted near the 20 m T/C recorder. This configuration was employed to measure close to the surface while providing some protection to the data and the mooring in the event that ice keels or extreme waves destroyed or removed the uppermost float. The configuration worked well. Although we lost four out of six 10 m instruments, we obtained data through the breakdown of fall stratification in both years. Also mounted on the 55 m moorings was a string of thermistors spaced 2-4 m apart between the 20 m and near-bottom T/C recorders.

Moorings on the 25 m isobath employed Oceanscience Group SeaSpider tripod frames. Each was equipped with a gimbaled upward-looking ADCP and T/C/P recorder with pumped intake about 1 m above the seafloor. On the 2009 recovery attempt, one 25 m tripod deployed just south of Nunivak Island was located acoustically, but never recovered. Based on visual inspection by divers we believe that the entire tripod was buried by sediment. As a consequence we did not re-deploy at this site in the second field year. The 2008-2009 N25 tripod popup buoy canister was also fouled by bottom sediment and unrecoverable from the surface, but we were able to recover it with the aid of divers in the summer of 2010.

4.3.2 Moored velocity data

With the exception of C55 (whose batteries died prematurely in late May 2009 and late February 2010), nearly two complete years of current measurements were recorded at all mooring sites. Velocity data were recorded with 307 KHz Teledyne RDI ADCPs using 30-minute ensembles and 1 m bins at 175 pings per ensemble. This protocol yields an expected standard deviation of 1.02 cm/s for each ensemble. Data were screened with the following thresholds: correlation limit of 64 counts, error

amplitude limit of 80 mm/s, and minimum of 40 percent-good pings within any ensemble. Both 3-beam and 4-beam solutions that achieved these criteria were retained. Velocity vector directions were corrected for magnetic declination based on the declination computed halfway through each deployment at each mooring site (corrections ranged from 8.9° to 11.3°).

Velocity data were de-tided using the MATLAB T_Tide [Pawlowicz *et al.*, 2002] harmonic analysis algorithm following Foreman [1978]. Low-pass filtering to isolate sub-tidal (> 35 hr) and long period (> 100 hr) currents was implemented with a 6th order bi-directional Butterworth filter. Subtracting both the harmonic tide prediction and the 35-hour low-pass signal from the original time series allows us to isolate non-tidal high frequency fluctuations (e.g., inertial motions).

Error estimates for the velocity components are based on estimates of the integral time scale, following Allen and Kundu [1978], Schumacher and Kinder [1983], and Emory and Thompson [2001]. Such computations are noisy in practice but analyses of the 35 hr low-pass filtered velocity records at all mooring sites suggest a decorrelation time scale less than 48 hours (87% of the estimates gave a time scale shorter than this). As a conservative estimate, therefore, we use 48 hours to define the effective degrees of freedom.

4.3.3 Moored pressure, temperature and salinity data

Each mooring hosted an assortment of T, T/C and T/C/P data loggers (Table 4.1). Seabird SBE-16 and SBE-37 instruments were calibrated at the manufacturer's facility prior to deployment and after recovery. (Exceptions were the 2009-2010 N55 20 m depth instrument, which failed beyond repair, and some of the 10 m SBE-37 instruments, which were lost during the course of the winter.) The magnitude of the drift of the SBE temperature probes was less than 0.001 °C over the course of the deployment. Drift of the conductivity cells resulted in salinity changes from -0.003 to -0.064 (measured at 3.0 S/m) with the exception of the 20 m instrument on C40, which drifted by -0.154. Inspection of the salinity time series suggests that the calibrations did not capture some drift. For example, by late spring of the first year, the near-bottom data logger on two of

the moorings showed water less dense than at 20 m. This likely resulted from silting of the near-bottom conductivity cell over the course of the winter, sediment that was not retained in the cell prior to the factory post-season calibration. All salinity data (moored and CTD) are based on the Practical Salinity Scale 1978 [UNESCO, 1981].

Onset HOBO Water Temp Pro v2 temperature loggers were mounted on the 55 m moorings in order to increase vertical resolution (Table 4.1) of temperature measurements. The HOBO loggers are accurate to within 0.2 °C, with a resolution of 0.02 °C. Mean temperature differences in February between the upper (20 m and 10 m SBE-37s) and lower (~45 m) Seabird instruments on the 55 m moorings is less than 0.01 °C. Therefore, the water column is nearly thermally homogeneous in February and we are able to compute offsets for each HOBO logger based on the average of the temperatures measured by the Seabird temperature probes. HOBO logger offset corrections range between -0.11 °C and +0.06 °C. We have no means to assess HOBO thermistor temperature-dependent bias or drift over the course of the deployment.

4.3.4 Shipboard temperature and salinity data

The BEST, BSIERP and BASIS programs sponsored 21 oceanographic cruises that sampled in the study region between March and mid-October over the five year interval 2006-2010. Data from 14 of these cruises falls within two seasonal intervals relevant to our analysis: March to early June and August to October. Moored observations made between 1995-2011 (an interval with near-continual in situ monitoring by moored sensors at NOAA station M2 in the southeast Bering Sea) show that the 2007-2010 cruises took place following relatively cold winters, while the 2005-2006 winter was close to average [Stabeno *et al.*, 2012]. Profiles collected by SBE-911 CTD instruments on these cruises are used to provide an overview of the seasonal changes in salinity stratification and to estimate geopotential height anomalies and geostrophic velocities associated with the *in situ* density structure. Processing techniques varied slightly amongst responsible institutions, but in each case we employ the final 1 db bin-averaged dataset. We estimate that temperatures are generally accurate to within 0.01 °C and salinity to within 0.02.

4.3.5 Gridded sea surface temperatures and ice concentrations

To supplement the moored temperature time series, we employ the Reynolds Optimum Interpolation Sea Surface Temperature (OISST) product, version OI.v2 [Reynolds and Smith, 1994; Reynolds *et al.*, 2002], which is generated daily on a $\frac{1}{4}^\circ$ grid and incorporates *in situ* (ship, buoy and drifter) observations along with satellite observations and simulated SST estimates in regions with sea ice [Reynolds *et al.*, 2002]. Satellite-based estimates of sea ice concentration are also included in the OI.v2 dataset. Comparing the OI.v2 surface temperatures to temperatures measured at 10 m depth on our six 55 m moorings, we find the OI.v2 data are biased by 0.54-0.94 °C, but significantly ($r > 0.95$, $p < 0.01$, Pearson's r correlation coefficient) cross-correlated with temperatures at 10 m.

By combining the daily OISST temperatures with our *in situ* moored measurements, we achieve a full water column depiction of thermal stratification at the 55 m isobath moorings. Given the loss of some 10-m instruments and the problems associated with satellite detection of SSTs near the ice edge, we do not resolve the upper water column thermal stratification well in May and June, however. Stratification due to salinity is not well resolved by our mooring measurements, but examination of CTD casts shows that the thermocline usually coincides with the halocline except in late spring and early summer, when there is salinity stratification from ice melt.

4.3.6 Reanalysis winds

Winds are from the National Center for Environmental Prediction (NCEP) North American Regional Reanalysis (NARR) model hindcasts [Mesinger *et al.*, 2006]. The 1979-present NARR model output includes surface pressure, wind, temperature and ocean-atmosphere heat fluxes every three hours on a 32 km grid, and thus provides higher resolution than the 2.5° , six-hourly output of the global NCEP Reanalysis [Kalnay *et al.*, 1996] used in many studies of the Bering shelf [e.g., Ladd and Bond, 2002; Mull, 2008; Stabeno *et al.*, 2010; Danielson *et al.*, 2011]. We chose the NARR product because we are interested in resolving spatial differences in the wind field across the mooring

array, and because other regional studies have found that the NARR provides good representations over the North Pacific and western Arctic [Pickart *et al.*, 2009].

4.3.7 Model-generated sea surface heights

Since we are unable to uniformly reference the moored pressure data to a common SSH, we use a model to estimate the daily mean SSH field. That field is then in turn used to investigate the regional ocean response to variable wind forcing. Zhang *et al.* [2010] describe the Bering Ecosystem Study ice-ocean Modeling and Assimilation System (BESTMAS) model, and we here update the integration through our mooring deployment period. The BESTMAS model was constructed to investigate the sea ice-ocean system of the Bering shelf. It is based on the coupled parallel ocean and sea ice model (POIM) of Zhang and Rothrock [2003], which consists of the Parallel Ocean Program (POP) ocean model [Smith *et al.*, 1992] and the thickness and enthalpy distribution sea ice model [Hibler, 1980; Zhang and Rothrock, 2001]. The model domain covers the northern hemisphere north of 39 °N with 30 vertical levels and a horizontal grid spacing that varies from ~50 km in the North Atlantic to less than 4 km in the northern Bering Sea. The BESTMAS model employs the ETOPO5 bathymetric digital elevation model, and errors in ETOPO5 may contribute to errors in the calculated SSH field, since, for example, just a 5 m offset represents a 20% water depth error at our shallow mooring sites.

4.4 Results

4.4.1 Shelf conditions, July 2008 to July 2010

We begin with a description of temperature, salinity, current, and wind records for the central shelf over the course of the July 2008-July 2010 mooring deployments. Examination of monthly mean conditions reveals three intervals for which seasonal averages are appropriate: January to March (strong winds, extensive ice cover, ice formation and brine expulsion, increasing salinity, little or no thermal stratification, and low river discharge); May to September (light or moderate winds, receding or absent ice cover, increasing or high levels of stratification, river discharge, fresh water content, and

heat content); and October to December (very strong winds, decreasing or low levels of stratification, river discharge, heat content and salinity). May is a transitional month and for some analyses could also have been grouped with January-April.

4.4.2 Temperature and salinity

Temperatures across the array closely follow the annual solar cycle, with surface heat fluxes largely controlling the annual cycle of water temperature changes [Reed and Stabeno, 2002; Danielson *et al.*, 2011]. Ocean temperatures are re-set each winter to the freezing point (~ -1.8 °C) and achieve their maximum values, e.g., ~ 10 °C near 20 m depth, in late summer or early fall. Along the 55 m isobath, late-summer water temperatures show a strongly stratified two-layer system (Figure 4.2) [compare Schumacher and Stabeno, 1998], with a thermocline consistently near 20 m depth through August and September 2008, but a progressively deepening one from June into October 2009. In the fall of both 2008 and 2009, strong wind mixing and surface heat loss homogenized the water column, first at S55 and C55 (in October) and then at N55 (in November). Following fall homogenization, cooling continues, such that by the end of December (N55) and January (C55 and S55) the entire water column is at the freezing point. An ice cover is often observed before temperatures at 10 m depth attain -1.5 °C, indicating that at these locations the presence of ice is due to advection from the north [Pease, 1980]. Temperatures largely remain at the freezing point through April. In four of the six deployments along the 55 m isobath, temperatures at 20 m rose above -1 °C prior to ice retreat, suggesting that ocean heat plays a role in the spring decay of the ice pack, either by advection or by absorbing solar radiation [Jackson, *et al.*, 2010].

In contrast to temperature, the salinity time series depict greater spatial heterogeneity and considerable variability on weekly to monthly timescales (Figure 4.3). Sites N25 and C25 are closest to the coast and least saline over most of the year, with annual salinity minima occurring in fall. The seasonal decline of salinity from late summer to a late fall/early winter annual minimum generally progresses from the shallowest (25 m) to the deepest (55 m) mooring sites. This is consistent with a westward movement of low-salinity coastal waters mixing with ambient shelf waters

offshore [Danielson *et al.*, 2011]. Curiously, waters at mooring C55 remain fresher than waters at either N55 or S55 over extended intervals, e.g. July 2008-April 2009 and January 2010-April 2010, suggesting that the low-salinity signal at C55 is not due to along-isobath advection from the south or the north. Sites N40 and N55, closest to the St. Lawrence Island polynya, were the most saline ($S_{MAX} > 32.5$) during winter 2009, while in winter 2010 the most saline waters were at N40 and N25 ($S_{MAX} > 33$). For parts of each winter (but especially in 2010) the salinity increased proceeding inshore from C55, C40 and C25. This pattern suggests that as the fresher inshore waters were advected away from the coast, they were replaced by higher-salinity waters and/or the shallow coastal waters experienced a greater degree of salinization due to freezing, an effect enhanced over shallow depths and in coastal polynyas.

In both winters, higher salinities occurred at N55, N40, N25 and C25 than at C55, C40, S55 or S40. At these temperatures salinity differences control the horizontal density gradients and the salinity distribution at winter's end implies a mid-shelf salinity minimum. Such a feature would promote an anti-cyclonic geostrophic velocity field with southward flow along its eastern boundary.

4.4.3 Currents and winds

Figures 4.4 and 4.5 show vertically averaged, sub-tidal (35-hr low-pass filtered) time series of the velocity components projected onto their along- and cross-principal axes of variation at each mooring site (this rotation maximizes the velocity variance in the along-axis direction). Positive (nominally northward) peaks in flow speeds have greater magnitude than negative (southward) excursions. Few of the time series exhibit seasonal mean velocity components that are statistically different than zero (Table 4.2) although all sites experience significant net mean flow over many weekly to monthly averaging intervals, such as the mean southward flow extending from March to May at C40 and S40 in 2010, and the mean northward flow at all mooring locations in February 2009. For October-April, typical and maximum 35 hr low-pass filtered current speeds are 6-12 cm s^{-1} and 50-70 cm s^{-1} across the mooring array, respectively. Over the May-September period, these ranges are 3-6 cm s^{-1} and 50-70 cm s^{-1} (Table 4.2).

The velocity time series show that synoptic-scale variability in the flow field is strongly seasonally modulated, with fewer peaks exceeding 25 cm s^{-1} occurring between May and September than in the rest of the year. This is also demonstrated by the fraction of the total kinetic energy accounted for by tides, viz., 61-93% between October and April and 80-97% between May and September (Table 4.2).

Seasonal changes in the flow field are captured with mean monthly principal axis ellipse decompositions (Figure 4.6). At most mooring sites, the fall, winter and early spring ellipses are larger, more elongated and more nearly parallel to the local isobaths than the ellipses of late spring through late summer. At N55, the ellipse amplitudes are much less variable over the course of the year, but the ellipse orientation is more variable.

Analysis of the vertical structure of the sub-tidal horizontal currents reveals that for the 55 m moorings, the mean 5-40 m current shear increases from 0.15 s^{-1} during May-December to 0.21 s^{-1} during January-April, with these means significantly different at the 95% confidence level (assuming a velocity decorrelation time of 48 hours, as noted in Section 4.3.2). In contrast, at the 25 m moorings the 5 – 20 m shear was largest in fall (0.44 s^{-1}), smallest from May-September (0.29 s^{-1}) and intermediate in January-April (0.37 s^{-1}), with all these means significantly different from one another.

Winds, strongest in fall months (Figure 4.7), reflect the evolution, location and strength of storms associated with the Aleutian Low [Wilson and Overland, 1986; Pickart *et al.*, 2009]. The raw (unfiltered) 3-hourly wind record from the NARR grid point closest to site C55 contains 20 wind speed peaks with magnitude $\geq 15 \text{ m s}^{-1}$. Of these, 17 occurred in October, November or December 2008 and 2009; the remaining three were in July and August 2009. Winds are not strongly polarized, and only 57% of the variance is directed along the principal axis. Rotary coherence calculations at all grid points across the shelf with respect to the grid point closest to 60°N , 170°W reveals that coherence-squared values of 0.8 occur within a radius of $\sim 200 \text{ km}$ for long ($\geq 32 \text{ hr}$) periods, but only within $\sim 100 \text{ km}$ for shorter periods (Figure 4.8). Thus, over short time scales the wind field is not uniform across the mooring array, which extends over 3 degrees of latitude and 4 degrees of longitude.

Figure 4.9 summarizes averages of the current meter and wind records for the periods January-April, May-September and October-December. Winds are in the mean northerly during each period, and are strongest in fall and weakest in summer. Along the 55 m isobath, vertically averaged currents are northward, but southward along the 25 m isobath. Mooring C40 vectors are remarkably different from those at the 55 m moorings, but are consistent with the flow field depicted by the N40, N25 and C25 moorings. In fall and winter, the near surface (5 and 10 m) mean currents often exceed 2 cm s^{-1} and are generally oriented 45° to 90° to the right of the wind.

In summary, synoptic variations in the flow field are large with respect to seasonal and annual means, but temperature and salinity fields are dominated by variability on monthly to annual time scales. Seasonal averages of the wind and current fields show that near-surface ($< 10 \text{ m}$) waters flow predominantly westward. Inner shelf currents averaged over the entire water column are directed to the south or to the west during the fall, winter and early spring. Consistent with this, low salinity is observed at the near-shore (shallow) sites in the fall and early winter, and only later in winter at the offshore moorings, at which time the moorings closest to St. Lawrence Island and the Alaskan mainland show water more saline than at the sites offshore and to the south.

The flow field is neither horizontally uniform, nor do the measurements suggest that flow at depth compensates for surface Ekman drift. Consideration both of along-shelf variations in the flow field and of the dynamics of surface and bottom boundary layers are therefore necessary to construct an adequate picture of the circulation field.

4.4.4 *The momentum balance*

We next examine the vertically integrated equations of motion in order to identify the relative importance of the various sources and sinks of momentum. Following *Brink* [1998], we vertically integrate the horizontal momentum balance (1), prescribing the along-shelf direction with (y, V) , positive along the northward-directed principal axis of variation (Figure 4.4), and the cross-shelf direction oriented 90° to the right with (x, U) .

$$\begin{aligned}
U_i - fV &= -\frac{P_x}{\rho_w} + \frac{1}{\rho_w}(\tau_0^x - \tau_B^x) \\
V_i + fU &= -\frac{P_y}{\rho_w} + \frac{1}{\rho_w}(\tau_0^y - \tau_B^y)
\end{aligned}
\tag{1}$$

From left to right in (1), the five terms represent local and Coriolis accelerations, horizontal pressure gradients, and surface and bottom stresses. The parameters include the Coriolis frequency (f) and water depth (h) appropriate for each site and the water density ($\rho_w = 1025.3 \text{ kg m}^{-3}$). The surface and bottom stress terms are computed using

$$\begin{aligned}
\tau_0^x &= \frac{C_d \rho_a}{h} W_u |W|, & \tau_0^y &= \frac{C_d \rho_a}{h} W_v |W| \\
\tau_B^x &= \frac{\rho_w r}{h} U, & \tau_B^y &= \frac{\rho_w r}{h} V
\end{aligned}
\tag{2}$$

where the neutral drag coefficient C_d is computed following *Large and Pond* [1981] and is doubled [*McPhee*, 1980] for intervals when the mooring site is covered with ice (concentration $\geq 30\%$). The linear bottom friction coefficient r is set to 5×10^{-4} after *Lentz and Winant* [1986]; air density (ρ_a) is 1.22 kg m^{-3} ; and the wind velocity vector $W = W_u + iW_v$ uses 3-hourly NARR wind velocities from the grid cell closest to each mooring site. The momentum balance is computed with the raw (unfiltered) time series of velocity and wind speeds. Each term is subsequently low-pass filtered (35 hr cutoff) in order to focus only on the coherent portion of the flow field (as justified below).

Nonlinear advective terms are neglected, because the Rossby number $R_o = U/fL \ll 1$ for characteristic subtidal speed and length scales of 10 cm s^{-1} and 100 km , respectively. The horizontal pressure gradient can not be directly estimated from our data and is therefore determined as the residual in the momentum balance. The approach used here depends on the surface and bottom drag coefficients. Sensitivity analysis shows that a factor of two change in the surface and/or bottom stress drag coefficients alters the magnitude of any season's mean pressure gradient term by typically 5-10% for sites along the 40 m and

55 m isobaths and by 10-30% for sites along the 25 m isobath. Maximum changes for these two depth groupings are 20% and 40%, respectively. Smaller sensitivities are associated with the cross-shelf momentum balances than with the along-shelf balances.

An example of all terms in (1) evaluated at one site (C25), which is representative of the other sites, is shown in Figure 4.10. The balance is primarily geostrophic in both the along-shelf and cross-shelf directions, because only the pressure gradient residual is large enough to balance the Coriolis term. Short intervals during which the other terms are important, or even dominant, include energetic wind events and transitions between positive and negative along-shelf flow, when our assumption of linearity is unlikely to hold. To quantify the relative importance of the terms in (1), we compute the seasonal mean root-mean-square (RMS) magnitude of each term and scale these as a fraction of the combined total at each site (Figure 4.11). For along-shelf currents, the Coriolis term is nearly balanced by the cross-shelf pressure gradient during all seasons, although surface stress can account for up to 20% of the balance. Stronger winds in fall generate surface stresses slightly larger than those of winter, despite enhanced frictional coupling by winter ice. Bottom stress and local accelerations together represent < 10% of the cross-shelf momentum budget, but up to 30% of the along-shelf balance. The contribution from bottom stress terms is proportionally larger (as expected) at the shallow sites, due to the dependence on the total depth. The pressure gradient and Coriolis terms also dominate the along-shelf momentum balance, however the local acceleration, wind stress and bottom friction terms can account for 15-40%, depending on the site and the season. The momentum balance averaged across all mooring sites varies little among seasons despite seasonal changes to the RMS value of the individual terms (Table 4.3). This suggests the importance of the wind in setting up the SSH gradients, regardless of season.

In addition to the water column's barotropic response to SSH gradients, horizontal variations in the thermohaline fields may play a role in forcing the shelf circulation field. We use late winter/spring and late summer/early fall CTD survey data collected between 2006 and 2010 to examine the mean seasonal changes of the dynamic topography, noting that the shallow water depths preclude referencing the computations to a realistic level of

no motion. We measure *in situ* shear with the current meters, but direct comparison to the baroclinic shear is difficult due to overlap between the surface Ekman layer, the bottom Ekman layer and the geostrophic shear.

Between spring and the end of summer, near-shore (shallow) waters warm proportionally more than do mid-shelf waters, and they also freshen due to the seasonal increase in runoff. In addition, the cold, saline sub-pycnocline waters on the middle shelf (including the cold pool) are dense and will therefore tend to stagnate on flat continental shelves [Hill, 1996]. By late summer, the juxtaposition of low-density nearshore waters with the denser cold-pool waters over the mid-shelf will promote a northward baroclinic flow along the eastern side of the cold pool. This hydrographic structure is evident in previous cross-shelf transects as well [Coachman, 1986; Kachel *et al.*, 2002; Danielson *et al.*, 2011]. We therefore average the late summer-early fall BASIS hydrography from 2006-2009 to generate the 0-30 db dynamic topography and associated geostrophic vectors shown in the right-hand panel of Figure 4.12. South of, but near, St. Lawrence Island, the relatively salty and cold waters advected eastward from the Gulf of Anadyr are denser than waters farther south. The resulting pressure gradient corresponds to a geostrophic eastward flow toward Shpanberg Strait, where the current veers northward upon encountering the fresher and warmer waters near the Alaska coast.

In March, April and May, mid- and inner shelf waters are nearly isothermal so that the late winter dynamic topography is determined primarily by salinity. Upon combining CTD profiles from the March to mid-June cruises of 2006-2010, we find a geopotential height minimum south of St. Lawrence Island and along the Alaskan mainland coast and a maximum farther offshore (left-hand panel of Figure 4.12). This reverses the late summer cross-shelf baroclinic pressure gradient so that by the end of winter inner and mid-shelf waters have a southward geostrophic tendency. Similar plots from individual year CTD data are generally consistent with this 5-year climatology. We note that a late winter salinity minimum over the middle southeastern shelf was also observed in an April 1979 cross-isobath transect [Coachman, 1986].

The baroclinic currents computed from these five years of shipboard data indicate that the surface (relative to 30 db) geostrophic vectors are of the same magnitude as the observed vertically averaged seasonal mean flow (Figure 4.9), so that the baroclinic field appears dynamically important. Whereas the northward baroclinic velocity vectors in summer oppose the mean southward (but weak) winds, the southward baroclinic vectors in winter are aligned with the prevailing winds. The late winter-spring and late summer-fall means in Figure 4.12 probably represent the strongest baroclinic pressure gradients, because they include the cumulative effects of cooling and salinization through winter and warming and freshening through summer. Very likely the baroclinic velocity field is therefore smaller in mid-winter and mid-summer.

The total pressure gradient is the sum of the barotropic pressure gradient ($\nabla P_{\text{barotropic}}$) due to wind-forced convergences and divergences and the baroclinic pressure gradient ($\nabla P_{\text{baroclinic}}$). We earlier computed $\nabla P = P_x + iP_y$ as the momentum balance residual. Here, we scale the baroclinic contribution against the other terms in equation (1). From Figure 4.12 and from inspection of the gridded velocity field for each individual cruises, we find that the typical (maximum) 0-30 db geostrophic velocity is about 1 (3) cm s^{-1} and $\nabla P_{\text{baroclinic}}$ is about 1 (3) $\times 10^{-6} \text{ m s}^{-2}$. In late winter and late summer, $\nabla P_{\text{baroclinic}}$ is therefore generally larger than the local accelerations, wind stress, and bottom friction, but 60-90% smaller than the Coriolis term. Comparing these results with the pressure gradient residual in equation (1) implies that $\nabla P_{\text{barotropic}}$ is 2-8 times greater than $\nabla P_{\text{baroclinic}}$. We note also that the SSH field changes rapidly in response to synoptic winds, while the temperature and salinity fields evolve more slowly. Hence, the cross-shelf baroclinic pressure gradient can alternately oppose and reinforce the changing barotropic pressure gradient.

In summary, the momentum balance at all sites is predominantly geostrophic and is a response to sea surface height gradients. Changes in the cross-shelf thermohaline structure, current and wind velocities, and sea ice seasonally modify the cross-shelf momentum balance. In the next section, we examine the vertical and horizontal structure of the current field and its relation to the wind field, and we show that Ekman dynamics

lead to a flow field that is highly sensitive to the wind direction and resultant sea surface topography.

4.4.5 Co-variability of the current, wind and SSH fields

We next examine the temporal and spatial structure of the flow field and their relation to winds. Following this, we use the BESTMAS model to relate wind and current variations to the structure of the SSH field.

Prior evaluations of the wind-current relationship found weak to moderate correlations [*Schumacher et al.*, 1982; *Muench et al.*, 1988; *Danielson et al.*, 2006] over the central shelf, although these estimates were primarily based on time-domain correlations. Here we first examine the rotary coherence structure (frequency domain relations) between near-surface currents and winds across specific portions of the frequency spectrum. All coherence computations are based on non-overlapped windows truncated with a Hanning tapering function. The velocity records used for the coherence computations were de-tided using harmonic analysis applied to month-long segments.

While energetic flows are roughly coincident across the array (Figures 4 and 5), close examination of differences in the phasing and magnitude of currents suggest a flow field that evolves with considerable spatial structure over short time scales and whose relative magnitude and phasing vary among the various energetic flow events. Figure 4.13 shows that at high frequencies (periods < 30 hrs), winds and 5 m depth currents are incoherent across the array. At low frequencies (periods > 100 hr) winds and currents are significantly coherent on average, but with the coherence-squared (γ^2) ~ 0.4 . Inspection of the phase shows that the wind leads the 5 m current by 45-90° for all periods greater than ~ 30 hr. The wind-current coherence peak in Figure 4.13 near 40 hrs is associated with a corresponding maximum in wind energy. Analysis of vertically averaged currents and the wind shows the same frequency dependence as for the 5 m currents, although γ^2 in the low-frequency band is smaller (~ 0.3).

Based on Figure 4.13, we divide the velocity time series into three frequency bands and use vertically averaged currents to compute γ^2 between each mooring pair,

shown in Figure 4.14 as a function of separation distance. The high frequency band (13-22 hr) was formed by band-pass filtering the velocity records after subjecting them to harmonic de-tiding of month-long segments. This band contains the inertial (13.8 hr at 60°N) and near-inertial periods. The mid-frequency band spans periods of 32 - 102 hr and the low-frequency band 128-512 hr.

The high-frequency portion of the spectrum has low coherence ($\gamma^2 < 0.4$) (with a slight linear dependency on separation), and most correlations are not significant at the 95% level. The mid-frequency band shows that $0.4 < \gamma^2 < 0.65$ at sites within 100 km of each other and these are all significant. Moreover, most sites within 200 km of each other are also coherent, but only weakly so. The low frequency band is coherent for nearly all mooring combinations; values range from $0.6 < \gamma^2 < 0.8$ at 50-100 km separation to $\gamma^2 < 0.5$ at separations > 250 km. With an average separation distance of ~ 85 km between adjacent moorings, the mooring array therefore resolves a large portion of the flow field at synoptic to fortnightly time periods.

We next examine the vertical structure of current co-variability in the mid-frequency portion of the spectrum. At the shallow (25 m) sites the currents are coherent over the entire water column, although there is some seasonal variation (Figure 4.15). Over the 40 and 55 m isobaths, the currents are vertically coherent between 5 m and 30 m depth ($\gamma^2 > 0.6$) during fall, winter and early spring, coincident with weak stratification and strong winds (see Figures 4.2 and 4.9). Coherence decreases ($\gamma^2 < 0.6$) between mid-spring and late summer below 20 m depth, consistent with Figure 4.2 and other observations that find the upper mixed layer is typically between 15 and 30 m depth [e.g., *Ladd and Stabenon*, 2012]. Slight differences in coherence between the fall and winter are statistically insignificant, but suggestive of the influence of ice cover.

We now turn to the SSH field. Pressure measurements made at seven of the eight mooring sites were de-tided with a 35-hr low-pass filter, and converted to equivalent SSH fluctuations (Figure 4.16). Variations from the record-length means greater than 0.5 m occur most often in fall, winter, and spring. The largest SSH excursions are at the 25 m sites, where storm surges of ~ 1 m are seen in December 2009. Record-length cross-

correlations between the BESTMAS model and observed SSH fields show that the model captures from 31% (at N55) to 61% (at N40) of the observed variability (Figure 4.16). With the exception of site N40, correlations between the observed and modeled SSH fields are stronger between October and May than during June-September (Table 4.4). The Rossby deformation radius $R_{bt} = (gH)^{1/2} f^{-1}$ varies from 120 km for water 25 m deep to 160 km for 40 m depths and 180 km for 55 m. For comparison, N25 (N40, N55) is ~ 70 km (170 km, 300 km) due west of the Alaskan mainland. The BESTMAS model and the above scaling indicates that mooring N55 was in a region with relatively small horizontal SSH gradients, so the lower levels of correlation here are not surprising.

The time of maximum correlation (r) between the wind and observed pressure fluctuations varies slightly with water depth, so that at the 25 m and 40 m sites the SSH tends to lag the winds by 0-8 hr, with $0.2 < r^2 < 0.5$, while at the deeper sites $r^2 < 0.3$ and the maximum correlation occurs with a lag of up to 20 hrs.

Table 4.3 and Figure 4.11 shows that the overall momentum balance is not strongly seasonally variable. Therefore, based on the direction of the mean regional wind vector (formed by equally weighting the NARR wind time series from all eight mooring sites), we made record-length averages of the mean wind vector, the BESTMAS SSH field, and the moored current measurements (Figure 4.17). Because the model output is daily, and because of the lagged wind-SSH relation, we made 24-hour averages of the wind vector preceding each current measurement to determine the wind direction bins used in assembling the panels of Figure 4.17.

Changes in wind velocity impact currents through SSH gradients (Figure 4.17). The near-surface (5 m and 10 m depths, red and yellow vectors) flow field is typically aligned to the right of the wind field, consistent with surface Ekman dynamics. Deeper in the water column, the current vectors generally rotate in a counter-clockwise direction, indicating the influence of the bottom Ekman layer. Two panels (wind toward 225 °T and 270 °T) show primarily clockwise rotation with depth, however. In this case the winds are directed off-shelf and the 5 m currents are directed nearly 90° to the right of the wind. We also note that currents at depth are more closely aligned along the model-

derived SSH contours than are those near the surface. In aggregate, these observations are consistent with the flow field being in near-geostrophic balance and responding strongly to the interaction of the wind-driven Ekman flow with the convoluted Bering Sea coastline.

The structure of the SSH field and its associated currents is highly sensitive to the wind direction. Northerly and northwesterly winds generate the strongest coastal divergence (depressed SSHs over Chirikov Basin, Norton Sound and the central shelf), but the cross-isobath SSH gradient weakens considerably where the local coastline changes from a predominantly north-south orientation (between Norton Sound and Nunivak Island) to a more west-east orientation (in Kuskokwim Bay and Bristol Bay). The shelf response switches rather abruptly from divergent (northerly winds) to convergent (easterly winds) conditions.

We note that the shelfbreak and outer shelf isobath orientations are well represented by a line extending from the northwest to the southeast and because the shelf flow field adjusts to northerly and easterly winds as described, we segregate all records into two modes based on the wind direction. The coastal convergent (i.e., downwelling) mode is associated with southeasterly winds and results in along-isobath currents directed toward Bering Strait. The coastal divergent (i.e., upwelling) mode is associated with northwesterly winds and results in currents directed away from Bering Strait. Divergent conditions occurred 64% of the time over the course of our field program; convergent conditions occurred the remaining 36% of the time. Southeasterly wind, though less frequent during our period of observations, leads to stronger currents than northwesterly wind. The net effect of these competing circulation modes yields the highly variable but small mean currents that characterize the flow field of the eastern Bering shelf.

4.5 Discussion

We have shown that currents over the central shelf are coherent over scales of ~200 km for most sub-inertial and sub-tidal frequencies and are moderately (but significantly) coherent with the local winds. Vertical coherence of the flow field is reduced during late spring and summer, coincident with reduced mean wind speeds and

increased ocean stratification. Variations in SSH and the underlying current field are sensitive to the direction of wind forcing through the upwelling and downwelling responses of the Ekman transport, and the transition from upwelling to downwelling conditions occurs for winds directed approximately to the southwest.

Our analysis suggests that the entire central Bering shelf circulation responds strongly to coastal convergence and divergence. Convergence is associated with enhanced northward flow resulting from coastal sea surface setup caused by on-shore Ekman transport driven by southeasterly winds. Coastal divergence results from off-shore Ekman transport driven by northwesterly winds. In general, southeasterly winds result in stronger flows, but northwesterly winds occur more often. Note that our observations were made during two relatively cold years [Stabeno, *et al.*, 2012]. We expect that warmer years will likely show a greater proportion of downwelling. The more energetic convergent response may be due to the propagation direction of storms across the shelf. Cyclones typically approach the shelf from the southwest and so first impart northward momentum with their leading edge of southeasterly winds; the trailing edge (northwesterly winds) must first decelerate the northward flow before reversing the current direction. Not all high wind events, however, are associated with propagating low-pressure systems.

Our synthesis of shelf behavior in fall and winter is consistent with the findings of Danielson *et al.* [2011], who used CTD survey data from the BASIS program to show that the freshwater content over the shelf is correlated with the October-May wind direction anomaly. Southward winds promote offshore spreading of low-salinity coastal waters, whereas westward winds promote northward along-shelf transport and presumably prevent offshore spreading of fresh water.

We have also shown that the baroclinic pressure field reverses direction, from promoting southward flow in late winter to promoting northward flow in late summer. Because effects of heating and freezing are enhanced in shallow waters, warm summers increase the magnitude of the cross-shelf density difference and thus enhance northward transport, and cold winters with increased ice production and brine rejection also

increased the magnitude of the (now reversed) cross-shelf density difference and enhance southward transport. Conversely, milder summers or winters lead to smaller cross-slope density differences, and thus weaker flow, and the greater preponderance of southeasterly winds will inhibit the offshore transport of dilute coastal waters. Thus, the baroclinic pressure gradients respond to the atmosphere's influence on both freezing and advective processes. (As a cautionary note, some atmospheric circulation patterns can result in warm Gulf of Alaska air being recirculated southward over the Bering Sea [Rodionov *et al.*, 2007], so that winds from the north are not always associated with enhanced ice production and brine rejection.) Although the baroclinic velocity is large enough to influence seasonal transports, it is not as important as the effect of the wind-driven convergences and divergences in setting up the shelf pressure field.

Transport through Bering Strait increases in summer due to larger horizontal density gradients and a reduction in southward winds [Roach *et al.*, 1995; Woodgate *et al.*, 2005a; 2005b]. Surprisingly, the mean summer flow we observe over the shelf is not uniformly northward over the inner shelf, despite a cross-isobath baroclinic pressure gradient that promotes northward flow in summer. This suggests that much of the increased summer flow through Bering Strait comes from the Gulf of Anadyr, either directly through Anadyr Strait or from the eastward transport on the southern side of St. Lawrence Island, and/or from Alaskan Coastal Current waters inshore of our mooring array. Intriguingly, the BESTMAS model SSH field averaged over May-September, shows that a large majority of the SSH contours in the Gulf of Anadyr pass through Anadyr Strait, with only a small fraction directed eastward south of St. Lawrence Island before turning north in Shpanberg Strait. During October-April all the SSH contours pass directly through Anadyr Strait. Taken together, these findings suggest that waters from the central Bering shelf contributed relatively little to the Bering Strait through-flow over the course of our field years, with the possible exception of summer waters immediately adjacent to the Alaskan coast, inshore of our moorings.

Based on our observations reported here, together with those of Schumacher *et al.* [1983] and Danielson *et al.*, [2006], we propose that waters originating in the Gulf of

Anadyr are a source of nutrient-rich waters to the central Bering shelf, particularly in winter. Indeed, the BESTMAS model SSH contours are consistent with our observations suggesting an advective pathway that extends eastward from the Gulf of Anadyr, passing south of St. Lawrence Island, and is then south- or southeastward toward Nunivak Island. This linkage occurs under northwesterly winds and is consonant with the mean October-April and May-September SSH fields (not shown). The model results of *Clement et al.* [2005] also show a southward flow tendency across the central shelf region in 1979, a year that their model indicated reduced northward transport through Bering Strait. Similarly, based on a two-month reversal of currents in Shpanberg Strait, *Muench et al.* [1988] schematically suggested a pathway for Chirikov Basin water (primarily of Anadyr origin) moving eastward north of St. Lawrence Island, and then southward through Shpanberg Strait. These various lines of evidence have important implications for biological production, since they suggest that the rich nutrient load in the Gulf of Anadyr can be brought onto the central shelf region at least as far south as Nunivak Island under sustained southeastward flow (e.g., a month-long mean speed of 10 cm s^{-1}). Indeed, this nutrient pathway may at least in part explain the recent observation of elevated net community production over the central shelf [*Mathis et al.*, 2010].

We further suggest that inter-annual variations in biological production over the central shelf may be linked to the long-term variability of the wind-driven southeastward circulation mode that we have described. We expect that winters with more northwesterly winds will increase the central shelf nutrient reservoir leading into spring and summer, while the fresh and nutrient-depleted coastal waters that normally reside over the central shelf will be carried south of Nunivak Island and farther offshore. Conversely, winters with more southeasterly winds will flush central shelf waters northward, some fraction possibly through Bering Strait, and increase on-shelf nutrient fluxes over the southern Bering shelf. Inter-annual variation in the preponderance and strength of northwesterly and southeasterly winds will therefore result in a variable supply of nutrients to large portions of the shelf, and possibly northward through Bering

Strait. These ideas can be tested with the data sets recently collected as part of the BEST-BSIERP program, along with analysis of new and existing numerical model integrations.

The central shelf circulation alternates between the two described modes, resulting in a flow that is small in the mean but highly variable both spatially and temporally. Within this variable regime, we estimate residence time for the central shelf as follows. The distance from each mooring to its closest neighbor is 61-142 km, with a mean of 85 km. To cover these distances in one month would require a flow of 2.3-5.5 cm s^{-1} . Given that flows are largely coherent at low frequencies and within 200 km of each other (Figure 4.14), we assume a uniform flow field and integrate the raw velocity record at each mooring with respect to time. By progressively shifting the integration start by one observation time step (30 minutes) through the velocity record, we compute the minimum time it would take a particle at 5 m depth to move 50 and 100 km from its initial position. We find that the probability distribution function is log-normal, with modal peaks centered near 6 and 12 days for the minimum time required to displace a particle in the upper water column 50 and 100 km, respectively. The durations lengthen to 14 and 34 days for currents at 30 m depth. For comparison, mean monthly vertically averaged velocities suggest typical monthly displacements of 30-90 km and maximum displacements of ~230 km. Taken together, these estimates suggest a mean residence time of many months, but two or three successive months of anomalous flow could largely flush the central shelf.

It is unclear what changes over the central shelf mean for the northward transport through Bering Strait. Although winds over the central shelf are not coherent with those over Chirikov Basin, Bering Strait and the southern Chukchi Sea (Figure 4.8), the model results show that northwesterly and southeasterly winds over the mooring array are associated with SSH anomalies that extend to Chirikov Basin and Norton Sound (Figure 4.17).

Our results also suggest that some fraction of the Yukon River discharge may be advected westward across the central shelf under the southeastward circulation mode, first being brought southward past Nunivak Island and then westward with the offshore

flow. Direct evidence is sparse, but tantalizing. Most notably, three of fifteen satellite-tracked drifters deployed near Nunivak Island in September 2002 headed west past Cape Navarin under the influence of generally northerly winds (*Danielson et al.* [2006]; also see <http://www.ims.uaf.edu/drifters/>). More generally, the central Bering shelf may constitute a branch point between subarctic and arctic domains, with freshwater, heat, larvae, or contaminants on the inner shelf being transported either westward toward the deep basin or northward toward the Arctic, depending on the wind-driven circulation.

The circulation of the central shelf may also play a role in the life history of upper trophic level organisms. For example, using data that extend back to 1961, *Mundy and Evenson* [2011] found that sea surface temperatures, air temperatures, and ice cover are predictors of the upriver migration timing of adult Yukon River Chinook salmon. All three environmental variables are linked to the heat budget and the circulation modes we have described, and so our results likely also bear on migration phenology.

Finally, retrospective analysis shows that the mean wind direction over the Bering shelf has changed in concert with recent climate and ecosystem regime shifts. One major change occurred during the mid 1970s North Pacific regime shift, coincident with a transition from more upwelling-favorable conditions to more downwelling-favorable [*Danielson et al.*, 2011]. Forecasts from global climate models suggest that climate warming may slightly deepen the Aleutian low and move it ~ 100 km northward within a few decades [*Salathé*, 2006]. Over the eastern Bering shelf, monthly mean sea level pressure (SLP) contours show little variability over 100 km scales, and so we would not expect a large change in wind direction over most of a year. September and October may be somewhat more sensitive to changes in the Aleutian low position, however, because the mean monthly isobars are oriented from NE to SW over the central shelf [*Pickart et al.*, 2009] and from NW to SE over the outer southeastern shelf. For these months, a northward shift of the low would subject more of the eastern shelf to upwelling winds and increase the eastward flux of nutrients from the Gulf of Anadyr. Additional insights on this issue might be achieved from climate projection models by focusing on seasonally dependent changes in the position of the Aleutian low.

4.6 Conclusions

We have analyzed the data from an array of eight current meter moorings distributed over the central Bering Sea shelf between the 25 and 55-m isobaths, between 58.6 °N and 62 °N. We find that the along-shore currents are primarily geostrophic and vary in response to the wind-forced sea level gradients associated with surface Ekman convergences and divergences. Cross-shore currents are also predominantly geostrophic, although surface stresses, bottom stresses, and local accelerations account up for up to 40% of the momentum balance, depending on season and location. Shelf waters near the mooring array alternately flow northward (under southeasterly winds) and southward (under northwesterly winds) in response to the winds and the sea level gradients they force, resulting in typical sub-tidal speeds of 3-12 cm s⁻¹, peak speeds of 65 cm s⁻¹, and vector means < 5 cm s⁻¹.

Steric height gradients vary seasonally and promote northward flow in late summer and southward flow in late winter. However, the baroclinic pressure field is of secondary importance in the momentum balance compared to the wind-forced barotropic pressure field, and baroclinic forcing is likely muted following warmer winters and cooler summers.

The two circulation modes associated with coastal convergence and divergence probably play a significant role in the freshwater, heat, and nutrient budgets of the central shelf. In particular, we suggest that waters from the Gulf of Anadyr (advected either eastward along the south side of St. Lawrence Island or southward from the Chirikov Basin) can provide inorganic nitrogen to the central shelf at least as far south as Nunivak Island. Wind direction controls the ocean circulation modes, and the transition between southward and northward currents occurs between winds directed southward and westward. One or two months of strongly anomalous flow conditions may be sufficient to replace large portions of the central shelf with nitrate-rich waters from the northwest.

We observed northwesterly winds nearly twice as often as southeasterly winds, but this is probably not representative of all years. Extended re-orientation of the mean wind direction would likely result in systematic changes to the circulation and a shelf-

wide reorganization of many physical, chemical and biological fluxes that impact regional heat and freshwater content, nutrient stocks, and primary production.

4.7 Acknowledgments

We thank the many scientists and ships crews involved in the BEST, BSIERP and BASIS programs for help with mooring deployments, recoveries, and CTD and hydrographic sampling and processing. We thank L. Eisner for the BASIS program CTD data and Jackie Grebmeier and Lee Cooper for spring CTD data collected during and before the BEST program years. The network of moored observations described here is a partnership between the University of Alaska Fairbank (UAF) and the University of Washington (UW). We thank D. Leech and J. Johnson for masterminding the moorings. S. Danielson and T. Weingartner received support from NSF Grant ARC-0732771, K. Aagaard from NSF Grant ARC-0732428, and J. Zhang and R. Woodgate from NSF Grant ARC-0611967.

4.8 References:

- Aagaard, K. A. T. Roach, and J. D. Schumacher, 1985. On the wind-driven variability of the flow through Bering Strait, *J. Geophys. Res.*, 90, 7213-7221.
- Aagaard, K., and E. Carmack, 1989. The role of sea-ice and other fresh water in the Arctic circulation, *J. Geophys. Res.*, 94, 14,485–14,498, doi:10.1029/ 89JC01375.
- Aagaard, K., T. J. Weingartner, S. L. Danielson, R. A. Woodgate, G. C. Johnson, and T. E. Whitlege, 2006. Some controls on flow and salinity in Bering Strait, *Geophys. Res. Lett.*, 33, L19602, doi:10.1029/2006GL026612.
- Allen, J. S., and P. K. Kundu, 1978. On the momentum, vorticity and mass balance on the Oregon Shelf, *J. Phys. Oceanogr.*, 8, 13-27.
- Bering Ecosystem Study and Bering Sea Integrated Ecosystem Research Project (BEST-BSIERP) Program Summary, 2010, North Pacific Research Board, Anchorage, AK. http://doc.nprb.org/web/BSIERP/zzWebsite/proj_mgmt/01.10_bsag_web.pdf.
- Bond, N. A., J. E. Overland, and P. Turet, 1994. Spatial and temporal characteristics of the wind forcing of the Bering Sea, *J. Climate*, 7(7), 1119-1130.

- Brabets, T. P., B. Wang, and R. H. Meade, 2000. Environmental and Hydrologic Overview of the Yukon River Basin, Alaska and Canada, *U.S.G.S. Water Res. Inves. Report, 99-4204*, Anchorage, AK.
- Brink, K. H., 1998. Wind-driven currents over the continental shelf, in *The Sea, the Global Coastal Ocean*, vol. 10, edited by K. H. Brink and A. R. Robinson, pp. 3-20, Wiley, New York, NY.
- Brower, W. A., Jr., R. G. Baldwin, C. N. Williams Jr., J. L. Wise, and L. D. Leslie, (Eds.), 1988. *Climate Atlas of the Outer Continental Shelf Waters and Coastal Regions of Alaska*, vol. 2, Bering Sea, Natl. Clim. Data Cent., Asheville, NC.
- Cherniawsky, J. Y., W. R. Crawford, O. P. Nikitin, and E. C. Carmack, 2005. Bering Strait transports from satellite altimetry, *J. Mar. Res.*, 63, 5, 887-900.
- Clement, J. L., W. Maslowski, L. W. Cooper, J. M. Grebmeier, and W. Walczowski, 2005. Ocean circulation and exchanges through the northern Bering Sea: 1979-2001, *Deep Sea Res. II*, 52, 3509-3540, doi:10.1016/j.dsr2.2005.09.010.
- Coachman, L. K., 1986. Circulation, water masses, and fluxes on the southeastern Bering Sea shelf, *Cont. Shelf Res.*, 5, 23-108.
- Coachman, L. K., K. Aagaard, and R. B. Tripp, 1975. *Bering Strait: The Regional Physical Oceanography*, Univ. of Wash. Press, Seattle, WA.
- Coachman, L. K., and K. Aagaard, 1988. Transports through Bering Strait: annual and interannual variability, *J. Geophys. Res.*, 93(C12), 15,535-15,539, doi:10.1029/JC093iC12p15535.
- Coachman, L.K., 1993. On the flow field in the Chirikov Basin, *Cont. Shelf Res.*, 13, 481-508.
- Danielson, S., and Z. Kowalik, 2005. Tidal currents in the St. Lawrence Island region, *J. Geophys. Res.*, 110, C10004, doi:10.1029/2004JC002463.
- Danielson, S., K. Aagaard, T. Weingartner, S. Martin, P. Winsor, G. Gawarkiewicz, and D. Quadfasel, 2006. The St. Lawrence polynya and the Bering shelf circulation: New observations that test the models, *J. Geophys. Res.*, J111, C09023, doi:10.1029/2005JC003268.
- Danielson, S., L. Eisner, T. Weingartner, and K. Aagaard, 2011. Thermal and haline variability over the central Bering Sea shelf: Seasonal and inter-annual perspectives, *Cont. Shelf Res.*, doi:10.1016/j.csr.2010.12.010.

- Drucker, R., S. Martin, and R. Moritz, 2003. Observations of ice thickness and frazil ice in the St. Lawrence Island polynya from satellite imagery, upward looking sonar, and salinity/temperature moorings, *J. Geophys. Res.*, 108(C5), 3149, doi:10.1029/2001JC001213.
- Emory, W. J., and R. E. Thompson, 2001. *Data analysis methods in physical oceanography, Second and Revised Edition*, Elsevier Inc., San Diego, CA.
- Favorite, F., 1974. Flow into the Bering Sea through Aleutian island passes, in *Oceanography of the Bering Sea*, edited by D.W. Hood and E. J. Kelley, Occ. Public. No. 2, Inst. Mar. Sci., University of Alaska, Fairbanks, Fairbanks, AK.
- Foreman, M. G. G., 1978. Manual for tidal currents analysis and prediction. *Pac. Mar. Sci. Rep.* 78-6, Institute of Ocean Sciences, Patricia Bay, Sidney, BC, 57 pp.
- Gill, A. E., 1982. *Atmosphere–Ocean Dynamics*, Academic Press, San Diego, CA.
- Hibler, W. D. III, 1980. Modeling a variable thickness sea ice cover, *Mon. Wea. Rev.*, 108, 1943–1973.
- Hill, A. E., 1996. Spin-down and the dynamics of dense pool gyres in shallow seas, *J. Mar. Res.*, 54, 471-486.
- Jackson, J. M., E. C. Carmack, F. A. McLaughlin, S. E. Allen, and R. G. Ingram, 2010. Identification, characterization, and change of the near-surface temperature maximum in the Canada Basin, 1993-2008, *J. Geophys. Res.*, 115, C05021, doi:10.1029/2009JC005265.
- Johnson, G. C., P. J. Stabeno, and S. C. Riser, 2004. The Bering Slope Current system revisited, *J. Phys. Oceanogr.*, 34, 384–398.
- Kachel, N. B., G. L. Hunt Jr., S. A. Salo, J. D. Schumacher, P. J. Stabeno, and T. E. Whitledge, 2002. Characteristics and variability of the inner front of the southeastern Bering Sea, *Deep-Sea Res. II* 49, 5889-5909.
- Kalnay E., M. Kanamitsu, R. Kistler, W. Collins, D. Deaven, L. Gandin, M. Iredell, S. Saha, G. White, J. Woollen, Y. Zhu, M. Chelliah, W. Ebsuzaki, W. Higgins, J. Janowiak, K. C. Mo, C. Ropelewski, J. Wang, A. Leetma, R. Reynolds, R. Jenne, and D. Joseph, 1996. The NCEP/NCAR 40-year reanalysis project, *Bull. Am. Meteorolog. Soc.*, 77, 437-470.

- Kinder, T. H., and J. D. Schumacher, 1981. Hydrographic structure over the continental shelf of the southeastern Bering Sea, in *The Eastern Bering Sea Shelf, Oceanography and Resources*, vol. 1., edited by D. W. Hood and J. A. Calder. pp. 31-52, Univ. of Wash. Press, Seattle, WA.
- Kinder, T.J., D. C. Chapman, and J. A. Whitehead, 1986. Westward intensification of the mean circulation on the Bering Sea shelf, *J. Phys. Oceanogr.*, 16, 1217-1229.
- Kowalik, Z., 1999. Bering Sea Tides, in *Dynamics of The Bering Sea: A Summary of Physical, Chemical and Biological Characteristics, and a Synopsis of Research on the Bering Sea*, edited by T. R. Loughlin and K. Ohtani, pp. 93-127, University of Alaska Sea Grant, Fairbanks, AK.
- Ladd, C., and N. Bond, 2002. Evaluation of the NCEP/NCAR reanalysis in the NE Pacific and the Bering Sea, *J. Geophys. Res.* 107 (C10), doi:10.1029/2001JC001157.
- Ladd, C., and P. J. Stabeno, 2012. Stratification on the Eastern Bering Sea Shelf, Revisited, *Deep-Sea Res. II*, <http://dx.doi.org/10.1016/j.dsr2.2012.02.009>.
- Large, W. G., and S. Pond, 1981. Open ocean momentum flux measurements in moderate to strong winds, *J. Phys. Oceanogr.*, 11, 324-336.
- Lentz, S. J., and C. D. Winant, 1986. Subinertial currents on the southern California shelf, *J. Phys. Oceanogr.*, 16, 1737-1750.
- Mathis, J. T., J. N. Cross, N. R. Bates, S. B. Moran, M. W. Lomas, P. J. Stabeno, and C. W. Mordy, 2010. Seasonal distribution of dissolved inorganic carbon and net community production on the Bering Sea shelf, *Biogeosci.*, 7, 1769-1787.
- McNutt, L., 1981. Ice conditions in the Eastern Bering Sea from NOAA and LANDSAT imagery: winter conditions 1974, 1976, 1977, 1979, *NOAA Tech. Memo. ERL PMEL-24*, NOAA Env. Res. Lab., Boulder, CO.
- McPhee, M. G., 1980. An analysis of pack ice drift in summer, in *Sea Ice Processes and Models*, edited by R. S. Pritchard, pp 62-75, Univ. of Wash. Press, Seattle, WA.
- Mesinger, F., and 19 Coauthors, 2006. North American regional re-analysis, *Bull. Amer. Meteor. Soc.*, 87, 343-360.
- Mofjeld, H. O., 1984. Recent observations of tides and tidal currents from the northeastern Bering Sea shelf, *NOAA Tech. Memo. ERL PMEL-57*, NOAA Pac. Mar. Env. Lab., Seattle, WA.

- Muench, R. D., and K. Ahlnas, 1976. Ice movement and distribution in the Bering Sea from March to June 1974, *J. Geophys. Res.*, 81, 24, 4467-4476.
- Muench, R. D., J. D. Schumacher, and S. A. Salo, 1988. Winter currents and hydrographic conditions on the northern central Bering Sea shelf, *J. Geophys. Res.*, 93(C1), 516–526, doi:10.1029/JC093iC01p00516.
- Mull, J. M., 2008. QuikSCAT measurements of the wind field over the Bering and Chukchi Seas, M. S. thesis, University of Alaska Fairbanks, Fairbanks, AK.
- Mundy, P. R., and D. F. Evenson, 2011. Environmental controls of phenology of high-latitude Chinook salmon populations of the Yukon River, North America, with application to fishery management, *J. Mar. Sci.*, 68, 1155-1164.
- Niebauer, H. J., N. A. Bond, L. P. Yakunin, and V. V. Plotnikov, 1999. An update on the climatology and sea ice of the Bering Sea, in *Dynamics of The Bering Sea: A Summary of Physical, Chemical and Biological Characteristics, and a Synopsis of Research on the Bering Sea*, edited by T. R. Loughlin and K. Ohtani, pp. 29-59, Univ. of Alaska Sea Grant, Fairbanks, AK.
- Orensanz, J., B. Ernst, D. Armstrong, P. Stabeno, and P. Livingston, 2004. Contraction of the geographic range of distribution of snow crab (*Chionoecetes opilio*) in the eastern Bering Sea: an environmental ratchet?, *CalCOFI Reports*, 45, 65–79.
- Overland, J. E., and C. H. Pease, 1982. Cyclone climatology of the Bering Sea and its relation to sea ice extent, *Mon. Wea. Rev.*, 110, 5-13.
- Overland, J. E., and A. T. Roach, 1987. Northward flow in the Bering and Chukchi seas, *J. Geophys. Res.*, 92, 7097-7105.
- Overland, J. E., M. C. Spillane, H. Y. Hurlburt, and A. J. Wallcraft, 1994. A numerical study of the circulation of the Bering Sea basin and exchange with the north Pacific Ocean, *J. Phys. Oceanogr.*, 24, 736-758, doi:10.1175/1520-0485.
- Pawlowicz, R., B. Beardsley, and S. Lentz, 2002. Classical tidal harmonic analysis including error estimates in MATLAB using T_TIDE, *Comput. Geosci.*, 28, 929-937.
- Pearson, C. A., H. O. Mofjeld, and R. B. Tripp, 1981. Tides of the Eastern Bering Sea shelf, in *The Eastern Bering Sea Shelf, Oceanography and Resources*, vol. 1., edited by D. W. Hood, and J. A. Calder, J.A., pp. 111-130, Univ. of Wash. Press, Seattle, WA.
- Pease, C. H., 1980. Eastern Bering Sea ice processes, *Mon. Wea. Rev.*, 108, 2015-2023.

- Pease, C. H., 1981. Eastern Bering Sea ice dynamics and thermodynamics, in *The Eastern Bering Sea Shelf, Oceanography and Resources*, vol. 1., edited by D. W. Hood and J. A. Calder, pp. 213-222, Univ. of Wash. Press, Seattle, WA.
- Pickart, R. S., G. W. K. Moore, A. M. Macdonald, I. A. Renfrew, J. E. Walsh, and W. S. Kessler, 2009. Seasonal evolution of Aleutian low-pressure systems: Implications for the North Pacific sub-polar circulation, *J. Phys. Oceanogr.*, 39, 1316-1339, doi:10.1175/2008JPO3891.1.
- Reed, R. K., and P. J. Stabeno, 2002. Surface heat fluxes and subsurface heat content at a site over the southeastern Bering Sea shelf, May–June 1996, *Deep-Sea Res. II*, 49, 5911-5917.
- Reynolds, R. W., and T. M. Smith, 1994. Improved global sea surface temperature analyses using optimum interpolation, *J. Climate*, 7, 929-948.
- Reynolds, R. W., N. A. Rayner, T. M. Smith, D. C. Stokes, and W. Wang, 2002. An improved in situ and satellite SST analysis for climate, *J. Climate*, 15, 1609-1625.
- Roach, A. T., K. Aagaard, C. H. Pease, S. A. Salo, T. Weingartner, V. Pavlov, and M. Kulakov, 1995. Direct measurements of transport and water properties through Bering Strait, *J. Geophys. Res.*, 100, 18,443-18,457.
- Roden, G. I., 1995. Aleutian Basin of the Bering Sea: Thermohaline, oxygen, nutrient, and current structure in July 1993, *J. Geophys. Res.*, 100(C7), 13,539-13,554.
- Rodionov, S. N., N. A. Bond, and J. E. Overland, 2007. The Aleutian low, storm tracks, and winter climate variability in the Bering Sea, *Deep-Sea Res. II*, 54(23–26), 2560-2577.
- Royer, T. C., and W. J. Emery, 1984. Circulation in the Bering Sea, 1982-83, based on satellite-tracked drifter observations, *J. Phys. Oceanogr.*, 14, 1914-1920.
- Salathé, E. P., Jr., 2006. Influences of a shift in North Pacific storm tracks on western North American precipitation under global warming, *Geophys. Res. Lett.*, 33, L19820, doi:10.1029/2006GL026882.
- Sambrotto, R.N., H.J. Niebauer, J.J. Goering, and R.L. Iverson, 1986. Relationships among vertical mixing, nitrate uptake and phytoplankton growth during the spring bloom in the southeast Bering Sea middle shelf, *Cont. Shelf Res.*, 5, 161–198.
- Schumacher, J. D., and T. H. Kinder, 1983. Low-frequency current regimes over the Bering Sea shelf, *J. Phys. Oceanogr.*, 13, 607–623.

- Schumacher, J., K. Aagaard, C. Pease, and R. Tripp, 1983. Effects of a shelf polynya on flow and water properties in the northern Bering Sea, *J. Geophys. Res.*, 88(C5), 2723-2732.
- Schumacher, J. D., C. A. Pearson, and J. E. Overland, 1982. On exchange of water between the Gulf of Alaska and the Bering Sea through Unimak Pass, *J. Geophys. Res.*, 87, 5785-5795.
- Schumacher, J. D., and R. K. Reed, 1992. Characteristics of currents over the continental slope of the eastern Bering Sea, *J. Geophys. Res.*, 97(C6) 9,423-9,433.
- Schumacher, J. D., and P.J. Stabeno, 1998. Continental shelf of the Bering Sea coastal segment, in *The Sea, the Global Coastal Ocean*, vol. 11, edited by A. R. Robinson and K. H. Brink, pp. 789-822, Wiley, New York, NY.
- Smith, R. D., J. K. Dukowicz, and R. C. Malone, 1992: Parallel ocean general circulation modeling, *Physica D*, 60, 38-61.
- Spaulding, M., T. Isaji, D. Mendelsohn, and A. C. Turner, 1987. Numerical simulation of wind-driven flow through the Bering Strait, *J. Phys. Oceanogr.*, 17, 1799-1816.
- Stabeno, P. J., N. A. Bond, N. B. Kachel, S. A. Salo, and J. D. Schumacher, 2001. On the temporal variability of the physical environment over the southeastern Bering Sea, *Fish. Oceanogr.*, 10 (1), 81-98.
- Stabeno, P. J., N. B. Kachel, M. Sullivan, and T. E. Whitledge, 2002a. Variability of physical and chemical characteristics along the 70-m isobath of the southeast Bering Sea, *Deep-Sea Res. II*, 49 (26), 5931-5943.
- Stabeno, P. J., R. K. Reed, and J. M. Napp, 2002b. Transport through Unimak Pass, Alaska, *Deep-Sea Res. II*, 49 (26), 5919-5930.
- Stabeno, P. J., C. Ladd, and R. K. Reed, 2009. Observations of the Aleutian north slope current, Bering Sea 1996-2001, *J. Geophys. Res.*, 114, C05015, doi:10.1029/2007JC004705.
- Stabeno, P. J., J. M. Napp, C. W. Mordy, and T. E. Whitledge, 2010. Factors influencing physical structure and lower trophic levels of the eastern Bering Sea shelf in 2005: Sea ice, tides and winds, *Prog. Oceanogr.* 85, 180-196, <http://dx.doi.org/10.1016/j.pocean.2010.02.010>.
- Stabeno, P., N. Kachel, S. Moore, J. Napp, M. Sigler, A. Yamaguchi, and A. Zerbini, 2012, Comparison of warm and cold years on the southeastern Bering Sea shelf, *Deep-Sea Res. II*, <http://dx.doi.org/10.1016/j.dsr2.2012.02.020>.

- Stigebrandt, A., 1984. The North Pacific: A global-scale estuary, *J. Phys. Oceanogr.*, 14, 464-470.
- Takenouti, A.Y., and K. Ohtani, 1974. Currents and water masses in the Bering Sea: a review of Japanese work, in *Oceanography of the Bering Sea*, edited by D.W. Hood and E. J. Kelley, pp. 39-58, Occ. Public. No. 2, Inst. Mar. Sci., Univ. of Alaska, Fairbanks, Fairbanks, AK.
- UNESCO, 1981. The Practical Salinity Scale 1978 and the International Equation of State of Seawater 1980. *Unesco Tech. Papers in Mar. Sci.* 36, Paris, France.
- Weingartner, T. J., S. L. Danielson, and T. C. Royer, 2005. Fresh water variability and predictability in the Alaska Coastal Current, *Deep-Sea Res. II*, 52, 169-191.
- Wespestad, V. G., L. W. Fritz, W. J. Ingraham, and B. A. Megrey, 2000. On relationships between cannibalism, climate variability, physical transport, and recruitment success of Bering Sea walleye pollock (*Theragra chalcogramma*), *J. Mar. Sci.*, 57, 268-274.
- Whitledge, T. E., W. S. Reeburgh, and J. J. Walsh, 1986. Seasonal inorganic nitrogen distribution and dynamics in the southeastern Bering Sea, *Cont. Shelf Res.* 5, 109-132.
- Wilderbuer, T. K., A. B. Hollowed, W. J. Ingraham, P. D. Spencer, M. E. Connors, N. A. Bond, and G. Walters, 2002. Flatfish recruitment response to decadal climate variability and ocean conditions in the eastern Bering Sea, *Prog. Oceanogr.*, 55, 235-248.
- Wilson, J. G., and J. E. Overland, 1986. Meteorology, in *The Gulf of Alaska, Physical Environment and Biological Resources*, edited by D. W. Hood and S. T. Zimmerman, Alaska Office, Ocean Assessments Division, NOAA, Wash. D.C.
- Woodgate, R. A., K. Aagaard, and T. J. Weingartner, 2005a. Monthly temperature, salinity, and transport variability of the Bering Strait through flow, *Geophys. Res. Lett.*, 32, L04601, doi:10.1029/2004GL021880.
- Woodgate, R. A., K. Aagaard, and T. J. Weingartner, 2005b. A year in the physical oceanography of the Chukchi Sea: Moored measurements from autumn 1990-1991, *Deep-Sea Res. II*, 52(24-26), 3116-3149.
- Woodgate, R. A., T. J. Weingartner, and R. Lindsay, 2010. The 2007 Bering Strait oceanic heat flux and anomalous Arctic sea-ice retreat, *Geophys. Res. Lett.*, 37, L01602, doi:10.1029/2009GL041621.

Zhang, J., and D. A. Rothrock, 2001. A thickness and enthalpy distribution sea-ice model, *J. Phys. Oceanogr.*, 31, 2986-3001.

Zhang, J., and D. A. Rothrock, 2003. Modeling global sea ice with a thickness and enthalpy distribution model in generalized curvilinear coordinates, *Mon. Wea. Rev.*, 131, 845-861.

Zhang, J., R. A. Woodgate, and R. Moritz, 2010. Sea ice response to atmospheric and oceanic forcing in the Bering Sea, *J. Phys. Oceanogr.*, 40, 1729-1747, doi:0.1175/2010JPO4323.1.

4.9 Tables

Table 4.1: Mooring deployment details. Columns denote the name, date, location and instrument depths (m). Mooring names beginning with N, C or S, signify the northern, central and southern array lines, respectively. The numbers 55, 40 or 25 denote the nominal water column depth at each deployment site. ADCP records for N40 in 2010 and C55 and S55 in both years ended early due to premature battery failure (see Figure 4 for actual duration of ADCP data coverage). **Mooring N25 was not recovered in 2009 due to a fouled recovery line canister;, but divers recovered it in 2010.

Mooring	Deployment Dates	Latitude (°)	Longitude (°)	Bottom depth (m)	ADCP depth (m)	SBE16 depth (m)	SBE37 depth (m)	HOBO depth (m)
N55	7/12/2008 - 7/15/2009	61.9620	-171.9700	54.4	49.4	19.4	52.2, 9.6	23.4, 25.9, 28.4, 30.9, 33.4, 35.9, 38.4, 40.9, 43.4, 45.9, 48.4
C55	7/12/2008 - 7/11/2009	60.1730	-170.0900	55	47	22	52, 10	23.6, 25.6, 26.8, 28.4, 30, 31.6, 33.2, 34.8, 36.4, 38, 39.6, 41.2, 42.8, 44.4, 46
S55	7/15/2008 - 7/9/2009	58.5900	-168.3900	55	47	22	52, 10	14, 17, 25.3, 26.8, 28.4, 30, 31.6, 33.2, 36.4, 38, 29.6, 41.2, 42.8, 44.4, 46
N40	7/13/2008 - 7/14/2009	61.8050	-169.2800	41.7	36.7	20	37.7	
C40	7/10/2008 - 7/11/2009	60.3390	-169.0200	40.5	35.5	20	36.5	
S40	7/7/2008 - 7/10/2009	59.1370	-167.9800	41.5	36.5	20	37.5	
N25	7/13/2008 - 7/25/2010 **	61.7000	-167.4500	25.6	24.8	24.6		
C25	7/10/2008 - 7/11/2009	60.6830	-167.3400	26	25.2	25		
N55	7/15/2009 - 7/28/2010	61.9690	-171.9800	54.2	49.2	17.1	50.0, 10.9	22, 24, 26, 28, 30, 32, 34, 48
C55	7/11/2009 - 7/27/2010	60.1730	-170.0900	56	47	20.7	51, 9.8	23.6, 25.2, 26.8, 28.4, 30, 31.6, 33.2, 34.8, 36.4, 38, 39.6, 41.2, 42.8, 44.4, 46
S55	7/9/2009 - 7/23/2010	58.5900	-168.3900	55.6	47	20.2	51, 10.2	14, 17, 23.6, 25.2, 26.8, 28.4, 30, 31.6, 33.2, 34.8, 36.4, 38, 39.6, 41.2, 42.8, 46
N40	7/14/2009 - 7/26/2010	61.8080	-169.2800	42	37	20	38	
C40	7/12/2009 - 7/26/2010	60.3380	-169.0200	40.6	35.6	20	36.6	
S40	7/10/2009 - 7/23/2010	59.1340	-167.9800	41.5	36.5	20	37.5	
N25	7/16/2009 - 7/25/2010	61.6910	-167.4200	24	23.2	23		
C25	7/11/2009 - 7/24/2010	60.6830	-167.3400	26	25.2	25		

Table 4.2: Seasonal current meter statistics at all mooring sites for the water column vertical average (VA) and depths 5, 10, 20, 30 and 40 m below the surface. N is the number of half-hour samples obtained over the course of the deployments. Net speed and direction computed for 35-hour LPF data. Percent tidal kinetic energy is determined from yearly harmonic tidal analyses at frequencies resolved with signal-to-noise greater than or equal to 10. The high-frequency band contains frequencies remaining after passing through a 35-hr high-pass filter, less the resolved harmonic analysis tidal portion. Mid-frequencies are band-pass filtered over the 35-100 hr range; low frequencies are low-pass filtered at 100 hrs. Net speeds greater than zero at the 95% confidence level are given in bold type, based on a decorrelation time scale of 48 hours.

Mooring	Season	N	Percent of Kinetic Energy				Net Speed (cm s ⁻¹)					Net Direction (°T)					Peak Speed (cm s ⁻¹)	Mean Speed (cm s ⁻¹)		
			Tidal	Inertial	Mid	Low	VA	5	10	20	30	40	VA	5	10	20			30	40
Depth →			VA	VA	VA	VA	VA	5	10	20	30	40	VA	5	10	20	30	40	VA	VA
N55	Jan-Apr	11520	68	3	9	20	0.42	1.73	0.78	0.25	0.50	0.21	209	227	233	156	173	207	38.1	7.8
C55	Jan-Apr	8587	80	3	5	12	0.74	2.69	2.11	1.21	0.64	0.67	329	282	303	344	56	128	40.1	7.8
S55	Jan-Apr	11520	91	2	2	5	1.54	3.24	2.76	1.63	0.97	0.21	303	274	293	311	320	318	25.7	6.0
N40	Jan-Apr	11520	63	4	11	23	1.16	0.63	0.80	1.54	1.47		80	160	80	72	90		48.6	9.1
C40	Jan-Apr	11520	80	2	5	12	1.94	2.56	2.03	1.87	1.85		169	186	174	167	166		41.5	9.8
S40	Jan-Apr	11520	88	2	3	7	0.47	1.14	0.56	0.59	0.96		139	220	208	113	102		38.3	7.6
N25	Jan-Apr	11520	63	3	11	22	1.38	2.34	1.44	0.93			188	198	190	167			48.6	10.6
C25	Jan-Apr	11520	91	2	3	4	1.11	1.75	1.09	0.65			192	201	194	175			32.3	6.9
N55	May-Sep	15459	84	2	4	10	0.51	0.89	1.05	0.81	0.45	0.46	81	70	89	79	80	302	23.7	5.5
C55	May-Sep	9332	94	3	1	3	1.39	2.06	1.72	1.74	1.19	0.35	339	313	321	349	3	308	19.5	3.4
S55	May-Sep	12467	95	2	1	3	2.96	3.97	3.76	2.87	2.77	1.42	328	306	318	327	337	325	13.0	4.2
N40	May-Sep	14582	84	5	3	8	0.94	0.56	0.56	1.10	1.02		29	345	26	35	39		23.9	5.0
C40	May-Sep	15426	94	2	1	3	0.36	0.91	0.69	0.38	0.48		308	275	305	316	182		22.8	4.7
S40	May-Sep	15483	95	2	1	2	0.82	0.98	0.75	0.78	0.74		140	165	152	137	139		17.3	3.9
N25	May-Sep	19000	88	3	4	5	0.65	0.24	0.63	0.79			104	159	91	97			33.4	5.2
C25	May-Sep	15329	97	1	1	1	0.31	0.93	0.42	0.23			220	214	235	289			17.4	3.5
N55	Oct-Dec	8832	66	4	9	21	1.48	2.23	2.06	1.68	1.03	1.10	307	294	302	312	318	296	36.5	8.8
C55	Oct-Dec	8832	73	2	8	17	3.46	4.58	4.50	3.98	2.88	2.27	336	322	325	336	348	346	65.3	9.4
S55	Oct-Dec	8832	84	2	4	11	4.09	4.69	4.88	4.42	3.79	2.96	327	310	318	328	334	336	45.8	8.2
N40	Oct-Dec	8832	61	5	11	24	0.75	0.50	0.25	1.02	1.38		108	215	113	94	111		50.4	10.0
C40	Oct-Dec	8832	73	3	8	16	3.01	4.36	3.90	2.75	1.74		273	269	272	278	269		61.5	11.8
S40	Oct-Dec	8832	84	2	5	9	1.87	1.92	2.18	2.06	1.71		347	315	329	352	11		46.3	8.8
N25	Oct-Dec	8832	63	4	14	20	1.11	1.47	0.88	1.70			183	235	191	152			59.1	11.6
C25	Oct-Dec	8832	88	2	4	5	2.08	3.76	2.42	0.32			218	219	221	209			41.9	8.3

Table 4.3: Relative contribution of individual momentum balance terms to the 35-hour filtered vertically integrated equations of motion, averaged across all mooring sites and separated by season. The column labeled RMS total depicts the sum of all five terms in the momentum balance multiplied by 10^5 ; the other columns show the fraction of the RMS explained by each of the five components of Equation (1). Despite large seasonal changes in the total kinetic energy, the relative contributions of the individual terms remain approximately the same.

	Averaging Interval	RMS total ($\times 10^5 \text{ m}^2 \text{ s}^{-2}$)	Local Acceleration	Coriolis	Horizontal Pressure Gradient	Surface Stress	Bottom Stress
Cross-shelf Balance	Jan-Apr	2.5	4%	46%	43%	6%	2%
	May-Sep	1.3	4%	44%	41%	8%	3%
	Oct-Dec	3.1	4%	45%	40%	9%	2%
Along-shelf Balance	Jan-Apr	1.5	9%	37%	35%	11%	8%
	May-Sep	1.0	8%	36%	34%	15%	6%
	Oct-Dec	2.0	9%	37%	32%	15%	7%

Table 4.4: Comparison of the cross-correlation (r) between observed SSH fluctuations and the BESTMAS model SSH hindcasts for two time intervals. All values are significant at the 95% level ($p < 0.05$).

	N55	C55	S55	N40	S40	N25	C25
October-May	0.60	0.67	0.65	0.77	0.66	0.86	0.81
June-September	0.32	0.58	0.64	0.80	0.48	0.71	0.64

4.10 Figures

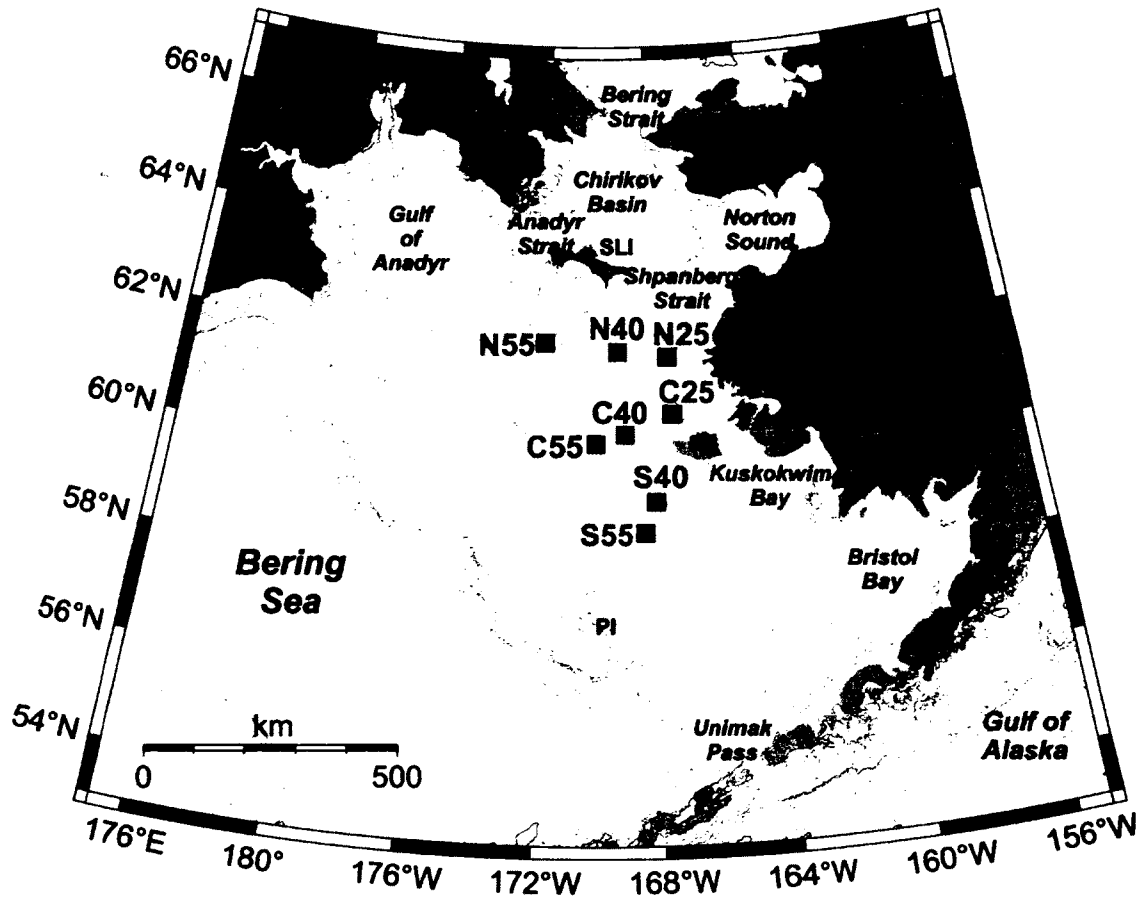


Figure 4.1: The eastern Bering Sea with place names and mooring sites (squares). SLI = St. Lawrence Island, NI = Nunivak Island, PI = Pribilof Islands. River names YR = Yukon River and KR = Kuskokwim River are placed near the river mouths. Bathymetric contours are for 25 m, 40 m, 55 m, 70 m, 100 m, 200 m, 500 m, 1000 m, 2000 m, 3000 m, 4000 m, and 5000 m.

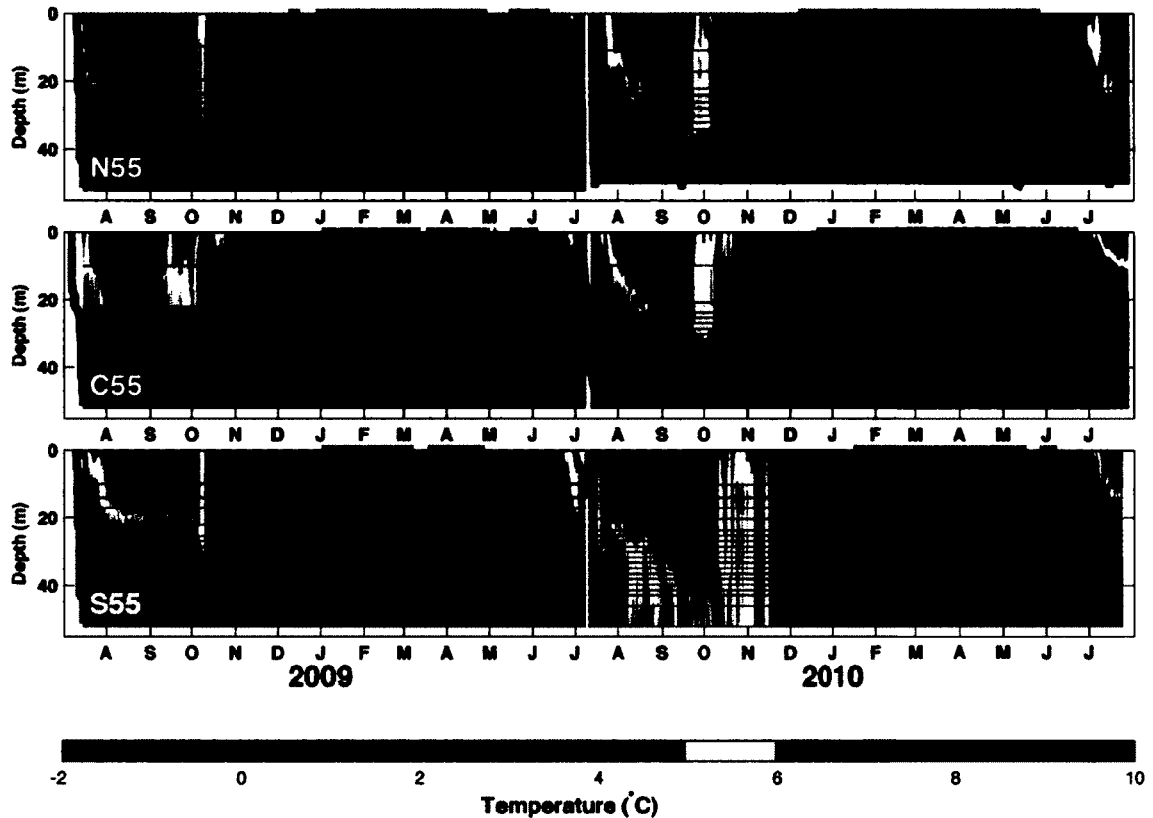


Figure 4.2: Contoured time series of temperature at moorings N55 (top), C55 (center), and S55 (bottom) from July 2008 to July 2010. The contours show the annual cycle, the depth of stratification, and the timing of stratification setup and breakdown along the 55 m isobath. Thin horizontal black lines denote the depth of temperature measurements; note that the ~ 10 m depth instruments on N55 and C55 were lost partway through each deployment. Hash marks at the top denote the presence of ice with concentrations > 30%. Ice concentrations and surface temperatures are from the daily gridded OISST dataset at the grid point closest to each mooring. Thick vertical black lines depict monthly mean observed salinity profiles taken by shipboard CTD casts within 50 km of each mooring site. The CTD salinity profiles are plotted so that their bottom-most measurement is located on the 15th day of month within which they were taken; horizontal spacing of one month is equivalent to $\Delta S = 1$.

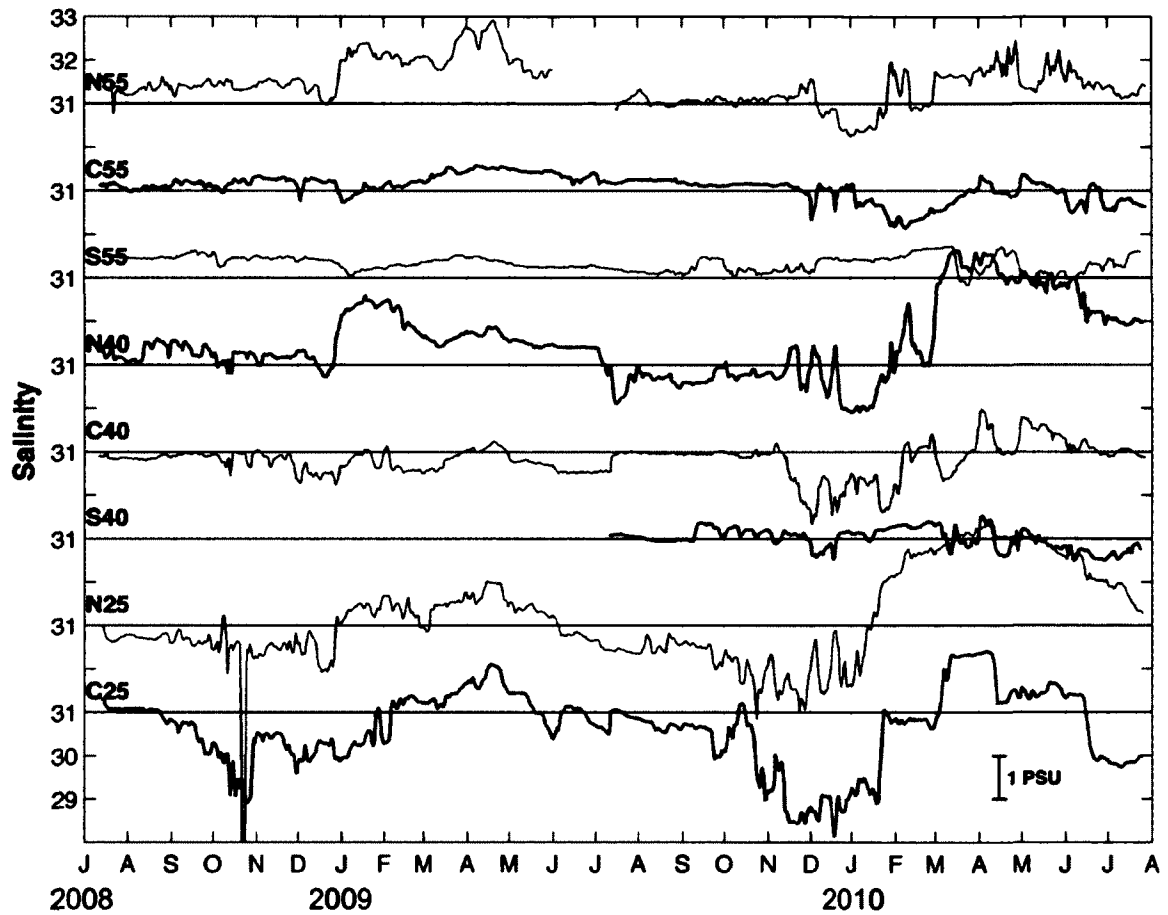


Figure 4.3: Daily mean salinity (S_p) time series. The annual salinity minimum in fall progresses from nearshore sites (C25 and N25) to the other sites in deeper waters. All instruments were located between 17 and 25 m depth. The distance between each 31 line is $\Delta S = 2$ on the vertical axis; vertical tick marks are spaced every $\Delta S = 1$. Every other record is plotted with thick (thin) lines for clarity.

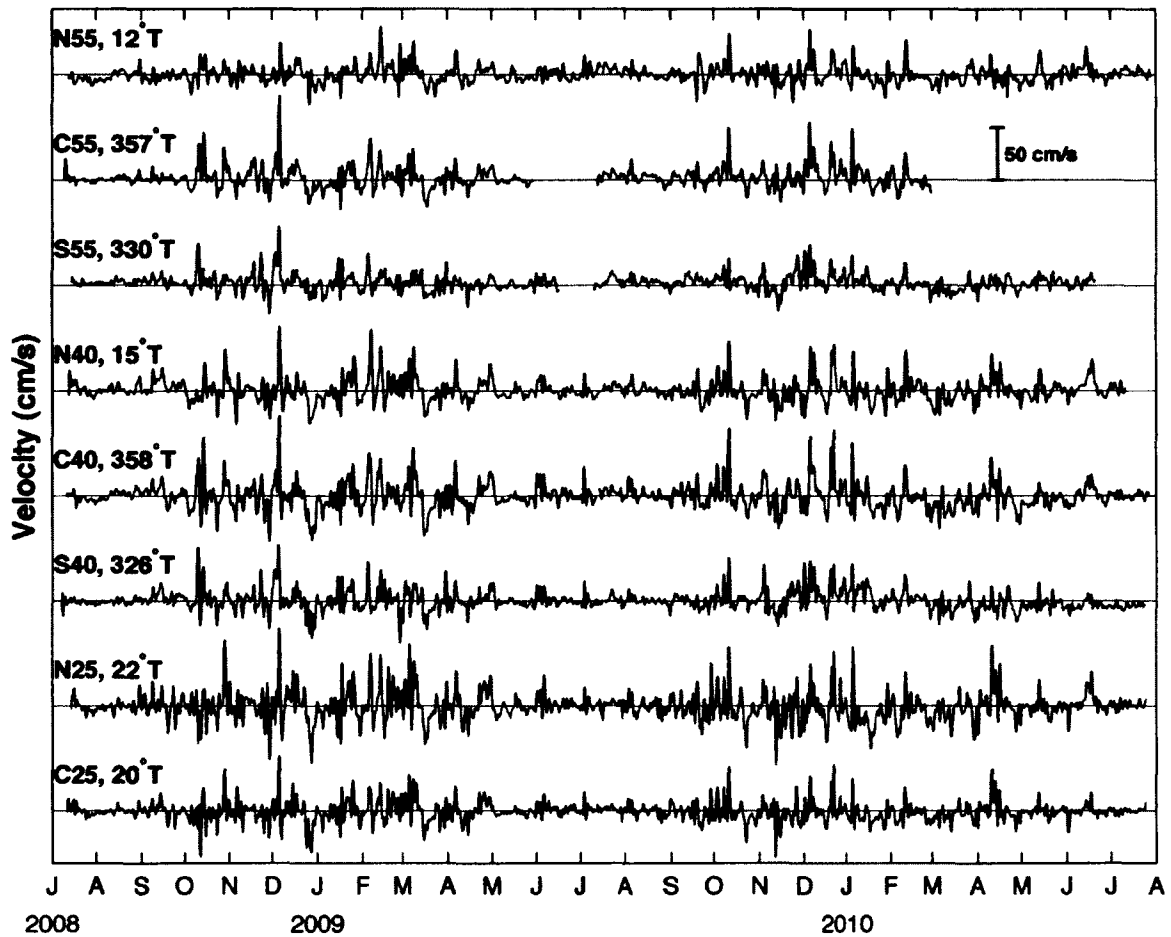


Figure 4.4: Time series of 35 hr low-pass filtered, water column average along-principal axis component of currents at each mooring site. Note the strongly seasonal change in variance. The axis orientation is computed from each low-pass filtered two-year timeseries composite and is noted next to each mooring site label. The distance between each zero line is 80 cm s^{-1} on the vertical axis.

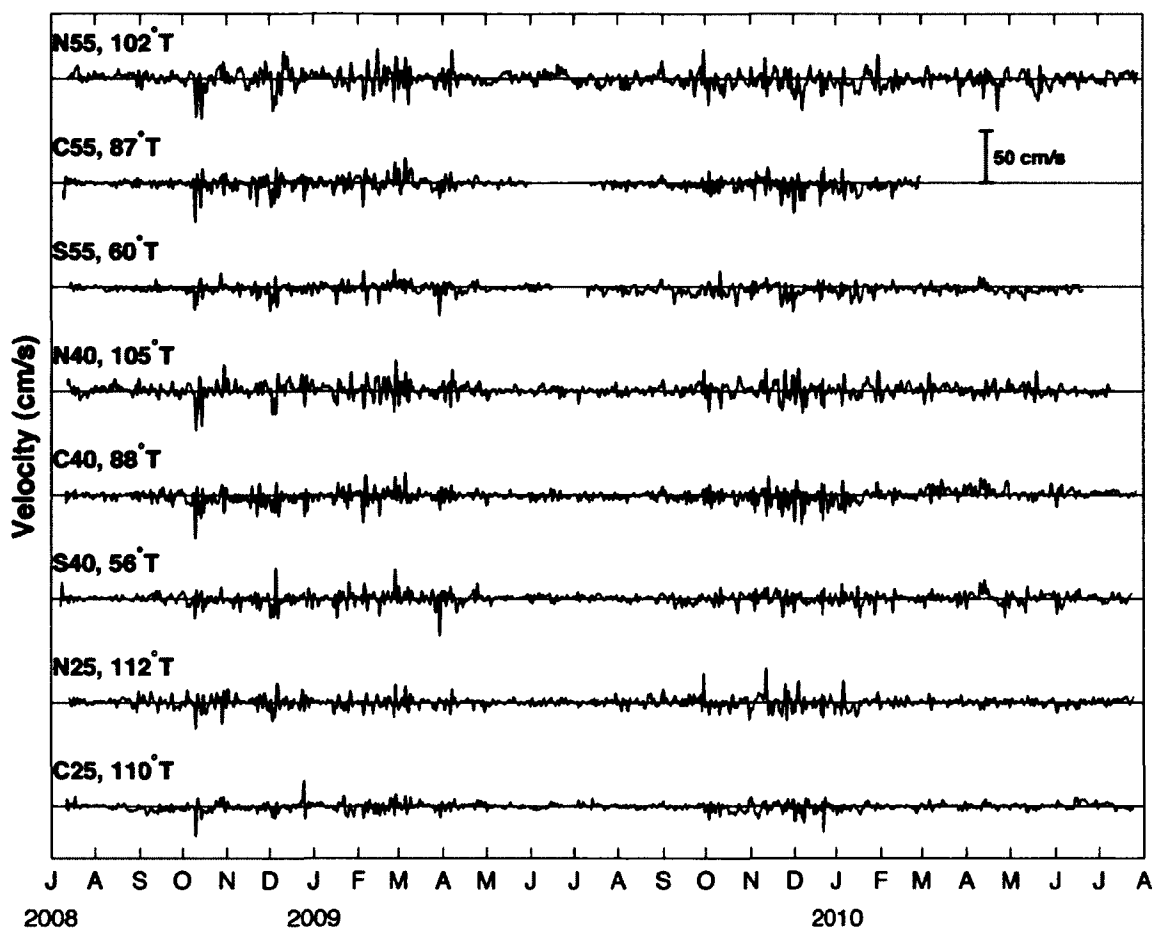


Figure 4.5: Time series of 35 hr low-pass filtered, water column average cross-principal axis component of the flow field at each mooring site. The axis orientation is computed from each low-pass filtered two-year timeseries composite and is noted next to each mooring site label. The distance between each zero line is equivalent to 80 cm s⁻¹ on the vertical axis.

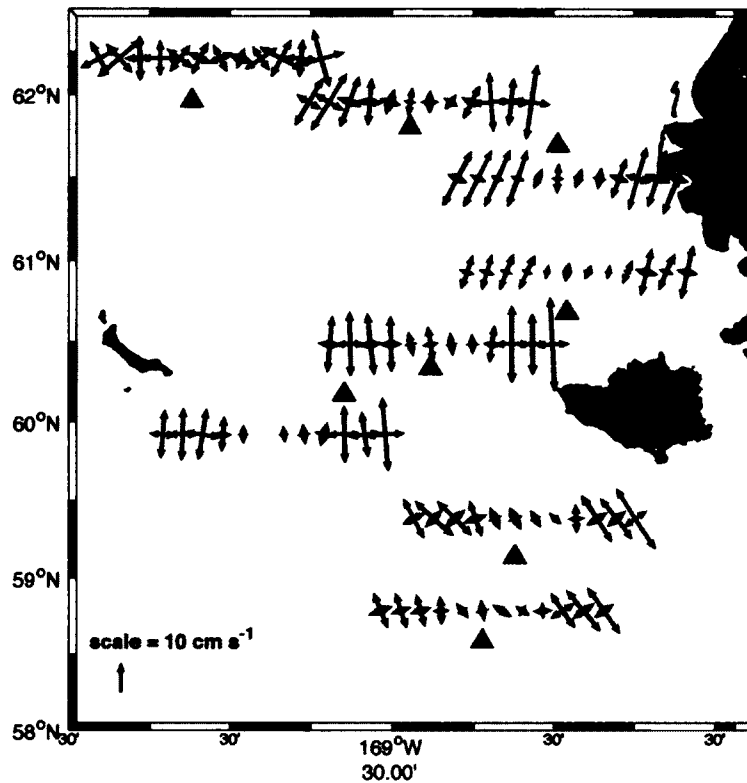


Figure 4.6: Mean monthly decomposition of the flow field into ellipses denoting the along- and cross-principal axis of variation for currents at 20 m depth. Most sites exhibit an annual modulation in magnitude and show relatively little variation of direction amongst months; N55 is a notable exception. Each set of axes begins with January on the left and ends with December on the right. Due to battery failures both years at C55, axes are missing in June for this mooring. Triangles denote the associated mooring location for each set of axes.

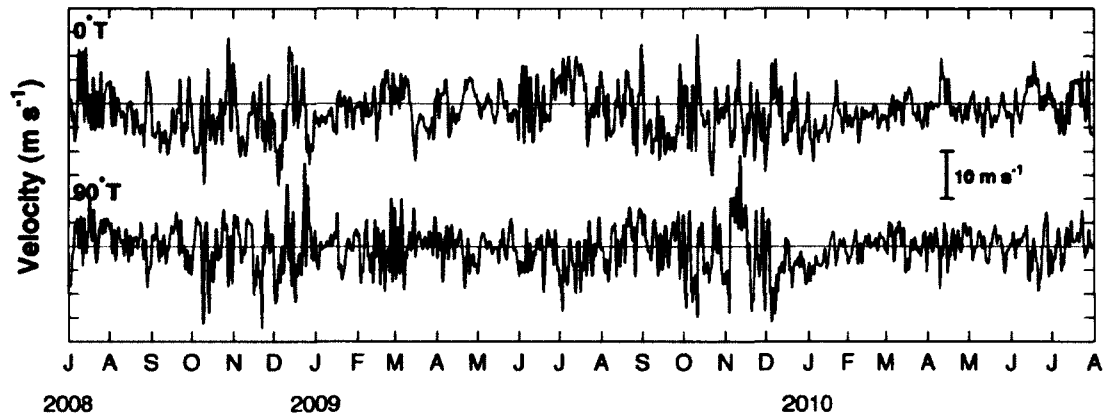


Figure 4.7: North-south (0°T) and east-west (90°T) wind components at the NARR grid point closest to mooring C55. For consistency with Figures 4 and 5, the time series have been 35 hr low-pass filtered.

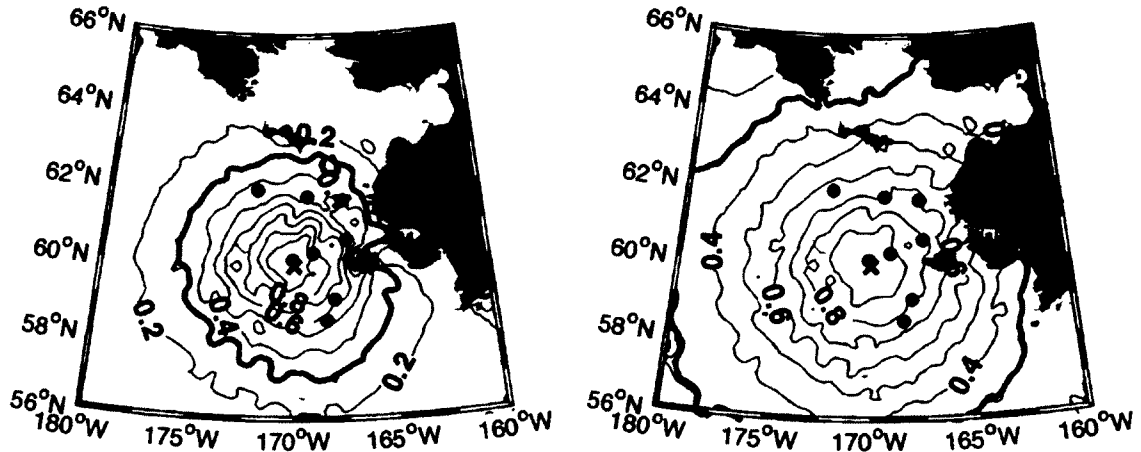


Figure 4.8 Coherence-squared of the NARR wind field with respect to NARR winds at a reference site located at 60 °N, 170 °W for short (< 32 hr, left) and long (>32 hr, right) periods from July 2008 to July 2010. Short period fluctuations have much smaller decorrelation length scales than those of longer period. The reference site is marked by x and the mooring sites by dots. The contours are plotted at intervals of 0.1, beginning with $\gamma^2 = 0.9$ for the innermost closed contour around the reference point. The thick black contour denotes $\gamma^2 = 0.31$, the level of statistically significant coherence at the 95% confidence level.

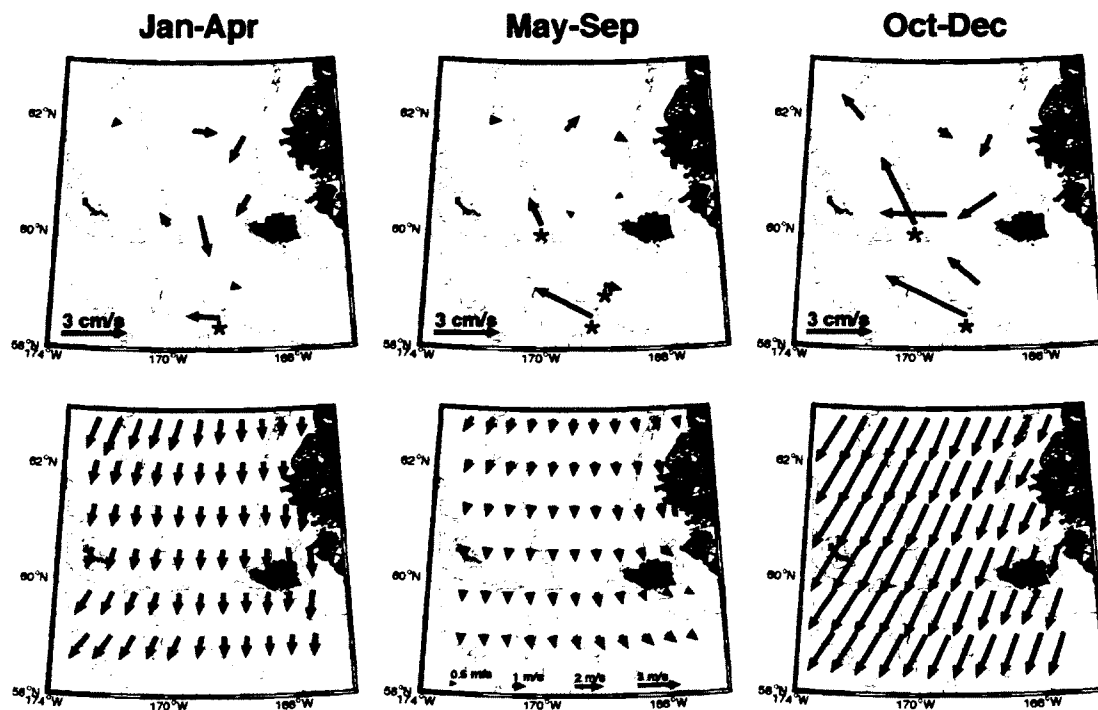


Figure 4.9: Seasonal averages of water column average currents (upper panels) and winds (lower panels) in the study region. Vectors marked with * are significantly different from zero. The ice-covered January to April period is on the left, the stratified May to September period in the middle, and the strong mean wind October to December period is on the right. Wind vectors from every 4th NARR grid cell are displayed.

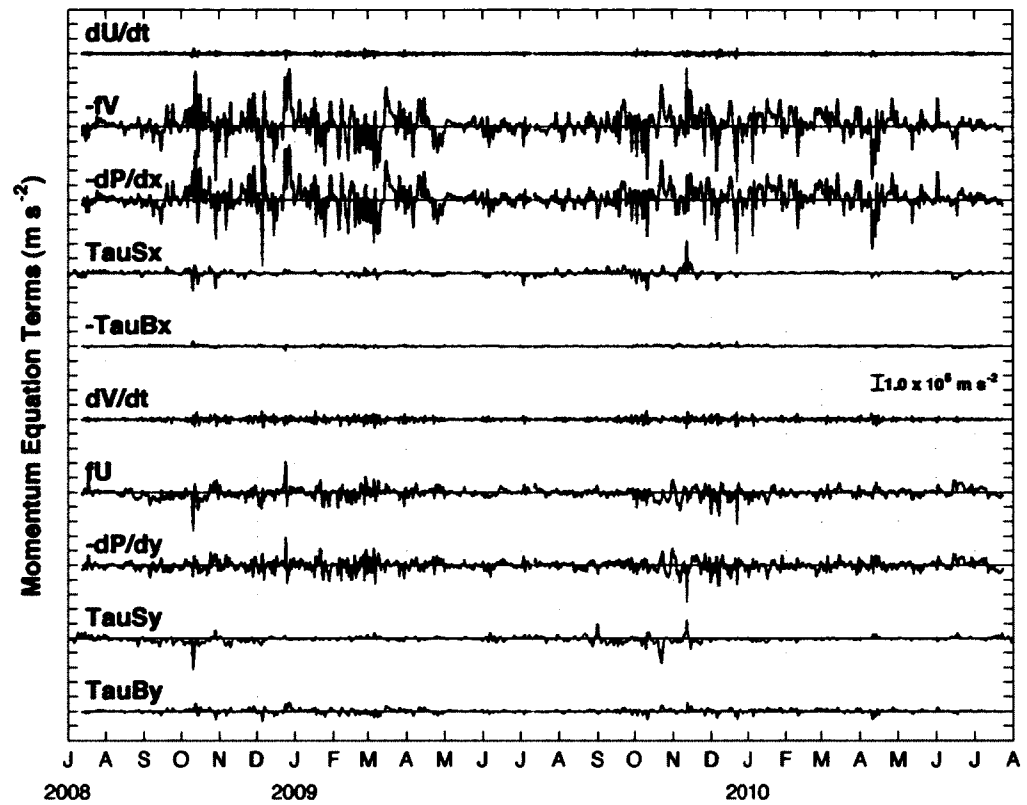


Figure 4.10: Time series of each term of the harmonically de-tided, vertically integrated equations of motion (eq. 1) at site C25. Zero lines are spaced every $5 \times 10^5 \text{ m s}^{-2}$ along the vertical axis and tick marks are every $1 \times 10^5 \text{ m s}^{-2}$.

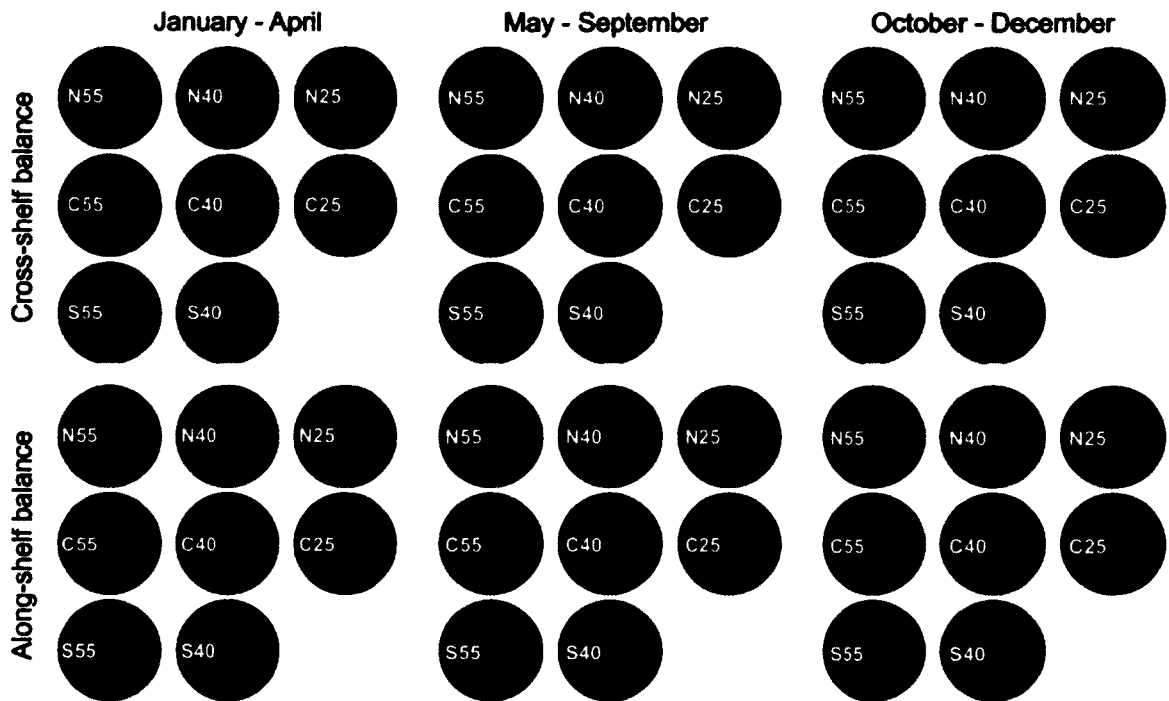


Figure 4.11: Pie charts depicting the relative contribution of the momentum balance terms to each site's total based on 35-hr low-pass filtered RMS magnitudes. The upper three rows depict the cross-shelf momentum balance and the lower three rows the along-shelf momentum balance (Equation 1). The left three columns show January-April, the center May-September, and the right October-December. Colors represent the Coriolis (light blue), local acceleration (dark blue), bottom stress (red), surface stress (orange) and horizontal pressure gradient (green) terms, respectively. Numbers denote the magnitude of the horizontal pressure gradient term multiplied by $10^5 \text{ m}^2 \text{ s}^{-2}$. Reduced magnitudes at all sites are evident in May-September but the relative importance of each term changes only slightly. The cross-shelf momentum balance shows little dependence on bottom friction or local accelerations.

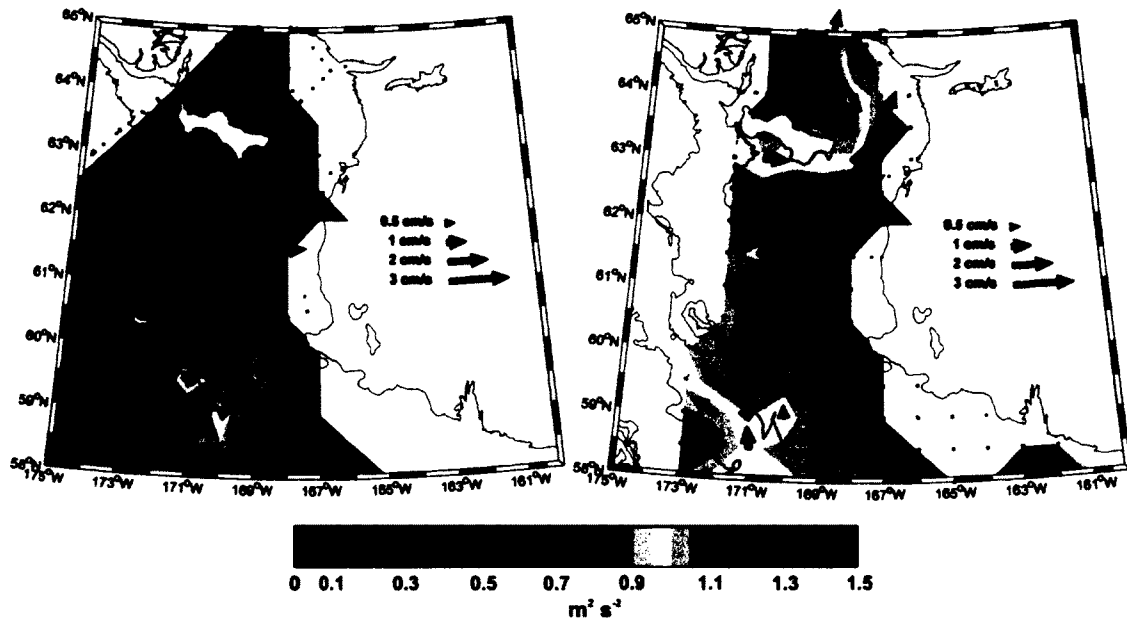


Figure 4.12: Geopotential height anomaly (color shading) and geostrophic current vectors computed over 0-30 db for 2006-2010 late winter and early spring (left) and late summer and early fall (right). Over much of the central shelf, the vectors depict a northward velocity tendency at the end of summer and a southward tendency at the end of winter: the cross-shelf baroclinic pressure gradient reverses sign between these periods. Small red dots depict the location of CTD casts.

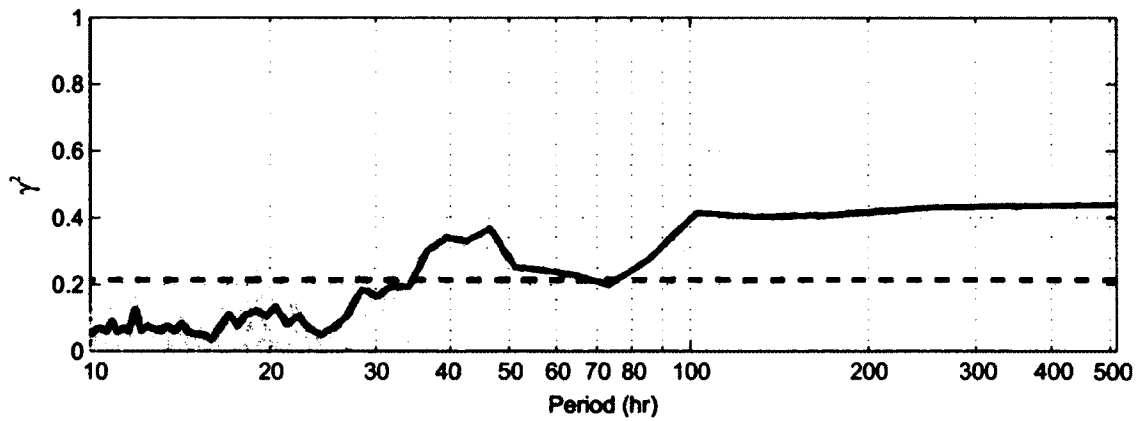


Figure 4.13: Coherence-squared (γ^2) between NARR winds at each mooring site with currents measured at 5 m depth. Sixteen comparisons (thin light traces) are shown, one for each yearlong deployment at each of the eight mooring sites. The thick dark line is the average of all sixteen. The dashed line shows the average significance level.

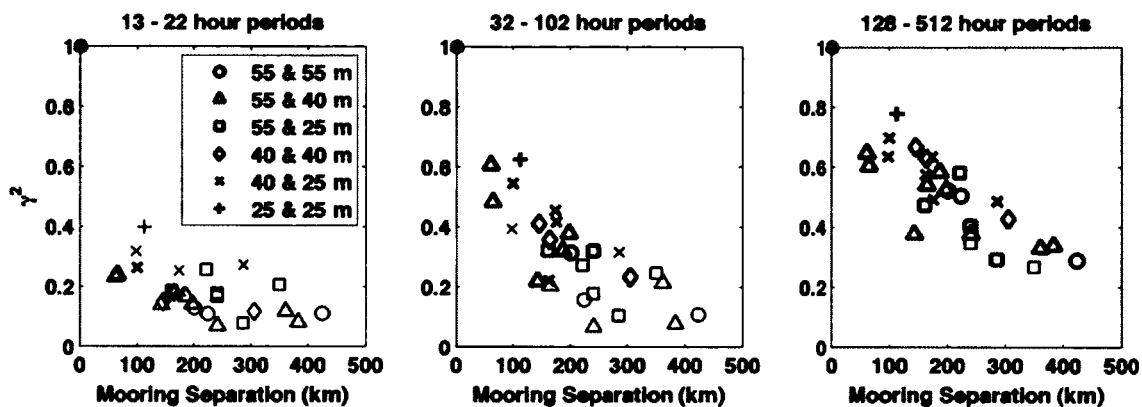


Figure 4.14: Rotary coherence-squared (γ^2) of vertically averaged currents from all mooring pair combinations. Symbols denote the depth combination for each comparison (see legend). Symbols plotted with thick lines are significantly coherent at the 95% confidence level.

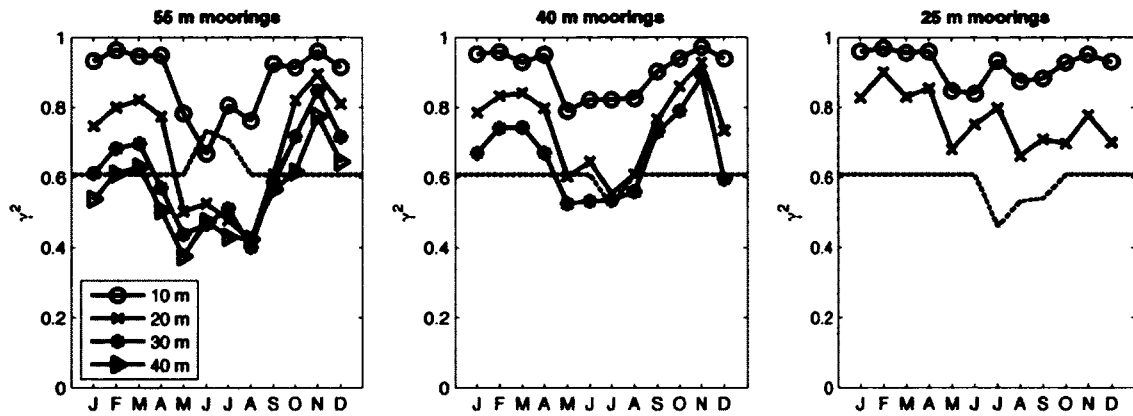


Figure 4.15: Rotary coherence-squared (γ^2) between currents at 5 m and those at 10 m, 20 m, 30 m and 40 m depths for the 55 m (left), 40 m (center) and 25 m (right) moorings for the mid-frequency band (32-102 hr) as a function of calendar month. The 95% significance level for coherence is shown by the dotted line.

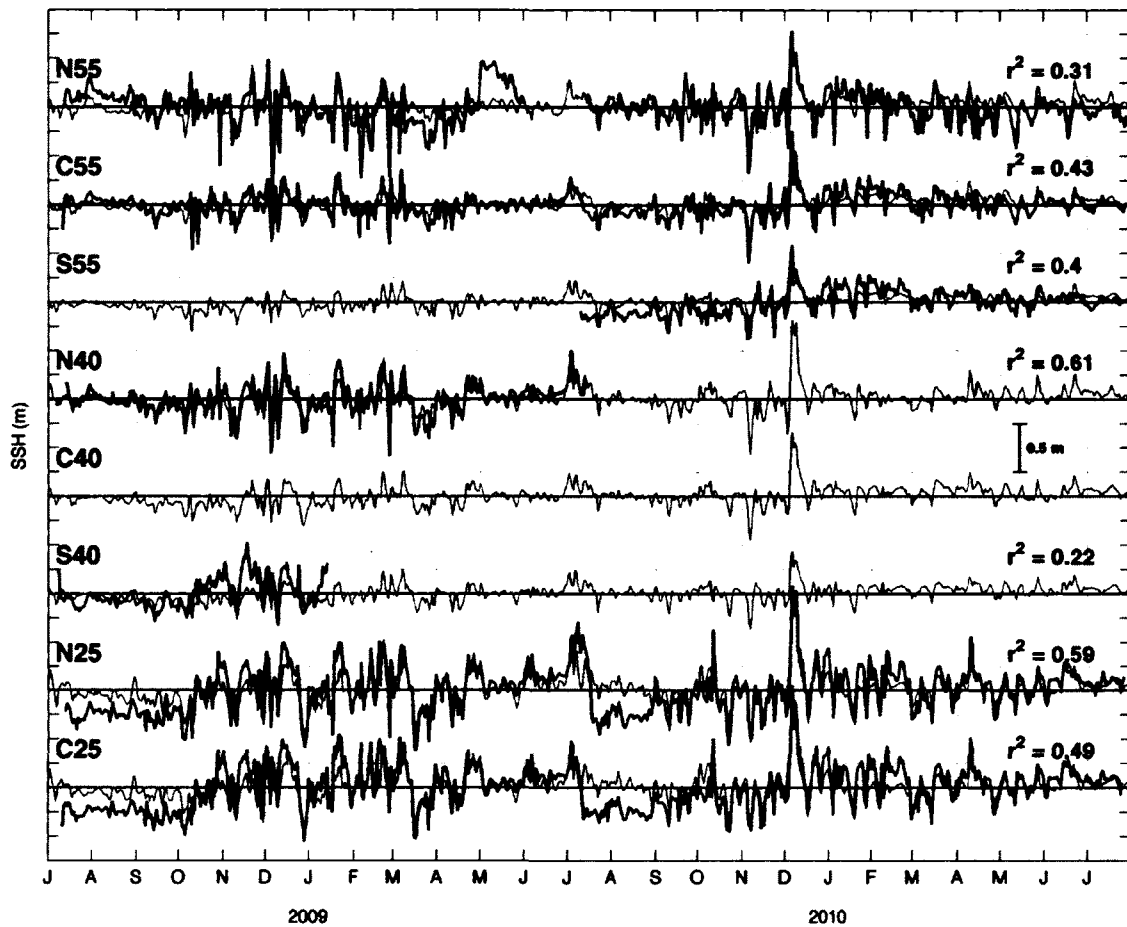


Figure 4.16: SSH time series. Moored pressure records are 35-hr low-pass filtered, demeaned, and converted to equivalent elevation changes (black lines); BESTMAS modeled SSH (gray lines) are daily values at each mooring site. The record-length cross-correlations squared are denoted along with each time series. All correlations are statistically significant at the 95% level except for the short record at mooring S40. On the vertical axis, the distance between the zero line for each time series is equivalent to 1 m SSH change, with tick marks every 0.25 m.

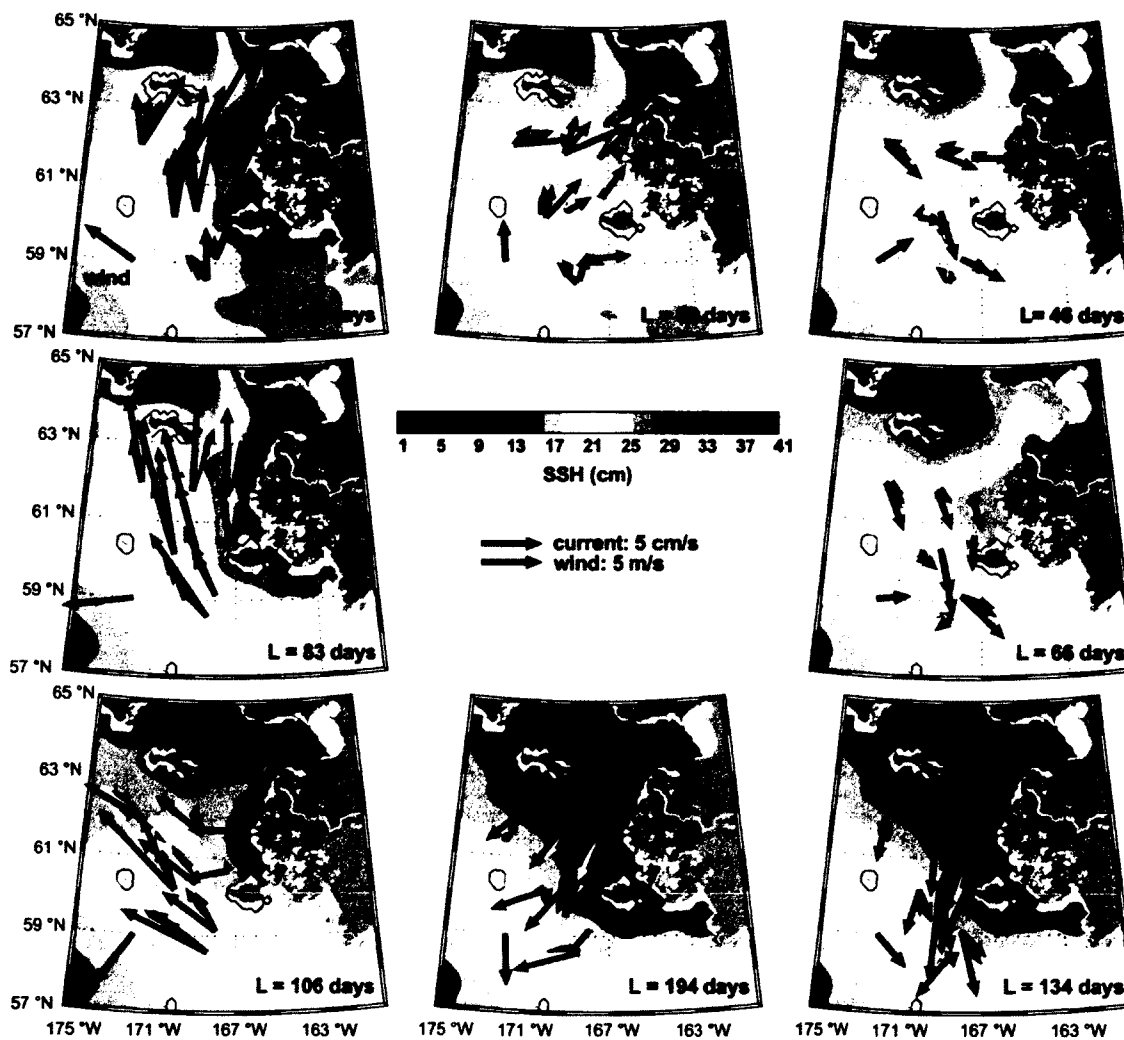


Figure 4.17: Composite oceanic response to various wind directions. Each panel is for a different set of wind directions (top center -22.5°T to $+22.5^{\circ}\text{T}$, etc). The mean wind vector is the black vector emanating from 59°N , 172°W . Current vectors are color-coded based on depth: 5 m = red, 10 m = yellow, 20 m = green, 30 m = blue, 40 m = black. The BESTMAS SSH field is contoured at 2 cm increments between 1 cm (blue) and 41 cm (red) elevations and is clipped at levels beyond this, so that the entire dynamic range is not fully represented. The mean wind direction is over the 24-hr period prior to the ocean current observation. L denotes the total time represented by each panel's average. A scale vector for both the wind and current is provided in the center panel.

Chapter 5: Wind-induced changes to the eastern Bering Sea shelf circulation field¹

5.1 Abstract

We present a simple framework for considering the variability of the eastern Bering Sea shelf circulation as a response to changes in wind direction. Both observations and numerical integrations show that much of the shelf flow reverses between northwesterly and southeasterly winds. While southeasterly winds are less frequent, they are associated with large on-shelf transport across most of the shelfbreak, and in October-April they are also accompanied by a reversal of the normally eastward flow near Cape Navarin. In contrast, northwesterly winds promote off-shelf transport across most of the shelfbreak, along with increased eastward transport near Cape Navarin. The westward-intensified flow in the Gulf of Anadyr adjusts to changes both in the flux across the long (~1000 km) shelfbreak and in the Bering Strait throughflow. These results also hold under the more stratified summer conditions (May-September), but weaker summer winds drive smaller flows across the shelf break, and the majority of the on-shelf transport is directly into the Gulf of Anadyr.

5.2 Introduction

Exchanges between the eastern Bering Sea shelf and the adjacent deep basin affect shelf salt and nutrient balances [Aagaard *et al.*, 2006]. These exchanges are reflected in the water properties carried northward through Bering Strait [Coachman *et al.*, 1975] and are essential to shelf biological production. The role of variable basin-shelf exchanges in ecosystem dynamics is not well understood, but several time-varying processes have been thought important, including shelfbreak eddies [Stabeno and Van Meurs, 1999], tidally mediated diffusion [Coachman and Walsh, 1981], and wind-driven exchange

¹Danielson, S., K. Hedstrom, K. Aagaard, T. Weingartner, and E. Curchitser, 2012. Wind-induced reorganization of the Bering shelf circulation, *Geophys. Res. Lett.*, doi:10.1029/2012GL051231

[Huthnance, 1995; Mull, 2008]. Using observations and numerical modeling, we present a new perspective on the Bering shelf circulation under varying wind conditions. We particularly emphasize the very different regional effects of northwesterly (winds blowing from the northwest) and southeasterly along-isobath winds.

5.3 Bering shelf circulation:

The numerical model and rotating tank experiments of *Kinder et al.*, [1986], hereafter referred to as KCW, showed that westward intensification due to the topographic beta effect exerts strong control over the regional flow field. We extend these results by first adding along-isobath winds to the KCW barotropic model and then introducing more realistic bathymetry, atmospheric forcing and thermohaline fields into a three-dimensional model of the shelf circulation.

We begin by noting that the KCW results are consistent with measurements of elevated salinity, nutrients and primary production levels in Chirikov Basin and Anadyr and Bering straits [*Coachman et al.*, 1975; *Sambrotto et al.*, 1984; *Walsh et al.*, 1989]. Current meter moorings deployed in Anadyr and Shpanberg straits also support KCW, indicating that ~80% of the Bering Strait throughflow has passed through Anadyr Strait [*Schumacher et al.*, 1983; *Aagaard et al.*, 1985; *Muench et al.*, 1988]. While other observational evidence for a westward-intensified flow in the Gulf of Anadyr is sparse, other model results also depict this feature [e.g., *Overland and Roach*, 1987; *Clement et al.*, 2005].

In addition to the topographic beta effect described by KCW, subtidal flows over the shelf are influenced by the mean northward transport through Bering Strait [*Coachman et al.*, 1975; *Woodgate et al.*, 2005; *Aagaard et al.*, 2006], by density gradients [*Schumacher and Kinder*, 1983; *Schumacher et al.*, 1983; *Coachman*, 1986; *Gawarkiewicz, et al.*, 1994], by flow through island passes [*Schumacher et al.* 1982; *Stabeno et al.*, 2002], by tidal rectification [*Kowalik and Stabeno*, 1999], and by winds that strengthen in fall, winter and early spring [*Overland and Roach*, 1987; *Muench et al.*, 1988]. These winds drive sea surface height gradient variations and thus exert strong control on fluctuations in the Bering Strait through-flow [*Aagaard et al.*, 1985].

Current measurements made during July 2008 - July 2010, show that the shelf circulation between Nunivak and St. Lawrence islands undergoes major reorganization between periods of northwesterly and southeasterly wind (Figure 1). These reorganized flows are in geostrophic balance, driven by Ekman transport and coastal divergence. Hindcast winds over the mooring array from the North American Regional Reanalysis (NARR) model [Mesinger, *et al.*, 2006] delineate the two modes. Presumably, the change in circulation is not limited to the shelf between Nunivak and St. Lawrence islands, and to explore this issue we turn to two numerical models.

5.4 Transport over an idealized Bering Sea shelf

We first examine the response of the flow field to along-isobath winds using an idealized barotropic model implemented within the Regional Ocean Model System (ROMS) framework, version 3.4. The model shelf is a 400 km (y) by 1000 km (x) rectangle within a 540 km by 1000 km domain with bottom depth (h) variations in the cross-shelf (y -axis) direction only (Figure 2). Our model is nearly identical to that of KCW, except that we use a hyperbolic tangent bathymetric profile rather than the KCW piecewise linear gradient; tests show no material difference between the two approaches. The model minimum water depth is 40 m and the shelf break is near $y = 114$ km, where $h = 220$ m; $h = 3056$ m along $y = 0$.

Following KCW, the vertically integrated, linear equations of motion describe a balance of the Coriolis force ($f = 1.27 \times 10^{-4} \text{ s}^{-1}$) with the horizontal pressure gradient due to SSH (ζ) variations and linear bottom friction (with coefficient $r = 10^{-3}$). We also include an along-shelf wind stress (τ_x), so that the full equations of motion are $-fv = -g\zeta_x + \tau_x - ruh^{-1}$ and $fu = -g\zeta_y - rvh^{-1}$. Since KCW found that the flow over the shelf is not sensitive to the off-shelf boundary condition, we employ an open boundary along $y = 0$. A transport sink of 1 Sv ($1 \text{ Sv} = 10^6 \text{ m}^3 \text{ s}^{-1}$) imposed along an 80 km segment of the northern boundary represents the Bering Strait through-flow.

Figure 2a shows our reproduction of KCW's Figure 11b. The northward flow through Bering Strait results in an asymmetric circulation with streamlines compressed

toward $x = 0$. A negative SSH anomaly (not shown) extends along the coast from the western shelfbreak to Bering Strait. The shelf south and east of Bering Strait is notably devoid of structure. Fluctuations seen along the continental slope are trapped shelf waves, which are a remnant of spin-up; a numerical instability at the western edge of the slope represents an unresolved boundary layer. Neither of these impacts the shelf circulation features of primary interest here. Reversal of the Bering Strait transport to -1 Sv, with no wind forcing, also results in a westward-intensified flow for which the spatial structure is similar to that in Figure 2a, but has a positive SSH anomaly along $x = 0$.

Figure 2b depicts the response to a spatially invariant southeasterly kinematic wind stress of $1 \times 10^{-4} \text{ m}^2 \text{ s}^{-2}$ and the 1 Sv northward Bering Strait transport. This stress corresponds to a 7.5 m s^{-1} wind and forces an onshore Ekman transport of ~ 0.8 Sv over 1000 km. In contrast to the no-wind scenario, streamlines spread out along the shelfbreak and a positive SSH anomaly develops along $y = 540$ km east of Bering Strait. Along-isobath flow for $y > 440$ km and $x > 200$ km is in the same direction as the wind. If the Bering Strait transport is increased to 2 Sv, the spatial pattern depicted in Figure 2b is unchanged for $x > 200$ km, since the result is the sum of panels 2a and 2b.

Northwesterly winds (Figure 2c) force currents off-shelf for $x > 200$ km. The on-shelf transport, restricted to $x < 200$ km and with a maximum near $y = 114$ km, increases to ~ 1.7 Sv to compensate. The off-shelf Ekman transport forms an asymmetric recirculation cell that connects shelf and slope waters. For $y > 440$ km and $x > 200$ km, currents are primarily oriented along-isobath and downwind, consistent with observations (Figure 1). A Bering Strait flow reversal to -1 Sv accompanied by northwesterly winds results in a streamline pattern similar to the southeasterly pattern (Figure 2b), but with flow in the opposite direction.

Thus, under both along-isobath wind conditions and both directions of Bering Strait transport, the westward-intensified flow in the Gulf of Anadyr controls the cross-shelf transport not directly forced by Ekman dynamics. These model results suggest that westward intensification exerts strong influence during a) weak winds (e.g., summer), b) northwesterly winds, and c) southeasterly winds when the Bering Strait northward

transport does not balance the on-shelf Ekman transport. Essentially, the westward-intensified flow adjusts to maintain continuity across the shelfbreak.

While Figure 2 shows flow reorganizations that are consistent with Figure 1, it is *a priori* not clear that the barotropic model results will hold under the influence of stratification or will persist long enough to appreciably alter the shelf environment under variable synoptic wind forcing. We therefore turn to a 3-dimensional numerical model.

5.5 Transport over a more realistic Bering Sea shelf

We use the sixth, and most recent, version of the Northeast Pacific (NEP6) model [Curchitser *et al.*, 2005], with a horizontal resolution of ~10 km and 50 vertical levels. This version includes realistic surface stresses and fluxes [Large and Yeager, 2008], surface and bottom boundary layers implemented with a k-profile parameterization [Large *et al.*, 1994], boundary conditions from the 1958-2008 Simple Ocean Data Assimilation (SODA) ocean reanalysis [Carton and Giese, 2008], tides [Egbert and Erofeeva, 2002], and sea ice growth and decay [Budgell, 2005]. The model domain extends 2000 km offshore from the North American west coast between 20°N and 68.5°N; the northern boundary lies ~300 km north of Bering Strait. Danielson *et al.*, [2011] undertook an extensive suite of model-data comparisons for NEP5, and found overlapping confidence limits on the observed and modeled velocity rotary spectra at nearly all periods between 10 hours and one year at 57°N, 164°W. Improvements since NEP5 include seasonally and inter-annually varying coastal discharge [Dai *et al.*, 2009], spatially variable water opacity to improve the incoming solar radiation vertical heat distribution, and a boundary condition that allows adjustment both to local wind forcing and to exchanges forced by SODA (the constant 0.8 Sv northward transport used along the NEP5 northern boundary is removed). The NEP6 results analyzed here are monthly averages of a 1987-2007 hindcast.

Because the barotropic model suggests that the sign and magnitude of transport through Bering Strait affects flow in the Gulf of Anadyr, we first compare observed monthly mean velocity data from mooring MA3 deployed in Bering Strait near 66.32 °N, 168.97 °W between 1990 and 2004 [Woodgate *et al.*, 2005] with the vertically integrated

monthly mean model hind-cast velocity for the same site. For each month we find no statistical difference (at the 95% confidence level) between the observed and modeled monthly means. Furthermore, cross-correlation of observed and modeled monthly anomalies (relative to the long-term monthly mean) shows that the model accounts for about half the observed variability ($r=0.70$, $p<0.001$).

We now ask how the currents across the entire shelf respond to the wind conditions used to delineate the two circulation modes shown in Figure 1, noting that in addition to the direct impact of Ekman transport, the shelf-wide response will also reflect bathymetric steering, Ekman pumping, and shelfbreak front and bottom boundary layer dynamics.

Based on NARR winds at $60^{\circ}\text{N}/170^{\circ}\text{W}$, we selected December 1999 and December 2000 as representative of strong northwesterly and southeasterly winds, respectively. For December 2000, the model displays a SSH maximum (not shown) along the western Alaskan coast that forces inner shelf waters northward (Figure 3b). A second SSH maximum in the Gulf of Anadyr forces westward flow past Cape Navarin. Inspection of the mean sea level pressure pattern (SLP, not shown) for this month reveals a low pressure cell centered over 54°N , 180° , with curved isobars that closely parallel large portions of the Siberian and Alaskan coasts. This SLP field clearly implies along-shore winds for most of the coast between Bristol Bay and Cape Navarin.

Under northwesterly winds (December 1999), flow over much of the northern and inner shelf reverses (Figure 3c) because of a SSH minimum that extends along the Alaskan coast from Bering Strait to Nunivak Island. The response is weaker than for the southeasterly wind case, in agreement with the observations of Figure 1. The SLP pattern for this month shows high pressure over Siberia and low pressure over the Gulf of Alaska.

The transport through Shpanberg Strait is -0.50 Sv for December 1999 and $+0.64$ Sv in December 2000, while the Anadyr strait transport is $+0.60$ Sv and -0.02 Sv for these two months. The two flow patterns therefore result in differing Bering shelf exports northward through Bering Strait. The two patterns also contrast with mean conditions, for

which the NEP6 model shows ~85% of the Bering Strait transport passing through Anadyr Strait (Figure 3a), consistent with earlier estimates [e.g., *Muench et al.*, 1988].

We are particularly interested in the effect of these two modes of circulation on cross-isobath exchange, and so we form a transect between the Siberian coast and the Alaska panhandle along the 100 m isobath (Figure 1), cutting across shallow isobaths near the coasts. For all months over 1987-2007 we compute the transport normal to this transect from vertically averaged velocities. Based on the fraction of each month that NARR winds at 60°N, 170°W are directed to the SE or NW, we do separate compilations for two seasonal intervals, *viz.*, October-April and May-September (Figure 4).

Under northwesterly winds during October-April, +0.2 Sv of the flow across the transect (hereafter referred to as on-shelf flow, noting that cross-transect flow near the coasts is along isobaths) occurs within 200 km of Cape Navarin, while +0.3 Sv occurs over the remaining 1300 km (Figure 4a). In contrast, southeasterly winds reverse the flow (-0.3 Sv) within 200 km of Cape Navarin and +1.3 Sv is distributed along the remainder of the transect.

Under the weaker winds and greater stratification of May-September, the responses of the shelf circulation near Cape Navarin to northwesterly and southeasterly winds are similar (Figure 4b), although transport across the vast remainder of the transect under southeasterly winds is still larger than for northwesterly winds. The surface Ekman layer shoals from about 40-60 m in winter months to 20-40 m in summer, and neglecting currents within 200 km of Cape Navarin, the mean cross-transect surface velocity is between -3 cm s^{-1} (with winter northwesterlies) and $+2 \text{ cm s}^{-1}$ (with summer southeasterlies). Below the surface Ekman layer, the mean flow is weakly on-shelf ($< 1 \text{ cm/s}$) for both wind directions although larger under southeasterly wind forcing.

Residual tides around the Pribilof Islands [*Kowalik and Stabeno*, 1999] generate enhanced exchanges across the shelf break (Figure 4) at a distance of ~1100 km from the Russian coast. Figure 4 also suggests that changes in isobath orientation elsewhere may correspond with localized regions of flow across the shelf break.

On the whole, the barotropic model and the NEP6 model provide qualitatively similar results. The NEP6 shows little evidence for net off-shelf transport during northwesterly winds, but this may be an artifact of the month-long averaging, since most months experience both wind directions, and the southeasterly response may well dominate. For example, the model suggests that month-long intervals dominated by southeasterly winds experience 3-4 times greater on-shelf transport across the shelfbreak away from Cape Navarin than do months with northwesterly winds. Over the NARR integration period (1979-present), southeasterly winds occurred 42% of the time between October and March (~ 3 mo/yr), and so we expect on-shelf flow into the Gulf of Anadyr ~ 9 mo/yr. Alternatively, the absence in the model results of a clear net offshore transport during northwesterly events may reflect other processes, such as rectification of tidal currents over the continental slope.

5.6 Discussion and conclusions

These results provide a new perspective on the Bering shelf circulation, and especially on cross-shelf fluxes, with their variability being strongly dependent on wind direction. Under weak winds, northward flow through Bering Strait is associated with topographically induced westward intensification in the Gulf of Anadyr, and on-shelf transport is confined to within ~ 200 km of Cape Navarin. In contrast, strong southeasterly winds promote on-shelf Ekman transport across most of the shelfbreak. If this on-shelf transport exceeds the transport through Bering Strait, then the flow in the Gulf of Anadyr reverses. Strong northwesterly winds promote off-shelf Ekman transport across most of the shelfbreak, and so the on-shelf flow within 200 km of Cape Navarin increases to compensate.

The mass balance of the Bering shelf depends on the transports through Bering Strait, across the shelfbreak within 200 km of Cape Navarin, and across the remainder of the shelfbreak that lies outside the narrow region of westward intensification. Imbalances result in sea level changes over the shelf. Locally, surface Ekman transport and subsurface compensating flows are not in balance. Rather, westward intensification generates a laterally asymmetric shelf circulation field that also meets the continuity

requirements for the regional shelf circulation. Coastal and shelf-break upwelling and downwelling processes are not two-dimensional, but instead appear to be strongly mediated by the three-dimensional aspects of the flow field.

Our findings are relevant to a variety of ecosystem processes, including nutrient exchange, shelf production, and advection of planktonic organisms [*Whitledge et al., 1986; Springer et al., 1996; Orensanz et al., 2004*]. Cold northerly winter winds promote ice growth and southward ice motion [*Pease, 1980*], and summers with cold waters on the southeastern shelf follow winters with extensive ice, whereas warmer summers follow winters with stronger northward flow during December-February [*Stabeno et al. 2012*]. *Smart et al. [2012]* showed that larval pollock are aggregated close to the outer shelf in cold winters, whereas in warmer winters these larvae are displaced toward the middle shelf. *Stabeno et al., [2001]* found that cold years with increased sea ice coincide with reduced on-shelf fluxes of salty, nutrient-rich waters. All these findings are consonant with and explainable by the wind-driven shelf circulation variability proposed here.

Our results contribute to a more complete appreciation of the Bering shelf circulation as an integral entity, the variability of which has wide consequences for the shelf ecosystem. Many of our ideas require further testing and exploration, including a refined delineation between northwesterly and southeasterly winds, analysis of the vertical structure of shelf break exchanges under varying stratification, determining the dynamics that control the cross-slope flow field, and relating the wind modes to the commonly used characterizations of the Bering shelf as variously warm, cold, with reduced ice, or with extensive ice. We expect also that with a new mechanistic understanding of the wind's influence, significant progress can be made on assessing the relative importance of wind, eddies, canyons, and tidal stirring on shelf-basin exchange.

5.7 Acknowledgements

We thank P. Stabeno, R. Woodgate and J. Zhang for helpful discussions; R. Woodgate for Bering Strait mooring data; F. Castruccio for contributions to the NEP6 model; and the two helpful reviewers. Our simulations were in part carried out at the National Center for Atmospheric Research and the Texas Advanced Computing Center.

This manuscript is BEST-BSIERP publication #60. National Science Foundation support was through awards ARC-1107804, ARC-0732431, OCE-0814702, OCE-0961454, ARC-0732428 and ARC-0732771.

5.8 References

- Aagaard, K. A. T. Roach, and J. D. Schumacher, 1985. On the wind-driven variability of the flow through Bering Strait, *J. Geophys. Res.*, 90, 7213-7221.
- Aagaard, K., T. J. Weingartner, S. L. Danielson, R. A. Woodgate, G. C. Johnson, and T. E. Whitledge, 2006. Some controls on flow and salinity in Bering Strait, *Geophys. Res. Lett.* 33, L19602. doi:10.1029/2006GL026612.
- Budgell, W.P., 2005. Numerical simulation of ice-ocean variability in the Barents Sea region: Towards dynamical downscaling, *Ocean Dyn.*, 55, 370-387.
- Carton, J. A., and B. S. Giese, 2008. A reanalysis of ocean climate using simple ocean data assimilation (SODA), *Mon. Wea. Rev.*, 136, 2999-3017.
- Clement, J. L., W. Maslowski, L. W. Cooper, J. M. Grebmeier, and W. Walczowski, 2005. Ocean circulation and exchanges through the northern Bering Sea: 1979-2001, *Deep-Sea Res. II*, 52, 3509-3540, doi:10.1016/j.dsr2.2005.09.010.
- Coachman, L. K., K. Aagaard, and R. B. Tripp, 1975. *Bering Strait: The Regional Physical Oceanography*, Univ. of Wash. Press, Seattle, WA.
- Coachman L. K., and J. J. Walsh, 1981. A diffusion model of cross-shelf exchange of nutrients in the Bering Sea, *Deep-Sea Res. A*, 28, 819-837.
- Coachman, L. K., 1986. Circulation, water masses, and fluxes on the southeastern Bering Sea shelf, *Cont. Shelf Res.*, 5, 23-108.
- Curchitser, E. N., D. B. Haidvogel, A. J. Hermann, E. L. Dobbins, T. M. Powell, and A. Kaplan, 2005. Multi-scale modeling of the North Pacific Ocean: Assessment and analysis of simulated basin-scale variability (1996-2003), *J. Geophys. Res.*, 110, C11021.
- Dai, A., T. Qian, K. E. Trenberth, and J. D. Milliman, 2009. Changes in continental fresh water discharge from 1948-2004, *J. Climate*, 22, 2773-2791.
- Danielson, S., E. Curchitser, K. Hedstrom, T. Weingartner, and P. Stabeno, 2011. On ocean and sea ice modes of variability in the Bering Sea, *J. Geophys. Res.*, 116, C12034.

- Egbert, G. D., and S. Y. Erofeeva, 2002. Efficient inverse modeling of barotropic ocean tides, *J. Atmos. Ocean. Technol.*, 19, 183–204.
- Gawarkiewicz G., J. C. Haney, and M. J. Caruso, 1994. Summertime synoptic variability of frontal systems in the northern Bering Sea, *J. Geophys. Res.*, 99, 7617-7625.
- Huthnance, J. M., 1995. Circulation, exchange and water masses at the ocean margin: the role of physical processes at the shelf edge, *Prog. Oceanogr.*, 35(4), 353-431.
- Kinder, T.J. D. C. Chapman, and J. A. Whitehead, 1986. Westward intensification of the mean circulation on the Bering Sea shelf, *J. Phys. Oceanogr.*, 16, 1217-1229.
- Kowalik, Z., and P. Stabeno, 1999. Trapped motion around the Pribilof Islands in the Bering Sea, *J. Geophys. Res.*, 104, 25,667-25,684.
- Ladd, C., and N. A. Bond, 2002. Evaluation of the NCEP/NCAR reanalysis in the NE Pacific and the Bering Sea, *J. Geophys. Res.*, 107(C10), 3158.
- Large, W. G., J. C. McWilliams, and S. C. Doney, 1994. Oceanic vertical mixing: A review and a model with a nonlocal boundary layer parameterization, *Rev. Geophys.*, 32, 363-403.
- Large, W.G., and S. G. Yeager, 2008. The global climatology of an interannually varying air-sea flux data set, *Clim. Dyn.*, 33, 341-364.
- Mesinger, F., and 19 Coauthors, 2006. North American regional re-analysis, *Bull. Amer. Meteor. Soc.*, 87, 343-360.
- Muench, R. D., J. D. Schumacher, and S. A. Salo, 1988. Winter currents and hydrographic conditions on the northern central Bering Sea shelf, *J. Geophys. Res.*, 93(C1), 516-526.
- Mull, J. M., 2008. QuikSCAT measurements of the wind field over the Bering and Chukchi Seas. M. S. thesis, University of Alaska Fairbanks, Fairbanks, AK.
- Orensanz, J., B. Ernst, D. Armstrong, P. Stabeno, and P. Livingston. 2004. Contraction of the geographic range distribution of snow crab (*Chionoecetes opilio*) in the eastern Bering Sea: an environmental ratchet?, *CalCOFI Reports*, 45, 65-79.
- Overland, J. E., and A. T. Roach, 1987. Northward flow in the Bering and Chukchi seas, *J. Geophys. Res.*, 92, 7097-7105.
- Pease, C. H., 1980. Eastern Bering Sea ice processes, *Mon. Wea. Rev.*, 108, 2015-2023.
- Sambrotto, R. N., J. J. Goering, and C. P. McRoy, 1984. Large yearly production of phytoplankton in the western Bering Strait, *Science*, 225(4667), 1147-1150.

- Schumacher, J., K. Aagaard, C. Pease, and R. Tripp, 1983. Effects of a shelf polynya on flow and water properties in the northern Bering Sea, *J. Geophys. Res.*, 88(C5), 2723-2732.
- Schumacher, J.D., and T. H. Kinder, 1983. Low-frequency current regimes over the Bering Sea shelf, *J. Phys. Oceanogr.*, 13, 607-623.
- Schumacher, J.D., C. A. Pearson, and J. E. Overland, 1982. On exchange of water between the Gulf of Alaska and the Bering Sea through Unimak Pass, *J. Geophys. Res.*, 87, 5785-5795.
- Smart, T., J.T. Duffy-Anderson, J.K. Horne, E.V. Farley, C.D. Wilson, and J.M. Napp, 2012. Influence of small- and large-scale environmental variability on walleye pollock eggs, larvae, and juveniles in the Bering Sea, *Deep-Sea Res. II*, <http://dx.doi.org/10.1016/j.dsr2.2012.02.018>.
- Springer, A., C. P. McRoy, and M. Flint, 1996. The Bering Sea Green Belt: shelf-edge processes and ecosystem production, *Fish. Oceanogr.*, 5, 205-223.
- Stabeno, P. J., and P. Van Meurs, 1999. Evidence of episodic on-shelf flow in the southeastern Bering Sea, *J. Geophys. Res.*, 104(C12), 29, 715-729.
- Stabeno, P.J., N. A. Bond, K. B. Kachel, S. A. Salo, and J. D. Schumacher, 2001. On the temporal variability of the physical environment over the southeastern Bering Sea, *Fish. Oceanogr.*, 10, 81-98.
- Stabeno, P., N. Kachel, S. Moore, J. Napp, M. Sigler, A. Yamaguchi and A. Zerbini, 2012. Comparison of warm and cold years on the southeastern Bering Sea shelf and some implications for the ecosystem, *Deep-Sea Res. II*, doi:10.1016/j.dsr2.2012.02.020
- Stabeno, P. J., R. K. Reed, and J. M. Napp, 2002. Transport through Unimak Pass, Alaska, *Deep-Sea Res. II*, 49, 5919-5930.
- Walsh J. J., and 20 Coauthors, 1989. Carbon and nitrogen cycling within the Bering Chukchi seas: source regions for organic matter effecting AOU demands of the Arctic Ocean. *Prog. Oceanogr.*, 22(4), 277-358.
- Whitledge, T. E., W. S. Reeburgh, and J. J. Walsh, 1986. Seasonal inorganic nitrogen distributions and dynamics in the southeastern Bering Sea, *Cont. Shelf Res.*, 5, 109-132.
- Woodgate, R.A., K. Aagaard, and T.J. Weingartner, 2005. Monthly temperature, salinity, and transport variability of the Bering Strait through flow, *Geophys. Res. Lett.* 32:L0460.

5.9 Figures

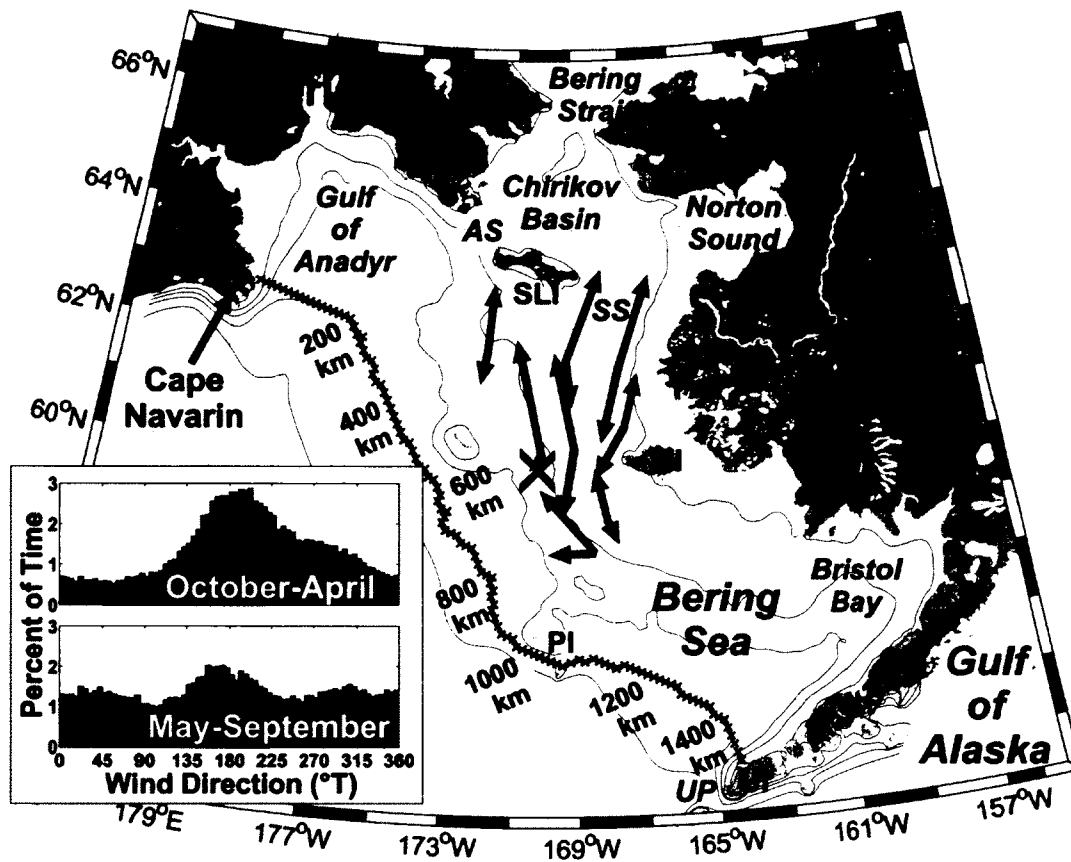


Figure 5.1: The Bering shelf. Vectors show mean vertically averaged currents during southeasterly (red) and northwesterly (blue) winds from July 2008 - July 2010. SLI = St. Lawrence I.; NI = Nunivak I.; PI = Pribilof I.; UI = Unimak I.; AS = Anadyr Str.; SS = Shpanberg Str.; UP = Unimak Pass. Isobaths are drawn at 200, 100, 70, 50 and 20 m. Model grid cells along the 100 m isobath used for Figure 4 are shown with small black crosses. Inset shows histograms of the direction (5° bins) to which the wind blows, compiled for the NARR grid point (X) at 60°N , 170°W for 1979-2010, over October-April and May-September.

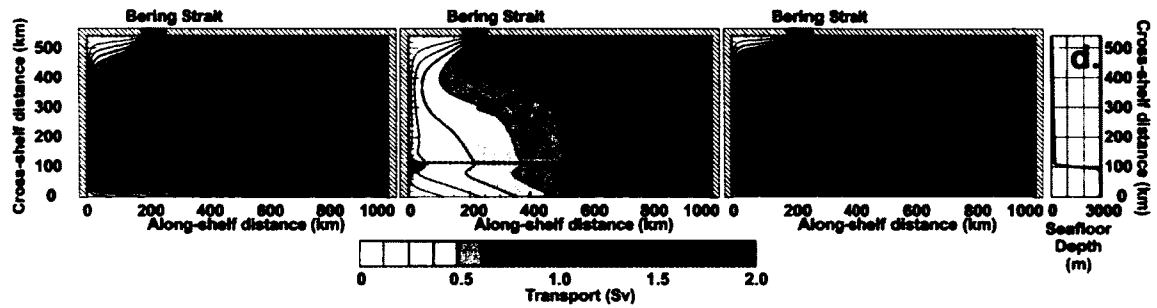


Figure 5.2: Barotropic model results for a) no wind, b) southeasterly wind and c) northwesterly wind. Panel d) shows bottom depths. Kinematic wind stress for the two right-hand panels is $10^{-4} \text{ m}^2 \text{ s}^{-2}$, indicated by the arrows. All three cases impose a northward 1 Sv Bering Strait transport. The shelfbreak is near $y = 114 \text{ km}$, denoted by the dotted line. Contours depict the cross-shelf transport integrated away from the western (left-hand) boundary and thus represent transport streamlines.

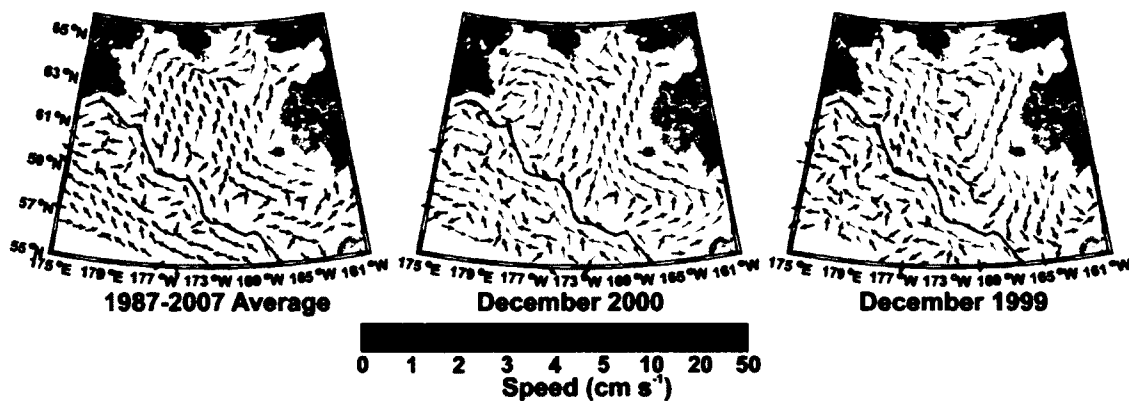


Figure 5.3: Vertically averaged current vectors from the three-dimensional model for a) the 1987-2007 mean, b) December 2000 (southeasterly winds) and c) December 1999 (northwesterly winds). The 200 m isobath is denoted with a thick black line. Each vector represents the average from the closest 36 grid cells (a 6x6 square).

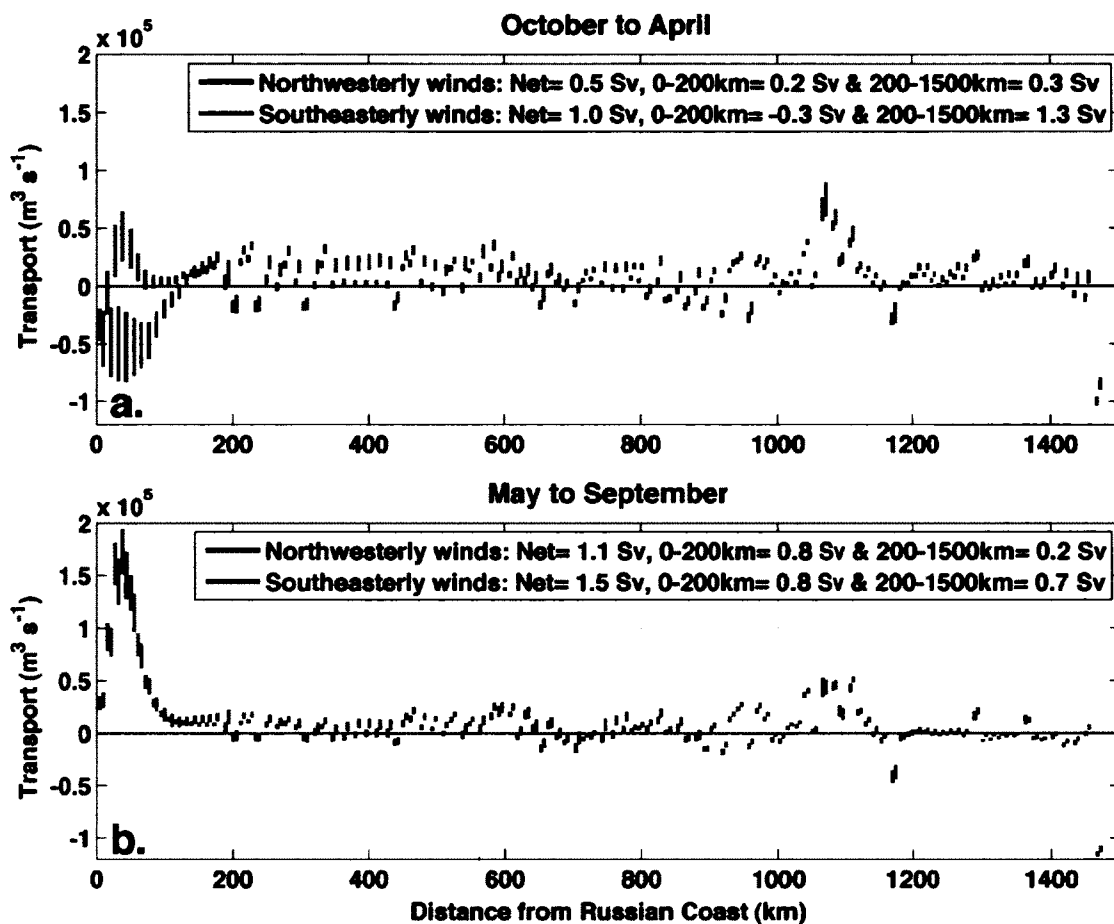


Figure 5.4: On-shelf transport at the grid points shown in Figure 1 for a) October-April and b) May-September. Positive (negative) transport is directed on (off) shelf. Red (blue) vertical bars depict 95% confidence limits on the northwesterly (southeasterly), based on 21 years of monthly averages. Insets give net transport, that within 200 km of Cape Navarin, and that between 200 km from Cape Navarin and the Alaska Peninsula (1500 km).

Chapter 6: Conclusions

6.1 Summary of results

In this dissertation, I identify spatial structure and temporal variations within the temperature, salinity and circulation fields of the eastern Bering Sea shelf. The Pacific-Arctic sea surface height gradient, tides, winds and horizontal density gradients all exert direct force upon the circulation field but variations in the wind direction and speed dominate current variability at synoptic to monthly time scales. While precipitation, evaporation, ice melt, river discharge, and air-sea heat exchanges (solar radiation, longwave radiation, sensible heat fluxes, latent heat fluxes) combine to drive the mean annual cycles of heat and fresh water content, my analyses show that the circulation field exerts strong control upon their inter-annual variations.

These findings stand in contrast to the common view that advection exerts little impact on the eastern Bering Sea shelf physical environment and ecosystem. A Google Internet search (29 January 2012) for the two terms “Bering Sea” and “sluggish flow” returns 155 results and a Google Scholar search returns 19 results. The reputation for sluggish flow on the Bering shelf [e.g., *Muench et al.*, 1988; *Niebauer et al.*, 1999; *Stabeno et al.*, 2001; *Cooper et al.*, 2002; *Rodionov et al.*, 2005] stems naturally from the small ($< 5 \text{ cm s}^{-1}$) vector mean magnitudes obtained when current meter records are subjected to long averaging intervals [*Schumacher and Kinder*, 1983] and the dynamic considerations of cold domes on continental shelves [*Hill*, 1996]. Instantaneous speeds are large, typically $\sim 30\text{-}60 \text{ cm s}^{-1}$ and due primarily to tidal currents [*Kowalik*, 1999]. Sub-tidal speeds vary seasonally with mean (maximum) speeds of up to 12 cm s^{-1} (65 cm s^{-1}). Therefore, I find that a better characterization of the shelf flows in the mean is one of high variance and small mean flows over long (> 12 month) integration periods. Characterizing the Bering Sea cold pool as sluggish may be accurate but this feeds the misconception that advection is not important to this shelf.

Sub-tidal flows variations are controlled primarily by synoptic atmospheric conditions. Under assumptions of a spatially uniform flow field, near-surface particle

displacements exceeding 150 km in one month likely occur regularly (Figure 6.1). Chapters 2, 4 and 5 show that the strongly polarized flow field with small net speeds is a result of variable wind speeds and directions, which are nearly equally divided between upwelling- and downwelling-favorable conditions. Due to water column homogenization during the fall, even near-surface currents can advect nutrients across the shelf during more than one-half the year.

I find that the central shelf is primarily controlled by geostrophy in both the along-shelf and the cross-shelf momentum balances. Bottom friction, wind stress and local accelerations contribute up to 40% of the balance, however. Fluctuations on time scales of 4-20 days of the vertically averaged current field are horizontally coherent over distances exceeding 200 km. This contrasts with high-frequency fluctuations (< 32 hours) that are incoherent at distances of 100-200 km. Vertical coherence in the current field decreases during May-September when stratification increases and wind speeds decrease.

Year-to-year variability in the thermal and haline fields of the Bering shelf (integrated over a volume of $9.3 \times 10^3 \text{ km}^3$) is driven by the oceanic response to atmospheric conditions. Heat budgets depend upon surface heat fluxes and along-isobath advection while fresh water budgets depend upon ice melt, precipitation, evaporation, river discharge and both along- and cross-isobath advection. Along-isobath Ekman transport variations over the heating season account for inter-annual heat content anomalies at the end of summer. Fresh water content anomalies at this time of year are primarily set by advection anomalies over the course of the previous winter. Both of these relations are tied to seasonal changes in the direction and strength of the wind field, a consequence of the position and strength of the Aleutian Low. Because the critical period of time for setting each of these anomalies occurs at a different portion of the year, their inter-annual variations are largely uncoupled.

Changes in winter atmospheric forcing have a two-fold impact upon the circulation field and both alter the horizontal pressure gradient. Ekman transport leads directly to changes in the barotropic pressure gradient such that enhanced southward winds generate coastal divergence and southward advection. Southward winds also

typically promote additional salt production during winter months through enhanced ice and brine production. This, in turn, results in higher salinity conditions in the coastal and northern portions of the central shelf. Because the entire central shelf is isothermal at the end of winter, baroclinic pressure gradients are driven only by changes in salinity and the elevated salinities to the north and east promote an anticyclonic flow field, which enhances flow toward the south over the inner and middle shelf. The barotropic pressure gradient dominates the dynamic balance but the baroclinic velocity field (referenced to 30 db) can support surface currents that are of the same order as the mean vertically averaged currents.

The baroclinic pressure gradient at the end of summer promotes northward flows due to warm and fresh coastal waters. The summer cross-shelf density gradients may also be sensitive to wind conditions because downwelling-favorable winds would tend to trap the Alaska Coastal Current (ACC) front close to shore and inhibit cross-shelf mixing, whereas upwelling-favorable winds could help disperse coastal waters in summer.

Northeast Pacific (NEP) numerical model result analysis (Chapters 3 and 5) shows that hind-cast integrations reproduce many observed aspects of shelf conditions but not all fields are hindcast with equal skill. Model strengths include simulation of the monthly thermal and annual ice extent anomalies over the Bering shelf (50% and 85% of the variance accounted for, respectively), so I find that the model provides useful proxy datasets over the 1970-2005 integration period.

I use the model to extend the record of satellite-based ice extent anomalies from 1979 back to 1970. In addition to changes in ice extent variance over time, the model and observations show a significant increasing trend (6.8 days/decade, $r = 0.52$, $p < 0.001$, Pearson's r correlation coefficient) in the duration of ice-free waters over 1970-2009.

In Chapter 3, analysis of the NEP near surface (0-20 m) temperature Empirical Orthogonal Function (EOF) principal components with various environmental indices shows that 67% variability is accounted for by the first three modes. Mode 1 (47% of the variance) is correlated (significant at the 95% confidence level, Pearson's r) with the

Pacific Decadal Oscillation, the North Pacific Index, the Bering Sea annually integrated ice extent anomaly, and the wind direction anomaly at 60 °N, 170 °W. Mode 2 (14% of the variance) is correlated with the North Pacific Gyre Oscillation, the Pacific-North American Index, near-bottom temperatures at oceanographic station GAK1 and the Gulf of Alaska fresh water discharge anomaly. Mode 3 (6%) of the variance is correlated with the ice extent anomaly and the wind direction anomaly at 60 °N, 170 °W. The wind direction anomaly is significantly correlated with modes 1 and 3 and this parameter describes variability of the advective field as a whole. Therefore, the wind direction anomaly may represent a critical mechanistic link between the advective and thermal fields. Chapters 2, 4 and 5 provide support and additional evidence for these links and suggestions of their importance to the ecosystem.

6.2 Future recommendations

The analyses presented here yield new insight to the Bering Sea shelf's physical environment but much remains unknown. I list below ten topics that, when addressed, will lead to further improved understanding of the Bering Sea's physical, chemical, and biological systems. These items follow from above identified gaps in knowledge and the new results presented in this thesis; some represent continued analyses of the datasets and model results currently in-hand; some require new observational studies.

1. Identify inter-annual variations of the nutrient field that are controlled in part by their responses to the upwelling and downwelling advection fields to better understand ecosystem-wide consequences of Bering Shelf circulation. Historical and recently collected nutrient data should provide sufficient records for initial analyses.
2. Describe and quantify the Bering Sea shelf sea ice budgets to better understand fresh water input and cold pool formation effects on Bering shelf circulation. This can be accomplished through analysis of the acoustic Doppler current profiler (ADCP) bottom-track data during periods of ice cover in conjunction with the moored ocean velocity, temperature and salinity

data, oxygen-18 isotope bottle data, numerical model hind-casts and *in situ* ice thickness measurements made on the spring BEST-BSIERP field surveys.

3. Investigate the relative roles of advection and diffusion over the eastern shelf to better understand the locations and rates of water mass mixing and shelf residence times. Employ the oxygen-18 isotope dataset collected as part of the BEST field program along with the satellite-tracked drifter, moored current, temperature, and salinity records.
4. Synthesize historical current meter data with respect to upwelling- and downwelling-favorable wind conditions, using the reanalysis wind products to provide a consistent basis for splitting the modes. This will provide a historical perspective of timing and variability of the two wind conditions and their effects on circulation.
5. Further improve the bathymetric digital elevation model for the Bering Sea by continuing to update it with newly collected bathymetric soundings to further improve the numerical models skill in reproducing observed ocean conditions.
6. Examine the vertical and horizontal structure of cross-isobath exchange along the Bering slope and over the shelf to better understand shelf nutrient replenishment and the shelf salt balance. This analysis needs to be considered in the context of stratification, wind conditions, proximity to canyons, shelfbreak front dynamics, slope flows, and the passage of slope eddies. Numerical model analysis will provide a starting point and can help guide field efforts but an observational program is required (although political constraints preclude access to Gulf of Anadyr *in situ* measurements). Increased model resolution is required to better resolve some processes such as internal wave dynamics at the shelf break.
7. Refine and continue the analysis of wind conditions that generate upwelling and downwelling responses over the shelf under varying levels of stratification in order to better understand the potential for each mode of circulation to impact the shelf conditions.

8. Continue the idealized Bering Sea shelf numerical experiments begun in Chapter 5 through modifications to the rectangular domain with no along-isobath variations. The next iteration (already underway) will include a barotropic model having realistic bathymetry and so will show the influence of local topography on the wind-driven response.
9. Determine the importance of nonlinear motions to cross-isobath exchange in regions where coastal (island or mainland) promontories may generate flow instabilities. This analysis will improve our understanding of water mass mixing and exchange processes here. High-resolution surface-mapping high-frequency radars along with current meter mooring deployments could address this issue.
10. Examine climate forecasts for an indication that shifts in the Aleutian Low under climate warming [*Salathé, 2006*] or variations in the sunspot cycle [*Christoforou and Hameed, 1997*] could seasonally influence the relative wind direction over the shelf. These analyses could lead to better predictions of future conditions over the Bering Sea shelf.

In many respects, my analyses conform with those of *Coachman* [1986], who viewed “the eastern Bering Sea shelf as one large physical system” because I have shown that advective continuity between adjoining portions of the shelf are important to the inter-annual variability of the thermal and haline fields. *Coachman* [1986] and others devoted considerable focus to the diffusive character of this shelf (caused primarily by tidal stirring) and he classified different regions as primarily diffusive, advective or advective-diffusive (Table 10 and Figure 63 of *Coachman* [1986]). These classifications largely hold today, but the results presented here provide a more complete basis from which to consider the heat, salt, fresh water and nutrient budgets. For example, we can now better consider the formation processes of Bering Shelf Water and its dependence on contributions from the southern shelf, the Gulf of Anadyr and coastal Alaskan sources. Advances in our understanding of both the tidal and sub-tidal circulation fields over the

last quarter century dictate that a re-evaluation of *Coachman's* [1986] seminal analysis is now warranted. Such a synthesis will better clarify the balance of advective and diffusive processes for the Bering Sea shelf as a whole and for its many local regions, each with uniquely defining physical, chemical, biological and geological characteristics.

6.3 References

- Christoforou, P., and S. Hameed, 1997. Solar cycle and the Pacific "centers of action", *Geophys. Res. Lett.*, 24, 293-296.
- Coachman, L. K., 1986. Circulation, water masses, and fluxes on the southeastern Bering Sea shelf, *Cont. Shelf Res.*, 5, 23-108.
- Cooper, L.W., J. M. Grebmeier, I. N. Larsen, V. G. Egorov, C. Theodorakis, H. P. Kelly, and J.R. Lovvorn, 2002. Seasonal variation in sedimentation of organic materials in the St. Lawrence Island polynya region, Bering Sea, *Mar. Ecol. Prog. Ser.*, 226, 13-26.
- Hill, A. E., 1996. Spin-down and the dynamics of dense pool gyres in shallow seas, *J. Mar. Res.*, 54, 471-486.
- Kowalik, Z., 1999. Bering Sea Tides, in *Dynamics of The Bering Sea: A Summary of Physical, Chemical and Biological Characteristics, and a Synopsis of Research on the Bering Sea*, edited by T. R. Loughlin and K. Ohtani, pp. 93-127, University of Alaska Sea Grant, Fairbanks, AK.
- Muench, R. D., J. D. Schumacher, and S. A. Salo, 1988. Winter Currents and Hydrographic Conditions on the Northern Central Bering Sea Shelf, *J. Geophys. Res.*, 93(C1), 516-526, doi:10.1029/JC093iC01p00516.
- Niebauer, H. J., N. A. Bond, L. P. Yakunin, and V. V. Plotnikov, 1999. An update on the climatology and sea ice of the Bering Sea, in *Dynamics of The Bering Sea: A Summary of Physical, Chemical and Biological Characteristics, and a Synopsis of Research on the Bering Sea*, edited by T. R. Loughlin and K. Ohtani, pp. 29-59, University of Alaska Sea Grant, Fairbanks, AK.
- Rodionov, S.N., Overland, J.E., Bond, N.A., 2005. The Aleutian low and winter climatic conditions in the Bering Sea. Part I: Classification. *Journal of Climate* 18, 160-177.
- Salathé, E. P., Jr., 2006. Influences of a shift in North Pacific storm tracks on western North American precipitation under global warming, *Geophys. Res. Lett.*, 33, L19820, doi:10.1029/2006GL026882.

Schumacher, J.D., and T.H. Kinder, 1983. Low-frequency current regimes over the Bering Sea shelf, *J. Phys. Oceanogr.*, 13, 607-623.

Stabeno, P. J., N. A. Bond, N. B. Kachel, S. A. Salo, and J. D. Schumacher, 2001. On the temporal variability of the physical environment over the south eastern Bering Sea. *Fish. Oceanogr.* 10 (1), 81-98.

6.4 Figures

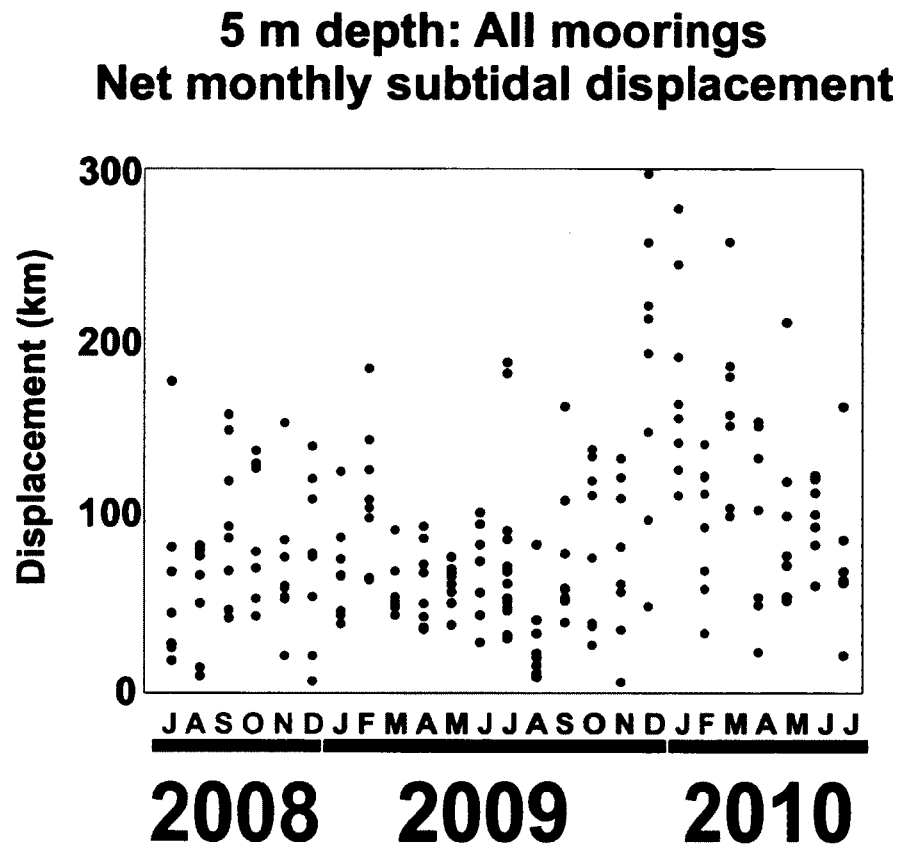


Figure 6.1: Theoretical particle displacements at 5 m depth based on the assumption of spatially uniform flow field. Each dot denotes the monthly mean displacement from one mooring site. Shading denotes months with typically lower winds and higher levels of stratification (May-September).

